

**Experimental Investigation on the Turbulence of Particle-Laden Liquid
Flows in a Vertical Pipe Loop**

By

Rouholluh Shokri

A thesis submitted in partial fulfillment of the requirements for the degree of

Doctor of Philosophy

In

Chemical engineering

Department of Chemical and Materials Engineering

University of Alberta

©Rouholluh Shokri, 2016

Abstract

The turbulent motion of particles and their interactions with the turbulence of the carrier phase make a complex system. Hence understanding the physics and consequently developing a well-established model becomes very difficult. With insufficient computational power to numerically resolve all the scales of these kinds of flows using Direct Numerical Simulation (DNS), experimental investigations still remain the sole source of information for these systems, especially at high Reynolds numbers. Lack of comprehensive experimental data for solid-liquid flows as well as limitation of the existing experimental data to low Reynolds numbers are the motivations for this investigation. The main goal of this research is to experimentally investigate solid-liquid turbulent flows in a vertical pipe and provide some insight into these flows, especially for an extended range of Reynolds numbers.

To fulfil the abovementioned goal, a 50.6 mm vertical pipe loop was constructed and dilute mixtures of water and glass beads were used. The glass bead diameters were 0.5, 1 and 2 mm and the volumetric concentration ranged from 0.05 to 1.6% depending on the particle size. The experiments were performed at three Reynolds numbers: 52 000, 100 000, and 320 000 which are referred to here as low, medium and high Re . A combined technique of Particle Image/Tracking velocimetry (PIV/PTV) was employed to perform the measurements. The measured and reported flow parameters are: mean axial velocity profiles of the solid and liquid phases, particle distribution over the cross section of the pipe (concentration profile), particle-particle interaction index, axial and radial fluctuating velocity profiles of both phases, and shear Reynolds stress and its correlation for both phases. The relatively wide range of different parameters tested here provided interesting and novel experimental results.

The results showed that the turbulent motions of the fluid and particles and their interactions varied drastically as Re increased. Moreover, the behavior of the particles and their impact on the fluid can be very different in the axial and radial directions. The results proved that the well-known criteria for axial turbulence modulation of the carrier phase could not perform well at high Reynolds numbers and their performance was much poorer for the radial direction modulation. The new data sets provided by the present study offer valuable insight into the processes or phenomena heavily influenced by turbulence, such as pipe wear rate, oil sand lump ablation, and pressure loss/energy consumption. In addition, these data sets can be utilised to evaluate and improve the existing correlations and models for particulate turbulent flows.

In addition, a quantitative analysis of the particle and carrier phase turbulence modulation was conducted. Particle turbulence intensities in present study were combined with other experimental data from the literature to propose a novel empirical correlation was proposed for axial particle turbulence in solid-liquid flows. Moreover, a novel empirical criterion/correlation was proposed to classify the carrier phase turbulence attenuation/augmentation phenomenon for both gas-solid and liquid-solid flows by employing a wide range of data from the present study and from the literature. Two major improvements of the proposed criterion/correlation are the prediction of the onset and the magnitude of the carrier phase turbulence augmentation. These new empirical correlations will assist the researchers in this field to effectively design and coordinate their experimental or numerical efforts.

Dedication:

This thesis is dedicated to my late father and my mother, for standing by me when no one else would.

Acknowledgements

It is needless to say that this dissertation would not be completed if there were not so many kind helping hands to assist me during my PhD program.

First and foremost, I would like to express my sincere appreciation and thanks to my supervisor *Dr. Sean Sanders* who provided me with the financial and technical support throughout this program. I would like to thank you for giving me the opportunities and allowing me to grow as a research scientist. In the face of many hardships and difficulties, it was you who graciously assisted me to move forward and accomplish things that I feared the most. You have been a tremendous mentor for me and your support and patience with me will not be forgotten.

I would especially like to extend my gratitude to my co-supervisor, Dr. David Nobes for his great technical contribution. Your in-depth mentorship and highly needed assistance during the program was crucial to the success of this dissertation. I would also like to offer my unconditional appreciation to Dr. Sina Ghaemi. Your invaluable and brilliant comments and suggestions for analysing and processing the data are greatly appreciated.

I would like to thank Ms. Terry Runyon which her kind assistance throughout this program. Moreover I would like to thank the technicians and staff of the Chemical and Materials Engineering Departments for their help. I should also thank all my colleague and friends for their help during my PhD.

This research was conducted through the support of the *NSERC Industrial Research Chair in Pipeline Transport Processes (RSS)*. The contributions of Canada's

Natural Sciences and Engineering Research Council (NSERC) and the Industrial Sponsors (Canadian Natural Resources Limited, CNOOC-Nexen Inc., Saskatchewan Research Council's Pipe Flow Technology CentreTM, Shell Canada Energy, Suncor Energy, Syncrude Canada Ltd., Total E&P Canada Ltd., Teck Resources Ltd., and Paterson & Cooke Consulting Engineering Ltd.) are recognized with gratitude.

Finally I could not thank enough my family for their support and love which made it possible for me to peruse my education to this stage.

Table of Contents

1	Introduction.....	1
1.1	Particulate turbulent flows: Governing equations	3
1.1.1	Single-phase turbulent flows	3
1.1.2	Two-phase turbulent flows	5
1.2	Particulate turbulent flows: experimental investigations	9
1.2.1	Carrier phase turbulence.....	16
1.2.2	Particulate phase turbulence	20
1.2.3	Summary and conclusions.....	24
1.3	Objectives.....	26
1.4	Contribution of the present study	26
1.5	Thesis outline	28
2	Experimental Setup and Measurement Techniques.....	30
2.1	Introduction	30
2.2	Experimental setup	30
2.3	Experimental conditions.....	32
2.4	Flow loop operation.....	34
2.5	PIV/PTV measurements	35
2.5.1	Imaging setup	40
2.5.2	Particle detection	43

2.5.3	PIV process.....	46
2.5.4	PTV process	48
2.6	Uncertainty analysis	52
2.6.1	Error/uncertainty sources	53
2.6.2	Random (precision) uncertainty level	57
3	Investigation of particle-laden turbulent pipe flow at high-Reynolds-number using particle image/tracking velocimetry (PIV/PTV)	59
3.1	Introduction	59
3.2	Experiments.....	68
3.2.1	Flow loop.....	68
3.2.2	PIV/PTV technique	70
3.2.3	Particle dynamics	75
3.3	Results	77
3.3.1	Mean velocity profiles.....	78
3.3.2	Particle concentration and interactions.....	82
3.3.3	Turbulent fluctuations	87
3.3.4	Ejection and sweep motions	91
3.4	Discussion: Fluid-phase turbulence and particle fluctuations.....	94
3.5	Conclusions	99
4	The particle size and concentration effects on fluid/particle turbulence in vertical pipe flow of a liquid-continuous suspension.....	102

4.1	Introduction	102
4.1.1	Carrier phase turbulence.....	103
4.1.2	Particulate phase turbulence.....	107
4.2	Experimental setup	110
4.3	Measurement techniques	114
4.4	Results and discussion.....	119
4.4.1	Mean velocity profiles.....	119
4.4.2	Turbulent fluctuation profiles.....	122
4.4.3	Shear Reynolds stress and correlation coefficient profiles.....	128
4.5	Conclusion.....	132
5	A quantitative analysis of the axial and carrier fluid turbulence intensities	134
5.1	Introduction	134
5.2	Experiments and measurement techniques.....	139
5.3	Results	143
5.3.1	Mean velocity profiles.....	144
5.3.2	Concentration profile.....	146
5.3.3	Turbulent fluctuations	148
5.3.4	Correlation between streamwise and radial fluctuations.....	152
5.4	Discussion	156
5.4.1	Turbulent fluctuations of particles	156

5.4.2	Turbulence modulation of the liquid phase	162
5.5	Conclusion.....	165
6	Conclusion and Future Work.....	168
6.1	General Conclusion	168
6.2	Novel contributions	171
6.3	Recommendations for future work.....	172
6.3.1	PIV/PTV measurements	173
6.3.2	Expanding the matrix of experiments	174
6.3.3	Correlations and models	175
	References	177
	Appendix A. Pump curve	198
	Appendix B. Comparison of measured single phase turbulence intensities with the literature	199
	Appendix C. Symmetry of the velocity profiles.....	208
	Appendix D. Extra Plot	212
	Appendix E. Uncertainty Plots	213
	Appendix F. PIV/PTV Matlab Code	239

List of Tables

Table 1-1. An overview of experimental investigations of particle-laden turbulent flows.....	14
Table 2-1: Matrix of experimental conditions	33
Table 2-2. Solid particle specifications obtained through PTV processing.	51
Table 3-1. An overview of experimental investigations of particle-laden turbulent flows.	61
Table 3-2. Matrix of the test conditions	69
Table 3-3. Particle specifications obtained through PTV processing.	73
Table 3-4. Particle response time, Stokes number and particle Reynolds number at the pipe centerline.	77
Table 3-5. Slip velocity at the pipe centerline and particle terminal settling velocity for different particles tested during the present investigation.	80
Table 4-1. Details of the experimental data shown in Fig.4-1.....	106
Table 4-2. Experimental conditions tested during the current investigation	112
Table 4-3. Particle specifications obtained through PTV processing.	118
Table 4-4. Classification of carrier phase turbulence modulation using three well-known criteria.....	123
Table 5-1. Matrix of the experiments.....	141
Table 5-2. Experimental data used in Figs.5-6 and 5-7.	157
Table 5-3. Experimental data used in Fig.5-8	164

List of Figures

Figure 1-1. Map of interactions in two-phase disperse flow (Elghobashi, 1991)	10
Figure 2-1. Schematic of the experimental setup consisting of (1) camera (2) laser, (3) acrylic pipe and viewing box, (4) magnetic flow meters, (5) double pipe heat exchanger, (6)-Feeding tank, (7) and centrifugal pump.....	34
Figure 2-2. Schematic of a planar PIV technique (Flow Master, 2007)	37
Figure 2-3. Schematic of phase discrimination and PTV procedure from Nezu et al., (2004) (With permission from ASCE).....	38
Figure 2-4. PIV/shadowgraphy of the bubbly flow using fluorescent tracers. The gray values along the crossing lines are shown on the bottom and right axes (Lindken and Merzkirch, 2002) (With permission from Springer).	40
Figure 2-5. Calibration target assembly	43
Figure 2-6. (a) the image of the target, (b) corrected image after calibration.....	43
Figure 2-7. Circle detection by CHT method. The dashed circles are defined based on the black dots (edge pixels) as their centers. Solid line circle is the detected one, with the red dot as its center.....	45
Figure 2-8. (a) A raw image showing the full field-of-view with 2 mm glass beads and PIV tracer particles ($\phi_v=0.8\%$, $Re=320\,000$). Note that $r/R=0$ and $r/R=1$ denote pipe centreline and pipe wall, respectively, while x/R is the streamwise (upward) direction. (b) Magnified view of the region identified by the red boundary specified in the full field-of-view image in (a). (c) Magnified view with in-focus and out-of-focus particles detected using the low edge-detection threshold later to be masked out for PIV	

analysis of the liquid phase. (d) Magnified view of the in-focus particles detected using the high-gradient threshold for PTV analysis 46

Figure 2-9. The PIV procedure for two-phase flow, (a) raw image of 2mm particles ($\phi_v=0.8\%$, $Re=320\,000$), (b) particles are detected and marked in Matlab, (c) image with the masked out particles in Davis 8.2 software, (d) applying cross correlation to obtain the instantaneous velocity of the flow field 48

Figure 2-10. Particle displacement population in (a) streamwise and (b) radial directions at the pipe centerline for 1mm glass beads at $Re=100\,000$, $\phi_v=0.4\%$ 50

Figure 2-11. Particle size distribution obtained from PTV analysis at $Re=100\,000$ 52

Figure 2-12. Cumulative distribution of particle size difference between frame#1 and frame#2 at $Re=100\,000$ 52

Figure 2-13. The effect of particle size on the discretization error (Ghaemi et al., 2010) (With permission from John Wiley and Sons). 56

Figure 2-14. Convergence of $\langle u^2 \rangle$ for 2mm particles, $Re=100\,000$, $\phi_v=0.8\%$ at (a) $r/R=0$, (b) $r/R=0.5$ and (c) $r/R=0.96$ 58

Figure 2-15. Convergence of $\langle u^2 \rangle$ for liquid phase laden with 2mm particles, $Re=100\,000$, $\phi_v=0.8\%$ at (a) $r/R=0$, (b) $r/R=0.5$ and (c) $r/R=0.96$ 58

Figure 3-1. A schematic of the experimental setup, which consists of (1) camera, (2) laser, (3) acrylic pipe and viewing box, (4) magnetic flow meters, (5) double-pipe heat exchanger, (6) feeding tank, (7) and the centrifugal pump, frequency drive and motor. 69

Figure β-2. (a) A raw image showing the full field-of-view with 2 mm glass beads and PIV tracer particles. Note that $r/R=0$ and $r/R=1$ denote pipe centreline and pipe wall, respectively, while x/R is the streamwise (upward) direction; (b) Magnified view of the region identified by the red boundary specified in the full field-of-view image in (a); (c) Magnified view with in-focus and out-of-focus particles detected using the low edge-detection threshold later to be masked out for PIV analysis of the liquid phase; (d) Magnified view of the in-focus particles detected using the high-gradient threshold for PTV analysis. 72

Figure β-3. Particle size distributions of the 0.5, 1 and 2 mm glass beads obtained from the images obtained for PTV analysis. 74

Figure β-4. Cumulative distribution of the difference in the diameter of paired glass beads detected in frame #1 and frame #2 of two successive images captured for PTV analysis. 75

Figure β-5. Mean velocity profiles for liquid and solid phases. 81

Figure β-6. (a) Normalized particle number density distributions and, (b) particle-particle interaction index profiles. 86

Figure β-7. (a) Streamwise turbulent fluctuations, (b) Radial fluctuating velocities, (c) Reynolds stresses $\langle uv \rangle$ for liquid and solid phases. 90

Figure β-8. Correlation strength of turbulent motions for fluid and particles across the pipe radius. 92

Figure β-9. Quadrant plots of u and v and average fluctuating vectors of each quadrant for (a&b) unladen liquid phase, (c&d) 0.5 mm and (e&f) 2 mm particles at $r/R=0$, and $r/R=0.96$ respectively. 94

Figure 3-10. Streamwise turbulence augmentation as a function of the ratio of the particle terminal settling velocity to the bulk liquid velocity. Only data sets for liquid-solid flows with relatively large particles, which produce liquid-phase turbulence augmentation, are included. 96

Figure 4-1. Axial fluid turbulence modulation versus particle concentration using experimental data from literature. The abbreviations used in the legend are described in detail in Table 4-1. 106

Figure 4-2. Schematic of the test rig consisting of (1) camera, (2) laser, (3) acrylic pipe and viewing box, (4) magnetic flow meters, (5) double-pipe heat exchanger, (6) feed tank, (7) and the centrifugal pump. 111

Figure 4-3. (a) A raw image showing the full field-of-view with 2 mm glass beads at $\phi_v=1.6\%$ and PIV tracer particles. The axis titles: r/R specifies the radial direction and x/R specifies the streamwise (upward) direction. (b) Magnified view of the highlighted area (outlined in red) in the full field-of-view image. (c) In-focus and out-of-focus particles are detected using the low edge-detection threshold. (d) In-focus particles detected using the high edge-detection threshold for PTV analysis. 116

Figure 4-4. (a) Particle size distributions obtained from PTV analysis, (b) Cumulative distribution of the difference in the diameter of pairs of glass beads detected in frame #1 and frame #2. The legend applies to both plots. 118

Figure 4-5. Velocity profiles of the liquid phase and the glass beads: (a) 0.5 mm, (b) 1 mm and (c) 2 mm. 121

Figure 4-6. (a), (c), (e) Streamwise and, (b), (d), (f) radial fluctuations of liquid and particles. The legend of each plot on the left applies also to the corresponding plot on the right. 124

Figure 4-7. (a), (c), (e) $\langle uv \rangle$ and, (b), (d), (f) C_{uv} of the liquid and particles over the pipe cross section. The legends of the plots on the left also apply to the corresponding figure on the right. 131

Figure 5-1. A schematic of the experimental setup consisting of (1) camera, (2) laser, (3) acrylic pipe and viewing box, (4) magnetic flow meters, (5) double-pipe heat exchanger, (6) feeding tank, (7) and the centrifugal pump. 142

Figure 5-2. (a) Mean velocity profiles of liquid and 2mm glass beads, (b) velocity profiles of unladen liquid and 2mm glass beads normalized by the centerline liquid velocity (U_c) at different Re 145

Figure 5-3. Concentration profile of 2 mm particles at different Re 147

Figure 5-4. Streamwise and radial fluctuations of liquid and solid particles. The legends of the plot on the right side are the same as the left one. 150

Figure 5-5. $\langle uv \rangle$ correlation and C_{uv} of liquid and solid particles over pipe cross section. The legends of the plot on the right side are the same as the left one 154

Figure 5-6. $\langle uv \rangle$ correlation Streamwise turbulence intensity and (b) radial turbulence intensity of particles vs Ψ' . The legend applies to both graphs. 161

Figure 5-7. Streamwise turbulence intensity (Ti_{xp}) and (b) radial turbulence intensity (Ti_{rp}) of particles vs. Ψ and fitted curves. The legend applies to both plots. ... 162

Figure 5-8. Mean streamwise turbulence modulation (Mx) vs $\log(\chi)$ and proposed correlation 165

Figure 1-1. Map of interactions in two-phase disperse flow (Elghobashi, 1991)	10
Figure 2-1. Schematic of the experimental setup consisting of (1) camera (2) laser, (3) acrylic pipe and viewing box, (4) magnetic flow meters, (5) double pipe heat exchanger, (6)-Feeding tank, (7) and centrifugal pump.....	34
Figure 2-2. Schematic of a planar PIV technique (Flow Master, 2007)	37
Figure 2-3. Schematic of phase discrimination and PTV procedure from Nezu et al., (2004) (With permission from ASCE).....	38
Figure 2-4. PIV/shadowgraphy of the bubbly flow using fluorescent tracers. The gray values along the crossing lines are shown on the bottom and right axes (Lindken and Merzkirch, 2002) (With permission from Springer).	40
Figure 2-5. Calibration target assembly	43
Figure 2-6. (a) the image of the target, (b) corrected image after calibration.....	43
Figure 2-7. Circle detection by CHT method. The dashed circles are defined based on the black dots (edge pixels) as their centers. Solid line circle is the detected one, with the red dot as its center.....	45
Figure 2-8. (a) A raw image showing the full field-of-view with 2 mm glass beads and PIV tracer particles ($\phi_v=0.8\%$, $Re=320\,000$). Note that $r/R=0$ and $r/R=1$ denote pipe centreline and pipe wall, respectively, while x/R is the streamwise (upward) direction. (b) Magnified view of the region identified by the red boundary specified in the full field-of-view image in (a). (c) Magnified view with in-focus and out-of-focus	

particles detected using the low edge-detection threshold later to be masked out for PIV analysis of the liquid phase. (d) Magnified view of the in-focus particles detected using the high-gradient threshold for PTV analysis 46

Figure 2-9. The PIV procedure for two-phase flow, (a) raw image of 2mm particles ($\phi_v=0.8\%$, $Re=320\,000$), (b) particles are detected and marked in Matlab, (b) image with the masked out particles in Davis 8.2 software, (d) applying cross correlation to obtain the instantaneous velocity of the flow field 48

Figure 2-10. Particle displacement population in (a) streamwise and (b) radial directions at the pipe centerline for 1mm glass beads at $Re=100\,000$, $\phi_v=0.4\%$ 50

Figure 2-11. Particle size distribution obtained from PTV analysis at $Re=100\,000$ 52

Figure 2-12. Cumulative distribution of particle size difference between frame#1 and frame#2 at $Re=100\,000$ 52

Figure 2-13. The effect of particle size on the discretization error (Ghaemi et al., 2010) (With permission from John Wiley and Sons)..... 56

Figure 2-14. Convergence of $\langle u^2 \rangle$ for 2mm particles, $Re=100\,000$, $\phi_v=0.8\%$ at (a) $r/R=0$, (b) $r/R=0.5$ and (c) $r/R=0.96$ 58

Figure 2-15. Convergence of $\langle u^2 \rangle$ for liquid phase laden with 2mm particles, $Re=100\,000$, $\phi_v=0.8\%$ at (a) $r/R=0$, (b) $r/R=0.5$ and (c) $r/R=0.96$ 58

Figure 3-1. A schematic of the experimental setup, which consists of (1) camera, (2) laser, (3) acrylic pipe and viewing box, (4) magnetic flow meters, (5) double-pipe heat exchanger, (6) feeding tank, (7) and the centrifugal pump, frequency drive and motor. 69

Figure β-2. (a) A raw image showing the full field-of-view with 2 mm glass beads and PIV tracer particles. Note that $r/R=0$ and $r/R=1$ denote pipe centreline and pipe wall, respectively, while x/R is the streamwise (upward) direction; (b) Magnified view of the region identified by the red boundary specified in the full field-of-view image in (a); (c) Magnified view with in-focus and out-of-focus particles detected using the low edge-detection threshold later to be masked out for PIV analysis of the liquid phase; (d) Magnified view of the in-focus particles detected using the high-gradient threshold for PTV analysis. 72

Figure β-3. Particle size distributions of the 0.5, 1 and 2 mm glass beads obtained from the images obtained for PTV analysis. 74

Figure β-4. Cumulative distribution of the difference in the diameter of paired glass beads detected in frame #1 and frame #2 of two successive images captured for PTV analysis. 75

Figure β-5. Mean velocity profiles for liquid and solid phases. 81

Figure β-6. (a) Normalized particle number density distributions and, (b) particle-particle interaction index profiles. 86

Figure β-7. (a) Streamwise turbulent fluctuations, (b) Radial fluctuating velocities, (c) Reynolds stresses $\langle uv \rangle$ for liquid and solid phases. 90

Figure β-8. Correlation strength of turbulent motions for fluid and particles across the pipe radius. 92

Figure β-9. Quadrant plots of u and v and average fluctuating vectors of each quadrant for (a&b) unladen liquid phase, (c&d) 0.5 mm and (e&f) 2 mm particles at $r/R=0$, and $r/R=0.96$ respectively. 94

Figure 3-10. Streamwise turbulence augmentation as a function of the ratio of the particle terminal settling velocity to the bulk liquid velocity. Only data sets for liquid-solid flows with relatively large particles, which produce liquid-phase turbulence augmentation, are included. 96

Figure 4-1. Axial fluid turbulence modulation versus particle concentration using experimental data from literature. The abbreviations used in the legend are described in detail in Table 4-1. 106

Figure 4-2. Schematic of the test rig consisting of (1) camera, (2) laser, (3) acrylic pipe and viewing box, (4) magnetic flow meters, (5) double-pipe heat exchanger, (6) feed tank, (7) and the centrifugal pump. 111

Figure 4-3. (a) A raw image showing the full field-of-view with 2 mm glass beads at $\phi_v=1.6\%$ and PIV tracer particles. The axis titles: r/R specifies the radial direction and x/R specifies the streamwise (upward) direction. (b) Magnified view of the highlighted area (outlined in red) in the full field-of-view image. (c) In-focus and out-of-focus particles are detected using the low edge-detection threshold. (d) In-focus particles detected using the high edge-detection threshold for PTV analysis. 116

Figure 4-4. (a) Particle size distributions obtained from PTV analysis, (b) Cumulative distribution of the difference in the diameter of pairs of glass beads detected in frame #1 and frame #2. The legend applies to both plots. 118

Figure 4-5. Velocity profiles of the liquid phase and the glass beads: (a) 0.5 mm, (b) 1 mm and (c) 2 mm. 121

Figure 4-6. (a), (c), (e) Streamwise and, (b), (d), (f) radial fluctuations of liquid and particles. The legend of each plot on the left applies also to the corresponding plot on the right.	124
Figure 4-7. (a), (c), (e) $\langle uv \rangle$ and, (b), (d), (f) C_{uv} of the liquid and particles over the pipe cross section. The legends of the plots on the left also apply to the corresponding figure on the right.	131
Figure 5-1. A schematic of the experimental setup consisting of (1) camera, (2) laser, (3) acrylic pipe and viewing box, (4) magnetic flow meters, (5) double-pipe heat exchanger, (6) feeding tank, (7) and the centrifugal pump.	142
Figure 5-2. (a) Mean velocity profiles of liquid and 2mm glass beads, (b) velocity profiles of unladen liquid and 2mm glass beads normalized by the centerline liquid velocity (U_c) at different Re	145
Figure 5-3. Concentration profile of 2 mm particles at different Re	147
Figure 5-4. Streamwise and radial fluctuations of liquid and solid particles. The legends of the plot on the right side are the same as the left one.	150
Figure 5-5. $\langle uv \rangle$ correlation and C_{uv} of liquid and solid particles over pipe cross section. The legends of the plot on the right side are the same as the left one.	154
Figure 5-6. $\langle uv \rangle$ correlation Streamwise turbulence intensity and (b) radial turbulence intensity of particles vs Ψ' . The legend applies to both graphs.	161
Figure 5-7. Streamwise turbulence intensity (Ti_{xp}) and (b) radial turbulence intensity (Ti_{rp}) of particles vs. Ψ and fitted curves. The legend applies to both plots. ...	162
Figure 5-8. Mean streamwise turbulence modulation (Mx) vs $\log(\chi)$ and proposed correlation.	165

List of Symbols

Symbol	Description	Unit
C_D	Drag Coefficient	---
C_L	Lift Coefficient	---
C_{uv}	Correlation coefficient	---
D	Pipe internal diameter	m
d_p	Particle size	m
F_g	Gravity Force	N
F_{vm}	Virtual mass Force	N
F_D	Drag force	N
F_{Ba}	Basset force	N
F_{pr}	Pressure force	N
F_L	Lift force	N
$f_{\#}$	Lens f-stop number	---
f_D	Darcy friction factor	---
f_{pp}	Particle-particle interaction index	---
f_d	Correction factor	---
g	Gravitational constant	m/s ²
k	Turbulent kinetic energy	m ² /s ²
L	Characteristic length of flow	m
l_e	Most energetic eddy length scale	m
l_m	Integral turbulence length scale	m
M	Turbulence Modulation	---
M_c	Camera magnification	---
m	mass	Kg
N_p	Number of particle at radial location	---
N_{total}	Total number of particle over cross section	---
P	Pressure	Pa
Pa_{st}	Particle moment number	---
R	Pipe radius	m
Re	Reynolds number	---
Re_p	Particle Reynolds number	---
r	Radial position	m

St_c	Collisional Stokes number	---
St_k	Kolmogorov Stokes number	---
St_L	Integral Stokes number	---
Ti	Turbulence intensity	---
t	Time	s
\tilde{u}	Instantaneous velocity	m/s
U	Axial average velocity	m/s
U_s	Slip velocity	m/s
U_τ	Friction velocity	m/s
U_b	Bulk velocity	m/s
U_c	Centerline velocity	m/s
u	Axial fluctuating velocity	m/s
uv	Reynolds shear stress	m^2/s^2
V	Radial average radial velocity	m/s
V_t	Terminal velocity	m/s
v	Radial fluctuating velocity	m/s
x	Axial position	m
ε	Dissipation rate of turbulent kinetic energy	m^2/s^3
η_k	Kolmogorov turbulence length scale	m
λ	Particle interspacing distance	m
λ_w	Laser wavelength	nm
μ_f	Fluid viscosity	Pa.s
μ_t	Eddy viscosity	Pa.s
ρ	Density	kg/m^3
τ_p	Particle response time	s
τ_L	Integral turbulence time scale	s
τ_k	Kolmogorov turbulence time scale	s
τ_c	Time between collisions	s
τ_w	Wall shear	Pa
ν	Kinematic viscosity	m^2/s
φ_m	Particle mass fraction	---
φ_v	Particle volume fraction	---

Subscripts

Symbol	Description
f	Fluid
i, j	Vector index notation
p	Particle
r	Radial direction
x	Axial (flow) direction

1 Introduction

Turbulence and turbulent flows have been a challenging topic for researchers of fluid dynamics for many decades. Many researchers continue to develop a better understanding of the concept of turbulence in single-phase flows (Eswaran, 2002). Due to the much higher complexity of multiphase flows, we are still in the very early stages of modelling them (Kolev, 2012; Balachandar and Eaton, 2010; Ekambara et al., 2009). Despite our lack of understanding, we wish to operate under turbulent conditions since heat and mass transfer processes are enhanced (over laminar flow); as well, turbulence is required for efficient particle suspension and transport during the operation of slurry pipelines (Gillies et al., 2004). Slurry transportation pipelines are a critical component of production facilities in the mining and mineral processing industries. In 2014, the total of Alberta bitumen production from mining was 379×10^6 barrels (Alberta Energy, 2015). The oil sands ore is composed of only a small fraction by bitumen (on average <12 % by weight) and large amounts of solids (84-86 % by weight) (Masliyah, 2009). Therefore, one can appreciate the importance of these pipelines for oil sands production when considering that such a huge amount of solids must enter and exit the plants in slurry form via pipelines. A great deal of work has been done to predict slurry pipeline design parameters including deposition velocity, pressure drop and delivered solids volume fraction (Wilson et al., 2006; Shook et al., 2002; Gillies and Shook, 2000; Doron and Barnea, 1993; Doron et al., 1987; Thomas, 1979). The SRC two-layer model is

commonly used to design and operate such pipelines (Gillies et al., 2004). The model was developed by the Saskatchewan Research Council (SRC) over decades of experimental studies and advances in slurry flow modeling (Spelay et al., 2015; Spelay et al., 2013; Shook et al., 2002; Gillies et al., 2000). This model uses macroscopic parameters as inputs to predict the required design parameters. The model is not appropriate for complex geometries (e.g. pumps, hydrocyclones) and cannot be used for three-phase systems. Moreover, the model cannot predict the local properties of the flow such as particle velocity, which is critical information for modeling pipeline erosion (Shook et al., 1990). To overcome these shortcomings we need to use a more advanced tool such as CFD, which is capable of providing information on both the macroscopic and microscopic scales.

Over the past 20 years, CFD has become a very reliable tool to investigate fluid flow behaviour in single-phase systems, but is still in its infancy in terms of highly concentrated flows. There are still many empiricisms and uncertainties in the CFD modelling of multiphase flows (Ekambara et al., 2009; Grace and Taghipour, 2004). One unresolved issue is that knowledge of the interaction of particles and the turbulence structures of the suspending fluid is limited; thus we are left to treat the problem assuming our perception of turbulence in single-phase flows is appropriate. In order to cope with the complexity of particle-laden turbulent flows, the first and most crucial step is to provide some experimental data. Thus, this thesis is primarily designed to provide some much needed experimental data for dilute slurry flows and to discuss the parameters that influence the turbulent motion of the particles and liquid phase.

1.1 Particulate turbulent flows: Governing equations

Since particulate flows mostly operate under turbulent conditions and the aim of this project is to investigate the turbulence characteristics of both the particulate and carrier phases, a summary of the basic concepts of turbulence and the corresponding equations describing the single-phase turbulent flows are first introduced. In the subsequent section, two-phase turbulent flows and the corresponding equations for both phases are discussed.

1.1.1 Single-phase turbulent flows

Turbulence occurs every day in many natural and engineering processes such as flows in rivers, pumps, compressors and around cars and ships (Pope, 2006; Tennekes and Lumley, 1972). An essential feature of turbulent flows is that the fluid velocity field varies in both space and time. Furthermore, this variation is always irregular and non-uniform, which makes it difficult to predict and model. Turbulence enhances the rates of mixing of mass, momentum transfer, and heat transfer in those industrial applications which makes the understanding and modelling of turbulence very valuable (Pope, 2006; Bernards and Wallace, 2002; Tennekes and Lumely, 1972; Hinz, 1959).

In turbulent flow, instantaneous velocity in i^{th} direction (\tilde{u}_i) can be decomposed using the Reynolds averaging method into a mean flow velocity (U_i) and fluctuating velocity (u_i) i.e. $i_i = U_i + u_i$. After applying the Reynolds averaging method, the continuity and Navier-Stokes equations for single-phase flow can be expressed as:

$$\frac{\partial \rho_f}{\partial t} + \frac{\partial}{\partial x_i} (\rho_f U_i) = 0 \quad (1-1)$$

$$\rho_f \left(\frac{\partial U_i}{\partial t} + U_j \frac{\partial U_i}{\partial x_j} \right) = \rho_f g_i - \frac{\partial P}{\partial x_i} + \frac{\partial}{\partial x_j} \left(\mu_f \frac{\partial U_i}{\partial x_j} - \rho_f \langle u_i u_j \rangle \right) \quad (1-2)$$

In the equations above, i and j are the index notations indicating direction and “ $\langle \rangle$ ” denotes the averaging operator. Also, ρ_f and μ_f are the fluid density and viscosity, respectively. The new additional term ($-\rho_f \langle u_i u_j \rangle$) is called the Reynolds stress tensor. Since those are unknown parameters, additional equations are needed to specify them. Many models have been adopted to evaluate these unknown fluctuating velocities (i.e. Reynolds stress tensor) by relating them to the mean flow variables: examples include the Reynolds stress model (RSM), eddy-viscosity models (EVM), and algebraic Reynolds stress models (ARSM) (Versteeg and Malalasekera, 1995). For instance, the EVM model uses the Boussinesq approximation to model the Reynolds stress (Versteeg and Malalasekera, 1995):

$$-\rho_f \langle u_i u_j \rangle = \mu_t \left(\frac{\partial U_i}{\partial x_j} + \frac{\partial U_j}{\partial x_i} \right) \quad (1-3)$$

where μ_t is the turbulent viscosity. To obtain μ_t , one can use models, such as the k - ε model, which is one of the most common EVM models. In this model two new variables are introduced: turbulence kinetic energy (k) and the rate of turbulence energy dissipation (ε):

$$k = \frac{1}{2} \langle u_i^2 \rangle \quad (1-4)$$

$$\varepsilon = \nu_f \left(\left\langle \frac{\partial u_i}{\partial x_j} \frac{\partial u_i}{\partial x_j} \right\rangle \right) \quad (1-5)$$

where ν_f is the fluid kinematic viscosity. Finally, μ_t can be defined as following:

$$\mu_t = C_\mu \rho_f \frac{k^2}{\varepsilon} \quad (1-6)$$

where C_μ is a constant. Eventually, the system of equations will be “closed” by writing the transport equations for k and ε (Versteeg and Malalasekera, 1995):

$$\rho_f \frac{Dk}{Dt} = \mu_t \left(\frac{\partial U_i}{\partial x_j} + \frac{\partial U_j}{\partial x_i} \right) \frac{\partial U_i}{\partial x_j} + \frac{\partial}{\partial x_j} \left(\frac{\mu_t}{\sigma_k} \frac{\partial k}{\partial x_j} \right) - \rho_f \varepsilon \quad (1-7)$$

$$\rho_f \frac{D\varepsilon}{Dt} = C_1 \mu_t \frac{\varepsilon}{k} \left(\frac{\partial U_i}{\partial x_j} + \frac{\partial U_j}{\partial x_i} \right) \frac{\partial U_i}{\partial x_j} + \frac{\partial}{\partial x_j} \left(\frac{\mu_t}{\sigma_\varepsilon} \frac{\partial \varepsilon}{\partial x_j} \right) - C_2 \rho_f \frac{\varepsilon^2}{k} \quad (1-8)$$

These equations (Eqs.1-6 to 1-8) represent the standard form of the k - ε model. The adjustable constants used in the standard form are $C_1=1.44$, $C_2=1.92$, $C_\mu=0.09$, $\sigma_k=1.0$, $\sigma_\varepsilon=1.3$ (Yan et al., 2006; Lightstone and Hodgson, 2004). These values were obtained through a comprehensive data fitting exercise, conducted with a huge number of data sets including many turbulent flow experiments (Versteeg and Malalasekera, 1995). Other forms of the k - ε model are also described in the literature. These have been developed to improve predictive capabilities under different flow conditions (see, for example, Lai and Yang, 1997; Hrenya and Bolio, 1995).

1.1.2 Two-phase turbulent flows

Due to the presence of two separate phases, the modelling approaches and hence the governing equations are classified into two main categories: Eulerian-Eulerian and Eulerian-Lagrangian. In the Eulerian-Eulerian approach, which is often referred to as a

“two-fluid Model”, each phase is considered as a separate continuous phase (Gidaspow, 1994; Ishii and Mishima, 1984). The governing equations are provided for both phases in the Eulerian framework. Therefore, two sets of conservation equations (mass, momentum and energy) are given for each phase. For particulate flows, the solid phase is modeled by kinetic theory of granular flow, which is based on the classical kinetic theory of gasses (Ekambara et al., 2009; Huilin and Gidaspow, 2003; Boemer et al., 1997; Ding and Gidaspow, 1990).

In the Eulerian-Lagrangian method, the fluid phase is modelled using the Eulerian approach and the governing equations for the particulate phase are derived based on a Lagrangian approach. This method tracks each individual particle throughout the system by accounting for the forces acting on each particle. This approach provides superior predictions of the dynamics of the dispersed phase compared to the Eulerian-Eulerian method but the disadvantage is that it is limited to low concentration (dilute) flows (De Jong et al., 2012; Shams et al., 2010). Below, the governing equations first for the fluid phase and then for the particulate phase are described.

The Reynolds-averaged continuity and momentum equations for the fluid phase can be written as (Liu et al., 2013; Alvandifar et al., 2011):

$$\frac{\partial}{\partial t}((1 - \varphi_v)\rho_f) + \frac{\partial}{\partial x_i}((1 - \varphi_v)\rho_f U_{f,i}) = 0 \quad (1-9)$$

$$\frac{\partial}{\partial t}((1 - \varphi_v)\rho_f U_{f,i}) + \frac{\partial}{\partial x_j}((1 - \varphi_v)\rho_f U_{f,j} U_{f,i}) = -(1 - \varphi_v) \frac{\partial P}{\partial x_i} \quad (1-10)$$

$$- \frac{\partial}{\partial x_j} \left(\rho_f (1 - \varphi_v) (\mu_f + \mu_t) \left[\frac{\partial U_{f,i}}{\partial x_j} + \frac{\partial U_{f,i}}{\partial x_i} \right] \right) + (1 - \varphi_v) \rho_f g_i + S_{pf,i}$$

In these equations, ϕ_v is the particle volume fraction, S_{pf} is the force exerted on the fluid by the particulate phase and the subscript f represents the “fluid” phase. Since the same closure problem described in the previous section for single-phase turbulence flows still exists, the Reynolds stress tensor must be modeled here as well. However, the Reynolds stress tensor will not be the same for two-phase flows due to the interactions between the fluid turbulence and the particles. A number of studies model the Reynolds stresses for particle-laden flows using the k- ϵ methods with the addition of the terms S_{kp} and S_{ep} to Eqs. (1-7) and (1-8), respectively, which account for presence of the particles (see, for example, Messa and Malavasi, 2014; Mando and Yin, 2012; Lightstone and Hodgson, 2004; Tu and Fletcher, 1994; Mostafa and Mongia, 1988; Chen and Wood, 1985).

For the particulate phase in the Eulerian-Lagrangian approach, Newton’s second law is used to obtain the particle velocity by considering all the affecting forces on the particle. The particle motion equation in shear flow based on the influential forces can be summed up as shown here (Vreman et al., 2009; Kleinstreuer, 2003; Armenio and Fiorotto, 2001; Ferry and Balachandar, 2001; Boivin et al., 2000; Maxey and Riley, 1983):

$$m_p \frac{d\mathbf{U}_p}{dt} = \mathbf{F}_g - \mathbf{F}_{vm} + \mathbf{F}_D + \mathbf{F}_{Ba} + \mathbf{F}_{Pr} + \mathbf{F}_L \quad (1-11)$$

The force terms on the right side are gravity, virtual mass, drag, Basset, pressure, and lift, respectively. The first term, (\mathbf{F}_g) accounts for the gravity force which is defined as below (Ferry and Balachandar, 2001):

$$\mathbf{F}_g = (m_p - m_f)\mathbf{g} \quad (1-12)$$

The virtual mass force (\mathbf{F}_{vm}) is related to the acceleration and deceleration of the particles in fluid flow. It can be obtained as (Ferry and Balachandar, 2001):

$$\mathbf{F}_{vm} = \frac{1}{2}m_f \frac{d(\mathbf{U}_p - \mathbf{U}_f)}{dt} \quad (1-13)$$

The viscous drag force (\mathbf{F}_D) acting on the particles is calculated as (Boivin et al., 2000):

$$\mathbf{F}_D = m_p \xi (\mathbf{U}_p - \mathbf{U}_f), \xi = \frac{3}{4} C_D \frac{\rho_f}{\rho_p} \frac{1}{d_p} |\mathbf{U}_p - \mathbf{U}_f| \quad (1-14)$$

$$C_D = \frac{24}{Re_p} (1 + 0.15 Re_p^{0.687}), Re_p = |\mathbf{U}_p - \mathbf{U}_f| d_p / \nu_f$$

The Basset force (\mathbf{F}_{Ba}) accounts for the lag in the formation of the boundary layer around the accelerating solid bodies through the fluid. This term can be defined as (Kleinstreuer, 2003):

$$\mathbf{F}_{Ba} = \frac{3}{2} \pi \mu_f d_p^2 \int_{t_0}^t \frac{dt'}{\sqrt{\pi \mathbf{U}_f (t - t')}} \frac{d(\mathbf{U}_p - \mathbf{U}_f)}{dt'} \quad (1-15)$$

The pressure gradient of the flow exerts the pressure force (\mathbf{F}_{pr}) on the particle and it is defined as (Kleinstreuer, 2003):

$$\mathbf{F}_{pr} = -V_p \nabla P \quad (1-16)$$

The lift force stems (F_L) from the fluid shear gradient and can be determined using (Auton, 1987):

$$\mathbf{F}_L = C_l m_p (\mathbf{U}_p - \mathbf{U}_f) \times (\nabla \times \mathbf{U}_f) \quad (1-17)$$

Also the velocity and the trajectory of the particles will be altered upon contact with the wall or other particles (wall or particle-particle collisions). There are some methods in literature to model such collisions (see, for example, De Jong et al., 2012; Vreman et al., 2009; Sommerfeld and Huber, 1999; Xu and Yu, 1997; Hoomans et al., 1996; Tsuji et al., 1993, 1992).

1.2 Particulate turbulent flows: experimental investigations

As mentioned earlier, the experimental investigations are still the main source for better understanding the complex issues of particulate turbulent flows. In this section, the available studies on the particle-laden turbulent flows are critically scrutinized to first understand the main parameters investigated in this field and the advancements made by the current studies. Finally, the main deficiencies involved with the available literature will be addressed, in order to cover by the present study.

The motion of solid particles and their interaction with the turbulent flow produces a system with extremely complicated behaviour. Elghobashi (1994) showed that the fluid-particle and particle-particle interactions in two-phase flows begin to occur at different particle concentrations (see Fig.1-1). For $\varphi_v < 10^{-6}$, the fluid affects the particles (one-way coupling) but the presence of the particles has no impact on the turbulence of the carrier phase. The two-way fluid-particle interactions come into play $\varphi_v > 10^{-6}$ (two-way coupling). At $\varphi_v > 10^{-3}$, interactions between particles occur and the

system can be described as having four-way coupling. As illustrated in Fig.1-1, the turbulent motions of particles in dilute particulate flows ($10^{-3} \leq \phi_v \leq 0.02$) can have considerable effect on the carrier phase turbulence and vice versa. The particle/fluid turbulence interactions, at the minimum, can be function of Reynolds number (Re), particle Reynolds number (Re_p) and Stokes number (St), particle/fluid density ratio (ρ_p / ρ_f), flow orientation, and solid phase volumetric concentration (ϕ_v) (Balachandar and Eaton, 2010; Gore and Crowe, 1991).

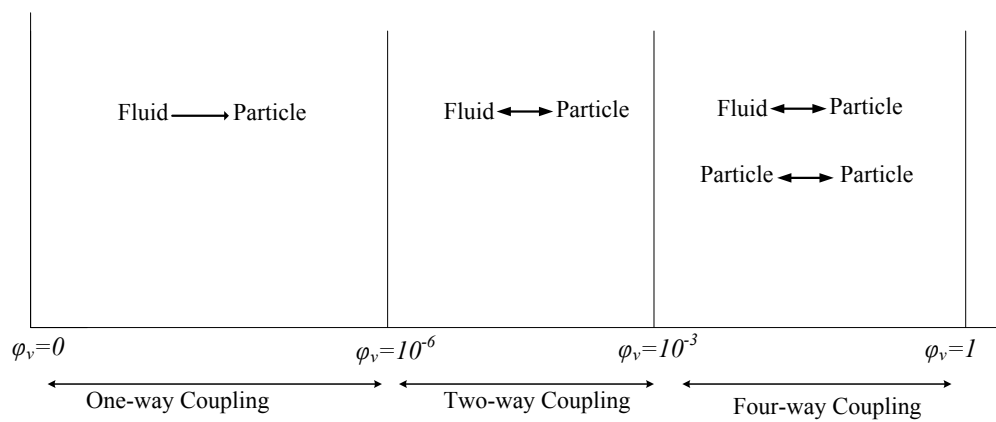


Figure 1-1. Map of interactions in two-phase disperse flow (Elghobashi, 1991)

The definitions for some of the aforementioned parameters are provided in following. The flow Re can be defined as

$$Re = \frac{\rho_f U_b D}{\mu_f} \quad (1-18)$$

where U_b and D are the bulk velocity and the pipe internal diameter, respectively. The Particle Reynolds number can be computed as:

$$Re_p = \frac{\rho_f V_t d_p}{\mu_f} \quad (1-19)$$

In the equation above, V_t is the particle terminal velocity settling in a quiescent fluid medium. The particle Stokes' number (St) is considered to be another important parameter which is specified as a ratio of particle response time to a fluid time scale. This number describes the degree of the particle interaction with a certain turbulence scale of the fluid phase. Two Stokes' numbers are usually defined for a turbulent flow; St_L and St_k which can be obtained using:

$$St_L = \frac{\tau_p}{\tau_L} \quad (1-20)$$

$$St_k = \frac{\tau_p}{\tau_k} \quad (1-21)$$

Where τ_p , τ_L , and τ_k are particle response time, the integral and Kolmogorov time scales, respectively. The particle response time (τ_p) is obtained by:

$$\tau_p = \frac{(\rho_p - \rho_f)d_p^2}{18\mu_f f_d} \quad (1-22)$$

where f_d is a correction factor of the drag coefficient for deviations from Stokes flow and is calculated as (Kussin and Sommerfeld, 2002):

$$f_d = 1 + 0.15Re_p^{0.687} \quad (1-23)$$

The integral time scale (τ_L) and the Kolmogorov time scale (τ_k) (Kussin and Sommerfeld, 2002):

$$\tau_L = \frac{2k}{9\varepsilon} \quad (1-24)$$

$$\tau_k = \left(\frac{\nu}{\varepsilon}\right)^{1/2} \quad (1-25)$$

where the turbulent kinetic energy k and the dissipation rate ε can be obtain as following (Milojevic, 1990):

$$k = 0.5(\langle u^2 \rangle + 2 \langle v^2 \rangle) \quad (1-26)$$

$$\varepsilon = C_\mu^{0.75} \frac{k^{1.5}}{l_m} \quad (1-27)$$

In above equations, u and v are the fluid fluctuating velocities in axial and radial directions, respectively. Moreover, the mixing length (l_m) can be estimated by $l_m/R=0.14-0.08(r/R)^2-0.06(r/R)^4$ (Schlichting, 1979). Also, The coefficient C_μ is considered equal to 0.09 as in the standard k - ε model (Milojevic, 1990).

When considering the whole body of work together, numerous studies found in the literature have shown the importance of the aforementioned parameters. However, those are not the independent parameters which can be directly varied during the experimental investigations. The main independent variables studied in the literature include; carrier phase (gas or liquid), flow orientation, Re , particle size (d_p), density ratios (ρ_p / ρ_f) and volumetric concentration (φ_v). Table 1-1 provides a detailed overview of previous experimental investigations of particle-laden turbulent flows specifying the range of their main parameters studied in the literature. In addition, the mass concentration (φ_m) is also provided as many studies, especially in gas-solid flows, did. Although φ_m for gas-solid systems is quite high; Table 1-1 clearly shows that the volumetric concentration is still very low.

There has been a considerable amount of work done to experimentally investigate the turbulent gas-solid flows in channels or pipes. For example, Borée and Carama (2005), Caraman et al. (2003), Varaksin et al. (2000) and Kulick et al. (1994) studied the

turbulent motion of the particulate phase along with fluid turbulence characteristics in a downward air-solid pipe flow at $Re < 15\,300$. Tsuji et al. (1984) and Lee and Durst (1982) used Laser Doppler Velocimetry (LDV) and measured the turbulent fluctuations of both the particles and the carrier phase in a gas-solid upward pipe flow at Re values of 22 000 and 8 000, respectively. Also Tsuji and Morikawa (1982) studied the effect of 0.2 and 3.4 mm plastic particles on the turbulence of the carrier phase (air) in a horizontal pipe flow at $Re < 40\,000$. Kussin and Sommerfeld (2002) tested glass beads in a size range of 60 to 625 μm in gas-solid flows of a horizontal pipe at $Re < 58\,000$. Wu et al. (2006) also studied the effect of the 60 and 110 μm polyethylene particles on the turbulence of gas phase in a horizontal channel flow at $Re = 6\,800$. Taniere et al. (1997) studied the saltation of particles in particle-laden gas flow of a horizontal channel at $Re < 6\,700$. The key results from each of the aforementioned studies will be discussed in detail in the following sections.

Table 1-1. An overview of experimental investigations of particle-laden turbulent flows.

REF.	Carrier Phases	Flow direction	d_p (mm)	Re	ρ_p / ρ_f	φ_m	φ_v
Wu et al. (2006)	Gas	Horizontal	0.06, 0.11	6 800	860	5×10^{-4} -0.04	6×10^{-7} - 5×10^{-5}
Boré and Caraman (2005)	Gas	Down	0.06,0.09	5 300	2100	0.1-0.52	$(0.5-5) \times 10^{-4}$
Caraman et al. (2003)	Gas	Down	0.06	5 300	2100	0.1	5×10^{-5}
Kussin and Sommerfeld (2002)	Gas	Horizontal	0.06-0.625	< 58 000	2100	0.09-0.5	$(0.5-5) \times 10^{-3}$
Varaksin et al. (2000)	Gas	Down	0.05	15 300	2100	0.04-0.55	$(0.2-5.8) \times 10^{-4}$
Taniere et al. (1997)	Gas	Horizontal	0.06,0.13	<6700	1200,2100	0.005, 0.01	4.5×10^{-6}
Kulick et al. (1994)	Gas	Down	0.05 to 0.09	13 800	2100,7300	0.02-0.44	$(0-4) \times 10^{-4}$
Tsuji et al. (1984)	Gas	Up	0.2-3	23 000	860	0.33-0.77	$(0.6-4) \times 10^{-3}$
Lee and Durst (1982)	Gas	Up	0.1- 0.8	8 000	2100	0.55-0.71	$(0.58-1.2) \times 10^{-3}$
Tsuji and Morikawa (1982)	Gas	Horizontal	0.2, 3.4	<40 000	830	0.29-0.77	$(0.5-4) \times 10^{-3}$
Kameyama et al. (2014)	Liquid	Up/down	0.625	19 500	2.5	0.002	0.006
Hosokawa and Tomiyama (2004)	Liquid	Up	1 to 4	15 000	3.2	0.002-0.006	0.007-0.018
Kiger and Pan (2002)	Liquid	Horizontal	0.195	25 000	2.5	6×10^{-4}	2.4×10^{-4}
Suzuki et al. (2000)	Liquid	Down	0.4	72 00	3850	0.001	3.2×10^{-4}
Sato et al. (1995)	Liquid	Down	0.34,0.5	5 000	2.5	0.005-0.031	0.002- 0.013
Alajbegovic et al. (1994)	Liquid	Up	1.79,2.32	42 000-68 000	0.032, 2.45	3×10^{-4} - 0.08	0.009-0.036
Zisselmar and Molerus (1979)	Liquid	Horizontal	0.053	100 000	2.5	0.007-0.024	0.017-0.056

Due to many industrial applications dealing with the transportation of the solids in liquid flows, turbulent statistics of such flows were experimentally studied as well. Kameyama et al. (2014) employed PIV to study turbulent fluctuations of water and glass beads (90.625 μm) in both downward and upward pipe flow at $Re = 19\,500$. Hosokawa and Tomiyama (2004) studied the effect of the 1 mm to 4 mm ceramic particles on the carrier phase turbulence in an upward pipe flow at $Re = 15\,000$ using LDV. Sato et al. (1995) studied both liquid phase and particle fluctuating velocities with the mixtures of water and 0.34 and 0.5 mm glass beads in a downward channel flow at $Re = 5\,000$. Alajbegovic et al. (1994) investigated the turbulence statistics of both particulate and liquid phases using mixtures of the water and expanded polystyrene particles as well as ceramic particles in an upward flow at $Re < 68\,000$. Kiger and Pan (2002) evaluated the liquid phase turbulence in presence of 0.2 mm glass beads in a horizontal channel flow at Re of 25 000. Suzuki et al. (2000) investigated the both particle and carrier phase turbulence for 0.4 mm ceramic beads and water in a downward channel flow at $Re = 7\,500$ using 3D-PTV. Zisselmar and Molerus (1979) investigated the liquid phase turbulence in presence of 0.053 mm glass beads in a horizontal pipe flow at $Re = 100\,000$.

As stated earlier, the turbulent motions of both phases will be influenced by one another in these types of flows. Consequently, the studies of particle-laden channel (or pipe) flows in which the turbulence of each phase are discussed will be reviewed the following.

1.2.1 Carrier phase turbulence

Generally, the experimental results summarized in Table 1-1 show that the presence of small particles most often attenuate the turbulence of the carrier fluid while the particle-laden flows containing larger particles will exhibit carrier phase turbulence augmentation (Hosokawa and Tomiyama, 2004; Kiger and Pan, 2002; Suzuki et al., 2000; Sato et al., 1995; Tsuji et al., 1984; Lee and Durst, 1982; Tsuji and Morikawa, 1982). The change in the carrier phase turbulence is quantified using a parameter M , which denotes turbulence modulation. Simply, ' M ' represents the magnitude of change in the fluid phase fluctuating velocities due to the particles. For instance, the axial fluid turbulence modulation (M_x) can be obtained from:

$$M_x = \frac{\left(\frac{\langle u^2 \rangle^{0.5}}{U_b}\right)_{TP} - \left(\frac{\langle u^2 \rangle^{0.5}}{U_b}\right)_{SP}}{\left(\frac{\langle u^2 \rangle^{0.5}}{U_b}\right)_{SP}} \quad (1-28)$$

where u and U_b are the bulk velocity and the axial fluctuating velocities, respectively and $\langle \rangle$ represents the ensemble averaging. The subscripts ' TP ' and ' SP ' stand for two-phase and single phase, respectively. Note that values less than 0 indicate attenuation while values > 0 indicate augmentation and M_r , turbulence modulation in the radial direction, is evaluated as per Equation (1-32) but using v (radial fluctuating velocity) instead of u . A review of the literature also shows that increasing the concentration of relatively large particles (which cause carrier phase turbulence augmentation) leads to even greater fluid turbulence augmentation (Hosokawa and Tomiyama, 2004; Kussin and Sommerfeld, 2002; Sato et al., 1995; Tsuji et al., 1984; Tsuji and Morikawa, 1982). Other studies show that increasing the concentration of relatively small particles (which cause the

turbulence attenuation) results in stronger fluid turbulence attenuation (Kussin and Sommerfeld, 2002; Varaksin et al., 2000; Kulick et al., 1994; Zisselmar and Molerus, 1979). Only the results of Tsuji et al. (1984) and Tsuji and Morikawa (1982) demonstrate a mixed effect resulting from changes in particle concentration. Their results show that the magnitude of turbulence attenuation produced by small particles first increases as the concentration increases; however, with any further increase in the particle concentration, the attenuation is reduced, i.e. becomes less negative.

The carrier phase turbulence augmentation/attenuation, observed in the experimental investigations in the literature, can occur through some possible mechanisms. Viscous drag on particles can cause carrier phase turbulence to be attenuated (Kim et al., 2005; Crowe, 2000; Yuan and Michaelides, 1992). Also attenuation occurs when particles interact with an eddy which may result in the eddy breakage (Lightstone and Hodgson, 2004). If these new eddies are of the same approximate size as the Kolmogorov length scale, then the dissipation rate increases. The main source for the fluid phase turbulence augmentation is considered to be the wake and vortex shedding behind the particles (Kim et al., 2005; Yuan and Michaelides, 1992).

The formulation of the above mentioned mechanisms is very difficult and the researchers at first opted for a criterion which, at least, can predict when the carrier phase turbulence is augmented or attenuated by the presence of particles. The two most well-known criteria for classifying the fluid turbulence modulation are proposed by Gore and Crowe (1989) and Hetsroni, (1989). Gore and Crowe (1989) analysed the turbulence modulation data available in the literature and concluded that turbulence modulation can

be classified based on the particle diameter. They proposed that if the ratio of the particle diameter (d_p) to the most energetic eddy length scale (l_e) is less than 0.1, then turbulence attenuation should occur. If $d_p/l_e > 0.1$, particles will cause carrier phase turbulence augmentation. For the pipe flows, l_e is estimated as 0.1D, where D is the pipe diameter (Hutchinson et al., 1971). Hetsroni (1989) also used particle diameter as the primary parameter for classification of turbulence modulation, but as part of the particle Reynolds number so that fluid properties were also taken into account. He proposed that if $Re_p < 100$, the particles are most likely to attenuate the carrier phase turbulence and the turbulence will be augmented for $Re_p > 400$. In the recent attempt to propose a new criterion, Tanaka and Eaton (2008) included more parameters for better predictions and introduced a new dimensionless parameter, Pa_{st} (particle moment number) to classify fluid phase turbulence attenuation and augmentation using a more complex approach:

$$Pa_{st} = St_k Re^2 \left(\frac{\eta}{L}\right)^3 \quad (1-29)$$

where η is the Kolmogorov length scale, St_k is the Stokes number based on the Kolmogorov time scale, and L is the characteristic length of the flow. They showed that turbulence attenuation is observed when $3 \times 10^3 \leq Pa_{st} \leq 10^5$ while outside this range turbulence augmentation occurs. Although these criteria are, to some extent, successful in classifying the augmentation/attenuation of the carrier phase turbulence in both gas-solid and liquid solid flows, they are not capable of providing any estimate of the magnitude of the modulation. Gore and Crowe (1991) suggested that the improved predictions of particles on the turbulence modulation of the fluid phase would require one to consider a function of a combination of non-dimensional parameters, i.e.:

$$M_x(\%) = f(Re, Re_p, \frac{u}{U_s}, \frac{\rho_p}{\rho_f}, \varphi_v) \quad (1-30)$$

where u and U_s are fluctuating velocity and slip velocity between phases, respectively.

One of the major shortcomings of the turbulence modulation criteria described above is that they are based on experimental data for relatively low Re (<100 000) flows. In fact, the same deficiency in the available experimental data also exists (Balachandar and Eaton, 2010): the experimental data for particulate flows are mainly restricted to Re < 30 000.

Additionally, Reynolds number (Re) which plays a critical parameter in the interaction between the solid and fluid phases, has not been adequately investigated. Tsuji and Morikawa (1982) showed that the axial carrier phase (air) turbulence modulation at the pipe centerline caused by 3.4 mm plastic particles at $\varphi_v = 0.7\%$ decreased from 220% to 100% as Re increased from 20 000 to 40 000 in a horizontal pipe flow. A review of the literature shows that the only work done on the liquid-solid flows at different Re was conducted by Alajbegovic et al. (1994), who tested two different particles, ceramic and expanded polystyrene (buoyant particles), with water as the carrier phase in a vertically upward pipe flow over range of Re from 42 000 to 68 000. Their results showed that the fluctuating velocities of the liquid phase were enhanced by increasing the Reynolds number. This is an expected result since the turbulent fluctuations increases as the flow velocity and Re increases. Unfortunately, there are two deficiencies associated with this study: (i) the main one is very limited range of Re tested here and (ii) the other shortfall of this work is that the unladen-liquid

turbulence statistics were not provided. Therefore, one cannot calculate the amount of turbulence modulation caused by presence of the particles using the provided data.

In summary, an experimental investigation on the effect of a broad range of Reynolds numbers, extending to high Re ($>100\,000$), on the carrier phase turbulence modulation can help improve the understanding of particle-fluid interactions in turbulent flows. This reviews exposes another important deficiency of the existing turbulence modulation criteria: that they consider only modulation in the streamwise direction (Lightstone and Hodgson, 2004; Lain and Sommerfeld, 2003; Crowe, 2000). This deficiency arises partly from the scarcity of the experimental data showing the turbulence modulation in, for example, the radial direction. A careful review of the literature reveals that turbulence modulation in the radial direction seems to differ considerably from that in the streamwise direction. For example, Kussin and Sommerfeld (2002), Varaksin et al. (2000), and Kulick et al. (1994) showed that turbulence attenuation in the radial direction for small particles is not as strong as the attenuation in streamwise direction (i.e. $M_r < M_x$). Sato et al. (1995) observed that while larger particles (340 and 500 μm glass beads) caused turbulence augmentation of the liquid phase at the pipe centerline, the fluid phase radial turbulence did not demonstrate any considerable modulation. Hence, more experimental data on the radial turbulence modulation of the carrier phase, especially at high Re , would be beneficial.

1.2.2 Particulate phase turbulence

In addition to the characterization of fluid turbulence in a dispersed two-phase system, a better understanding of the turbulent motion of particles is also critical. Since the unladen phase turbulence (i.e. single-phase turbulence) is relatively well-established,

the experimental data on the particulate phase are customarily compared to those of the unladen carrier phase which covers the first portion of the review. Then, the effects of the main parameters tested in the available literature on the particulate phase turbulence and their corresponding shortcomings will be discussed.

In an early study, Lee and Durst (1982) showed that the axial turbulent fluctuations of 0.8 mm glass beads in an upward gas flow was greater than those of the carrier phase at the core of the flow but the relative magnitudes were reversed in the near-wall region. Kulick et al. (1994) and Varaksin et al. (2000) found that for small particles ($d_p \leq 70 \mu\text{m}$) in a downward gas flow, particle axial fluctuations were greater than those of the unladen carrier phase. However the lateral turbulent velocities of the particles were lower than those of the unladen carrier phase. Caraman et al. (2003) provided experimental data showing the turbulent statistics of 60 μm glass beads in a downward gas flow. They showed that the particles had higher axial fluctuating velocities than the unladen gas flow and the fluctuating velocities in the radial direction were almost identical for both the particulate and fluid phases. Kameyama et al. (2014) reported that both radial and axial fluctuating velocities of 0.625 mm glass beads were equal to or greater than those of the unladen-liquid phase (water) in both up/downward flow directions.

By reviewing the experimental results of the studies mentioned in Table 1-1, one can reach somewhat different conclusions for the axial and lateral (radial) particle fluctuations. While it can be concluded that the axial fluctuations of the particles are at least equal to or greater than those of the unladen fluid phase, there is no such agreement on the fluctuating velocities of particles in the radial direction. While the majority of

experimental works report that the magnitude of the lateral fluctuations of particles are at least equal to or greater than those of the unladen fluid phase, Kulick et al. (1994) and Varaksin et al. (2000) showed the lateral fluctuations are smaller than those of the unladen fluid. Vreman (2007) attributed these discrepancies to the experimental issues such as electrostatics and channel wall roughness. It appears that this comment is at least partly justified. Kussin and Sommerfeld (2002) measured particle turbulent fluctuations of a particle-laden air flow in a horizontal pipe with different wall roughness and proved that the wall roughness has a significant effect on the turbulence intensity of the solid particles. Additionally, Varaksin et al. (2000) and Kulick et al. (1994) speculated that their results might have been affected by insufficient pipe length and electrostatic charges on the particles, respectively.

Now we focus on the main parameters (d_p , φ_v , and Re) whose effects on the particulate phase turbulence were studied in the literature. The literature shows that increasing the particles size will enhance the axial fluctuating velocities of the particles. Borée and Caraman (2005) showed that the fluctuating velocities of 90 μm glass beads were larger than those measured for 60 μm particles. Also Kussin and Sommerfeld (2002) reported that turbulence intensities of the particles are enhanced by increasing the particle size from 60 μm to 190 μm . Wu et al. (2006) obtained similar trend 60 and 110 μm polyethylene particles in an air channel flow. Sato et al. (1995) also showed the greater particle fluctuations for 500 μm glass beads than 340 μm ones particle-laden liquid flows. Unfortunately, studies investigating the effect of particle size on particle turbulent fluctuations have been limited to relatively small particles sizes ($d_p \leq 500 \mu\text{m}$).

Although it is clear that the particle concentration will influence the particle turbulence (Kussin and Sommerfeld, 2002; Varaksin et al., 2000), the effect appears to be very different in the radial and streamwise directions. For example, Varaksin et al. (2000) showed that the radial fluctuations of 50 μm particles decrease with an increase in particle concentration while axial fluctuations decrease also but only in the core region ($r/R < 0.7$). In the near wall region, the particle axial fluctuations are dramatically enhanced as the particle concentration increases. Borée and Caraman (2005) showed that radial fluctuations of both 60 and 90 μm glass beads were enhanced by increasing the particle concentration. The same results also demonstrate that the 90 μm glass beads have lower streamwise fluctuations at higher concentration whilst streamwise fluctuations of 60 μm particles slightly increase in core of the flow ($r/R < 0.7$) and they slightly decrease in the near-wall region. Kussin and Sommerfeld (2002), who tested a particle-laden gas flow in a horizontal channel, showed that increasing the particle concentration with d_p ranging from 60 to 190 μm decreased the particle fluctuating velocities in both axial and lateral directions. In summary, experimental investigations of the effects of particle concentration on particulate phase turbulence statistics in gas flows are limited to relatively small particles (up to 200 μm).

Compared to gas-solid flows, relatively few experimental investigations have been conducted to characterize the turbulent motions of particles in liquid channel/pipe flows. The work of Kameyama et al. (2014), Kiger and Pan (2002), and Sato et al. (1995) represent the entire of such studies. Unfortunately, the impact of the particle concentration on axial and radial particle fluctuations was not studied. Additional (new) experimental investigations of effects of concentration could be conducted.

Another parameter affecting the turbulent motion of the particles is the Reynolds number. The only work investigating Re effects on particulate phase turbulence is Alajbegovic et al. (1994). They tested ceramic and expanded polystyrene particles in an upward liquid pipe flow at $42\,000 \leq Re \leq 68\,000$. They showed the particle fluctuations increased as the Re increased.

This review reveals that there are two main deficiencies with the current literature regarding the effects of Re on particulate phase turbulence: (i) The data are extremely scarce and (ii) they are limited to a very low range of Reynolds numbers. Moreover, any experimental work done on the particulate phase turbulence investigated only the effect of one or two parameters (such as particle diameter, particle concentration and Re) over limited ranges. There is no aggregate investigation on the main parameters affecting particle fluctuations. For example, turbulence intensity (the ratio of the fluctuating velocity to the bulk velocity) of the fluid phase at the pipe centerline is solely a function of Re and can be estimated as $0.16 \times Re^{-1/8}$ (ANSYS-Fluent, 2013). However, no study is currently available in the literature which can present such functionality for particulate phase turbulence.

1.2.3 Summary and conclusions

The review of the available experimental studies of the particle-laden turbulent flows in the literature is summarized as:

- All the particle-laden flows investigated in the literature are limited to low Re ($< 100\,000$).

- The experimental data on the effects of Re on both the carrier phase and particulate phase turbulence modulation are extremely scarce and are restricted to a very narrow range.
- The particle effects on the carrier phase turbulence modulation in radial direction proved to be greatly different from that of the axial direction based on the available data. However, the available data for the radial direction is still limited compared to that in the axial direction which prohibits drawing any solid conclusions.
- The literature shows that increasing particle concentration can have a mixed effect (increase or decrease) on the particle turbulence in particulate gas flows. Unfortunately, no experimental data were found investigating the particle concentration effects on the particulate phase turbulence in liquid-continuous flows.
- Although the experimental data in the literature provided the effects of one or two parameter(s) at a time on the particulate phase turbulence, there is no work in the literature to aggregately investigate the important parameters affecting the particle turbulence in particulate turbulent flows.
- The available turbulence modulation criteria are usually consider one parameter to classify the carrier phase turbulence modulation. Consequently they are not capable of providing any estimate for the magnitude of the modulation.

1.3 Objectives

This research project has the following objectives:

- To experimentally investigate the turbulent motions of the carrier phase and particles in dilute particle-laden liquid flows over a broad range of Re ($52\ 000 \leq Re \leq 320\ 000$), and especially at high Reynolds numbers, for different particle sizes (0.5, 1, and 2 mm) and concentrations ($0.05 \leq \varphi_v \leq 1.6\%$)
- To study the turbulence modulation (M_x) of the carrier phase caused by particles, and propose an improved empirical criterion/correlation for M_x using the results of this study along with the liquid-solid and gas-solid data available in the literature.
- To conduct a study of the particulate phase turbulence and propose a novel empirical correlation in solid-liquid turbulent flows using the results of this study and data from the literature.

1.4 Contribution of the present study

Providing new experimental data sets for particle-laden turbulent flows

The main contribution of this study is to provide valuable experimental data for both the fluid and particulate phases in particle-laden flows using a combined PIV/PTV technique. The experimental data for particle-laden flows are provided at an unprecedented Re ($= 320\ 000$). These new experimental investigations provide insight into the behavior of the particulate phase and its effects on the carrier phase turbulence when the particle concentration or Re varies. The most important contribution of these

new experimental data sets is their employment to validate the existing or an improved multiphase flow model(s) for the new conditions tested here.

A novel empirical functionality for particle turbulence in liquid-solid flows

For the first time, a consolidated study was conducted considering all the important parameters affecting the particle turbulence to propose a novel empirical functionality for the particle turbulence intensities, using the results of the present study and available data in the literature for liquid-solid flows. The new functionality can assist the prospect investigators to efficiently design their experiments for cases in which the particulate phase turbulence plays an important role. Moreover, the proposed functionality and correlation will help us to develop more accurate models for particle-laden turbulent flows by knowing the weight of each important parameter affecting the particle turbulence.

A novel empirical correlation predicting the fluid phase turbulence augmentation

An empirical correlation for predicting the turbulence augmentation of the carrier phase was proposed for both solid-liquid and solid-gas flows. In order to develop the new correlation, all the data from the present study alongside many other experimental data on the carrier phase turbulence modulation were employed. The proposed correlation can predict the onset of the carrier phase turbulence augmentation as well. In addition, new correlation can be utilized as a criterion for classifying the axial attenuation/augmentation of the carrier phase turbulence. This is a great advancement compared to the existing criteria which cannot predict either the onset or the magnitude of the carrier phase turbulence augmentation. The novel correlation is greatly beneficial

to understand the phenomena in which the carrier phase turbulence is highly important such as pipe wear rate, oil sands lump ablation rate in hydrotransport pipelines, bubble size distribution in presence of particles.

1.5 Thesis outline

This thesis includes 6 chapters; a brief description of each of the following chapters is provided here:

Chapter 2 provides the details of the experimental setup, materials, test conditions and the operation procedure of the test rig. The imaging setup and image processing techniques employed in this study are provided in this chapter. Finally, an uncertainty analysis is conducted.

Chapter 3 describes an experimental investigation of the dilute solid-liquid flow at high Re . The mean and fluctuating velocity profiles of both phases for three different particle sizes (0.5, 1, and 2 mm) are given. Concentration profiles along with the particle-particle interactions are discussed. Later the sweep-ejection patterns of the solid and liquid phases are investigated. Finally, the main sources for particle fluctuating velocities along with the particle effect on the turbulence modulation at high Re are discussed in details. It is worth mentioning that a version of this chapter has been submitted to International Journal of Multiphase flow and is in revision. It is co-authored by R. Shokri, S. Ghaemi, D.S. Nobes, and R.S. Sanders.

In Chapter 4, the effects of particle concentration ($0.05 \leq \phi_v \leq 1.6\%$) on turbulent motions of both the liquid phase and particles are experimentally studied. The particle diameters tested here are 0.5, 1, and 2 mm and the test is conducted at $Re = 100\,000$. The

concentration effect on the mean velocities of both phases is investigated. Moreover, the radial and axial fluctuations of both phases are studied at different particle concentrations. Finally, the concentration effect on the shear Reynolds stresses and correlation coefficients of both phases are examined. A version of this chapter, co-authored by R. Shokri, S. Ghaemi, D.S. Nobes, and R.S. Sanders, is submitted to *Int. J. Heat and Fluid Flow* and is under review.

Chapter 5 provides the experimental investigation of the effects of the Reynolds number ($52\,000 \leq Re \leq 320\,000$) on the turbulent motions of the particles (2 mm glass beads) and liquid phase in an upward turbulent pipe flow. First the experimental data for mean and fluctuating velocity profiles for both phases as well as the particle concentration profile are provided and discussed over the tested Reynolds numbers. Then a study on the particle turbulence intensity is carried out which leads to an empirical correlation for predicting the particle turbulence intensities in particulate liquid flows. Finally, a new correlation is proposed for the carrier phase turbulence modulation in axial direction for both solid-gas and solid-liquid flows which can predict the magnitude and onset of the axial turbulence augmentation of the carrier phase. Note that a version of this chapter, co-authored by R. Shokri, S. Ghaemi, D.S. Nobes, and R.S. Sanders, is submitted to the *Journal of Powder Technology* and is under review.

Chapter 6 summarizes the important conclusions attained by the present study. Also, a list of recommendations for the future work is provided in this chapter.

2 Experimental Setup and Measurement

Techniques

2.1 Introduction

In order to investigate the turbulent motion of the particles in liquid turbulent flows, a 2 in (nominal diameter) pipe loop was constructed. Glass beads with different sizes were used as the particulate phase while the water was the carrier phase. In the first sections of this chapter, the experimental setup, materials, and operational procedures are discussed. Also, the imaging equipment and PIV/PTV techniques are described in detail. Finally, an uncertainty analysis of the results is carried out.

2.2 Experimental setup

A schematic of the closed slurry loop is shown in Fig.2-1. The nominal pipe diameter is 2 in and the overall height of the test rig is about 7 m. The horizontal sections of the loop before and after the pump were replaced with 1 in pipe in order to prevent particles from settling at flowrates corresponding to $Re < 300\ 000$ (see Section 2.3 for more details about the test conditions). The replaced pipes include the pipes from the flange labeled “Flange-1” in Fig.2-1 to the pump inlet and from the pump outlet to “Flange-2”. The feeding tank capacity is about 85 L and the total volume of the closed loop is 33.9 ± 0.1 L (29.2 ± 0.1 L when the pipe size of horizontal section is reduced to 1 in).

The loop operates using a centrifugal pump controlled by a variable frequency drive (VFD). The pump is 2/1.5 B-WX Battlemountain from Atlas Co. which has a 2 in inlet and a 1.5 in outlet. The pump is driven by a 545 voltage electrical motor which provides 15 kW power to the pump. The top speed of the pump is 1775 rpm at which it can provide about 20 psig pressure rise while delivering a flow rate more than 700 L/min. The pump curve is provided in Appendix.1. Flow rates are measured with a magnetic flow meter (FoxBoro IM T25) whose accuracy is $\pm 0.25\%$ of the measured values. The temperature is held constant at $25 \pm 1^\circ\text{C}$ throughout each experiment using a double pipe heat exchanger. The heat exchanger uses domestic cold water as the coolant with a temperature range of 5 to 10 $^\circ\text{C}$ (i.e. it varies seasonally). The temperature and flowrate measurements are collected and logged into the computer during the experiments at a frequency of 1 Hz using an interface developed in the software package, Labview.

Turbulence measurements are made using a combined particle image/tracking velocimetry (PIV/PTV) technique involving a laser and a camera as shown in Fig.2-1. The flow field velocity measurements are made in the upward flow pipe section which has an inner pipe diameter (D) of 50.6 mm. A transparent test section made from acrylic is located $80D$ downstream of “Flange-2”, which is expected to provide sufficient length to produce fully developed turbulent pipe flow at the measurement location. The measurement location is also situated $15D$ upstream of the upper bend, which has a radius of $11D$. In order to minimize image distortion due to the curvature of the pipe wall, a rectangular acrylic box filled with water is placed around the test section. The viewing box has dimensions of $13 \times 13 \times 85$ cm and can hold about 13 L of water.

2.3 Experimental conditions

The particulate flows consist of water as the carrier phase and glass beads as the particulate phase. Table 2-1 shows the experimental conditions at which tests were carried out. Experiments were conducted for single-phase and two-phase flows at three different Reynolds numbers: 52 000, 100 000, and 320 000 which are referred to low, medium and high Reynolds numbers. These Reynolds numbers correspond to the frictional Reynolds numbers (Re_τ) of 2 580, 4 720, and 13 600 which are calculated as following:

$$Re_\tau = \frac{\rho_f U_\tau D}{\mu_f} \quad (2-1)$$

where ρ_f and μ_f are the fluid density and viscosity and U_τ is the frictional velocity, which is defined as:

$$U_\tau = \sqrt{\frac{\tau_w}{\rho_f}} \quad (2-2)$$

where τ_w is the wall shear stress which can be expressed as:

$$\tau_w = f_D \frac{\rho_f U_b^2}{8} \quad (2-3)$$

Finally Darcy's friction factor (f_D) is obtained using the Colebroke equation (Young et al., 2004):

$$\frac{1}{\sqrt{f_D}} = -2.0 \log \left(\frac{\epsilon/D}{3.7} + \frac{2.51}{Re\sqrt{f_D}} \right) \quad (2-4)$$

The particulate phase consists of glass beads (A-series, Potters Industries Inc.) with nominal average diameters of 0.5, 1, and 2 mm. Glass beads have a true density of 2500 kg/m³ resulting in $\rho_p / \rho_f = 2.5$ where ρ_p and ρ_f are the particle and fluid density, respectively. At low Reynolds number ($Re = 52\,000$), particle-laden flow tests were performed using only for 2 mm glass particles with $\phi_v = 1.6\%$. In order to observe the concentration impact on the turbulent motions of both phases, all particle sizes were tested with two different concentrations at medium Reynolds number ($Re = 100\,000$) as shown in Table 2-1. The maximum concentration for each size of glass beads was set at a concentration beyond which the PIV technique could no longer be used effectively because of the excessive number of glass beads. It means that the glass beads would fill the entire image, making it technically impossible to find the seeding particles to apply PIV. Once the maximum concentration was determined for each particle size, the experiments were repeated at 50% of the maximum concentration. At high Reynolds numbers, all three particle sizes were tested at only one particle concentration as shown in Table 2-1.

Table 2-1: Matrix of experimental conditions

Re	Re_c	U_b (m/s)	d_p (mm)	ϕ_v (%)
52 000	2 580	0.91	2	1.6
			0.5	0.05, 0.1
100 000	4 720	1.78	1	0.2, 0.4
			2	0.8, 1.6
			0.5	0.1
320 000	13 600	5.72	1	0.4
			2	0.8
			0.5	0.1

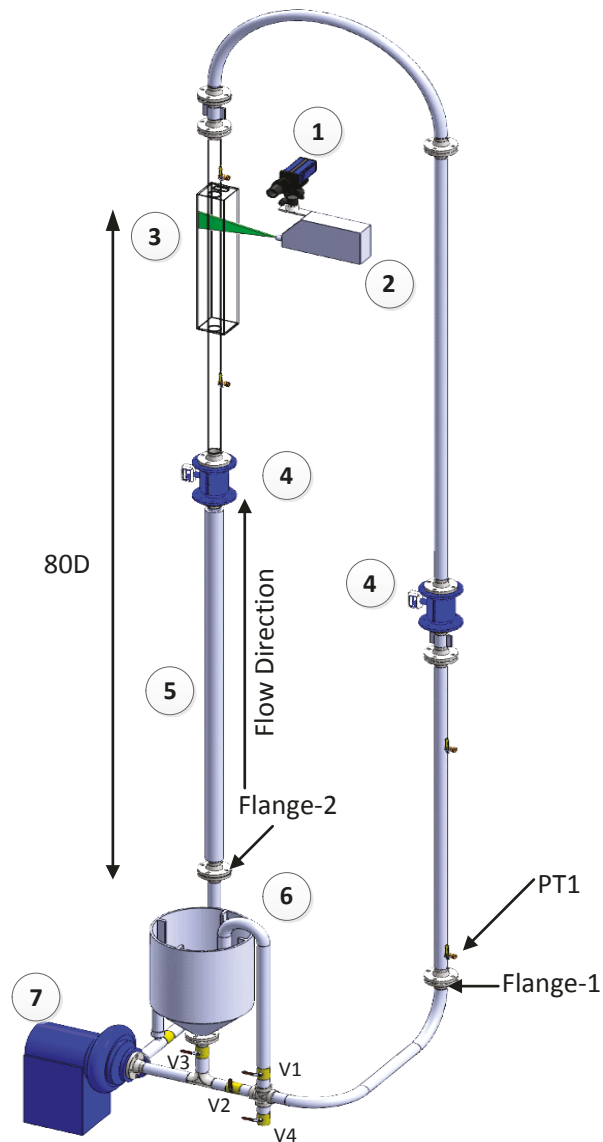


Figure 2-1. Schematic of the experimental setup consisting of (1) camera (2) laser, (3) acrylic pipe and viewing box, (4) magnetic flow meters, (5) double pipe heat exchanger, (6)-Feeding tank, (7) and centrifugal pump.

2.4 Flow loop operation

First water is loaded to the loop through feeding tank while all the valves are open except for the drain valve, which is labeled as V4 in Fig.2-1. Then the Valve V2 is

closed and the pump is switched on. In this configuration, the flow is forced to circulate through the feeding tank so that the air in the system can escape through the feeding tank. This procedure continues for about 10 min to ensure that the air is completely purged. PIV tracers are then added into the feeding tank to be mixed with the water. Valve V2 is then opened and the Valves V1 & V3 are closed to isolate the tank from the circuit so that the water flows through a closed (recirculating) loop. At this stage, the single-phase experiments are carried out.

In the case where two-phase flows are to be tested, the aforementioned procedures (i.e. water loading, air purging and flow tracer addition) will have been completed before loading the glass particles. Valve V3 is then opened and the desired mass of glass beads is gradually added through the feeding tank into the flow. Once the loop is loaded with the particles, the tank is bypassed and flow circulates through the closed loop. At the end of the experiments, the glass beads are collected above the feeding tank using a sieve basket. Water is then drained through Valve V4. At the lowest flowrate ($Re=52\ 000$), the pressure of the loop is elevated by connecting the loop to a pressure vessel in order to prevent negative pressure at the top of the loop. The pressure vessel is connected to the loop through a pressure tap on the downward leg, labeled as “PT1” in Fig.2-1. The vessel can be pressurized up to 50 psig however; the pressure was set always at 10 psig in this study.

2.5 PIV/PTV measurements

In order to measure the flow velocity field, a planar particle image velocimetry (PIV) method has been chosen. It is a non-intrusive technique which allows for the measurement of the instantaneous velocity field in a plane. If the image acquisition rate

is high enough, this method can provide the time-resolved measurements of the velocity field as well. The PIV technique provides two dimensional vector fields whereas laser Doppler velocimetry (LDV) is capable of measuring the fluid velocity only at a specific point at a time. Therefore, PIV can allow us to detect the spatial structures in the flow field (Raffel et al., 2007). Since 1984, when the PIV term first appeared in the literature (Adrian, 2005), it has been commercialized and is constantly improving, which allows it to provide accurate quantitative measurements of fluid flow velocity in different applications (Flow Master, 2007).

The planar PIV setup consists of a laser and a camera as shown in Fig.2-1. The laser creates a sheet which illuminates the plane of interest in the flow field. The camera is set up perpendicular to the laser sheet and captures two successive images at a time interval of δt . The flow is seeded by fluid tracers whose response time (τ_p) is so small that they can successfully follow the motion of the fluid. The main principle of PIV is that the displacement of the fluid tracers over the interval δt of the two images gives an instantaneous velocity vector (Bernards and Wallace, 2002). In order to obtain a complete map of the vector field, the image is broken up to smaller sections which are called interrogation windows (Fig.2-2). A cross correlation algorithm is applied to each interrogation windows which yields the total displacement of those tracers in the specific window. Finally, the instantaneous velocity vector is given for all the interrogation windows. While PIV tracks a group of tracers, the main principle for PTV is to track each individual tracer between two successive images to obtain the instantaneous velocity vector for each tracer in the image. For more information about PIV and PTV, please see Adrian and Westerweel (2011) and Raffel et al. (2007).

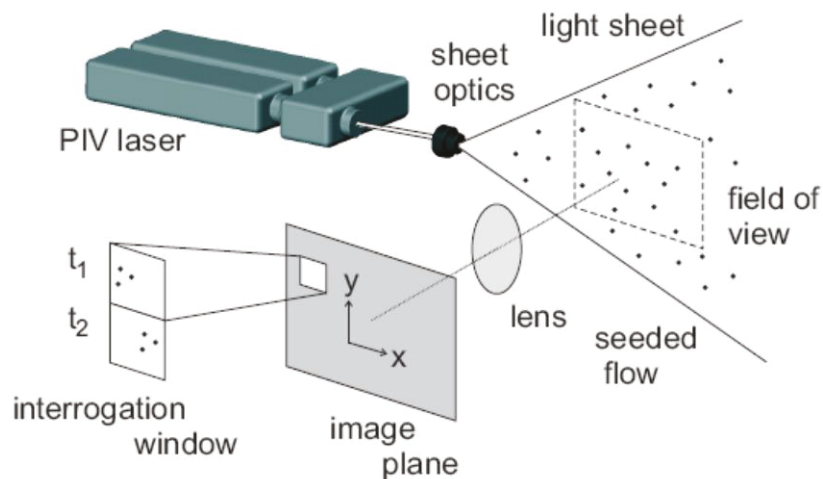


Figure 2-2. Schematic of a planar PIV technique (Flow Master, 2007)

The PIV and/or PTV techniques have been employed in two-phase flows where there is a dispersed phase along with the flow tracers. The main issue for such systems is that one must discriminate between the dispersed phase and the flow tracers. One approach is to detect the dispersed phase through image processing. Nezu et al. (2004) and Noguchi & Nezu (2009) performed PTV measurements for solid-liquid flows in an open channel. After adjusting the brightness and binarizing the images, they discriminated particles from the tracers based on the size of the individual particle image. The PTV algorithm was then applied to the particles and the fluid tracers to obtain the vector fields of both phases (Fig.2-3). Muste et al. (1998) and Muste et al. (2008) used a PIV/PTV technique to obtain the instantaneous velocities of the particles and the liquid phase. After employing an enhancement technique, they detected all the particles and the tracers using an edge detection technique followed by image binarization. They then determined the size and the centroid of the particles and the tracers with sub-pixel precision with a Gaussian sub-pixel fit estimator method (Cowen and Monismith, 1997).

The PIV algorithm was applied to both particles and the tracers to obtain an initial pixel shift. Afterwards, the PTV algorithm provides the accurate velocity vectors of the flow field for both the particles and tracers. Finally, the velocity vectors are divided into particles and tracers based on the corresponding particle sizes in the image. Jing et al. (2010) performed a PIV technique for solid-gas flows. They removed the solid particles from images by applying a threshold on the size and brightness, and then obtained the velocity field of the gas phase by applying cross correlation on the tracers.

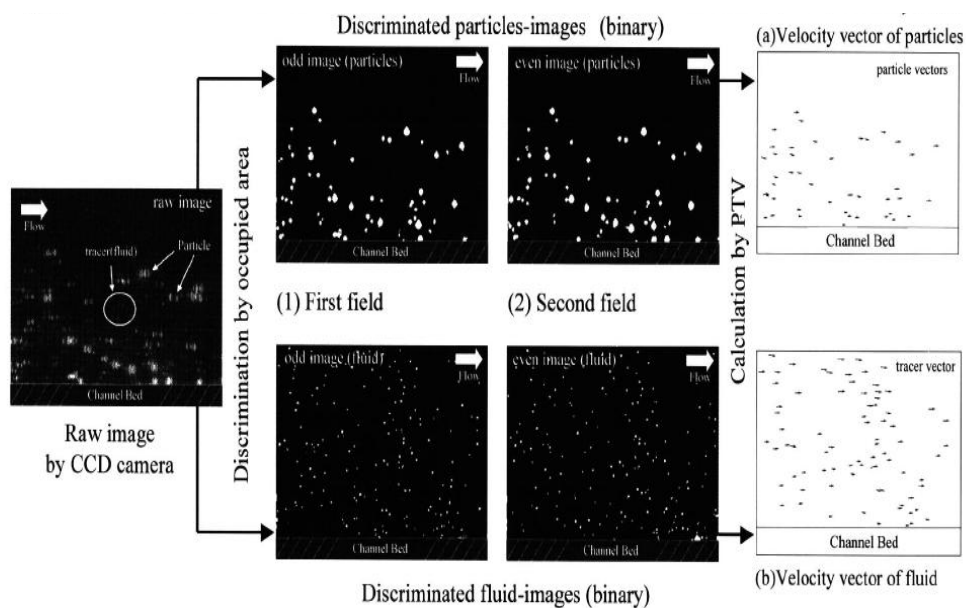


Figure 2-3. Schematic of phase discrimination and PTV procedure from Nezu et al., (2004) (With permission from ASCE)*

The other way to discriminate the dispersed phase from the tracers is to do so optically at the image acquisition stage; e.g. the use of fluorescent tracers which emit

* This material may be downloaded for personal use only. Any other use requires prior permission of the American Society of Civil Engineers

light at a different wavelength after being illuminated by the laser sheet. Since the dispersed phase still emits light with the same wavelength as the laser sheet (532 nm), the phases can be discriminated using appropriate optical filters placed in front of the lens. This method is called PIV/LIF where LIF stands for Laser Induced Fluorescence (Adrian and Westerweel, 2011). Lindken and Merzkirch (2001) used PIV/LIF technique for a bubbly column. They used a filter through which only light from the fluorescent tracers would pass. The gas bubbles were shadow-graphed through backlighting using an LED light source. The image contained bright fluid tracers and shadows of the bubbles as shown in Fig.2-4. Since the shadows had lower gray values (intensity), a cut-off filter was applied to easily discriminate the shadows from the background noise. The tracers were removed using a 7×7 pixel median filter. Finally, the image was binarized and the bubble images were masked out for PIV processing on the fluid tracers. Fujiwara et al. (2004) used the same technique for a gas-liquid flow in a column. However, they used a second camera to separately capture the shadows of the gas bubbles. Bröder and Sommerfeld (2002) used a PIV/LIF technique to measure the velocity statistics of a bubbly column using two cameras with appropriate optical filters to separately capture the images of the tracers and gas bubbles. Phase discrimination using fluorescent tracers can be seen in other works, such as Jing et al. (2010), Sathe et al. (2010), and Kosiwczuk et al. (2005).

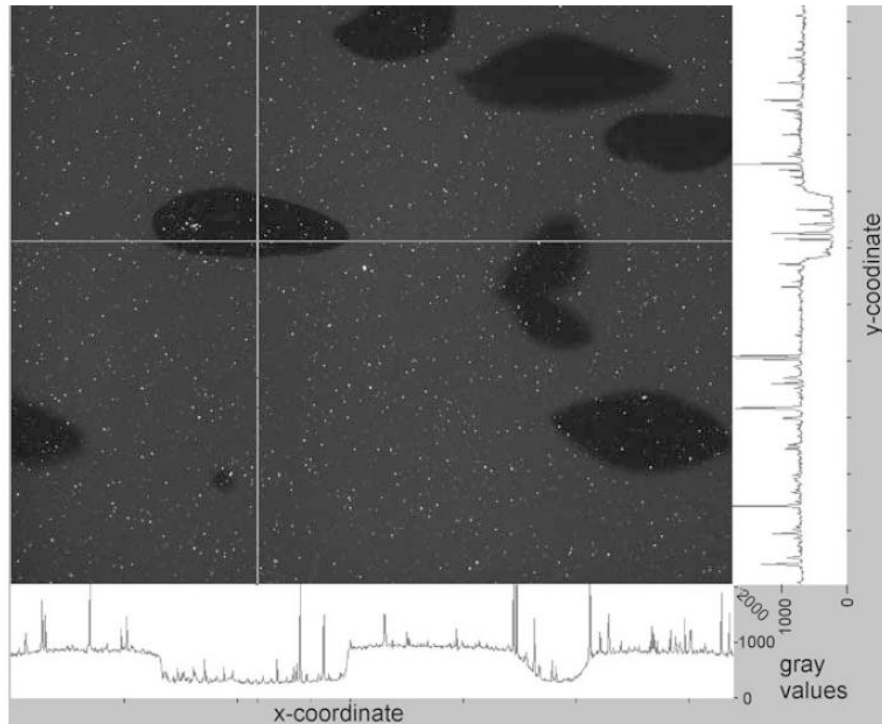


Figure 2-4. PIV/shadowgraphy of the bubbly flow using fluorescent tracers. The gray values along the crossing lines are shown on the bottom and right axes (Lindken and Merzkirch, 2002) (With permission from Springer).

In the present study, the particulate phase is discriminated using an image analysis technique after capturing the image. A method based on circle detection is adopted to detect the glass beads. After phase discrimination, a PIV algorithm is employed to capture the instantaneous velocities of the liquid phase while the particulate phase is evaluated using a PTV algorithm. The details will be provided in subsequent sections.

2.5.1 Imaging setup

A planar PIV/PTV technique is employed to capture the motion of both liquid and particulate phases. The flow is seeded with 18 μm hollow glass tracers (60P18

Potters Industries) that have density of 600 kg/m^3 and a response time of $7\mu\text{s}$. The relaxation time of the tracers is much less than the Kolmogorov time scale of the flow for the conditions tested here; thus, the tracers are able to follow the turbulent motions of the fluid flow (Westerweel et al., 1996). Images are captured with a CCD camera (Imager Intense, LaVision GmbH) that has 1376×1040 pixel resolution with a pixel size of $6.45 \times 6.45 \mu\text{m}^2$. The required PIV illumination is provided by an Nd:YAG laser (Solo III-15, New Wave Research). The laser can produce 50 mJ per pulse at 15 Hz repetition rate with 3-5 ns pulse duration. The laser beam is transformed into a light sheet which has a thickness slightly greater than 1 mm. For each set of experiments, more than 10 000 pairs of double-frame images are acquired and processed using commercial software (DaVis 8.2, LaVision GmbH). A 60 mm Nikkor SLR lens with an aperture setting of $f/16$ is used in in these experiments. In order to calculate the depth of field, one must obtain the magnification (M_c) of the camera, defined as (Raffel et al., 2007):

$$M_c = \frac{\text{size of the image on the sensor}}{\text{real size of the image}} \quad (2-5)$$

Based on the image resolution, 1mm of the real image is 42.6 pixels. By having the physical resolution of the sensor equal to $6.45\mu\text{m}/\text{pix}$, the 42.6 pixel will be translated to 0.27 mm on the image sensor. Therefore, $M_c = 0.27$ for this system. The depth of field (δ_z) can be computed using (Adrian and Westerweel, 2011):

$$\delta_z = 4\left(1 + \frac{1}{M_c}\right)^2 f_{\#}^2 \lambda_w \quad (2-6)$$

where $f_{\#}$ is the f-stop of the lens aperture, which is set at 16 in these experiments, and λ_w is the wavelength of the laser (532 nm). After substituting the values of the parameters, the depth of field is calculated to be about 12 mm.

The first step of the PIV procedure is to calibrate the system which means translating the (x,y) location of the image in pixels to the (x,y) location of the real world dimension in mm (Quenot et al., 2001). Fig.2-5 shows the calibration assembly used in these experiments. The assembly is a half cylinder with the dimension of 50mm (width) \times 80 mm (length) \times 25.3 mm (depth). The calibration plate is a water resistant adhesive paper covered with 0.75mm dots whose centers are separated by a distance of 1.5 mm. The calibration plate is attached to the front face of an assembly, as shown in Fig.2-5a. The calibration assembly is lowered into the test section through an access window that is located about 13D above the test section. As shown in Fig.2-5b, a magnet bar is inserted in the back of the assembly, which means the assembly can be pulled into place using a strong magnet held on the outside of the test section. This holds the assembly securely in the middle of the pipe and up against the pipe wall. Also this configuration allows for fine-tuning the location of the target inside the pipe.

After taking images of the target (Fig.2-6a), the target images are processed using commercial software (DaVis 7.2, La Vision GmbH). The dots are detected and then a third-order polynomial mapping function is applied to calibrate the image (Fig.2-6b). The root-mean-square error of the mapping function is 0.28 pixel (0.007 mm), which is acceptable according to the software manual (Flow Master, 2007). This mapping error is mainly caused by the near-wall distortion. This error introduces some bias uncertainties in specifying the real location of each pixel in the image. However, its effect on the particle displacement measurement is expected to be negligible.

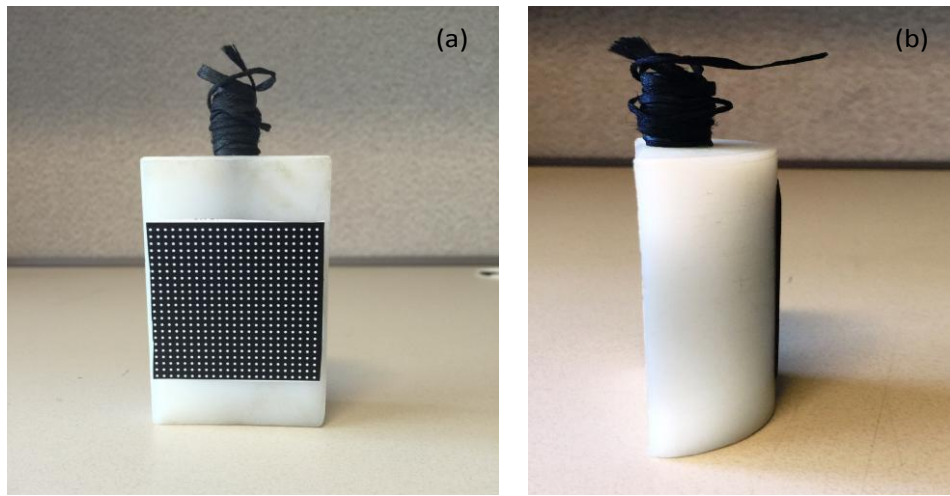


Figure 2-5. Calibration target assembly

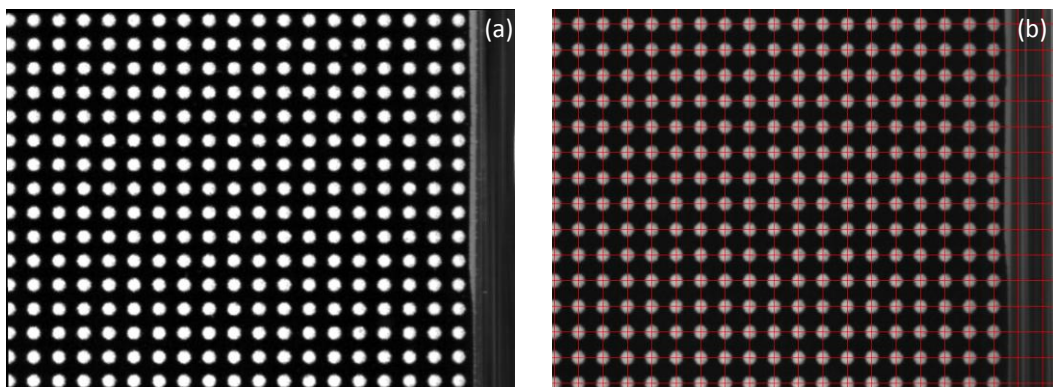


Figure 2-6. (a) the image of the target, (b) corrected image after calibration

2.5.2 Particle detection

The images capture both the large glass beads and the PIV tracers. The large glass beads are detected using “imfindcircle” function in MATLAB (*MATLAB R2013a*)

which is based on the Hough transform for detection of circular objects (Davies, 2012; Atherton and Kerbyson, 1999; Yuen et al., 1990). First, by applying a gradient based threshold, the edge pixels will be selected for the Circular Hough Transform (CHT) procedure. A circle in a 2D image can be represented as:

$$(x - a)^2 + (y - b)^2 = r^2 \quad (2-7)$$

If an image contains many points (candidate edge pixels), some of them fall on the perimeters of circles represented by Eq.(2-7). Therefore, the CHT procedure is designed to find the parameter triplet (a,b,r) which can best fit every circle in the image. For example, consider three points on the perimeter of a circle (the dots on the solid circle) shown in Fig.2-7. A circle is defined in the Hough parameter space centered at (x, y) location of each edge pixels (the black dots) with radius r, shown with dashed lines in Fig.2-7. An “accumulator matrix” is used for tracking the intersection points. In the Hough parameter space, the point with a greater number of intersections creates a local maximum point (the red point in the center). The position (a,b) of the maximum will be the center of the original circle (Davies, 2012).

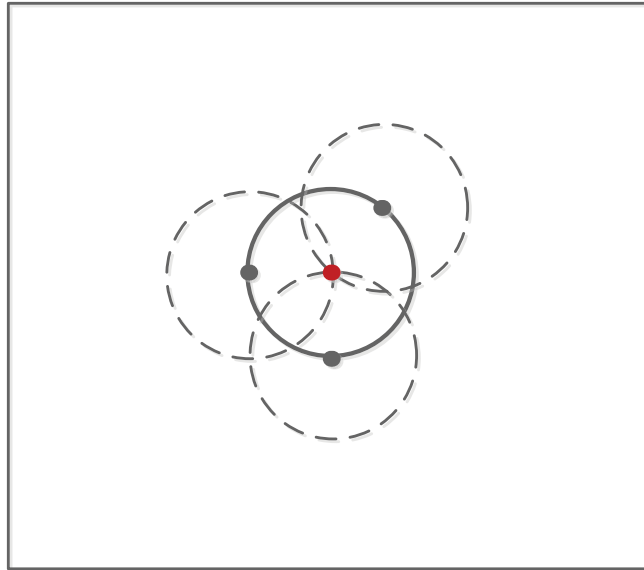


Figure 2-7. Circle detection by CHT method. The dashed circles are defined based on the black dots (edge pixels) as their centers. Solid line circle is the detected one, with the red dot as its center.

The captured images consist of both glass beads and the flow tracers as shown in Fig2-8a (full field of view) and in Fig.2-8b (a magnified section). As mentioned earlier, the glass beads are detected using the “imfindcircle” which requires the range of acceptable particle radius (set to $\pm\%40$ of average particle radius) and also a gradient-based threshold for edge detection as input parameters. The latter is based on the high intensity gradient at the sharp boundary of in-focus particles while the out-of-focus particles have a smooth gradient. Two different low and high gradient-based thresholds are considered for edge-detection. The low threshold is applied to detect and mark all the in-focus and out-of-focus particles from both frames for the PIV analysis of the liquid phase (Fig.2-8c). A higher threshold is applied to detect only the in-focus particles for the PTV process (Fig.2-8d).

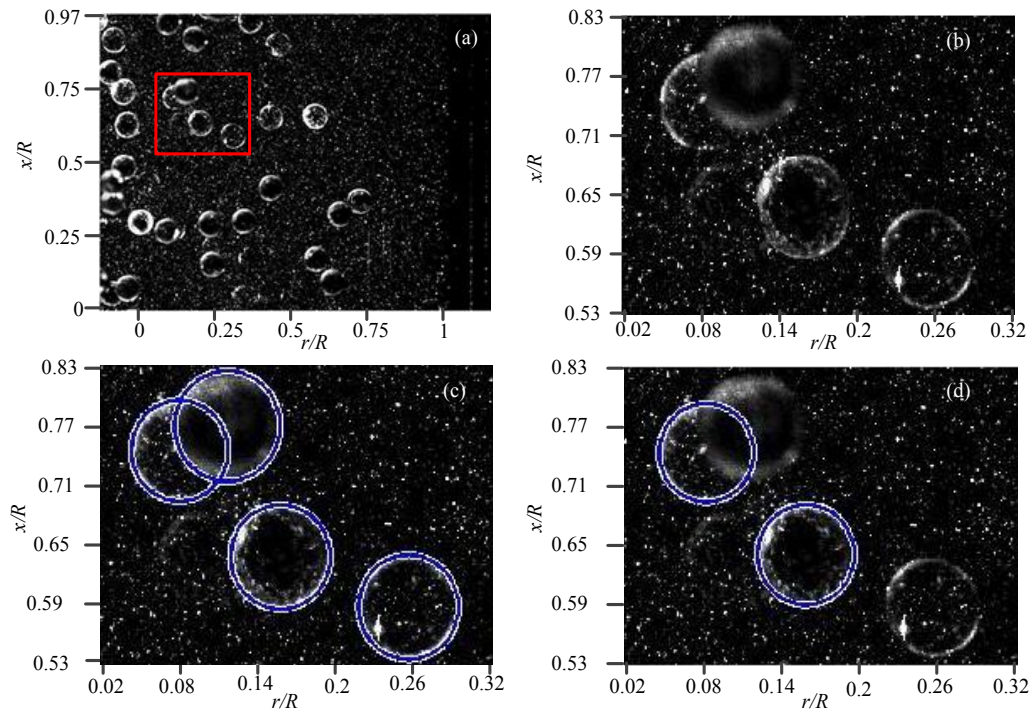


Figure 2-8. (a) A raw image showing the full field-of-view with 2 mm glass beads and PIV tracer particles ($\phi_v=0.8\%$, $Re=320\,000$). Note that $r/R=0$ and $r/R=1$ denote pipe centreline and pipe wall, respectively, while x/R is the streamwise (upward) direction. (b) Magnified view of the region identified by the red boundary specified in the full field-of-view image in (a). (c) Magnified view with in-focus and out-of-focus particles detected using the low edge-detection threshold later to be masked out for PIV analysis of the liquid phase. (d) Magnified view of the in-focus particles detected using the high-gradient threshold for PTV analysis

2.5.3 PIV process

First, the intensities of the pixels of the captured images (Fig.2-9a), which range from 0 to 4096, are normalized to the new range of 0 to 4090. The in-focus and out-of-focus particles in the image are then detected and marked using Matlab. The detected circles (the glass beads) are marked with the highest intensity of 4096 and the images are stored as new images in TIFF format (Fig.2-9b). The different intensity level of detected glass beads will be subsequently exploited to discriminate the glass beads from the tracers in the particle masking scheme. In order to eliminate any influence of the particles on the PIV results, the particle movement in both successive frames will be

marked in both frames. This creates an elongated circle in the marked images as shown in Fig.2-9b. Note that the particles moving in/out of the frame (incomplete circles) at the image border will not be marked because the probability of detecting incomplete circles is poor. Anyhow, the border areas are removed from the PIV analysis.

The images are imported into the Davis 8.2 software to calculate the liquid phase velocity field. First the detected particles will be masked out by an algorithm masking scheme. The scheme masks out areas of the image where the image intensity is higher than 4090. As mentioned above, only glass beads have the intensity of 4096 (>4090) and thus the detected beads will be masked out. The masked particles in the image are shown in Fig.2-9c. Two nonlinear filters, including subtract sliding background and particle intensity normalization filters, are applied to the images. Cross-correlation with 32×32 pix^2 (equal to $0.77 \times 0.77 \text{ mm}^2$) window size and 75% window overlap is applied to obtain the instantaneous velocity field of liquid phase (Fig.2-9d). The interrogation windows, which have more than 1% overlap with the masked areas, are rejected ensuring no bias in the measurement of the liquid phase.

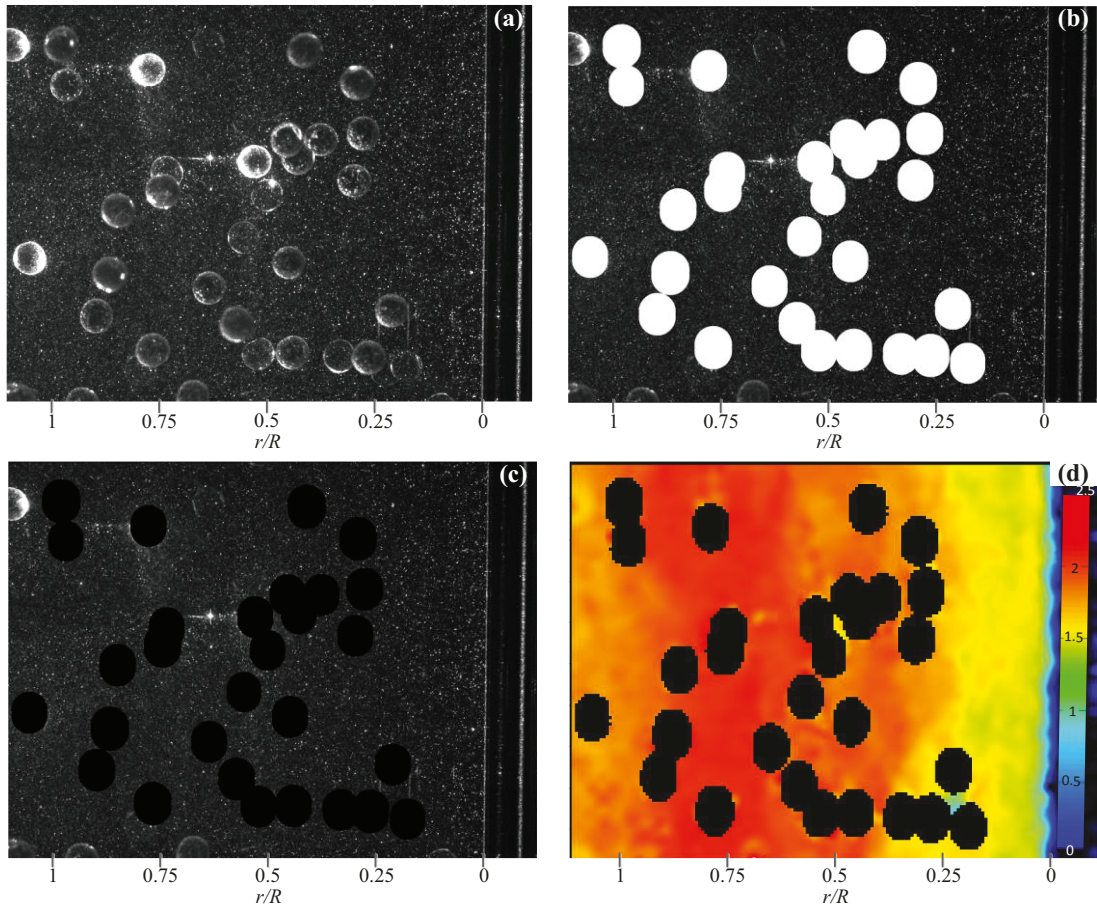


Figure 2-9. The PIV procedure for two-phase flow, (a) raw image of 2mm particles ($\phi_v=0.8\%$, $Re=320\ 000$), (b) particles are detected and marked in Matlab, (c) image with the masked out particles in Davis 8.2 software, (d) applying cross correlation to obtain the instantaneous velocity of the flow field

2.5.4 PTV process

Recall that the “imfindcircle” function finds the best fit of a circle to the detected edges and returns the radius and the center location of the circle at a sub-pixel precision. In PTV processes, a higher threshold for particle detection is employed, in order to detect in-focus particles that are most likely to be in contact with the laser sheet. To obtain the velocity of individual particles, one must find the displacement of the particles from frame#1 to frame#2. The PTV algorithm has been developed in MATLAB to track each

individual particle from frame#1 to frame#2 and compute the velocity of each particle based on the particle displacement in the given time difference. The PTV scheme used in the present study is called ‘relaxation technique’ (Baek and Lee, 1996). The algorithm loops through all of the detected particles in frame#1 searching for each corresponding particle in frame#2 by defining a search radius in the image. Here, the dominant axial velocity, low radial velocity and the large particle size helped to narrow the search area to a specific region. We know that the particles slightly lag behind the flow in the axial direction and they may have equal or somewhat larger radial fluctuations than the liquid phase. Therefore, a sufficiently large range of displacement in both radial and axial directions was applied, initially estimated using the liquid velocity profile, to define the search region. For each particle in frame#1, the algorithm loops through all the particles in frame#2 to find the corresponding particle whose center is located in the search area of: $+4 \text{ pixel} < \Delta x < +20 \text{ pixel}$ and $-4 \text{ pixel} < \Delta r < +4$. Figure 2-10 shows the particle displacement ranges for 1 mm particles in the radial and axial directions at the pipe center obtained through PTV processing. The uncertainty in the PTV technique is closely related to the accuracy of the particle center detection. The accuracy of any object detection technique deteriorates as the size of the object in the image decreases. As shown by Ghaemi et al. (2010), the discretization error becomes negligible when the particle image size becomes larger than 50 pixels. Here, the particle image size for each particle, in pixels, is; 25 (0.5 mm); 45 (1 mm); and 85 (2 mm). The convergence plots for the uncertainties of the particle mean and fluctuating velocities are provided in Appendix D.

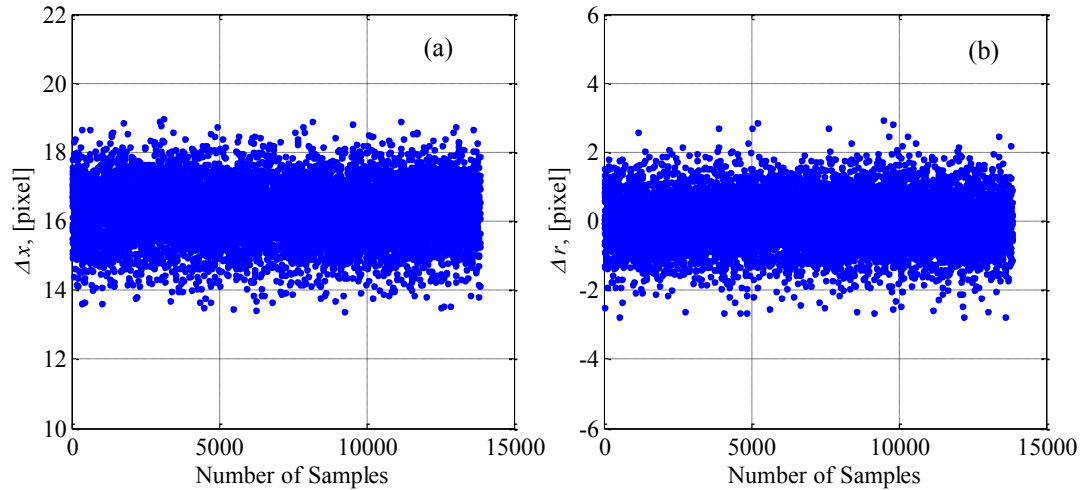


Figure 2-10. Particle displacement population in (a) streamwise and (b) radial directions at the pipe centerline for 1mm glass beads at $Re=100\ 000$, $\phi_v=0.4\%$

Because the diameters of the in-focus particles are obtained through the particle detection process, the particle size distribution based on the size of the particle with respect to the average particle size, $\langle d_p \rangle$ can be plotted, as shown in Fig.2-11. In order to produce a size distribution that is independent of the bin size selected, the number frequency percentage is divided by the size of the bin. The results show that the particle size distributions (PSDs) of the tested glass beads are nearly symmetric. Some particle-related details obtained through the particle detection scheme are summarized in Table 2-2. The results show that the average diameter is near the nominal size provided by the supplier, and the standard deviations (SD) of the different sizes are similar which means that all the particles have similar size distributions.

Table 2-2. Solid particle specifications obtained through PTV processing.

Nominal d_p (mm)	Measured $\langle d_p \rangle$ (Pixel)	Measured $\langle d_p \rangle$ (mm)	Standard deviation (mm)
0.5	25.03	0.5947	0.0435
1	44.64	1.067	0.0532
2	85.54	2.042	0.0458

Inspection of the double-frame images shows slight deviations in the size of an individual particle between the two frames. The difference most probably stems from the variation of the surface glare of the glass beads, from glass beads getting slightly in/out of focus because of out-of-plane motions, and/or actual particle non-sphericity. Since the deviations affect the PTV accuracy, a filter is applied to discard the glass bead images whose diameter difference in two frames is greater than 1 pixel (0.024 mm). Fig.2-12 shows the cumulative distribution of diameter difference for the detected glass beads between the first (d_{p1}) and the second (d_{p2}) frames. As Fig.12-2 illustrates, about 15-20% of the data points in each set were discarded after applying the aforementioned filter. This filter has significantly reduced the data noise and has resulted in more rapid statistical convergence.

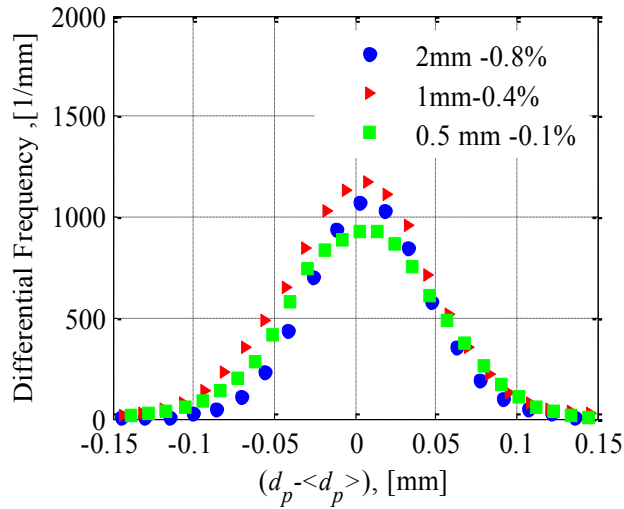


Figure 2-11. Particle size distribution obtained from PTV analysis at Re=100 000

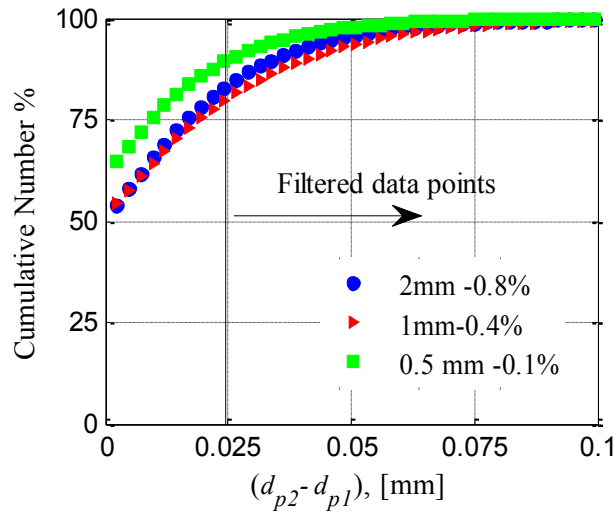


Figure 2-12. Cumulative distribution of particle size difference between frame#1 and frame#2 at Re=100 000.

2.6 Uncertainty analysis

Uncertainties are part of any experimental measurements. They can originate from a lack of accuracy in the measurement equipment, random variation of the measuring variable in experiments, and/or approximation of quantity correlations in a

measurement technique (Wheeler and Ganji, 1996). The uncertainty is classified into two categories: “random uncertainties” and “bias uncertainties”. The random uncertainties are caused by imprecision in the measurements. The bias uncertainties are the maximum fixed error and they are related to the accuracy of the measurement equipment and the applied techniques (Wheeler and Ganji, 1996). Below, the sources of uncertainty in the PIV/PTV technique are discussed.

2.6.1 Error/uncertainty sources

There are some sources in PIV/PTV measurements that cause uncertainties or error. These sources are discussed and investigated in this section. The uncertainty sources for PIV and PTV calculations are described in that order.

2.6.1.1 Uncertainty sources in PIV

The first issues with PIV measurements are related to the near-wall measurements. The near-wall measurements are usually biased because of the strong velocity gradient (Kähler et al., 2012). The high velocity gradient gives particles very different velocities in a specific interrogation window. Consequently, the velocity vector will be averaged out, which leads to a reduction in the measurement accuracy. The other source of error in the near-wall region is reflection. In order to suppress the wall reflection, one can use fluorescent particles as in micro-fluidic experiments (Santiago et al., 1998). Through the inspection of the image, the width of the reflection is about 10 pixels. Since 32×32 pixel windows and 75% overlap were used for the PIV calculations, about 3-4 data points adjacent to the wall are expected to be heavily influenced by the reflection. Moreover, the near-wall measurements are affected by wall curvature. There was no calibration point within about 0.5 mm of the distance to the wall, and only one

calibration point is provided in region $r/R > 0.9$. This is not sufficient to resolve the high image distortion in this region. Therefore, greater uncertainties are expected in the near wall region.

Another source of uncertainty is the “low resolution of PIV measurements”, specifically at higher Reynolds numbers. This can be attributed to the selected window size which is not sufficiently small. The window size is 32×32 pixel² in these PIV calculations, which is approximately equal to 0.8×0.8 mm². This size of the window is too large for resolving turbulence in all scales in the near-wall region, especially at $Re = 320\,000$. The smallest coherent structures that contribute to the average fluctuations have a size of 20 times the wall units (Stanislas et al., 2008), which ranges from 0.08 to 0.4 mm over the range $52\,000 \leq Re \leq 320\,000$. Therefore, some turbulent fluctuations will be filtered and the final results become dampened, especially at the highest Re tested.

The seeding particles could be another source of uncertainty. Because of the finite size and density of the particles, there is a slip velocity between the two phases which can be estimated using the particle terminal settling velocity (Adrian and Westerweel, 2011). For these tracers, the terminal velocity is 7×10^{-5} m/s, which indicates that the error caused by the slip velocity of the tracers is negligible. Moreover, the relaxation time of the tracers is $7 \mu\text{s}$ which is much smaller than the Kolmogorov time scale (1 ms to 20 ms) for the conditions tested here. This also implies that the tracers will follow the liquid phase turbulent motions. In summary, the uncertainties related to the seeding particles are negligible (Westerweel et al., 1996).

Finally, there are very few large glass beads in the images that cannot be detected and masked. The failure to capture these particles is mainly because they are very out-of-focus.

2.6.1.2 Uncertainty sources in PTV

Perhaps the most important source of uncertainty in PTV calculations is the accuracy of the center detection. Although the circular Hough transform technique yields the size and center location of the particles at a sub-pixel precision, the accuracy can be variable mainly due to the size of the particles. Since particle detection is based on the edge detection, the accuracy of the particle size and the center location is directly related to the particle diameter. Ghaemi et al. (2010) showed that as the particle diameter decreases, the discretization error increases (Fig.2-13). Particle image size for each particle, in pixels, is; 25 (0.5 mm); 45 (1 mm); and 85 (2 mm). Therefore the accuracy of the center detection is expected to decrease as the particle size decreases.

As mentioned earlier, particle non-sphericity and the particle glare may cause the particles to have slightly different sizes from frame#1 to frame#2. This size difference may also lead to a slight change in the center location and hence error in particle velocity measurements. In order to reduce this effect, a filter has been applied to the detected particles. The filter discards the particles whose diameter difference between two frames is more than 1 pixel (Fig.2-12).

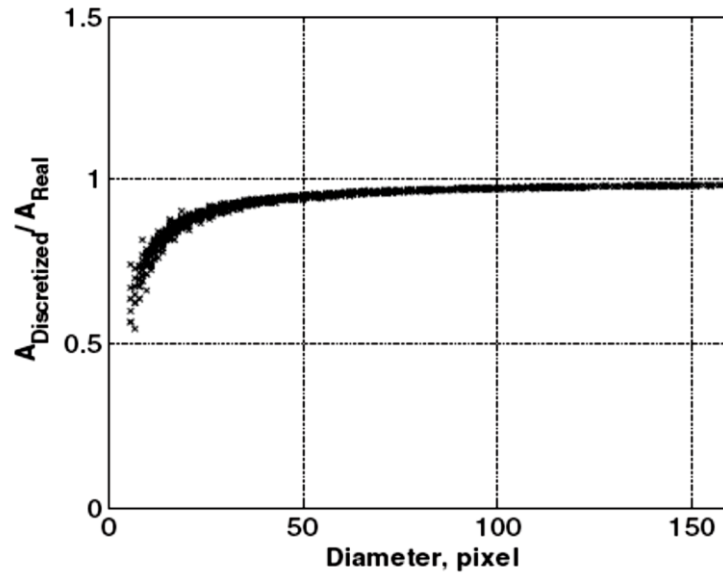


Figure 2-13. The effect of particle size on the discretization error (Ghaemi et al., 2010) (With permission from John Wiley and Sons).

As mentioned earlier, the thickness of the light sheet is less than 1mm. Because of the relatively large size of the particles, there is a high probability that those particles are only partially in the light sheet. Hence, the particles detected for the PTV analysis may not be located in the middle plane, which leads to uncertainties in PTV measurements. Moreover, having large particles with a chance of being slightly away from the middle plane (plane of focus) raises a question around the depth of field in the experiments. The large depth of field (around 6 mm from middle plane on either side) proves that the particles are in focus very well beyond the middle plane. Hence, the bias uncertainty in PTV measurements due to the particles being out-of-focus is negligible.

The other uncertainty comes from the measurement spatial resolution in the radial direction. For the PTV measurements, the radial direction is divided into 12 bins. This means that the measurement area is binned into 2.1 mm wide stripes in the radial

direction and the measured particle parameters are going to be averaged out in those specific 2.1 mm wide bands. The larger bin size lowers the resolution of the measurement and it leads to more dampening of the turbulence statistics.

2.6.2 Random (precision) uncertainty level

These uncertainties are determined by repeating the measurements of the intended parameters (Wheeler and Ganji, 1996). All the variables in these experiments, including $\langle U \rangle$, $\langle u^2 \rangle$, $\langle v^2 \rangle$, and $\langle uv \rangle$ of both phases are obtained through averaging a large number of samples at many locations over the pipe cross section. These quantities converge to a final mean number with a small level of variation. These small variations from the final mean value can be called random (precision) uncertainty.

As shown in Fig.2-14, the averaged value $\langle u^2 \rangle$ of the 2mm particles for three different locations ($r/R=0$, $r/R=0.5$, and $r/R=0.96$) approaches the final values after a certain number of samples. Clearly, a greater number of samples reduce the random uncertainties. By scrutinizing the results, it can be seen that more than 4000 samples are needed to reach a steady statistical average. However, some variance from the mean value can be seen even after very large number of samples. Therefore, standard deviation in the last 25% of the samples is calculated to report the random uncertainty level. The random uncertainties for $\langle u^2 \rangle$ of the 2mm particles at $Re = 100\ 000$ and $\phi_v=0.8\%$ are 1.0×10^{-4} , 1.8×10^{-4} , and 7.3×10^{-4} at $r/R=0$, $r/R=0.5$, and $r/R=0.96$ respectively. This shows that the uncertainties for the data at $r/R=0.96$ are the highest because of the lower number of the samples. The uncertainties of the values at $r/R=0.96$ for higher concentration of 2mm particles as well as other sizes are far lower due to the greater number of samples. Similar plots are provided for the liquid phase in Fig.2-15 at the

same flow condition as Fig.2-14. Tables of the uncertainty data along with the full matrix of uncertainty plots are provided in the Appendix D for the values of $\langle U \rangle$, $\langle u^2 \rangle$, $\langle v^2 \rangle$, and $\langle uv \rangle$ of both phases, for all conditions tested here and at three locations: $r/R=0$, $r/R=0.5$, and $r/R=0.96$.

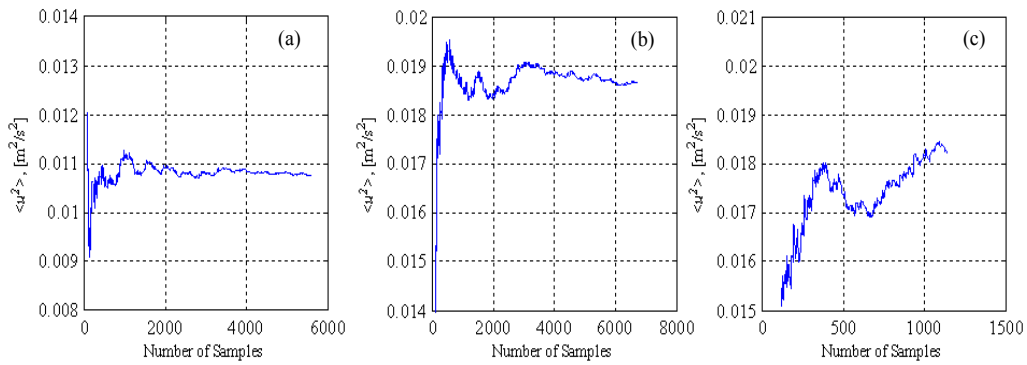


Figure 2-14. Convergence of $\langle u^2 \rangle$ for 2mm particles, $Re=100\ 000$, $\phi_v=0.8\%$ at (a) $r/R=0$, (b) $r/R=0.5$ and (c) $r/R=0.96$

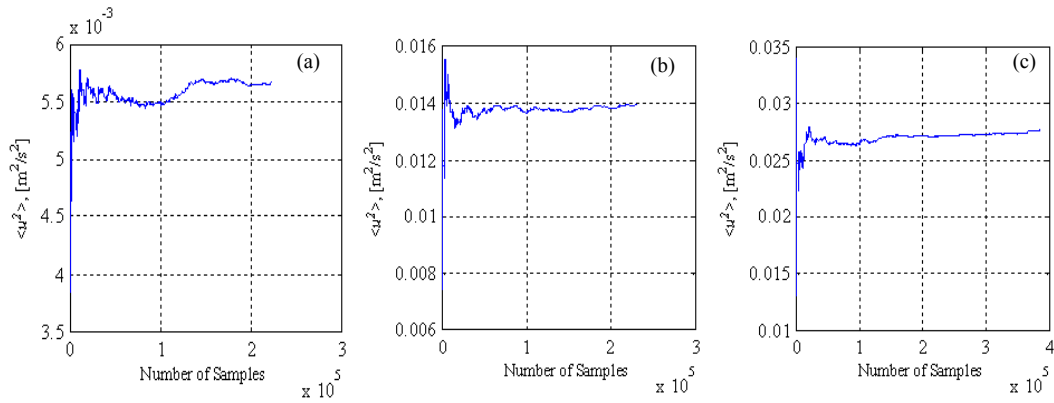


Figure 2-15. Convergence of $\langle u^2 \rangle$ for liquid phase laden with 2mm particles, $Re=100\ 000$, $\phi_v=0.8\%$ at (a) $r/R=0$, (b) $r/R=0.5$ and (c) $r/R=0.96$

3 Investigation of particle-laden turbulent pipe flow at high-Reynolds-number using particle image/tracking velocimetry (PIV/PTV)*

3.1 Introduction

In turbulent particulate flows, particles can have a significant effect on the transport properties of the mixture, e.g. heat and mass transfer (Sivakumar et al., 1988; Yoon et al., 2014). The motion of particles and their interaction with the turbulent fluid produces a system with extremely complicated behaviour, which is a function of, at the minimum, Reynolds number, particle Reynolds number (Re_p) and Stokes number (St), particle/fluid density ratio (ρ_p / ρ_f), flow orientation, and solid phase volumetric concentration (ϕ_v). This complexity has restricted analytical models and numerical simulations of particle laden-flows to simplified conditions and relatively low Reynolds numbers. Although higher values of Re are accessible by experimental investigation (Balachandar and Eaton, 2010), measurement in turbulent particle-laden flows have generally been limited to $Re < 30\,000$, far lower than most industrial applications.

* A version of this chapter has been submitted to International Journal of Multiphase flow and is in revision. It is co-authored by R. Shokri, S. Ghaemi, D.S. Nobes, and R.S. Sanders.

Table 3-1 provides a detailed overview of previous experimental investigations of particle-laden turbulent flows at low dispersed phase volume fractions. The table presents the main independent variables of each study. As shown in the table, however, for gas-solids systems the mass concentration (φ_m) is quite high even at low volumetric concentrations. The investigations summarized in Table 3-1 can be classified into two main categories based on the carrier phase, i.e. gas- or liquid-continuous particle-laden flows. Kulick et al. (1994) measured the turbulent statistics of particles and the carrier phase (air) in a downward gas-solid rectangular channel flow at $Re = 13\ 800$. Varaksin et al. (2000), Caraman et al. (2003) and Borée and Caraman (2005) studied particle and fluid turbulence in a downward air-solid pipe flow at $Re < 8\ 000$. Lee and Durst (1982) and Tsuji et al. (1984) employed laser Doppler velocimetry (LDV) to measure the turbulent statistics in a gas-solid upward pipe flow with $Re = 8\ 000$ and $23\ 000$, respectively. Also Tsuji and Morikawa (1982) investigated the effect of the 0.2 and 3.4 mm plastic particles on the turbulence intensities of the gas phase in a horizontal pipe flow at $Re < 40\ 000$.

Table 3-1. An overview of experimental investigations of particle-laden turbulent flows.

REF.	Carrier Phases	Flow direction	d_p (mm)	Re	ρ_p/ρ_f	φ_m	φ_v
Boré and Caraman (2005)	Gas	Down	0.06,0.09	5 300	2100	0.1-0.52	$(0.5-5)\times 10^{-4}$
Caraman et al. (2003)	Gas	Down	0.06	5 300	2100	0.1	5×10^{-5}
Kussin and Sommerfeld (2002)	Gas	Horizontal	0.06-0.625	< 58 000	2100	0.09-0.5	$(0.5-5)\times 10^{-3}$
Varaksin et al. (2000)	Gas	Down	0.05	15 300	2100	0.04-0.55	$(0.2-5.8)\times 10^{-4}$
Kulick et al. (1994)	Gas	Down	0.05 to 0.09	13 800	2100,7300	0.02-0.44	$(0-4)\times 10^{-4}$
Lee and Durst (1982)	Gas	Up	0.1- 0.8	8 000	2100	0.55-0.71	$(0.58-1.2)\times 10^{-3}$
Tsuji et al. (1984)	Gas	Up	0.2-3	23 000	860	0.33-0.77	$(0.6-4)\times 10^{-3}$
Tsuji and Morikawa (1982)	Gas	Horizontal	0.2, 3.4	<40 000	830	0.29-0.77	$(0.5-4)\times 10^{-3}$
Kameyama et al. (2014)	Liquid	Up/down	0.625	19 500	2.5	0.002	0.006
Hosokawa and Tomiyama (2004)	Liquid	Up	1 to 4	15 000	3.2	0.002-0.006	0.007-0.018
Kiger and Pan (2002)	Liquid	Horizontal	0.195	25 000	2.5	6×10^{-4}	2.4×10^{-4}
Suzuki et al., (2000)	Liquid	Down	0.4	7200	3850	0.001	3.2×10^{-4}
Sato et al. (1995)	Liquid	Down	0.34,0.5	5 000	2.5	0.005-0.031	0.002- 0.013
Alajbegovic et al. (1994)	Liquid	Up	1.79,2.32	42 000-68 000	0.032, 2.45	3×10^{-4} - 0.08	0.009-0.036
Zisselmar and Molerus (1979)	Liquid	Horizontal	0.053	100 000	2.5	0.007-0.024	0.017-0.056

Kussin and Sommerfeld (2002) investigated particle-laden gas flow in a horizontal pipe with glass beads (60 to 625 μm) at $Re < 58\,000$. Liquid-solid mixtures, which are important in many industrial applications, have also been investigated, but to a lesser extent than gas-solid flows, as can be seen from Table 3-1. Sato et al. (1995) experimented with 340 and 500 μm glass beads in a downward liquid rectangular channel flow at $Re = 5\,000$. Hosokawa and Tomiyama (2004) performed some experiments using a mixture of water and ceramic particles at $Re = 15\,000$ in an upward pipe flow. Kameyama et al. (2014) employed PIV to measure turbulent fluctuations of water and glass beads in both downward and upward pipe flow at $Re = 19\,500$. Alajbegovic et al. (1994) investigated the turbulence of the solid and liquid phase with buoyant polystyrene particles and ceramic particles in an upward flow at $Re < 68\,000$. Suzuki et al. (2000) investigated both the particle and the carrier phase turbulence for 0.4 mm ceramic beads and water in a downward channel flow at $Re = 7\,500$ using 3D-PTV. Two investigations of turbulent solid-liquid flow involved horizontal flows: Kiger and Pan (2002) studied 0.195 mm particles at $Re = 25\,000$ and Zisselmar and Molerus (1979) investigated the effect of relatively small particles (0.053 mm) on the liquid-phase turbulence at $Re = 100\,000$. It is clear that all previous experimental studies are limited to $Re \leq 100\,000$ which is much lower than most industrial applications such as slurry transport pipelines. The low Reynolds number limitation could be partially due to the fact that the focus of previous investigations was air-continuous particle-laden flows; likely, the difficulty of making measurements at high Re is another factor.

In addition to the characterization of fluid turbulence in a dispersed two-phase system, a better understanding of the turbulent motion of particles is also very important.

Lee and Durst (1982) showed that streamwise turbulent intensity of 0.8 mm glass beads in an upward gas flow was higher than the carrier phase at the core of the flow but smaller in the near-wall region. Kulick et al. (1994) and Varaksin et al. (2000) illustrated that for small particles (50 to 70 μm) in a downward gas flow, the particle streamwise turbulence intensity is higher than that of the single phase. However, the lateral turbulence intensity of the particles is lower than that of the single phase flow. Caraman et al. (2003) reported the turbulent statistics for 60 μm glass beads in a downward gas flow. They found that the particles had higher streamwise fluctuating velocities than the gas and the fluctuations in the radial direction were almost identical for both phases. Borée and Caraman (2005) used the same experimental setup as Caraman et al. (2003) to study a bidispersed mixture of glass beads (60 μm and 90 μm) in a gas flow and showed that, at a higher particle concentration than that of Caraman et al. (2003), fluctuating particle velocities in the radial direction were much higher than the fluid fluctuations. Kameyama et al. (2014) showed that both radial and streamwise turbulence fluctuations of 0.625 mm glass beads were equal to or higher than those of the liquid phase (water) in both the upward and downward flow directions. Suzuki et al. (2000) also observed that the particle (0.4 mm ceramic beads) turbulence statistics of any direction are higher than those of the liquid phase in a downward channel flow.

While most studies of particle turbulence statistics show that the particle streamwise fluctuations are at least equal to (and usually greater than) those of the liquid phase, there is no such agreement on the lateral (radial) particle fluctuations. While the majority of experimental works suggest that lateral particle fluctuations are equal to or greater than those of the surrounding fluid, Kulick et al. (1994) and Varaksin et al. (2000) found the

opposite. Vreman (2007) suggested that wall roughness and particle electrostatics, which were not characterized in the experimental investigations, could be the cause of their observations. The latter effect was also mentioned by Kulick et al. (1994) in their analysis of their own data. In a separate study, Kussin and Sommerfeld (2002) measured particle turbulence intensities in particulate gas flow in a horizontal pipe and showed that wall roughness significantly affected the turbulence intensity of the particles. Finally, one should note that Varaksin et al. (2000) speculated that their results may have been affected by insufficient pipe length to produce fully developed flow at the measurement location.

The summary, given above, clearly shows that (i) continuous phase turbulence statistics for liquid-solid flows have been collected in very few studies when compared to gas-solid flows, (ii) dispersed-phase turbulence statistics are almost non-existent in liquid-solid flows (again, compared with gas-solid flows) and (iii) almost all studies have been conducted at $Re \leq 100\,000$. In addition, the extrapolation of particle motion in gas flows to liquid flows at high Reynolds numbers is not straightforward because of the difference in density ratios (ρ_p/ρ_f) and particle Stokes numbers. Therefore, experimental investigations of high Reynolds number, liquid particle-laden flows are required to address three main concerns: the extent to which fluid turbulence is modulated by the presence of particles in high Reynolds number flows; to determine if existing approaches for predicting turbulence modulation are accurate; and to investigate the magnitudes of the particle streamwise and radial fluctuations compared to those of the liquid.

Turbulence modulation (M) is defined as the magnitude of the change in the fluid phase fluctuating velocities because of the presence of the particles. For example, the turbulence modulation in the axial (streamwise) direction (M_x) can be defined as (Gore and Crowe, 1989):

$$M_x = \frac{\left(\frac{\langle u^2 \rangle^{0.5}}{U_b}\right)_{TP} - \left(\frac{\langle u^2 \rangle^{0.5}}{U_b}\right)_{SP}}{\left(\frac{\langle u^2 \rangle^{0.5}}{U_b}\right)_{SP}} \quad (3-1)$$

where u and U_b are the axial fluid fluctuating velocity and bulk velocity, respectively and $\langle \rangle$ denotes ensemble averaging. The subscripts TP and SP stand for “two phase” and “single phase”, respectively.

Criteria are available in the literature to predict if the presence of a particulate phase produces augmentation or attenuation of the carrier phase turbulence. For example, Hetsroni (1989) proposed that if the particle Reynolds number (Re_p) is less than 100, turbulence attenuation occurs. Both augmentation and suppression of continuous phase turbulence can be expected when $100 < Re_p < 400$, while turbulence augmentation should be expected if $Re_p > 400$. Elghobashi (1994) suggested that for dilute particle concentrations ($10^{-6} \leq \phi_v \leq 10^{-3}$), the particle Stokes' number (St_k), based on the Kolmogorov time scale, can be used to distinguish between conditions that provide turbulence attenuation and augmentation. If $St_k < 100$, continuous phase turbulence should be attenuated. The definition of St_k is provided in Section 2.3. Gore and Crowe (1989) analysed the turbulence modulation data available in the literature and concluded that the smaller particles tend to attenuate the

turbulence while the larger ones augment it. Gore and Crowe (1989) proposed that if the ratio of the particle size to the most energetic eddy length scale (d_p/l_e) is less than 0.1, turbulence attenuation should occur. For $d_p/l_e > 0.1$, particles will cause the carrier phase turbulence to be augmented. The Length scale l_e is estimated as $0.1D$ for the fully-developed pipe flows (Hutchinson et al., 1971). Although the criteria are to some extent successful in classifying the augmentation/attenuation of fluid turbulence in both gas-solid and liquid-solid flows, it is not capable of providing any estimation of the magnitude of the modulation. In other words, more parameters, in addition to what mentioned above, must play important roles in characterizing the effect of the particulate phase on the fluid turbulence. Gore and Crowe (1991) suggested that turbulence modulation could be described using a combination of non-dimensional parameters, i.e.:

$$M\% = f(Re, Re_p, \frac{u}{U_s}, \frac{\rho_p}{\rho_f}, \varphi_v) \quad (3-2)$$

In Eq.(3-2), U_s is the slip velocity between the fluid and a particle and all other variables have been previously introduced. Tanaka and Eaton (2008) introduced a new dimensionless parameter, Pa_{st} (particle momentum number) to classify attenuation and augmentation of fluid turbulence by particles:

$$Pa_{st} = St_k Re^2 \left(\frac{\eta}{L}\right)^3 \quad (3-3)$$

where η is the Kolmogorov length scale, St_k is the Stokes number based on the Kolmogorov time scale (see Section 2.3 for more detailed definition), and L is the

characteristic dimension of the flow. They showed that turbulence is attenuated when $3 \times 10^3 \leq Pa_{st} \leq 10^5$, while outside this range the fluid turbulence is augmented. This criterion, however, was developed based on experimental data sets for $Re < 30\,000$ (Balachandar and Eaton, 2010). As shown in Eqs.(3-1) and (3-2), Reynolds number has a direct impact on the particle-phase effects on the fluid turbulence. Again, this is taken as justification for the extension of experimental investigation to higher Reynolds numbers.

The present study provides detailed characterization of the turbulent motion of particles dispersed in water flowing upward through a vertical pipe with an inner diameter of 50.6 mm at $Re = 320\,000$. In this vertical flow, the interaction between the fluid turbulence and particles is not additionally complicated by having to account for the effect of gravity acting perpendicularly to the flow, producing asymmetric particle concentration profiles. Glass beads were used as the particulate phase with diameters of 0.5, 1 and 2 mm tested at volumetric concentrations of $\phi_v = 0.1, 0.2, \text{ and } 0.8\%$. A combined PIV/PTV technique is applied for simultaneous measurement of turbulent statistics of both phases, as detailed in the subsequent sections. These experiments aim to expand the boundaries of experimental investigations of turbulent particle-laden flows, which were summarized in Table 3-1, to solid-liquid flows at higher *Reynolds* numbers and to provide new understanding of the turbulence of both dispersed and carrier phases under these conditions.

3.2 Experiments

3.2.1 Flow loop

The experimental investigations are carried out in a recirculating slurry loop as shown in Fig.3-1. The loop operates using a centrifugal pump controlled by a variable frequency drive (Schneider Electric-Altivar61) and connected to a 15 kW motor (2/1.5 B-WX, Atlas Co.). The flow rates are measured by a magnetic flow meter (FoxBoro IM T25) and the fluid temperature is held constant at 25°C during each experiment using a double-pipe heat exchanger. Water and then particles are loaded through the feeding tank. Once the loop is loaded with the mixture, the tank is bypassed and flow circulates through a closed loop. Measurements are conducted in the upward flow pipe section, which has an inside diameter of $D = 50.6$ mm. An acrylic transparent test section is located more than $80D$ after the lower bend providing sufficient length to provide a fully developed turbulent pipe flow at the measurement location, which is also $15D$ upstream of the long-radius upper bend ($R_b = 11D$). In order to minimize image distortion due to the curvature of the pipe wall, a rectangular acrylic box filled with water is placed around the test section. The distance between the camera (front element of the lens) and the measurement plane is 250 mm.

A summary of the test conditions is provided in Table 3-2. Glass beads (A-series, Potters Industries Inc.) used in the tests have true densities of 2500 kg/m^3 resulting in $\rho_p / \rho_f = 2.5$. The average mixture velocity selected for the tests is 5.72 m/s, which correspond to $Re = 320\,000$ and frictional Reynolds number (Re_τ) of 13 600. The latter can be computed using the friction velocity (U_τ) (Takeuchi et al., 2005):

$$U_\tau = \sqrt{\frac{\tau_w}{\rho_f}} \quad (3-4)$$

The wall shear stress (τ_w) can be calculated using the Darcy friction factor and Colebrook equation (Young et al., 2004).

Table 3-2. Matrix of the test conditions

U_b (m/s)	Re	d_p (mm)	ϕ_v (vol%)
5.72	320 000	0.5	0.1
		1	0.4
		2	0.8

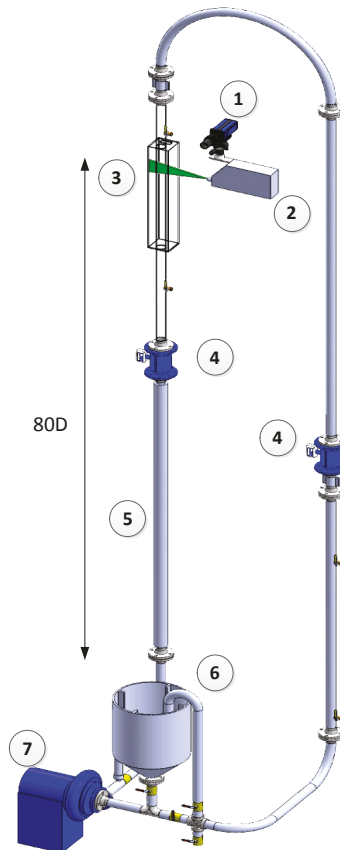


Figure 3-1. A schematic of the experimental setup, which consists of (1) camera, (2) laser, (3) acrylic pipe and viewing box, (4) magnetic flow meters, (5) double-pipe heat exchanger, (6) feeding tank, (7) and the centrifugal pump, frequency drive and motor.

3.2.2 PIV/PTV technique

A planar PIV/PTV technique is employed to capture the motion of both the liquid and the particulate phases. The flow is seeded with 18 μm hollow glass beads with density of 600 kg/m^3 (Spherical 60P18, Potters Industries Inc.). The seeding particles have a relaxation time of 7 μs while the Kolmogorov time scale is 1.4 ms (see Section 2.3 for the calculations), showing that the seeding particle time scale is very small compared to the Kolmogorov time scale and the tracers can accurately follow the turbulent motion of the fluid (Westerweel et al., 1996). Images are captured with a CCD camera (Imager Intense, LaVision GmbH) that has 1376 \times 1040 pixel resolution, translating to a physical pixel size of 6.45 \times 6.45 μm . The required PIV illumination is provided by an Nd:YAG laser (Solo III-15, New Wave Research). The laser can produce 50 mJ per pulse at 15 Hz repetition rate with 3-5 ns pulse duration. The laser beam is transformed into a light sheet which has a thickness less than 1 mm. For each set of experiments, 10 000 pairs of double-frame images are acquired and processed using commercial software (DaVis 8.2, LaVision GmbH). Magnification and spatial resolution of the imaging system are set at 0.27 and 42.6 pixel/mm, respectively. A 60 mm Nikkor SLR lens with an aperture setting of $f/16$ is used in all experiments discussed here.

The images capture both the large glass beads and the PIV tracers, as shown in Fig.3-2a and also as a magnified view in Fig.3-2b where the area highlighted in Fig.3-2a is shown. The large glass beads are detected using the “imfindcircle” function of MATLAB (*MATLAB R2013a*, The MathWork Inc.) which is based on the Hough transform for detection of circular objects (Atherton and Kerbyson, 1999; Davies, 2012; Yuen et al., 1990). The

algorithm requires the range of acceptable particle radius (set to $\pm 40\%$ of the nominal particle radius) and also a gradient-based threshold for edge detection as input parameters. The latter is based on the high intensity gradient at the sharp boundary of in-focus particles while the out-of-focus particles have a smooth gradient. Two different low and high gradient-based thresholds are considered for edge-detection. The low threshold is applied to detect and mask out all particles (in-focus and out-of-focus) from both frames for the PIV analysis of the liquid phase as shown in Fig.3-2c. The higher threshold is applied to only detect the in-focus particles for the PTV process as illustrated in Fig.3-2d.

The liquid phase velocity is calculated by first masking out all the large glass beads based on the lower threshold of the edge gradient. Two nonlinear filters, subtraction of a sliding background and particle intensity normalization, are applied to increase the signal-to-noise ratio. Cross-correlation of double-frame images with 32×32 pixel² window size and 75% window overlap is applied to obtain the instantaneous liquid phase velocity field. The interrogation windows, which have more than 1% overlap with the masked areas, are rejected to ensure no bias occurs in the measurement of the liquid phase.

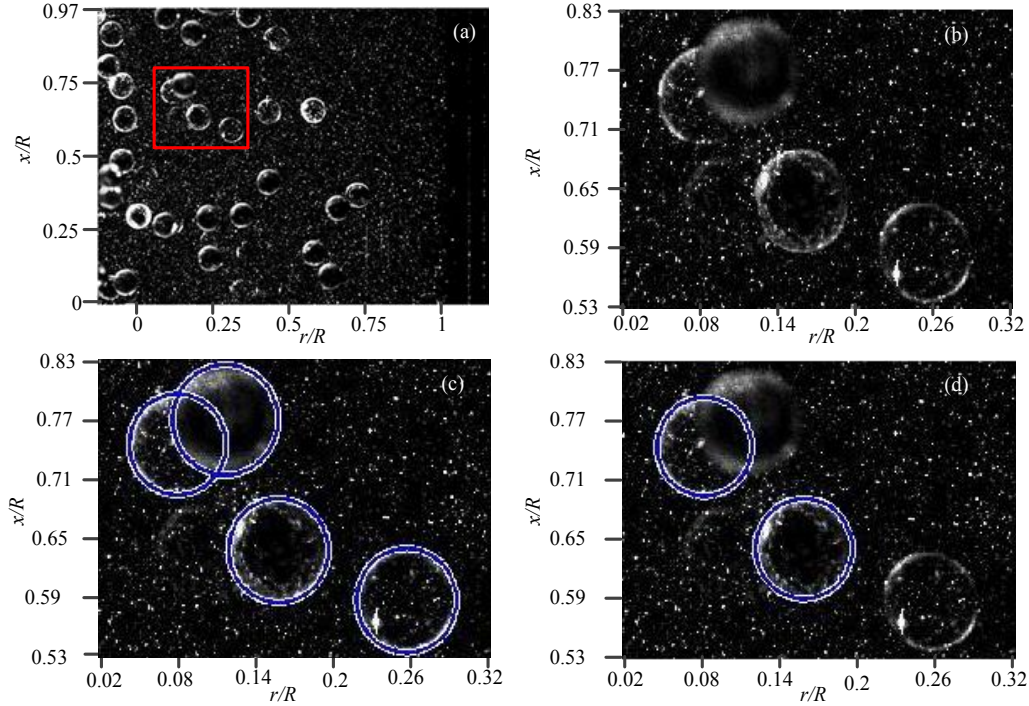


Figure 3-2. (a) A raw image showing the full field-of-view with 2 mm glass beads and PIV tracer particles. Note that $r/R=0$ and $r/R=1$ denote pipe centreline and pipe wall, respectively, while x/R is the streamwise (upward) direction; (b) Magnified view of the region identified by the red boundary specified in the full field-of-view image in (a); (c) Magnified view with in-focus and out-of-focus particles detected using the low edge-detection threshold later to be masked out for PIV analysis of the liquid phase; (d) Magnified view of the in-focus particles detected using the high-gradient threshold for PTV analysis.

The centroid location, the radius, and the displacement (velocity) of the in-focus glass beads are measured by a PTV algorithm developed in MATLAB (MATLAB Release R2013a). The algorithm uses the mean velocity of the fluid flow to impose an appropriate pixel shift range for the glass beads from frame #1 to frame#2. The PTV processing algorithm provides details about the particle sizes as well. Fig.3-3 shows the size distribution (in differential frequency form) of the detected 0.5, 1, and 2 mm glass beads as a function of the deviation of particle diameter (d_p) with respect to the average quantity ($\langle d_p \rangle$). Note that the frequency distributions are normalized by the bin size, i.e. presented as differential frequency distributions, in order to produce distributions that are independent of the bin

sizes selected for the analysis. The results show that the particle size distributions (PSD's) of the glass beads are quite symmetric. The details obtained from the PTV-based particle size characterization, including mean particle diameter (in pixels and mm), standard deviation (SD), and the total number of particles detected through the PTV measurements, are summarized in Table 3-3. The average particle sizes $\langle d_p \rangle$ are very similar to the corresponding nominal sizes provided by the supplier (Potters Industries Inc.). Additionally, the distribution of particle sizes about the mean is similar for the three particle types, as shown in Table 3-3. The last column in Table 3-3 reports the total number of in-focus particles in each set of experiments that were used for the PTV calculations, i.e. particle size characterization and particle velocity statistics. Although the experiments involving the 2 mm particles were conducted at the highest concentration, fewer in-focus particles were detected because the area occupied by a particle varies with d_p^2 .

Table 3-3. Particle specifications obtained through PTV processing.

Nominal d_p (mm)	Measured $\langle d_p \rangle$ (Pixel)	Measured $\langle d_p \rangle$ (mm)	Standard deviation (mm)	Total No. of particles detected
0.5	24.77	0.5904	0.0413	1.19×10^5
1	45.31	1.082	0.0359	1.20×10^5
2	86.13	2.056	0.0379	3.30×10^4

Based on the particle characterization analysis, it was expected that the particles found in the image-pairs would not be identical and subsequent inspection of the images confirmed this. It should also be noted that even a single particle could appear to be a different size in two image pairs because of slight differences in surface glare and in-focus

particle diameter (caused by out-of-plane motions) between a pair of images. A filter was therefore applied to ensure that in cases where the diameter difference in two successive frames was greater than 1 pixel (0.024 mm), the images were discarded. Fig.3-4 shows the cumulative distribution of diameter difference for the detected glass beads between the first (d_{p1}) and the second (d_{p2}) frames. As Fig.3-4 illustrates, approximately 15-20% of the data points in each set were discarded when the aforementioned filter was applied. This filter significantly reduced the data noise and resulted in more rapid statistical convergence.

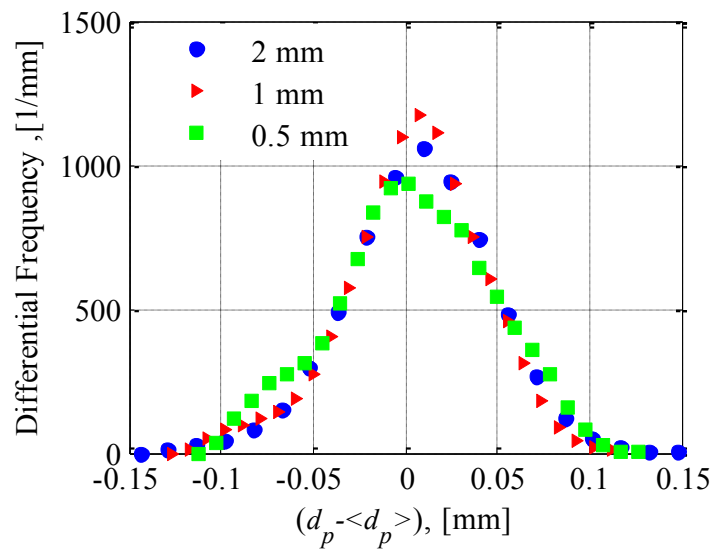


Figure 3-3. Particle size distributions of the 0.5, 1 and 2 mm glass beads obtained from the images obtained for PTV analysis.

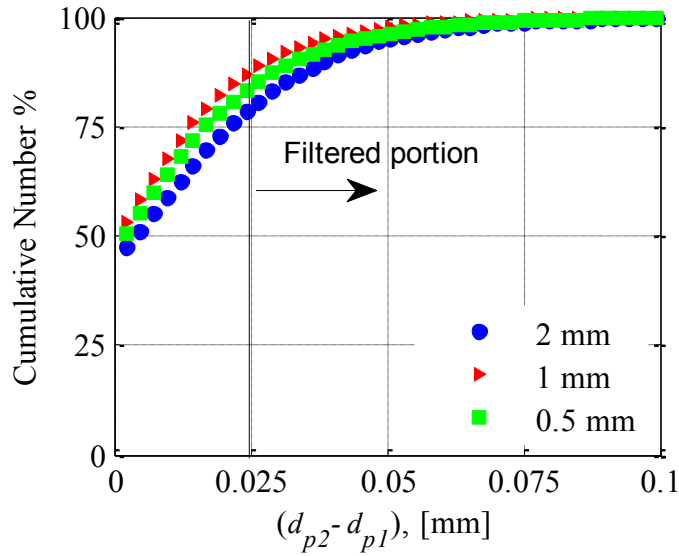


Figure 3-4. Cumulative distribution of the difference in the diameter of paired glass beads detected in frame #1 and frame #2 of two successive images captured for PTV analysis.

3.2.3 Particle dynamics

The Stokes number (St) is often used to describe the interaction between a particle and the suspending fluid as it compares the particle response time to a characteristic time scale of the flow field. Two different Stokes numbers, integral Stokes number (St_L) and Kolmogorov Stokes number (St_k), are usually defined for turbulent particulate flows based on the integral time scale (τ_L) and the Kolmogorov time scale (τ_k) of the fluid phase turbulence:

$$St_L = \frac{\tau_p}{\tau_L} \quad (3-5)$$

$$St_k = \frac{\tau_p}{\tau_k} \quad (3-6)$$

The particle response (relaxation) time (τ_p) is defined as:

$$\tau_p = \frac{(\rho_p - \rho_f)d_p^2}{18\mu_f f_d} \quad (3-7)$$

where μ_f is the fluid viscosity and f_d corrects the drag coefficient for deviations from Stokes flow and is calculated as (Kussin and Sommerfeld, 2002):

$$f_d = 1 + 0.15Re_p^{0.687} \quad (3-8)$$

where Re_p is defined as $Re_p = (\rho_f d_p V_t) / \mu_f$ based on V_t which is the terminal settling velocity of the particle in a quiescent fluid. The integral time scale (τ_L) and the Kolmogorov time scale (τ_k) can be written as:

$$\tau_L = \frac{2}{9} \frac{k^{1.5}}{l_m} \quad (3-9)$$

$$\tau_k = \left(\frac{\nu}{\varepsilon} \right)^{1/2} \quad (3-10)$$

where ν and l_m are kinematic viscosity and turbulent mixing length of the fluid, respectively.

The turbulent kinetic energy k and the dissipation rate ε are (Milojevic, 1990):

$$k = 0.5(\langle u^2 \rangle + 2 \langle v^2 \rangle) \quad (3-11)$$

$$\varepsilon = C_\mu^{0.75} \frac{k^{1.5}}{l_m} \quad (3-12)$$

Streamwise and radial fluctuating velocities, u and v respectively, can be obtained from the PIV measurements of the unladen flow at the pipe centreline. Dissipation rate and fluid time scales τ_L and τ_k are calculated using estimations of mixing length (Schlichting, 1979) and C_μ (Milojevic, 1990) at the centreline, i.e. $l_m=0.14R$ and $C_\mu=0.09$, respectively. Table 3-4 shows the response time of the glass beads, along with calculated values of St_L and St_k for conditions at the pipe centre. For $St \approx 1$, a particle is partially responsive to the flow motion of the corresponding length scale and for $St \gg 1$, the particle becomes nonresponsive (Varaksin, 2007). Therefore, the data presented in Table 3-4 imply that whilst particles can be involved with the large scale turbulence, they are non-responsive to the Kolmogorov-scale turbulent fluctuations.

Table 3-4. Particle response time, Stokes number and particle Reynolds number at the pipe centerline.

Nominal d_p (mm)	τ_p (ms)	St_L	St_k	Re_p
0.5	7.9	0.344	3.9	42
1	15.3	0.683	7.7	167
2	28.1	1.252	14.0	607

3.3 Results

In this section, the experimental findings showing the effect that the particles have on the liquid-phase turbulence at a high Reynolds number are presented. The results of the present study are considered in the context of previous research reported in the literature, some of which was conducted with similar particle sizes and concentrations but at much lower Re . Turbulence statistics for the particulate phase, obtained from PTV analysis, are also introduced and compared with results available in the literature. Initially, though, the

mean velocity profiles (liquid and particle) are presented, along with the mean local particle concentration profiles, as this information is required to properly introduce the liquid- and particle- fluctuations. Overall, this section provides a detailed summary of the trends obtained through the analysis of the experimental data collected during the present study. In the Discussion (Section 3.4), explanations for the extent of liquid-phase turbulence modulation and for the unexpected trends in the streamwise and radial particle fluctuations are provided.

3.3.1 Mean velocity profiles

The average velocity profiles for the single-phase liquid flow (unladen flow) and also both the liquid phase and the solid phase of the particle-laden flows are shown in Fig.3-5. In this figure, where $r/R=0$ and $r/R=1$ denote the centreline and wall of the pipe, respectively. The finite size of the particles ($0.01R$, $0.02R$, and $0.04R$) limits the closest measurement point to the wall. For ease of comparison and statistical convergence (ensuring sufficient number of samples) all the particles are binned into $0.08R$ radial intervals starting at $r/R=0$ up to 0.96 in Figs.3-5 through 3-8. Again, the symbols (U, V) and (u, v) represent the average velocity and fluctuating velocities in the streamwise and radial directions, respectively.

As shown in Fig.3-5, the liquid-phase mean velocity profiles for the particle-laden flows are almost identical to the unladen flow, indicating that the particles have a negligible effect on the mean velocity of the liquid phase at the experimental conditions studied here. The velocity profiles of the solid phase (glass beads) are flatter than the liquid phase profile,

which has been observed in previous experimental investigations (Varaksin et al., 2000; Kulick et al., 1994; Lee and Durst, 1982; Tsuji et al., 1984). Moreover, the results show that the velocity profiles become flatter as the particle size increases, which again is in agreement with others, most notably with the results of Lee and Durst (1982) and Tsuji et al. (1984). The mean velocity of the glass beads is lower than the carrier phase in the core region of the flow ($r/R < 0.85$). This velocity lag is greater for the larger particles due to their higher Stokes' number (or weight). The maximum lag (or slip) for the each particle size is observed at the pipe centreline.

It is customary to estimate the slip velocity between the continuous and the dispersed phase based on the terminal settling velocity of a single particle in a quiescent fluid medium (Ghatage et al., 2013). The local slip velocity in the pipe, however, is affected by other factors such as particle concentration (Lee, 1987), distance from the wall (i.e. wall effect) (Kameyama et al., 2014; Tsuji et al., 1984; Lee and Durst, 1982), and carrier fluid turbulence (Doroodchi et al., 2008). Therefore, the slip velocity should be most closely approximated by the terminal settling velocity at the pipe centreline where the turbulence fluctuations are (comparatively) low and the distance from the wall is the greatest. Terminal velocities of the particles used in the present investigation are compared with their slip velocities at the pipe centreline in Table 3-5. The results show that the centreline slip velocities are in good agreement with the calculated terminal velocities. Sato and Hishida (1996) obtained similar results. However, Kameyama et al. (2014) reported the slip velocity of glass beads in water flow to be smaller than the particle terminal velocity, possibly due to the short developing section used in their experiments (approximately 35D). Based on the

results obtained in the present study, and by others (Kameyama et al., 2014; Sato et al., 1995), it is evident that another significant difference between gas-particle and liquid-particle flows is that the terminal velocity (hence slip velocity) for a particle in a liquid medium is orders of magnitude smaller than its terminal velocity in a gas. The importance of this difference can be appreciated by considering the fact that the slip velocity plays a major role in turbulence modulation, as was illustrated in Eq.(3-2).

Table 3-5. Slip velocity at the pipe centerline and particle terminal settling velocity for different particles tested during the present investigation.

d_p (mm)	Terminal velocity (m/s)	Slip velocity (m/s)
0.5	0.08	0.09
1	0.15	0.17
2	0.27	0.25

The difference between the average velocity of the particles and the liquid phase velocity becomes smaller near the wall. At a position of $r/R \approx 0.85$, referred to here as the “crossing point”, the liquid and particle velocities are nearly equal. In the near-wall region ($r/R > 0.85$), the particle velocity is higher than the liquid velocity. It is also observed that the largest particles have the highest velocity in the near-wall region ($r/R > 0.85$). In other words, the relative velocity of the particles and the fluid in the near-wall region is in the opposite direction of that in the core of the flow. This phenomenon, which has been reported by other investigators (Kameyama et al., 2014; Lee and Durst, 1982; Tsuji et al., 1984), can be attributed to the fact that the fluid velocity gradient is steep in the near-wall region (to fulfil the no-slip boundary condition) whereas particles do not have the same boundary

condition (Tsuji et al., 1984). The particles bounce off the wall and preserve most of their momentum (Sommerfeld and Huber, 1999; Sommerfeld, 1992). Moreover, high-velocity particles are transported from the core of the flow to the wall region by their lateral motion. These large particles have a high relaxation time (τ_p) and do not quickly decelerate when they enter the region near the wall where the liquid velocity is lower. Therefore, the larger particles continue to travel at a higher velocity in near-wall region than the surrounding liquid phase.

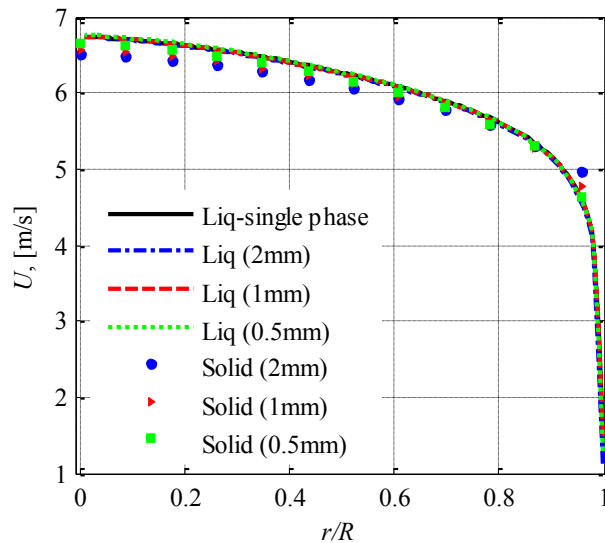


Figure 3-5. Mean velocity profiles for liquid and solid phases

In the present investigation, the crossing point occurs at nearly the same location (i.e. $r/R \approx 0.85$) for all the particle sizes tested. Lee and Durst (1982) found in their experiments that the location of the crossing point changes considerably with increasing particle size in an upward gas-solid flow: specifically, they showed that the crossing point is $0.8R$ for 100

μm particles and $0.9R$ for $200 \mu\text{m}$ particles. In this case, a doubling of the particle diameter dramatically increases the slip velocity between the particles and the gas phase with respect to the fluid velocity, which leads to a drastic reduction in the ratio of the particle velocity to the fluid velocity (U_p/U_f). By increasing the particle diameter from $100 \mu\text{m}$ to $200 \mu\text{m}$, the particle velocity in the core of the flow is reduced from 90% to 70% of the carrier phase velocity (Lee and Durst, 1982). As a result, the $200 \mu\text{m}$ particles have a far lower velocity across much of the pipe cross section. Generally, the crossing point occurs at a lower velocity for larger particles, meaning that the crossing point moves towards the wall when the particle size is increased. For the solid-liquid flows tested here, however, the slip velocity of the different particles with respect to the fluid velocity is rather small. The mean velocity of the glass beads is always within 5% of the liquid phase velocity at the Reynolds number at which the tests were conducted ($Re = 320\,000$). The small variation in particle velocity in liquid flows is believed to be the reason that the location of the crossing point does not vary considerably with the change of the particle size from 0.5 to 2 mm.

3.3.2 Particle concentration and interactions

Particle concentration profiles are obtained from the PTV images and shown in Fig.3-6a as the number of particles (N_p) across the radius normalized by the total number of detected particles (N_{total}). Starting from the pipe centreline, the profiles of the 0.5 and 1 mm particles initially slightly decrease with increasing r/R . A local concentration maximum is observed for the 1 mm particles at $r/R \approx 0.7$ which is followed by a sharp decline in the vicinity of the wall. The local maximum is not clear for the 0.5 mm particles; however, this

profile is also shows a sharp decline after $r/R \approx 0.7$. A similar trend was observed by Kameyama et al. (2014) for 625 μm glass beads in an upward solids-laden liquid flow.

The concentration profile for the 2 mm particles obtained during the present investigation decreases linearly from the pipe centreline to the pipe wall, which is sometimes referred to as “core-peaking”. A similar trend (core-peaking profile) was observed by Oliveira et al. (2015b) in their recent study of the upward flow of 0.8 mm polystyrene particles dispersed in water, where $Re = 10\,300$. An opposite result was obtained by Hosokawa and Tomiyama (2004), who showed that 2.5 and 4 mm ceramic particles in an upward liquid particulate flow had wall-peaking concentration profile at $Re = 15\,000$. Clearly, pipe Reynolds number alone does not dictate the shape of the concentration profile, and one must consider the summative effects of flow Re , particle and fluid properties, along with system conditions, e.g. insufficient entry length as described by Varaksin et al. (2000).

The shape of the particle concentration profiles is determined by the balances of forces in the radial direction (Lucas et al., 2007; Sumner et al., 1990). Specifically, turbulent dispersion forces and particle-particle interactions tend to disperse the particles uniformly over the cross-section while the lift force can, under some circumstances, provide a relatively strong force that pushes particles towards the centreline (Lucas et al., 2007; Marchioli et al., 2007; Burns et al., 2004; Huber and Sommerfeld, 1994; Lee and Durst, 1982). Particles subjected to a fluid-phase velocity gradient will experience such a lift force (Moraga et al., 1999; Lee and Durst, 1982). The shapes of the concentration profiles

measured during the present study suggest that the lift force plays an important role, specifically in the case of the 2 mm particles. Auton (1987) derived the following equation for lift force on a sphere in an inviscid flow:

$$\vec{F}_L = C_L \rho_f V_p \vec{U}_s \times \frac{\partial \vec{U}}{\partial \vec{r}} \quad (3-13)$$

In Eq.(3-13), V_p is the sphere volume and the lift coefficient, C_L , is constant and equal to 0.5 for inviscid flows. Values for the lift coefficient obtained from numerical simulations of the vertical particle-laden flows have been reported to be in the range of $0.01 \leq C_L \leq 0.15$ (Moraga et al., 1999). As inspection of Eq.(3-13) shows that the lift force will change the direction when the sign (direction) of the slip velocity (U_s) changes. Therefore, particles to the left of the crossing point ($r/R < 0.85$), where the particles are relatively far from the wall and the slip velocity is positive, are pushed towards the pipe centreline (Lee and Durst, 1982). In the core of the flow ($r/R \leq 0.7$) the velocity gradient is small and thus the lift force is reduced, which partially explains the relatively flatter concentration profiles for 0.5 mm and 1 mm particles in the core of the flow relative to the 2 mm particles. The concentration profile of the 2 mm particles suggests that the lift force can still be effective even at $r/R < 0.7$ due to their large size, pushing the particles towards the centreline and contributing to the center-peaked concentration profile. Lee and Durst (1982) pointed out that if a particle has enough momentum to go beyond the crossing point ($r/R > 0.85$) towards the wall then the lift force direction is reversed since the slip velocity changes sign in this region. Accordingly, particles will collide with the wall and subsequently are thrown back towards the pipe centre.

In this study, the mean velocities are measured in an Eulerian frame of reference with the assumption that there is a negligible accumulation of the inertial particles in certain zones of the liquid phase turbulence (e.g., low or high speed streaks). The subsequent interpretation based on the negative slip velocity and the reversal of the transverse lift force is based on the aforementioned framework. The interpretation will hold in the Lagrangian frame-of-reference as long as the sign of the slip velocity does not change. For additional information on this aspect of the interpretation, the reader is referred to Bagchi and Balachandar (2003), Marchioli et al. (2003) and Aliseda et al. (2002).

Particle-particle collisions/interactions can profoundly influence both the particle fluctuations and the particle concentration profiles in particulate flows (Borée and Caraman, 2005; Kussin and Sommerfeld, 2002). In the present study, overlapping particles in the PTV images are detected and analysed to estimate the number of particle-particle interactions in the measurement plane. In fact, not every image of overlapping particles can be assumed to be an indication of particle collision, as some of these particles, which are clearly in close azimuthal proximity, will be driven away from each other by lubrication forces and by their interacting flow fields before they collide (Zhang et al., 2005; Barnocky and Davis, 1989). We therefore assume that the number of overlapping particles can be regarded as an index for particle-particle interactions. The basis for this assumption is that the frequency of particle-particle interactions depends strongly on local particle concentration, i.e. the greater number of particles in close proximity, the greater number of particle-particle interactions. Here, the frequency of particle-particle interactions (f_{pp}) is defined as the ratio of the number of overlapping particles in the images to the number of particles at each radial position. The

results are shown in Fig.3-6b. As expected, the profiles of Fig.3-6b show the same trends as Fig.3-6a, indicating that the frequency of particle-particle interactions is directly related to the particle number density at each radial position. The results of Fig.3-6b also show that particle interaction frequencies are much lower in the near-wall region than in the core, which is expected based on the low particle concentration in this region. Note that the interaction index for the 0.5 mm particles is much lower than it is for the other particle sizes because of their small size and relatively low concentration (see Table 3-2). One can conclude that the particle-particle interactions do not strongly influence the particle fluctuations and concentration profiles in the near-wall region. In the core of the flow, however, the particle-particle interactions are much more important for the 1 and 2 mm particles than for the 0.5 mm particles.

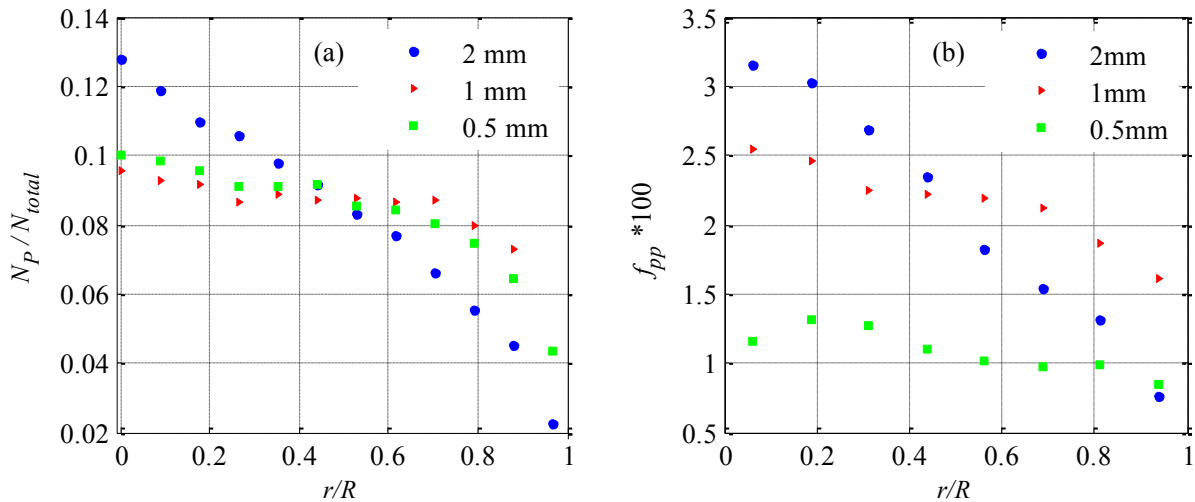


Figure 3-6. (a) Normalized particle number density distributions and, (b) particle-particle interaction index profiles.

3.3.3 Turbulent fluctuations

The streamwise turbulent fluctuations $\langle u^2 \rangle$ of the liquid phase change very little with the addition of particles, as observed in Fig.3-7a. The highest modulation in the liquid turbulence intensity is observed near the wall. The liquid phase $\langle u^2 \rangle$ shows negligible variation with the addition of the 1 and 2 mm glass beads expect for small augmentation in the near wall region with 2 mm particles. A slight attenuation of $\langle u^2 \rangle$ is observed upon addition of the 0.5 mm particles. Fig.3-7b shows that the particles also introduce small changes in the radial velocity fluctuations $\langle v^2 \rangle$ of the liquid phase. It is noteworthy that the average turbulence modulation in both the radial and streamwise directions does not exceed 5%. The average turbulence modulation can be obtained, for instance in the axial direction, from:

$$\overline{M_x} = \frac{\int_0^R M_x 2\pi r dr}{\pi R^2} \quad (3-14)$$

The observed turbulence modulation in the present study is very small in comparison with the results of other studies (e.g. Hosokawa and Tomiyama, 2004; Sato and Hishida, 1996; Sato et al., 1995; Tsuji and Morikawa, 1982; Tsuji et al., 1984). Hosokawa and Tomiyama (2004) showed that 1 and 2.5 mm ceramic particles at $\phi_v \approx 0.008$ in an upward water flow with $Re = 15\ 000$ augmented the turbulent intensity by about 100% at the pipe centreline. A more detailed discussion on the effect of Re on turbulence modulation is presented in Section 3.4, after some additional, relevant experimental measurements can be introduced.

The PTV analysis provides the particle fluctuations in the streamwise and radial directions. These are shown, along with the particle-phase Reynolds stresses, $\langle uv \rangle$, in Figs.3-7a through 3-7c. The larger $\langle u^2 \rangle$ values of the particles in comparison with the carrier phase (shown in Fig.3-7a) follow the trends shown in the literature. For example, Varaksin et al. (2000), Caraman et al. (2003), and Borée and Caraman (2005) showed that the particles have higher streamwise fluctuations than the fluid in downward gas flows. Also Kulick et al. (1994) and Lee and Durst (1982) observed equal or higher streamwise particle fluctuations than the gas phase in an upward turbulent gas flow. Kameyama et al. (2014) found that the particles have streamwise fluctuations that are almost identical to the liquid phase in upward pipe flow; however, in downward flow, they are slightly higher for the particles than for the liquid. Suzuki et al. (2000) also showed that the 0.4 mm ceramic particles had higher axial turbulence than the liquid phase in the downward solid-liquid flow. The streamwise turbulent intensity is larger for the larger particles at the pipe centreline while the smaller ones have a higher intensity near the wall. This phenomenon has not been sufficiently scrutinized in the literature, despite the fact that $\langle u^2 \rangle$ profiles in Borée and Caraman (2005) showed the same trend. They provided profiles for $\langle u^2 \rangle$ for 60 μm and 90 μm particles and showed that 60 μm particles have a larger $\langle u^2 \rangle$ in the near-wall region than the fluid. Also, Varaksin et al. (2000) observed that 50 μm glass particles have a much higher $\langle u^2 \rangle$ than the carrier phase at the wall region. These trends are mainly linked to the higher transport rate of particles in the radial direction and will be investigated in greater detail in the Discussion section.

The results of Fig.3-7b show that the particle fluctuations in the radial direction are higher than those measured for the fluid. The 2 mm glass beads, for example, exhibited radial fluctuations that were 4-5 times higher than the liquid phase. As pointed out earlier, previous investigations of particle radial velocity fluctuations show widely varying results. Varaksin et al. (2000) and Kulick et al. (1994) observed that the radial fluctuations of particle are lower than the fluid. However, many investigations, including those of Kameyama et al. (2014), Borée and Caraman (2005), Caraman et al. (2003), Kiger and Pan (2002), and Suzuki et al. (2000) and Lee and Durst (1982) showed that the particle radial fluctuating velocities are either equal to or greater than those of the fluid. As mentioned previously, Varaksin et al. (2000) and Kulick et al. (1994) speculated that their results might have been affected by having insufficient length (Varaksin et al., 2000) to obtain fully developed flow and by having electrostatic charges on their particles (Kulick et al., 1994).

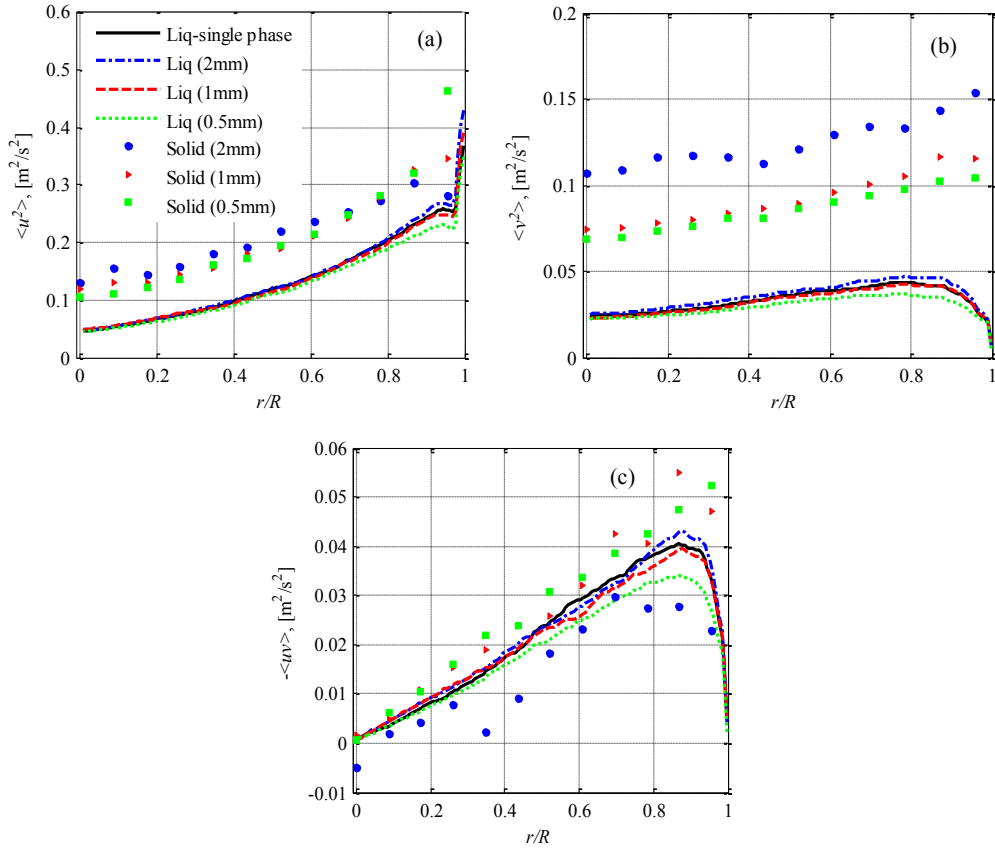


Figure 3-7. (a) Streamwise turbulent fluctuations, (b) Radial fluctuating velocities, (c) Reynolds stresses $\langle uv \rangle$ for liquid and solid phases.

The Reynolds stress ($-\langle uv \rangle$) profiles for the liquid phase and the glass beads are provided in Fig.3-7c. Reynolds stresses ($-\langle uv \rangle$) for 0.5 and 1 mm particles are slightly higher than those of the unladen single phase while the Reynolds stresses of the 2 mm particles are lower than those of the unladen fluid. Borée and Caraman (2005) and Caraman et al. (2003) showed that ($-\langle uv \rangle$) profiles for 60 and 90 μm glass beads in air are slightly larger than the fluid. In general, the particle fluctuating velocities in both radial and axial directions were observed to increase with particle size, as shown in Figs. 3-7a and 3-7b. However, the 0.5 and 1 mm particles have a larger Reynolds stress than the 2 mm particles

(see Fig.3-7c). This requires further investigation; the first step is to determine the extent to which the streamwise and radial fluctuations are correlated.

3.3.4 Ejection and sweep motions

In order to investigate the relatively lower Reynolds stresses of the 2 mm particles in comparison to the smaller particles, the correlation strength (C_{uv}) between u and v is calculated (Caraman et al., 2003):

$$C_{uv} = \frac{\langle uv \rangle}{(\langle u^2 \rangle^{0.5})(\langle v^2 \rangle^{0.5})} \quad (3-15)$$

The C_{uv} profiles for both phases are shown in Fig.3-8. The correlation strength of u and v for the liquid phase agrees well with the literature (Caraman et al., 2003; Kim et al., 1987; Sabot and Comte-Bellot, 1976). The results illustrate that the radial and streamwise motions of the largest particles are most poorly correlated even though the motion of these particles in the radial direction was more intense (see Fig.3-7b). The relatively low correlation strength (C_{uv}) for the larger particles indicates that they are less affected by the turbulent motions (ejection and sweep) of the liquid phase. The turbulent motions of these particles are most likely to be influenced by the non-correlating sources such as lift force and particle-particle interactions. The C_{uv} correlation of the liquid phase is approximately the same for all the particle sizes, indicating that the presence of the particles does not alter the fluid turbulence (ejection and sweep events).

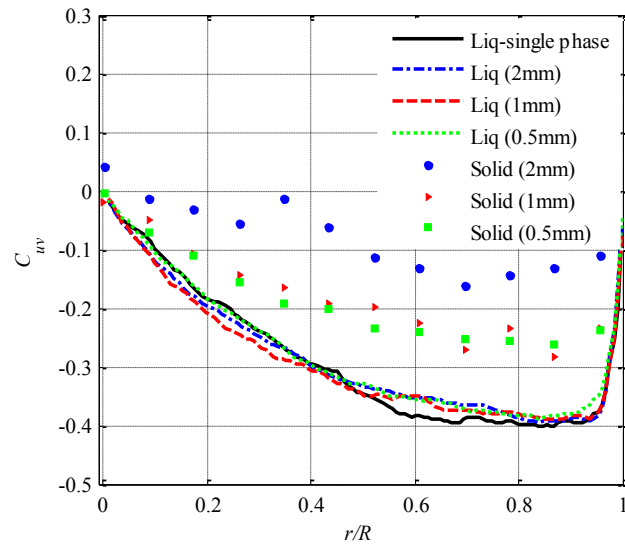


Figure 3-8. Correlation strength of turbulent motions for fluid and particles across the pipe radius.

Additionally, a quadrant analysis of the Reynolds stresses yields detailed information about the contribution of the sweep and ejection events to the total turbulence production (Bennett and Best, 1995; Lu and Willmarth, 1973). It also provides the opportunity to compare the quadrant analysis of each particle size with that of the fluid. The quadrant plot divides the fluctuating field into 4 different sections based on the values of u and v . The main events contributing to the Reynolds shear stresses are sweep and ejection events. The second quadrant (Q2), where $u < 0$ and $v > 0$, refers to the motion of the fluid away from the wall (ejection) and the fourth quadrant (Q4), where $u > 0$ and $v < 0$, contains the fluid moving towards the wall (sweep). The quadrant plots of u and v (the probability of the fluctuations) and the average vector in each quadrant are shown in Fig.3-9 for the unladen liquid flow, and for the 0.5 mm and 2 mm particles at the pipe centreline ($r/R = 0$) and in the vicinity of the wall ($r/R = 0.96$). The average vector is obtained by calculating the net of the

fluctuating velocities in each quadrant and then dividing by the number of the samples. Plots for the 1 mm particles are not shown here as they are almost identical to the 0.5 mm plots. The quadrant plots for the unladen liquid, shown in Figs.3-9a and 3-9b, clearly demonstrate the symmetrical distribution of fluctuations due to the symmetry in the turbulent motions at the centerline and dominant sweep and ejection events in near wall region. The same symmetrical pattern is observed for particles at the centerline as well (Figs.3-9c and 3-9e). However, the quadrant plots for liquid phase at the near wall region shows much stronger sweep and ejection events (Fig.3-9a) than the particles in this region (Figs.3-9d, 3-9f). The implication is that fluctuating velocities of the liquid phase are more correlated than they are for the particulate phase, which should be expected based on the relatively lower C_{uv} values presented in Fig.3-8. The 2 mm particles show a more isotropic distribution of u and v at the near wall region (Fig.3-9f). In particular, the strong radial fluctuations, which are not correlated with streamwise fluctuations (large v and small u), are evident. The quadrant plots for the 0.5 mm particles (Figs.3-9d) show stronger correlation between u and v fluctuations than the 2 mm particles in the near-wall region as these particles are more likely to follow the liquid phase, which would be expected because of their lower Stokes number. Oliveira et al. (2015b) also observed similar near-wall sweep and ejection patterns for 0.8 mm polystyrene (almost neutrally buoyant) particles in an upward liquid pipe flow $Re = 10\ 300$. In their study, the slight differences between the particle and liquid phases indicated that the particles did not perfectly follow the sweep and ejection patterns of the liquid phase. They also showed that the particles exhibited a slight radial drift, which was attributed to lift forces.

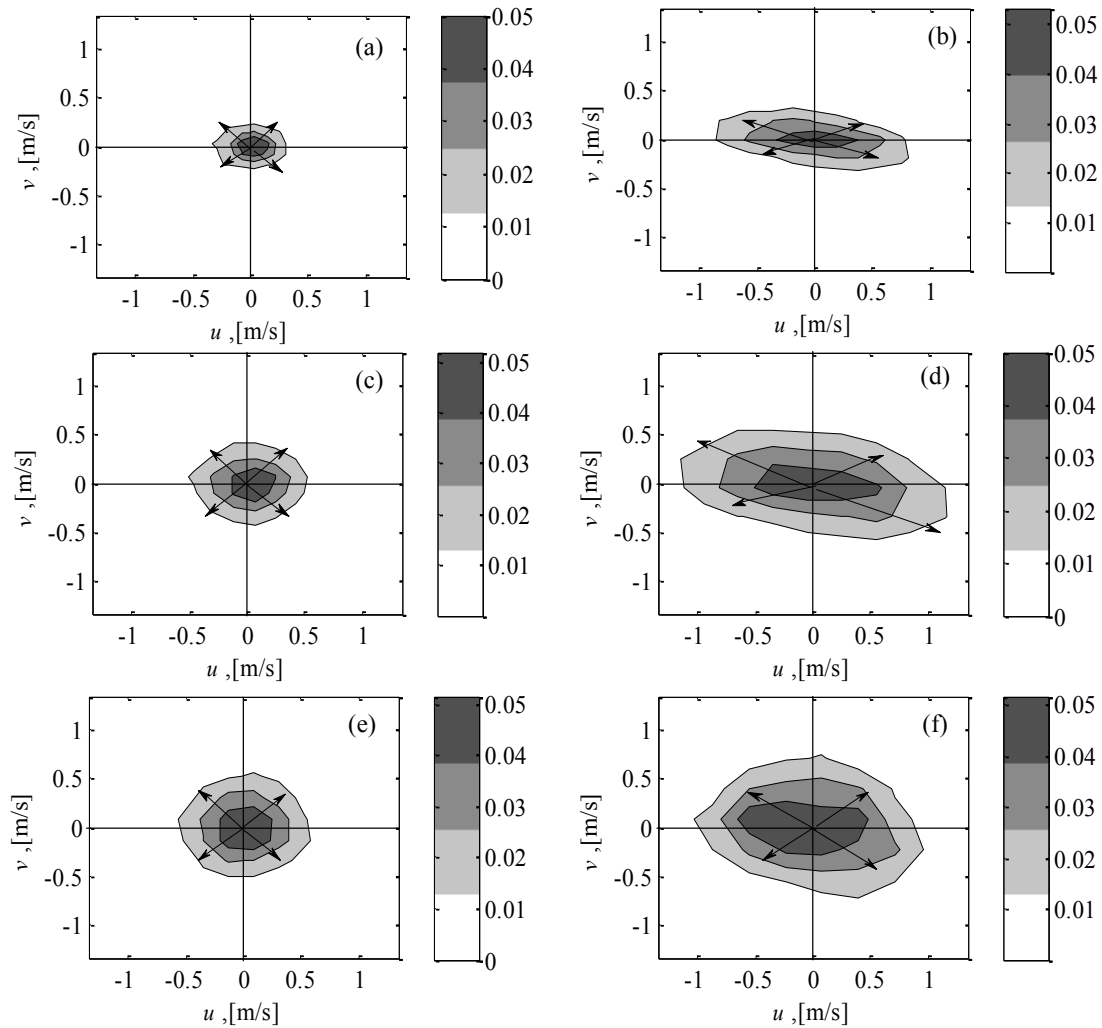


Figure 3-9. Quadrant plots of u and v and average fluctuating vectors of each quadrant for (a&b) unladen liquid phase, (c&d) 0.5 mm and (e&f) 2 mm particles at $r/R=0$, and $r/R=0.96$ respectively.

3.4 Discussion: Fluid-phase turbulence and particle fluctuations

In the previous section, it was clearly shown that the large particles tested here have a negligible effect on the fluid turbulence (see, for example, Fig.3-7a). The observed modulation is less than 5%. Since $St_k < 100$ for the conditions tested here, turbulence

attenuation is expected based on the Elghobashi (1994) criterion, although one caution is that the particle concentrations are higher than 10^{-3} , which was the upper limit for that criterion. If one considers the Hetsroni (1989) criterion, which is based on Re_p , the 0.5 mm particles should attenuate the fluid turbulence while the 2 mm particles are expected to strongly augment the fluid turbulence. The 1 mm particles, however, may attenuate or augment the fluid turbulence. Based on the Gore and Crowe (1989) criterion, the particles tested during the present study, which have $d_p/l_e \geq 0.1$, should provide strong turbulence augmentation. Moreover, the particle momentum number Pa_{st} given by Eq.(3-3), ranges from 80 to 300; thus, augmentation is also predicted based on this criterion.

As mentioned earlier, though, these criteria do not capture all the parameters that affect turbulence modulation: for example, Hosokawa and Tomiyama (2004) showed that the extent of modulation increases with increasing U_s/u . Since the mean (or centreline) fluctuating velocity (u) is a function of the bulk velocity (U_b), the velocity ratio can be rewritten as U_s/U_b . In the previous section, it was shown that the slip velocity (U_s) at the pipe centre is equal to the particle terminal settling velocity (V_t). Hence, we can see that the turbulence modulation is a function of V_t/U_b . In the present study, since the ratio V_t/U_b approaches zero, we expect modulation to be negligible. The fluid-phase turbulence modulation produced by the relatively large particles ($d_p/l_e \geq 0.1$) in liquid-solid flows of the present study and results from other investigations of solid-liquid mixtures (Kameyama et al., 2014; Hosokawa and Tomiyama, 2004; Kiger and Pan, 2002; Suzuki et al., 2000; Sato et al., 1995) are plotted against the ratio V_t/U_b in Fig.3-10. One should note that the data shown in Fig.3-10 have similar particle concentrations and d_p/l_e values for only solid-liquid

turbulent flows. The plot clearly shows the direct relation between turbulence augmentation and V_t/U_b , with the coarse particle liquid-solid flows of the present study showing almost no fluid-phase turbulence modulation.

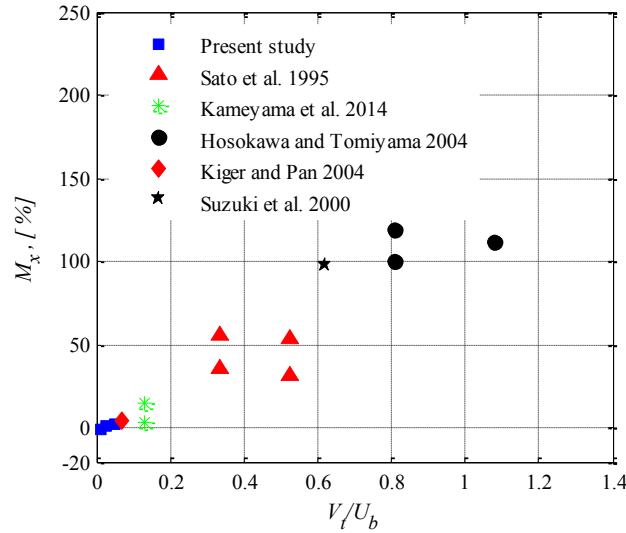


Figure 3-10. Streamwise turbulence augmentation as a function of the ratio of the particle terminal settling velocity to the bulk liquid velocity. Only data sets for liquid-solid flows with relatively large particles, which produce liquid-phase turbulence augmentation, are included.

Focusing now on the particle fluctuations, it can be observed that the streamwise and radial fluctuations are greater for the particles than for the fluid (see Figs.3-7a and 3-7b). Recall that $St_L \approx 1$ in the central region of the flow for each of the three particle types tested here (0.5 mm, 1 mm and 2 mm particles); therefore, these particles can be regarded as partially responsive to fluid turbulence in this region where the fluid time scale is longer (Varaksin, 2007; Borée and Caraman, 2005). In the near-wall region, the integral length scale dramatically decreases, leading to large values of St_L for all three particle types and thus they are less likely to be responsive to the fluid turbulence in this region (Varaksin et

al., 2000). Hence fluid turbulence is expected to be a source of particle turbulence production only in the core of the flow but should not contribute in any significant way to the particle fluctuations in the near-wall region. Moreover, the results that provide information about the ejection and sweep patterns show the relative importance of this source. As shown in Figs.3-8 and 3-9, the 0.5 and 1 mm particles are more likely to be affected by the fluid's turbulence. The 2 mm particles are most likely to be affected by fluctuation sources such as particle-particle interactions and lift force rather than the fluid turbulence.

Other factors, in addition to the effects of fluid turbulence, can contribute to the production of streamwise particle fluctuations: for example, particle polydispersity (Varaksin et al., 2000) and particle displacement in the radial direction (Caraman et al., 2003). Although both are mentioned here, the latter is expected to have a more dominant effect than the former in the present study, since the particles tested here have uniform densities and are rather narrowly distributed in size. However, a population of particles that is distributed in size or density (i.e. polydisperse) will have a range of axial velocities. Any variation in a given particle velocity from the mean axial velocity (due to the polydispersity) could be assumed to be a streamwise fluctuation. This source is not effective in the radial direction since gravity does not act in this direction. For the particles under consideration here, streamwise particle fluctuations are also generated by their long radial displacements (Caraman et al., 2003). Since the particles have high inertia, they can move further in the flow field while keeping their initial streamwise momentum, which partially explains why the particles studied here have larger streamwise turbulent fluctuations than the liquid phase.

Caraman et al. (2003) also measured the radial transport of streamwise and radial fluctuating velocities of particles ($\langle vu^2 \rangle_p$ and $\langle vv^2 \rangle_p$ respectively) and showed that particles have higher rates of radial transport of turbulent energy than the fluid. Of the particles tested here, the 2 mm particles are expected to produce more particle fluctuations due to their higher inertia which causes a higher rate of transport in the core. This holds for most of the pipe radius except for a small region near the wall where the production of streamwise turbulence for 0.5 mm particles is larger than the other particles. As Varaksin et al. (2000) state, streamwise particle turbulence can be produced by radial particle movement in the near-wall region. As shown in Fig.3-5, the 0.5 mm particles have a much steeper mean velocity gradient than the other particle sizes in the near-wall region. Any lateral movement of 0.5 mm particles will lead to much higher particle fluctuations for these particles (compared to the 1 and 2 mm particles) in the near-wall region. The steeper velocity gradient observed for the 0.5 mm particles is related with the interaction of these particles with the sweep and ejection motions of the carrier phase.

As discussed in the previous section, the particle concentration profiles – and the radial fluctuations – are determined by the relative magnitudes of the forces acting on the particles. Therefore, in order to investigate the sources of the particle radial fluctuations, we can start by referring to the forces that determine the particle concentration profiles, i.e. fluid turbulence (turbulence dispersion), particle-particle interactions and lift as the main sources of the radial fluctuations. In the core of the flow, particles are subject to all the above-mentioned sources. The information pertaining to the sweep and ejection patterns (Figs.3-8 and 3-9) indicates that the 2 mm particles are least affected by fluid turbulence. On the other

hand, based on the study on the concentration profile and the particle-particle interaction index (Fig.3-6), the lift force and the particle-particle interactions are stronger for 2 mm particles. Finally one can conclude that that the higher lift and particle-particle interactions will lead to higher radial particle fluctuations in the core of the flow for the 2 mm particles in comparison with the 0.5 and 1 mm particles. The particles become almost non-responsive to the fluid turbulence in the near-wall region. Also, particle-particle interactions are not significant in the near-wall region, simply because of the very low particle concentrations, as shown in Fig.3-6. In this region the lift force is reversed due to the change in sign of the slip velocity between the particles and the fluid. The reversal in sign of the slip velocity and consequent change in direction of the lift force pushes particles towards the wall. It is therefore suggested that the “reverse” lift force and particle-wall collisions are regarded as the main sources generating radial fluctuations in the particles in this region. Again, the higher fluctuating velocities of 2 mm particles can be attributed to the larger reverse lift force followed by more vigorous particle-wall collisions.

3.5 Conclusions

The turbulent motion of particles has been investigated in an upward flow with dilute mixtures of water and glass beads. The glass beads had diameters of 0.5, 1 and 2 mm and volumetric concentrations of 0.1, 0.4, and 0.8%, respectively. Experiments were performed at a high Re (320 000) and a combined PIV/PTV technique was used to simultaneously measure the velocities of particles and the fluid phase. The presence of the particles had a negligible effect on the liquid phase turbulence at the investigated conditions. This is

believed to be due to the fact that the ratio of the slip velocity between the solid and liquid phase to the bulk velocity (U_s/U_b) is very small at the high Reynolds number tested here.

Particles lag behind the fluid in the core of the flow ($r/R < 0.85$) because of the gravitational force. The slip velocity is observed to be almost equal to the terminal settling velocity of the particles at the pipe centreline. Larger particles have a larger slip in the core region which becomes smaller close the wall. The particles and the fluid have roughly identical velocities at a radial position of $r/R \approx 0.85$. At radial positions beyond this crossing point ($r/R > 0.85$), the particles have a higher mean velocity than the fluid. This phenomenon can be attributed to the fact that the particles -on the contrary to the fluid phase- don't follow the no-slip condition at the wall. The 2mm particles also have the highest velocity in near-wall region in comparison with the other particles.

Turbulent particle fluctuations in both the streamwise and radial directions are larger than those of the liquid phase. The streamwise fluctuations are the highest for the 2 mm particles at the pipe centreline while the 0.5 mm particles show the largest streamwise fluctuations in the near-wall region. The larger turbulent kinetic energy of the particles is mainly associated with the higher radial transport of streamwise momentum by the particles due to their inertia. This radial transport is higher for the 2 mm particles, resulting in their larger streamwise fluctuations (compared to the 0.5 and 1 mm particles) in the core of the flow. In the near-wall region, the gradient of the velocity profile for the 0.5 mm particles is larger which leads to greater production of streamwise turbulent fluctuations for these particles. The production sources for radial particle fluctuations in the core region include

fluid turbulence, particle-particle interactions and the lift force (towards the pipe centre). The production sources in the near-wall region are the “reversed” lift force and particle-wall collisions, which are strongest for the largest particles tested, and therefore the 2 mm particles have the largest radial fluctuations.

The radial variation of particle concentration is mainly influenced by the lift force which accumulates the particles in the core region. Because of stronger lift in the case of the 2 mm particles, the concentration distribution appears to be linear with a maximum occurring at the pipe centreline. The lift force becomes insignificant for smaller (0.5 and 1 mm) particles in the core region ($r/R < 0.7$) and thus the concentration profiles of these particles become almost constant in this region.

4 The particle size and concentration effects on fluid/particle turbulence in vertical pipe flow of a liquid-continuous suspension[‡]

4.1 Introduction

Particulate turbulent liquid flows are encountered in natural phenomena like sediment transport in rivers to a broad range of industrial applications, such as slurry pipelines. While the effects that the suspending liquid phase has on the dispersed particles is often of primary consideration, the presence of the particles can also have a profound impact on the turbulence of the liquid phase. Elghobashi (1994) showed that the particulate and carrier phase motions reciprocally influence each other (i.e. two-way coupling) at particle volume fractions (ϕ_v) greater than 10^{-6} . At $\phi_v > 10^{-3}$, particle-particle interactions also come into play. Therefore, experimental investigations of the different aspects turbulent particulate flows have been conducted over the past 50 years. In this section, we review some of the important literature in the field of particle-laden turbulent flows, focusing

[‡] A version of this chapter, co-authored by R. Shokri, S. Ghaemi, D.S. Nobes, and R.S. Sanders, is submitted to Int. J. Heat and Fluid Flow and is under review.

initially on the carrier phase turbulence and then on particulate phase turbulence in particle-laden channel flows.

4.1.1 Carrier phase turbulence

It is well known that the presence of particles, even at low volume fractions (on the order of 10^{-3}), can modulate the carrier fluid turbulence (Hosokawa and Tomiyama, 2004; Sato et al., 1995; Tsuji et al., 1984; Lee and Durst, 1982). Fluid turbulence can be attenuated because of particle drag (Kim et al., 2005; Yuan and Michaelides, 1992) and through the particle-eddy interactions, which reduce the size of the eddies (Lightstone and Hodgson, 2004). If these new eddies are of the same size as the Kolmogorov length scale then the dissipation rate increases (Lightstone and Hodgson, 2004). The main source for augmentation is considered to be the wake and vortex shedding behind the particles (Kim et al., 2005; Yuan and Michaelides, 1992).

The three most well-known criteria for prediction of the carrier phase turbulence modulation (augmentation or attenuation) are those of Gore and Crowe (1989), Hetsroni (1989), and Tanaka and Eaton (2008). Gore and Crowe (1989) proposed that if the ratio of the particle size to the most energetic eddy length scale (d_p/l_e) is greater than 0.1, turbulence augmentation should occur; otherwise the carrier phase turbulence is most likely to be attenuated. The most energetic eddy length scale can be estimated as $0.1D$ (D is the pipe diameter) in fully developed pipe flows (Hutchinson et al., 1971). Hetsroni (1989) proposed that if the particle Reynolds number (Re_p) is less than 100, turbulence should be attenuated and for $Re_p > 400$, turbulence augmentation is predicted. Both augmentation and suppression

can be observed when $100 < Re_p < 400$. In the Hetsroni criterion, Re_p is defined as $Re_p = (\rho_f d_p V_t) / \mu_f$ where ρ_f and μ_f are fluid density and dynamic viscosity, respectively and V_t is the terminal settling velocity of the particle. Recently, Tanaka and Eaton (2008) proposed a new dimensionless parameter, Pa_{st} (particle momentum number) to classify attenuation and augmentation of fluid turbulence by the particulate phase:

$$Pa_{st} = St_k Re^2 \left(\frac{\eta}{L} \right)^3 \quad (4-1)$$

where η is the Kolmogorov length scale, St_k is the Stokes number based on the Kolmogorov time scale (see Section 2 for more detailed definition), and L is the characteristic dimension of the flow. They showed that turbulence is attenuated when $3 \times 10^3 \leq Pa_{st} \leq 10^5$, while outside this range the fluid turbulence is augmented.

Although the abovementioned criteria can be used (in many cases) to distinguish between augmentation and attenuation, they cannot quantify the extent of the change in turbulence. A much more complex analysis is required for such a purpose, and would necessarily include all the influential parameters such as Reynolds number (Re), particle Reynolds number (Re_p), ratio of particle diameter to the integral length scale of turbulence (d_p/l_e), ratio of the particle density to the fluid density (ρ_p/ρ_f), and volumetric concentration of the particles (ϕ_v) (Gore and Crowe, 1991). Presently, the effect of any one of these parameters is not clearly understood. Consider, for example, the impact of particle concentration along with the parameter (d_p/l_e) introduced by Gore and Crowe (1989): the available literature shows that increasing the concentration of relatively large particles ($d_p/l_e \geq 0.1$) leads to greater fluid

turbulence augmentation (Hosokawa and Tomiyama, 2004; Kussin and Sommerfeld, 2002; Sato et al., 1995; Tsuji and Morikawa, 1982; Tsuji et al., 1984), and as expected, others show that increasing the concentration of relatively small particles ($d_p/l_e \leq 0.1$) cause greater fluid turbulence attenuation (Kussin and Sommerfeld, 2002; Varaksin et al., 2000; Kulick et al., 1994; Zisselmar and Molerus, 1979). There are some results, though, that demonstrate a mixed concentration effect such as Tsuji et al. (1984) and Tsuji and Morikawa (1982) for the small particles ($d_p/l_e \leq 0.1$). Their results show that the amount of turbulence attenuation by small particles first increases as the particle concentration increases, but that further increases in particle concentration reduce the extent (magnitude) of the modulation. To demonstrate, the variation of axial fluid turbulence modulation (M_x) at the pipe centerline is plotted against the particle volumetric concentration in Fig.4-1, for results taken from the literature. The abbreviations used in the legend, along with the references to the experimental data and the corresponding test conditions, are provided in Table 4-1. Here, axial fluid turbulence modulation (M_x) is defined as the magnitude of change in the axial fluid fluctuating velocities due to the presence of the particles (Gore and Crowe, 1989):

$$M_x = \frac{\left(\frac{\langle u^2 \rangle^{0.5}}{U_b}\right)_{TP} - \left(\frac{\langle u^2 \rangle^{0.5}}{U_b}\right)_{SP}}{\left(\frac{\langle u^2 \rangle^{0.5}}{U_b}\right)_{SP}} \quad (4-2)$$

where u and U_b are the axial fluid fluctuating velocity and the bulk velocity, respectively and $\langle \rangle$ denote the ensemble averaging. The subscripts TP and SP stand for “two phase” and

“single phase”, respectively. Turbulence modulation in the radial direction, M_r , is defined similarly but considers the radial fluctuation fluid velocities, v .

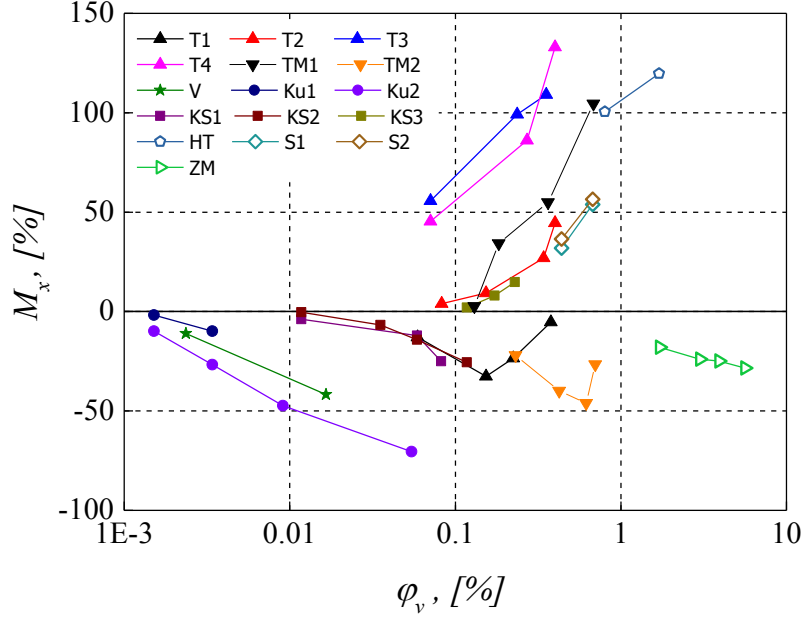


Figure 4-1. Axial fluid turbulence modulation versus particle concentration using experimental data from literature. The abbreviations used in the legend are described in detail in Table 4-1.

Table 4-1. Details of the experimental data shown in Fig.4-1.

REF.	Abbreviation	d_p (mm)	Carrier phase	Re
Kussin and Sommerfeld (2002)	KS1	0.1	Gas	<58 000
	KS2	0.19		
	KSA	0.625		
Varaksin et al. (2000)	V	0.05	Gas	15 300
Kulick et al. (1994)	Ku1	0.05	Gas	13 800
	Ku2	0.07		
Tsuji et al. (1984)	T1	0.2	Gas	22 000
	T2	0.5		
	T3	1		
	T4	3		
Tsuji and Morikawa (1982)	TM1	3.4	Gas	<40 000
	TM2	0.2		
Sato et al. (1995)	S1	0.34	Liquid	5 000
	S2	0.5		
Zisselmar and Molerus (1979)	ZM	0.05	Liquid	100 000

In addition to some uncertainty over the effect of particle concentration on turbulence modulation (attenuation), another important deficiency is that only the streamwise direction has been considered for modeling the carrier phase turbulence modulation (Lightstone and Hodgson, 2004; Lain and Sommerfeld, 2003; Crowe, 2000). The reality is that there is very limited data available showing fluid turbulence modulation in the radial direction and the data that are available show that radial modulation differs considerably from that in the streamwise direction. For example, Kussin and Sommerfeld (2002), Varaksin et al. (2000), and Kulick et al. (1994) show that small particles cause less fluid turbulence attenuation in radial direction than they do in streamwise direction. Sato et al. (1995) observe that while large particles (340 and 500 μm glass beads) produced axial fluid turbulence augmentation, the radial turbulence modulation is negligible. In addition to the fact that few studies have reported radial turbulence statistics of the particulate liquid flows, to the best authors' knowledge, no study on the concentration effect of large particles ($d_p/l_e \geq 0.1$) on liquid phase turbulence modulation in radial direction is available in the literature. Moreover, the tests of the concentration effect of relatively large particles ($d_p/l_e \geq 0.1$) on the carrier phase turbulence are limited to low Re ($Re < 60\,000$), as seen in Table 4-1. Therefore, the present experimental investigation, where the concentration effect of the large particles ($d_p/l_e \geq 0.1$) on both radial and axial fluid turbulence modulation at $Re > 60\,000$ provides valuable new insights on this particular subject.

4.1.2 Particulate phase turbulence

In particulate flows, turbulent motions of both the fluid phase and the solid particles are of importance; therefore, experimental investigations can play an important role in

understanding these very complicated interactions. A review of the literature on the particle fluctuations in particle-laden flows indicates that:

- (i) the particles usually have radial and axial fluctuating velocities that are equal to, or higher than those of the carrier phase (Shokri et al., 2015; Kameyama et al., 2014; Borée and Caraman, 2005; Caraman et al., 2003; Kussin and Sommerfeld, 2002; Varaksin et al., 2000; Suzuki et al., 2000; Sato and Hishida, 1996; Sato et al., 1995; Lee and Durst, 1982).
- (ii) Moreover, analysis of the limited literature available shows that the influence of concentration on the radial and streamwise particle fluctuations can be very different. For example, Varaksin et al. (2000) show that the radial fluctuations of 50 μm particles decrease throughout the flow domain with an increase in particle concentration from 0.002 to 0.017% (by volume). However, streamwise particle fluctuations decrease only in the core region ($r/R < 0.7$) and they are dramatically enhanced in the region near the wall as the concentration increases. Borée and Caraman (2005) show that the radial fluctuations of both 60 and 90 μm glass beads are enhanced by increasing the concentration, but for the 90 μm glass beads, an increase in concentration reduces the magnitude of the streamwise fluctuations. The streamwise fluctuations of 60 μm particles are slightly enhanced in core of the flow ($r/R < 0.7$) by increasing the concentration but decrease in the near-wall region.

- (iii) the experimental studies of the concentration effect on both axial and radial particle fluctuations are limited to relatively small particles (up to 100 μm) for gas-solid channel flows

Compared to gas-solid flows, there is relatively limited information available on the turbulent motions of particles in liquid channel flows (Shokri et al., 2015; Kameyama et al., 2014; Kiger and Pan, 2002; Suzuki et al., 2000; Sato et al., 1995). Most importantly, the concentration effect on the streamwise and radial particle fluctuations has not been investigated so far. It will be essential for further development of our understanding of particle-laden liquid flows to provide experimental data showing the concentration effect on the turbulent motions of particles in liquid particulate flows.

Consequently, the main objective of the present study is to investigate the concentration effect on the mean velocity and turbulent statistics of the liquid and solid phases for different particle sizes in a dilute liquid-solid pipe flow. A comprehensive experimental investigation was performed using mixtures of water and glass beads in a 50.6 mm (diameter) vertical loop. The loop was operated at a bulk velocity of 1.78 m/s, corresponding to $Re = 100\ 000$. The particulate phase was, for separate tests, 0.5, 1, and 2 mm glass beads whose concentrations were varied from 0.05 to 1.6% (by volume). Changes in the concentration of these large particles ($d_p/l_e \geq 0.1$) at relatively high Re ($Re = 100\ 000$) produced novel results which provide new information in the area of particle/fluid turbulence interactions.

4.2 Experimental setup

The flow experiments were performed with a 50.6 mm vertical pipe loop having a total height of 7 m, as shown in Fig.4-2. Flow is produced using a centrifugal pump (2/1.5 B-WX, Atlas Co.) and 15 kW motor / variable frequency drive (Schneider Electric-Altivar61). All experiments were carried out at a constant temperature (25 °C), which was controlled with a double-pipe heat exchanger. A magnetic flow meter (FoxBoro IM T25) provides flow rate measurements. Mixtures of water and glass particles are prepared and loaded through the feed tank. After loading the mixture into the flow loop, the tank is isolated from the circuit and the particle-laden flow circulates through a closed loop. The velocity measurements of both the liquid and solid phases were made with a planar particle image/tracking velocimetry (PIV/PTV) technique. This measurement technique includes a camera and a laser, as shown in Fig.4-2. Additional details on the PIV/PTV technique employed in the current study are provided in the subsequent section. The PIV/PTV measurements were made in the upward leg of the loop. The test section is located 80D downstream of the lower bend which is expected to provide fully developed conditions (Crawford et al., 2007). The transparent test section is made of acrylic pipe encased in a water-filled rectangular acrylic box to minimize the image distortion due to the curvature of the pipe wall. Also, measurements were made 15D from the long-radius upper bend ($R_b = 11D$).

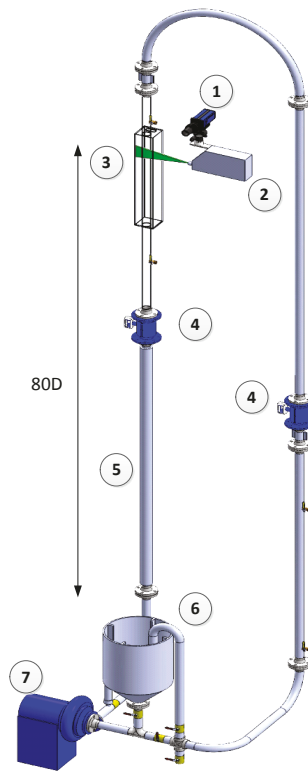


Figure 4-2. Schematic of the test rig consisting of (1) camera, (2) laser, (3) acrylic pipe and viewing box, (4) magnetic flow meters, (5) double-pipe heat exchanger, (6) feed tank, (7) and the centrifugal pump.

The experimental conditions and the particle specifications are provided in Table 4-2. Glass beads of different size (0.5, 1 and 2 mm) were used as the dispersed phase. Volumetric concentrations, ϕ_v , of 0.05 to 1.6% were tested. As shown in Table 4-2, the particle number density, N_d , is of the same order of magnitude for all the tests conducted here. Note that the number density is calculated using $N_d=6(d_p)^3/\pi\phi_v$. For each particle size, the highest concentration of glass beads is set at a “maximum” concentration, beyond which

the PIV technique could no longer be used effectively because of the excessive number of glass beads. It means that the glass beads would fill the entire image, making it technically impossible to find the seeding particles to apply PIV. Once the maximum concentration was determined for each particle size, the experiments were repeated at 50% of the maximum concentration so that the impact of the particle concentration on fluid and particle motions could be observed. The glass beads (A-series, Potters Industries Inc.) have a true density of 2500 kg/m^3 resulting in $\rho_p / \rho_f = 2.5$. The average bulk velocity (U_b) was held constant at 1.78 m/s, which correspond to a Reynolds number (Re) of 100 000 and frictional Reynolds number (Re_τ) of 4 740. The latter is estimated using the Colebrook–White equation to obtain the Darcy friction factor and wall shear stress. Moreover, the particle Reynolds number ranges from 42 to 607, as shown Table 4-2.

Table 4-2. Experimental conditions tested during the current investigation

Re	U_b (m/s)	d_p (mm)	ϕ_v (%)	N_d (m^{-3})	Re_p	St_k (at $r/R=0$)	St_L (at $r/R=0$)
100 000	1.78	0.5	0.05	7.6×10^6	42	1.29	0.15
			0.1	1.5×10^7			
		1	0.2	3.8×10^6	167	2.52	0.26
			0.4	7.6×10^6			
		2	0.8	1.9×10^6	607	4.62	0.52
			1.6	3.8×10^6			

The integral Stokes number (St_L) and Kolmogorov Stokes number (St_k) at the pipe centerline, which are provided in Table 4-2, are defined as:

$$St_L = \frac{\tau_p}{\tau_L} \quad (4-3)$$

$$St_k = \frac{\tau_p}{\tau_k} \quad (4-4)$$

where τ_p , τ_L and τ_k are the particle response (relaxation) time and integral and Kolmogorov time scales of the carrier phase turbulence, respectively. The particle response time is calculated using:

$$\tau_p = \frac{(\rho_p - \rho_f)d_p^2}{18\mu_f f_d} \quad (4-5)$$

where f_d is a drag coefficient correction factor accounting for deviation from Stokes' flow and is calculated as (Kussin and Sommerfeld, 2002):

$$f_d = 1 + 0.15Re_p^{0.687} \quad (4-6)$$

The integral time scale (τ_L) and the Kolmogorov time scale (τ_k) of the fluid phase are defined as (Kussin and Sommerfeld, 2002):

$$\tau_L = \frac{2k}{9\varepsilon} \quad (4-7)$$

$$\tau_k = \left(\frac{\nu}{\varepsilon}\right)^{1/2} \quad (4-8)$$

where ν and l_m are kinematic viscosity and turbulent mixing length of the fluid, respectively. The turbulent kinetic energy k and the dissipation rate ε can be obtained from (Milojevic, 1990):

$$k = 0.5(\langle u^2 \rangle + 2 \langle v^2 \rangle) \quad (4-9)$$

$$\varepsilon = C_\mu^{0.75} \frac{k^{1.5}}{l_m} \quad (4-10)$$

In order to obtain k and the streamwise and radial fluctuating velocities, u and v respectively, PIV measurements of the unladen flow are made. Dissipation rate and finally τ_L and τ_k are calculated using estimations of mixing length (l_m) and C_μ . The mixing length is estimated using $l_m/R=0.14-0.08(r/R)^2-0.06(r/R)^4$ (Schlichting, 1979). Finally, $C_\mu =0.09$ is considered as in the standard k - ε method (Milojevic, 1990). A particle is considered to be responsive to the specific turbulence scale of the carrier phase when its corresponding Stokes number (St) is less than 1. It is considered partially responsive when St is of order of 1 and it is said to be nonresponsive to the specified turbulence scale for $St \gg 1$ (Varaksin, 2007; Varaksin et al., 2000). Based on the Stokes numbers of the particles tested here (see Table 4-2), the particles are responsive to the large scale turbulence of the liquid phase in the core of the flow. Also, these particles are partially responsive to smallest scales of the turbulence at the pipe centerline.

4.3 Measurement techniques

A two dimensional PIV/PTV technique is employed to measure the velocities of the liquid and particulate phases. The flow is seeded with 18 μm hollow glass beads with density of 600 kg/m^3 (60P18 Potters Industries) whose response time is about 7 μs . The relaxation time of the tracers is much smaller than the Kolmogorov time scale of the flow (6ms), and thus the tracers can follow the turbulent motions of the liquid phase (Westerweel et al., 1996). PIV images are captured with a CCD camera (Imager Intense, Lavis) that

has a pixel resolution of 1376×1040 and a physical pixel size of $6.45 \times 6.45 \mu\text{m}$. A Nd:YAG laser (Solo III-15, New Wave Research) is used to illuminate the middle plane of the pipe. The light sheet has a thickness of less than 1 mm. The laser can produce 50 mJ per pulse at 15 Hz repetition rate with 3-5 ns pulse duration. For each set of experiments, 20 000 double-frame images are captured using a commercial software package (DaVis 8.2, LaVision GmbH). Magnification and spatial resolution of the imaging system are set at 0.27 and 42.6 pixel/mm, respectively. A 60mm Nikon SLR lens with an aperture of $f/16$ is used in the experiments.

A sample raw image, in which both the 2 mm glass beads and the PIV tracers are visible, is shown in Fig.4-3a. A magnified view of the highlighted area in Fig.4-3a is shown as Fig.4-3b. In order to obtain the velocity field of the liquid phase, all the glass beads must be first detected and removed from images. The “imfindcircle” function of MATLAB (MATLAB R2013a, The MathWork Inc.) is used to detect the glass beads. This function is based on Hough transform for detection of circular objects (Davies, 2012; Atherton and Kerbyson, 1999; Yuen et al., 1990). The algorithm requires the range of acceptable particle radius (set to $\pm 40\%$ of the nominal particle radius) and also a gradient-based threshold for edge detection as input parameters. Since an in-focus particle has sharper edges, in-focus particles acquire larger threshold than the out-of-focus ones. Hence, two different low and high gradient-based thresholds are considered for edge-detection. The low threshold is applied to detect and mask out the in-focus and out-of-focus particles from both frames for PIV analysis of the liquid phase, as shown in Fig.4-3c. The higher threshold is used in order to detect only the in-focus particles for the PTV analysis as illustrated in Fig.4-3d.

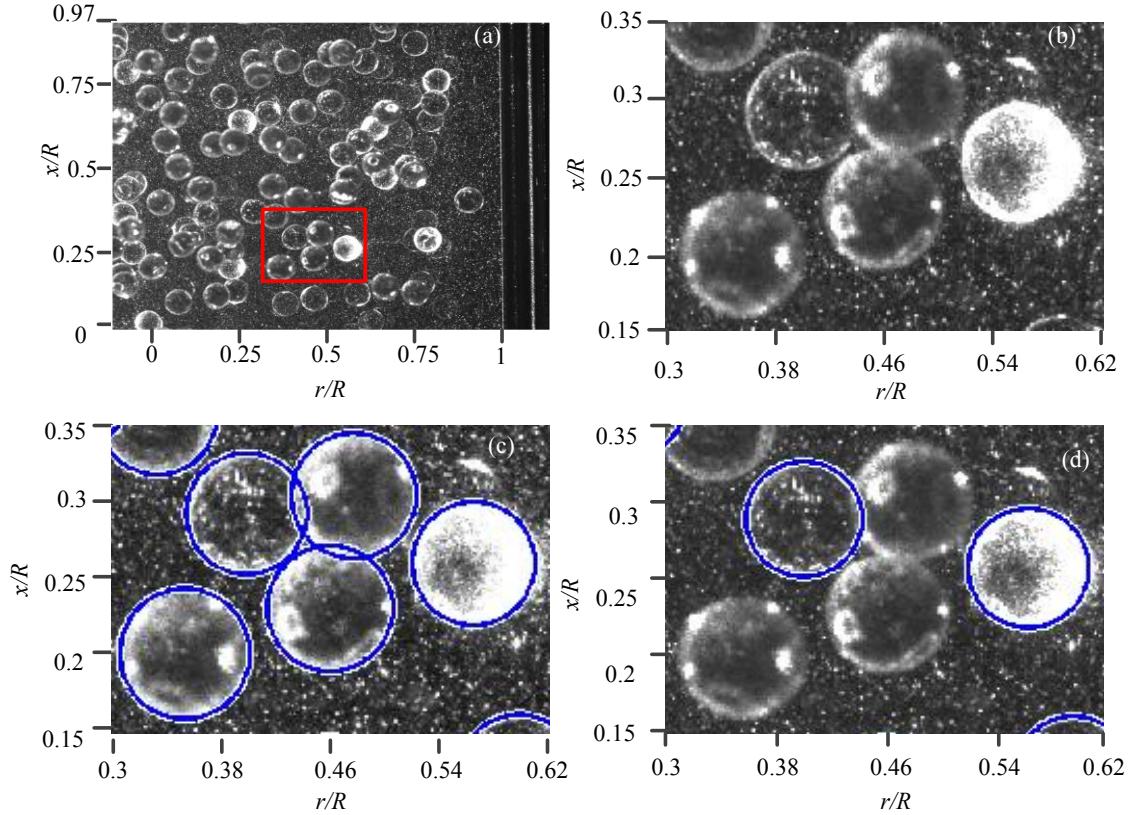


Figure 4-3. (a) A raw image showing the full field-of-view with 2 mm glass beads at $\phi_v=1.6\%$ and PIV tracer particles. The axis titles: r/R specifies the radial direction and x/R specifies the streamwise (upward) direction. (b) Magnified view of the highlighted area (outlined in red) in the full field-of-view image. (c) In-focus and out-of-focus particles are detected using the low edge-detection threshold. (d) In-focus particles detected using the high edge-detection threshold for PTV analysis.

The first step in calculating the liquid phase velocities is to mask out all the detected particles. Two nonlinear filters are then applied to the masked-out images to increase the signal-to-noise ratio. First, subtraction of a sliding background and subsequently particle intensity normalization filters are employed. The instantaneous velocity vector field of the liquid phase is obtained by cross-correlation of the double-frame images with $32 \times 32 \text{ pix}^2$ window size and 75% window overlap. Since the inclusion of the masked area into the interrogation window might have an undesired impact on the final results, we reject

interrogation windows that have more than 1% overlap with the masked areas (the glass beads). This approach ensures zero impact of the masking area on the liquid phase velocity measurements.

The centroid location and the diameter of each of the in-focus particles are obtained with sub-pixel precision by using the aforementioned particle detection technique. A PTV algorithm has been developed in MATLAB to obtain the centroid displacement of each in-focus glass bead and hence the instantaneous particle velocity. The PTV code pairs each individual glass bead from frame #1 to frame #2 using an appropriate pixel shift range estimated from the liquid phase velocity. Also, by measuring the diameter of the in-focus particles through the particle detection algorithm, the particle size distribution is obtained. In Fig.4-4a, the deviation of the measured particle size from the mean ($d_p - \langle d_p \rangle$) is shown as a differential frequency distribution, i.e. the number frequency percentage is divided by bin size. The results show that the particle size distributions (PSD's) of the tested glass beads are quite symmetric. Other particle-related details obtained through the particle detection algorithm are summarized in Table 4-3. The computed average particle diameter is approximately equal to the nominal size provided by the supplier, for each particle size. Also, standard deviations of all the tested glass beads are approximately equal, implying that the three different sizes of glass beads have the same span of size distribution. Finally, the number of the in-focus particles used to obtain the averaged quantities of the PTV outcomes, e.g. turbulence statistics of the particulate phase, is also provided.

Table 4-3. Particle specifications obtained through PTV processing.

Nominal d_p (mm)	ϕ_v (%)	Measured $\langle d_p \rangle$ (Pixel)	Measured $\langle d_p \rangle$ (mm)	Standard deviation (mm)	Total number of in-focus particles
0.5	0.05	25.03	0.60	0.043	104 000
	0.1	24.85	0.59	0.044	192 100
1	0.2	44.64	1.07	0.053	92 400
	0.4	44.93	1.07	0.049	184 500
2	0.8	85.54	2.04	0.046	82 300
	1.6	85.37	2.04	0.041	156 400

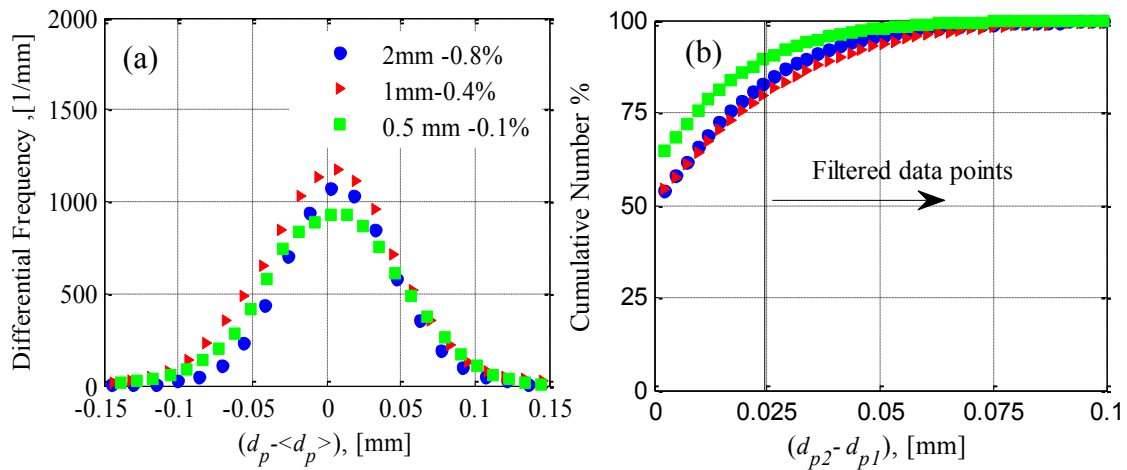


Figure 4-4. (a) Particle size distributions obtained from PTV analysis, (b) Cumulative distribution of the difference in the diameter of pairs of glass beads detected in frame #1 and frame #2. The legend applies to both plots.

In the analysis of the PTV results, it is possible that the size of the same individual particle captured in two subsequent frames can vary slightly. This effect is most probably caused by the variation of the surface glare of the glass beads, by glass beads that are slightly in/out of focus because of out-of-plane motions, and although less likely, bead non-sphericity. In order to minimize the effect of apparent particle diameter deviations on the

accuracy of the PTV, a filter is applied to discard the data where the difference in glass bead diameter in two frames is greater than 1 pixel (0.024 mm). The cumulative distribution of diameter difference for the detected glass beads between the first and the second frames for each particle (d_{p1} and d_{p2} , respectively) is shown in Fig.4-4b. Approximately 10-20% of the data points in each set were discarded as a result, as shown in Fig.4-4b. Application of this filter significantly reduced the data noise and resulted in more rapid statistical convergence.

4.4 Results and discussion

The results showing the particle concentration effect(s) on the mean and turbulent fluctuating velocities of both phases are discussed in this section.

4.4.1 Mean velocity profiles

The mean velocity profiles for both the liquid phase and the large particles are shown in Fig.4-5. In this figure, $r/R=0$ and $r/R=1$ denote the centerline and wall of the pipe, respectively. Note that the averaging for the particulate phase is done over radial intervals of $0.08R$, from $r/R=0$ to 0.96 . The symbols (U , V) and (u , v) represent average and fluctuating velocities in the streamwise and radial directions, respectively.

As illustrated in Fig.4-5, the particles travel more slowly than the fluid in the core of the flow and the lag is enhanced as the particle size increases. Similar results have been reported previously (Shokri et al., 2015; Tsuji et al., 1984; Lee and Durst, 1982). The slip velocity between the solid and liquid phases at the pipe centerline is observed to be approximately equal to the particle terminal velocity, which is in agreement with previous studies of vertical solid-liquid flows (Sato et al., 2000, 1995; Shokri et al., 2016a).

The liquid phase at the wall is subject to the no-slip boundary condition (Tsuji et al., 1984) whereas the particle velocity at the wall does not go to zero (Sommerfeld and Huber, 1999; Sommerfeld, 1992). Moreover, these large particles can make long lateral movements from high velocity (core) region to the lower velocity (near-wall) region (Vreman, 2007). In addition, their relatively poor response to the surrounding liquid phase means that a particle may have a higher velocity than the liquid phase in the near-wall region. As shown in Fig.4-5, the slip velocity decreases as r/R increases (moving towards the wall) and finally the mean axial particle velocity reaches a “crossing point” at about $r/R=0.96$ where it is equal to the local mean streamwise velocity of the liquid phase.

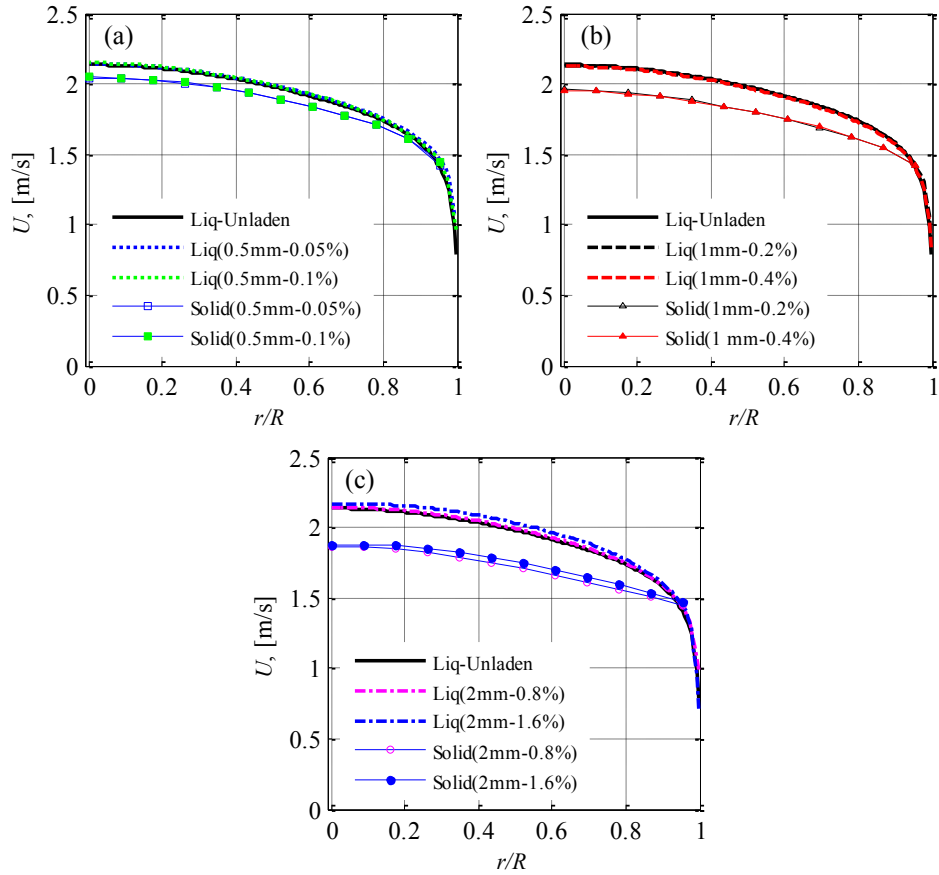


Figure 4-5. Velocity profiles of the liquid phase and the glass beads: (a) 0.5 mm, (b) 1 mm and (c) 2 mm.

Shokri et al. (2015) showed that the crossing point was located at $r/R=0.85$ for the same size particles in an upward solid-liquid flows at $Re = 320\,000$, indicating that a reduction in Re shifts the crossing point towards the wall. This can be attributed to the change in the ratio of the particle velocity to the liquid (or bulk) velocity (U_p/U_b) at different Re . Although the slip velocity does not change by decreasing the Reynolds number, the velocity ratio of U_p/U_b is reduced as Re decreases. For example, 2 mm particles move at 96% of the bulk velocity at the pipe centerline for $Re = 320\,000$ while at $Re = 100\,000$, the velocity of the same particles (again at the pipe center) is 88% of U_b , implying that the

particles travel at a lower velocity (with respect to the bulk velocity) at $Re = 100\ 000$. Consequently, the particles will reach the same velocity as the liquid phase at a location nearer to the wall at the lower Re .

The results of Fig.4-5 also show that an increase in particle concentration has almost no effect on the mean velocity profile of either phase for mixtures of 0.5 and 1 mm particles (Figs.4-5a and 4-5b). In the case of the 2 mm particles, however, a slight increase (about 2%) in the velocity profiles of both phases at the higher concentration was observed (Fig.4-5c). This implies that the actual flow rate was slightly higher than the one registered by flowmeter due to the error at the higher concentration test ($\phi_v=1.6\%$). Generally, though, for the conditions tested here (particle size and concentration ranges) a significant impact of the particle concentration on the mean velocity profiles of either phase was not observed.

4.4.2 Turbulent fluctuation profiles

Streamwise and radial turbulent fluctuations of the liquid phase and the particles for the conditions tested are shown in Fig.4-6. Prior to discussing the results, though, the three well-known criteria described earlier, i.e. those of Gore and Crowe (1989), Hetsroni (1989) and Tanaka and Eaton (2008), for the classification of carrier phase turbulence modulation are evaluated for the each of the test conditions, as shown in Table 4-4. For the 0.5 mm particles, the classifications of turbulence modulation obtained using the three different criteria are inconsistent, i.e. the Gore and Crowe (1989) criterion suggests that either attenuation or augmentation could occur, while the Hetsroni (1989) approach indicates attenuation and the Tanaka and Eaton (2008) particle momentum number criterion provides

an indication that augmentation should occur. For the 1 mm particles, the Gore and Crowe (1989) and the Tanaka and Eaton (2008) both predict turbulence augmentation will occur, while the Hetsroni (1989) approach suggests either could occur. All three criteria predict carrier phase turbulence augmentation for the 2 mm particles. In the following paragraphs, the experimental results are examined, and the relevance of the predictions obtained using the three criteria is discussed.

Table 4-4. Classification of carrier phase turbulence modulation using three well-known criteria

d_p (mm)	Gore and Crowe (1989)		Hetsroni (1989)		Tanaka and Eaton (2008)	
	d_p/l_e	Classification	Re_p	Classification	Pa_{st}	Classification
0.5	0.1	Either	42	Attenuation	41	Augmentation
1	0.2	Augmentation	167	Either	81	Augmentation
2	0.4	Augmentation	607	Augmentation	150	Augmentation

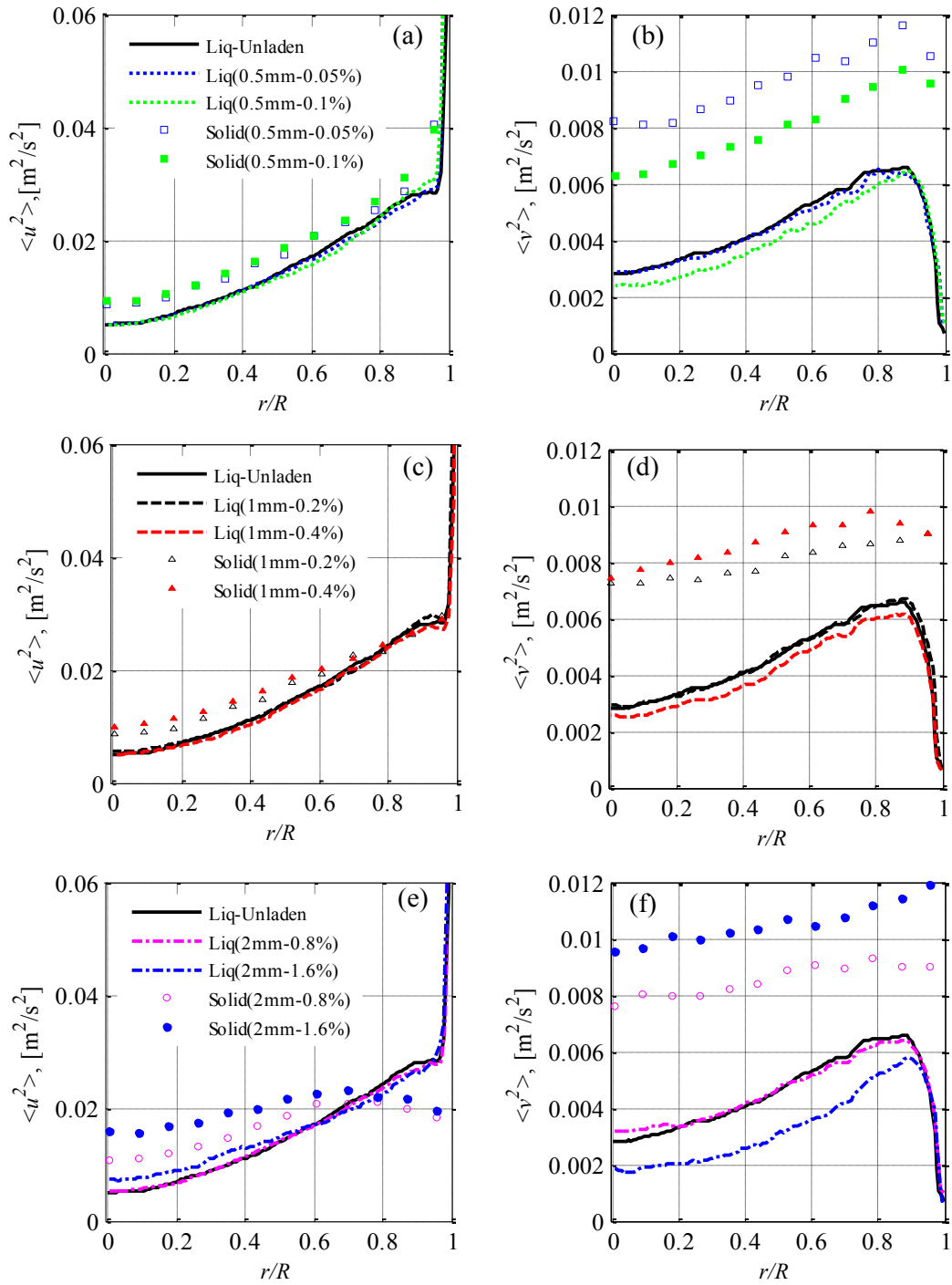


Figure 4-6. (a), (c), (e) Streamwise and, (b), (d), (f) radial fluctuations of liquid and particles. The legend of each plot on the left applies also to the corresponding plot on the right.

The experimental results of the present study show that the presence of the 0.5 or 1 mm particles does not have any significant effect on the carrier phase axial turbulence, for the concentrations tested here (see Figs.4-6a and 6c). For the 2 mm particles, however, the axial liquid fluctuations are significantly augmented as the concentration is increased from 0.8 to 1.6% (Fig.4-6e). The axial turbulence modulation (M_x) reaches 20% at the pipe centerline. Comparison of the results and the predictions cited in Table 4-4 shows that the criteria are not generally accurate in classifying the type of turbulence modulation of the axial liquid turbulence, especially for the 0.5 and 1 mm particles. For the highest concentration of 2 mm particles ($\phi_v = 1.6\%$), all three criteria correctly indicated that turbulence augmentation would occur. Interestingly, the magnitude of axial liquid turbulence augmentation observed for the 2 mm particles at $\phi_v=1.6\%$ is considerably lower than that reported by other researchers who used similar particle sizes (d_p/l_e) but conducted their experiments at much lower Re (Hosokawa and Tomiyama, 2004; Lee and Durst, 1982; Tsuji et al., 1984). For instance, Hosokawa and Tomiyama (2004) showed that 1, 2.5, and 4 mm ceramic particles with $0.7\% \leq \phi_v \leq 1.8\%$ at $Re = 15\ 000$ obtained $M_x \sim 100\%$ at the pipe centerline. Shokri et al. (2015) showed that the axial fluid turbulence modulation for relatively large particles ($d_p/l_e \geq 0.1$) can be directly related to the ratio of the particle terminal velocity to bulk velocity (V_t/U_b). Accordingly, the much lower axial turbulence augmentation observed here can be attributed to the very low ratios of V_t/U_b for the particle-laden mixtures tested as part of the present study.

As mentioned earlier, very few studies have provided any information on the effect of the particulate phase on the radial carrier phase turbulence modulation. In Figs.4-6b, 6d

and 6f, this information is provided for the 0.5, 1 and 2 mm particles, respectively. The results show that, for the lowest particle concentration tested for each particle size, there is almost no change in the radial liquid turbulence. With an increase in concentration for the 0.5 mm and 1 mm particles, radial liquid turbulence attenuation (Figs.4-6b and 6d) is observed, with $M_r \sim -10\%$ for the 0.5 mm particles and $M_r \sim -8\%$ for the 1 mm particles, at the pipe centerline. When the concentration of 2 mm particles is increased, the radial liquid turbulence is considerably attenuated, to a value of $M_r \sim -20\%$ at the pipe centerline (Fig.4-6f).

Generally, the results presented here show either no modulation or, at higher particle concentrations, some attenuation in radial liquid phase turbulence. In other words, the turbulence modulation in the radial direction is less than the modulation in streamwise direction, which is agreement with the results of Sato et al. (1995). They also observed considerable carrier phase turbulence augmentation in the axial direction but almost no modulation in the lateral direction. By comparing the results of the present investigation with the predictions shown in Table 4-4, it is evident that the turbulence modulation criteria are not suitable for prediction of the radial fluid turbulence modulation. Consider, for example, the significant radial turbulence attenuation associated with the highest concentration of 2 mm particles: all three criteria predicted strong augmentation. Although the criteria have rarely been tested against radial turbulence modulation measurements, their inability to predict such behavior should not be surprising since these criteria were developed using axial turbulence modulation data. The important message here is that the

axial and radial turbulence modulation should not be assumed to be similar in sign or in magnitude.

We now turn our attention to the particulate phase. The results of the present investigation, as shown in Fig.4-6, indicate that the concentration effect on the streamwise particle turbulence is negligible for the 0.5 mm and 1 mm particles. For the 2 mm particles, however, the concentration increase significantly intensifies the streamwise particle turbulence. On the other hand, the increase in concentration considerably suppresses the radial turbulence of the 0.5 mm particles. The concentration increase slightly augments the radial turbulent fluctuations of the 1 mm particles. Also, the increase in the concentration of 2 mm particles leads to a significant augmentation of the radial particle turbulence. It can therefore be concluded that increasing the particle concentration has a mixed effect on the particle turbulence, depending on the particle size and the directional (axial/radial) component of the turbulence under consideration.

As mentioned earlier, the literature also shows that an increase in the particle concentration can have both intensifying and suppressing effects on the particle turbulence, and that the effect can vary significantly in the axial and radial directions. For example, Varaksin et al. (2000) showed that an increase in concentration of 50 μm particles led to particle axial turbulence suppression in the core region and significant augmentation in the near-wall region. The radial particle fluctuations, however, decreased throughout the flow domain with the increase in concentration. Borée and Caraman (2005) also reported a mixed concentration effect on particle turbulence for both 60 and 90 μm glass beads. For the 90 μm

glass beads, they showed that an increase in concentration led to a suppression of the axial particle turbulence and enhancement in the radial particle fluctuations. However, they obtained both suppression and enhancement of the radial particle turbulence for 60 μm glass beads over the cross section while the overall suppression of axial particle turbulence was observed with an increase in concentration. The mixed effect of concentration on the particle fluctuating velocities implies a very complex system of particle-fluid interactions that is not yet understood.

4.4.3 Shear Reynolds stress and correlation coefficient profiles

The shear Reynolds stress ($-\langle uv \rangle$) as well as the correlation coefficient of u and v (C_{uv}) are plotted in Fig.4-7 for both liquid and particulate phases. The correlation coefficient is given by (Sabot and Comte-Bellot, 1976; Kim et al., 1987; Caraman et al., 2003):

$$C_{uv} = \frac{\langle uv \rangle}{(\langle u^2 \rangle^{0.5})(\langle v^2 \rangle^{0.5})} \quad (4-11)$$

The presence of 0.5 mm and 1 mm particles at different concentrations does not have any noticeable impact on the liquid phase shear Reynolds stress ($-\langle uv \rangle$) profiles, as shown in Figs.4-7a and 7c. Moreover, the liquid phase correlation coefficient of u and v (C_{uv}) does not change upon adding the 0.5 and 1 mm particles (Figs.4-7b and 7d), implying that the concentrations of 0.5 mm and 1mm particles tested here were not high enough to change either $\langle uv \rangle$ or C_{uv} of the liquid phase at the tested condition. This was expected since no significant changes were observed in liquid axial or radial fluctuating velocities upon addition of 0.5 and 1 mm particles.

Increasing the concentration of 2 mm particles led to reductions in both $\langle uv \rangle$ and C_{uv} of the liquid phase, as shown in Figs.4-7e and 7f. The decrease in the liquid phase C_{uv} can be attributed to the fact that liquid turbulence is, to some extent, linked to the particle behavior rather than the sweep and ejection patterns associated with the unladen flow of the liquid phase. As described earlier, the particles can interfere with the liquid turbulence through phenomena such as eddy breakup or wake and vortex shedding behind the particles. Consequently, these new structures weaken the strength of the liquid phase correlation. As mentioned earlier, the liquid phase $\langle uv \rangle$ is reduced as the concentration of 2 mm particles increases. This is very interesting when we consider that almost the same level of axial turbulence augmentation and radial turbulence attenuation of the liquid phase have been observed for this condition. These results suggest that the weakened correlation, as well as the radial turbulence attenuation, has overcome the axial turbulence augmentation, which finally leads to lower liquid phase $\langle uv \rangle$ at the higher concentration.

Also, Fig.4-7 shows that all the particles always have lower C_{uv} than the liquid phase which is in agreement with the results from Caraman et al. (2003) and Shokri et al. (2015). The lower C_{uv} of these relatively large particles can be attributed to the fact that the motion of these particles are significantly affected by non-correlating forces such as lift force and particle-particle collisions in addition to any effect the carrier phase turbulence has on these particles (Oliveira et al., 2015; Shokri et al., 2016a). Overall, Fig.4-7 shows that particle concentration has only a slight effect on the particle $\langle uv \rangle$ and C_{uv} . On the other hand, $\langle uv \rangle$ and C_{uv} of the particulate phase significantly decrease as the particle diameter increases. These results suggest that the particle diameter effect on the particle $\langle uv \rangle$ and C_{uv} is far

more important than the concentration, at least for the conditions tested here. This can be attributed to the particle Stokes number (St_L). The smaller particles have a smaller Stokes number, which means that they more readily respond to the carrier phase turbulence. Accordingly, they show higher $\langle uv \rangle$ and C_{uv} values than the larger particles, which are less responsive to the fluid turbulence.

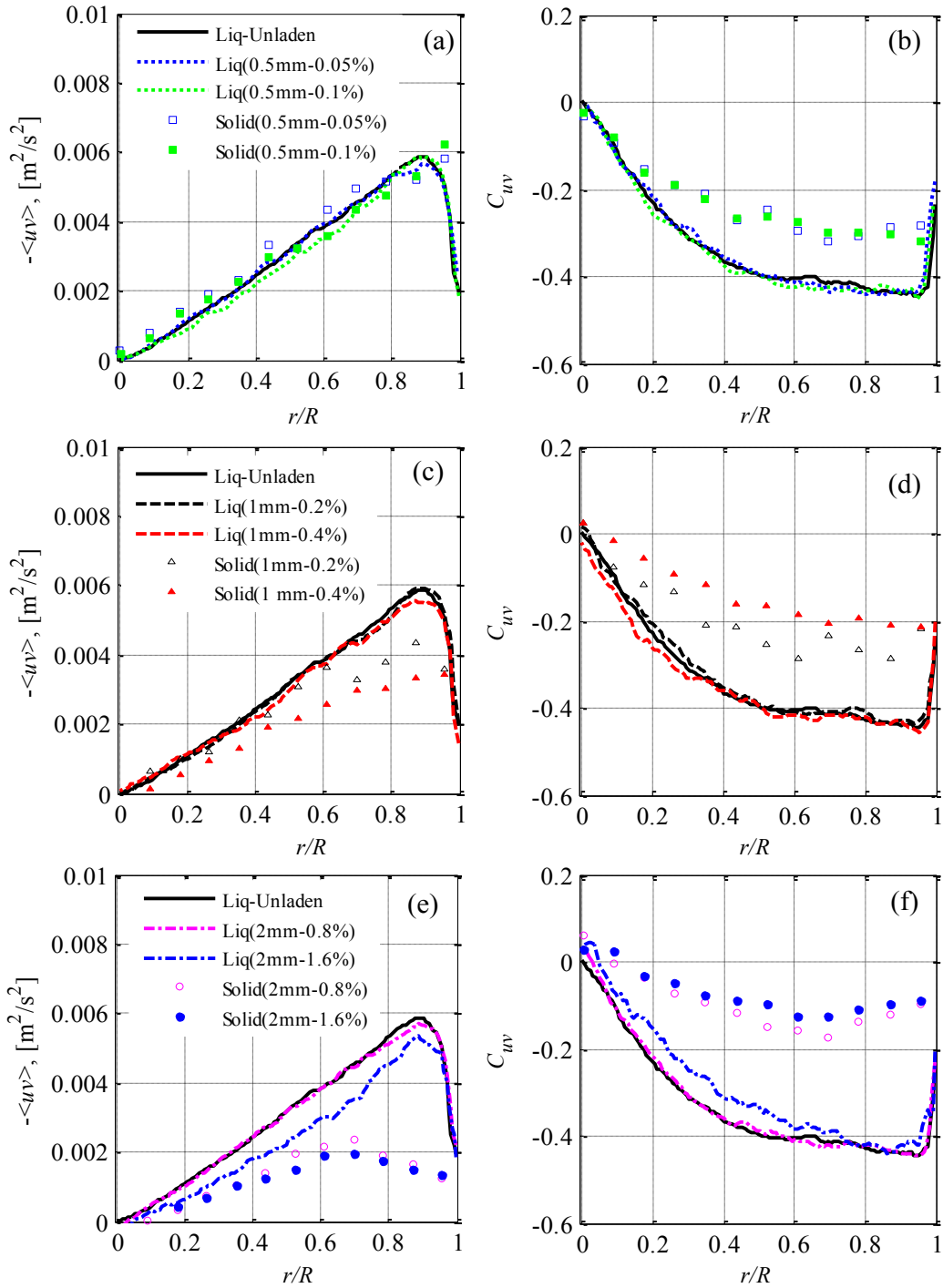


Figure 4-7. (a), (c), (e) $\langle uv \rangle$ and, (b), (d), (f) C_{uv} of the liquid and particles over the pipe cross section. The legends of the plots on the left also apply to the corresponding figure on the right.

4.5 Conclusion

In this study, the particle concentration effect on the mean flow and turbulence statistics of both the solid and liquid phases was investigated. This study represents the first time the concentration effect on the turbulence statistics of a particle-laden liquid continuous flow has been studied experimentally. Moreover, the study of large glass beads, (0.5, 1 and 2 mm in diameter), and a high Reynolds number ($Re = 100\ 000$) chosen for the present study produced some novel results which extend considerably the database of experimental results available. The results of the present study showed that the particles lagged behind the liquid phase at the centerline and the slip velocity between particles and fluid becomes zero in the near-wall region ($r/R=0.96$). Moreover, an increase in particle concentration had no noticeable impact on the mean velocity profiles of either phase.

The results also show that the particle concentration effect on the axial liquid turbulence modulation was significantly different from the effect observed in the radial direction. The concentration increase caused axial turbulence augmentation only for the experiments conducted with 2 mm particles. Meanwhile, the radial liquid turbulence was attenuated as a result of an increase in solids concentration for all particle sizes tested here. Also, evaluation of three well-known criteria used to predict the nature of carrier fluid turbulence modulation indicated that predictions of axial-direction conditions were, at best, mixed. The results clearly show that the criteria should not be applied to attempt to carrier phase turbulence modulation in the radial direction.

The results presented here show that an increase in particle concentration produced mixed effects in terms of particulate phase turbulence suppression or enhancement. The increase in concentration of the 0.5 mm particles resulted in suppression of radial particle turbulence. However, the concentration increase of the 2 mm particles significantly intensified the both axial and radial particle turbulence.

Additionally, this investigation indicated that only 2 mm particles at $\phi_v=1.6\%$ altered the shear Reynolds stress $\langle uv \rangle$ and correlation coefficient C_{uv} of the liquid phase. Moreover, the results showed that the $\langle uv \rangle$ and C_{uv} of particles were significantly reduced as the particle size increased. Moreover, increasing the concentration had much less impact on the particle $\langle uv \rangle$ and C_{uv} than the differences in particle diameter did.

5 A quantitative analysis of the axial and carrier fluid turbulence intensities[§]

5.1 Introduction

Particulate turbulent flows can be found in abundance in industrial applications such as slurry pipelines, pneumatic conveyers, and catalytic reactors. However, our understanding of such flows is extremely limited, mainly due to the complicated interactions existing in this type of flow. Elghobashi (1994) showed that four-way interactions between particles and the fluid occur when particle volume fraction (ϕ_v) is larger than 10^{-3} . These interactions include particle-particle interactions and fluid-particle interactions. If one must also consider particle-wall interactions, the behavior of the particulate phase becomes very complicated. This complex set of interactions governs the turbulent motions of particles and the fluid in particle-laden flows. Therefore, reliable experimental data sets on the fluid and particulate phase turbulence statistics in particle-laden flows are needed in order to develop an improved understanding of such complex systems.

[§] A version of this chapter, co-authored by R. Shokri, S. Ghaemi, D.S. Nobes, and R.S. Sanders, is submitted to the Journal of Powder Technology and is under review.

In particulate turbulent flows, one of the main parameters investigated experimentally in the literature is the particle effect on the carrier phase turbulence. Tsuji and Morikawa (1982) and Tsuji et al. (1984) used dilute mixtures of plastic particles and air in horizontal and vertical pipes, respectively, to determine the carrier phase turbulence modulation caused by the particles, whose diameters ranged from 0.2 to 3.4 mm, at Reynolds numbers below 40 000. They showed that larger particles augmented the axial fluid turbulence and smaller ones caused attenuation of the axial fluid turbulence. Similar results were obtained by Kussin and Sommerfeld (2002) for a particle-laden gas flow in a horizontal pipe with glass beads 0.06 to 1 mm in diameter at $Re < 58\ 000$. Kulick et al. (1994) and Varaksin et al. (2000) showed that small particles attenuated the gas turbulence in a downward flow at $Re \leq 15\ 300$. Hosokawa and Tomiyama (2004) investigated the effect of ceramic particles with 1 to 4 mm in diameter on the liquid turbulence in an upward pipe flow at $Re = 15\ 000$. They showed that those large particles augmented the liquid phase turbulence.

By collecting the experimental data in the literature on the carrier phase modulation caused by particles, Gore and Crowe (1989) and Hetsroni (1989) proposed what are probably the most well-known criteria to classify carrier phase turbulence modulation into augmentation or attenuation events. Fluid turbulence modulation is defined as the magnitude of change in the axial or radial fluid fluctuating velocities due to the presence of the particles. For instance, the axial fluid turbulence modulation (M_x) is given by (Gore and Crowe, 1991):

$$M_x = \frac{\left(\frac{\langle u^2 \rangle^{0.5}}{U_b}\right)_{TP} - \left(\frac{\langle u^2 \rangle^{0.5}}{U_b}\right)_{SP}}{\left(\frac{\langle u^2 \rangle^{0.5}}{U_b}\right)_{SP}} \quad (5-1)$$

In this equation, u and U_b are the axial fluid fluctuating velocity and bulk velocity respectively, and $\langle \rangle$ denotes ensemble averaging. The subscripts TP and SP stand for “two phase” and “single phase”, respectively. Gore and Crowe (1989) proposed that if the ratio of the particle size to the most energetic eddy length scale (d_p/l_e) is greater than 0.1, turbulence augmentation should occur; otherwise carrier phase turbulence is most likely to be attenuated. The most energetic length scale can be estimated as 0.1D (where D pipe diameter) in fully developed pipe flows (Hutchinson et al., 1971). According to Hetsroni (1989), a particle Reynolds number (Re_p) less than 100 indicates turbulence attenuation occurs and for $Re_p > 400$, turbulence augmentation is most likely. Although those criteria, to some extent, satisfactorily predict the augmentation or attenuation of the carrier phase turbulence, they are not capable of predicting the magnitude of the modulation. Gore and Crowe (1991) proposed that the turbulence modulation is a function of parameters such as the ratio of particle diameter to the integral length scale of turbulence (d_p/l_e), volume fraction of the particles (ϕ_v), particle Reynolds number (Re_p), ratio of the particle density to the fluid density (ρ_p/ρ_f), and Reynolds number (Re). Consequently, it is not reasonable to think an estimation of the magnitude of turbulence modulation could be obtained based on any of these parameters alone.

As mentioned above, Re is a key parameter in describing the interaction between the solid and fluid phases. For example, Tsuji and Morikawa (1982) showed that the axial

carrier phase (air) turbulence modulation at the pipe centerline caused by 3.4 mm plastic particles at $\phi_v = 0.7\%$ decreased from 220% to 100% as Re increased from 20 000 to 40 000 in a horizontal pipe flow. It seems that the only study of liquid-solid flows at different Re was conducted by Alajbegovic et al. (1994). They tested two different particles; ceramic and expanded polystyrene (buoyant particles) with water as carrier phase in a vertically upward pipe flow, and considered a range of Re from 42 000 to 68 000. The ceramic particles were 2.32 mm in diameter and were tested at a concentration of about 3% by volume. Their results showed that the liquid fluctuating velocities were enhanced by increasing the Reynolds number. This is an expected result since the turbulent fluctuations increase as the flow velocity and Re increases. Aside from the fact that a relatively narrow Re range was tested, the main deficiency of this work is that the unladen-liquid turbulence statistics were not provided. Therefore, one cannot calculate the amount of turbulence modulation caused by presence of the particles directly from the provided results.

In summary, there is a scarcity of experimental data that shows clearly Re effect on turbulence modulation, especially for particle-laden liquid flows. Therefore, a comprehensive experimental investigation on the effect of a broad range of Reynolds numbers on the turbulence modulation of the carrier phase can be essential for this field.

In particle-laden flows, the other focus of the experimental investigations has been on the turbulent motions of the particles. There have been studies in the literature that provide experimental data for the turbulent statistics of particles in the liquid and gas particulate flows (Borée and Caraman, 2005; Caraman et al., 2003; Kameyama et al., 2014;

Kussin and Sommerfeld, 2002; Sato et al., 1995; Suzuki et al., 2000; Varaksin et al., 2000). After reviewing the available experimental data, Shokri et al. (2015a) concluded that the particle fluctuating velocities are usually either equal to or greater than those of the unladen carrier phase. The turbulent motion of particles is a function of particulate flow parameters such as Reynolds number (Re), particle Reynolds number (Re_p) and Stokes number (St), particle/fluid density ratio (ρ_p / ρ_f), and solid phase volumetric concentration (ϕ_v) (Shokri et al., 2016a). The aforementioned experimental investigations typically focused on one or two parameters and generally tests were conducted over a narrow range of the parameter(s) of interest. It appears that there is no study in the literature which investigates the aggregate effects of these parameters on particulate phase turbulence.

Therefore, the two main objectives of the present study are as following: (i) experimental investigation of the Re effect in a very broad range on the solid and the liquid turbulence in a particle-laden pipe flow for better understanding the impact of Re and (ii) evaluating the contribution of the influential parameters to the carrier phase turbulence modulation and particle turbulent fluctuations using the experimental data in the literature and proposing new empirical correlations to quantify those contributions. Mixtures of water and 2 mm glass beads were studied in vertical (upward) flow in a 50.6 mm diameter pipe loop. The loop was operated at bulk velocities ranging from 0.91 to 5.72 m/s, corresponding to $52\,000 \leq Re \leq 320\,000$. A combined particle image/tracking velocimetry (PIV/PTV) technique was employed to measure the turbulence statistics of both liquid and particulate phases. First, the effect of Re on the mean and fluctuating velocities of the both phases and on the particle concentration profiles was thoroughly studied. Then, the parameters having

the greatest effects on the particle turbulence intensity in liquid-continuous flows are discussed and an empirical correlation is proposed. Finally, a new correlation for the estimation of the carrier phase turbulence augmentation is developed.

5.2 Experiments and measurement techniques

A schematic of the experimental setup used in this study is shown in Fig.5-1. The vertical loop has diameter of 50.6 mm at test section. First the water and then 2 mm glass beads are loaded into the loop from the feeding tank. The mixture is pumped through the loop using a 15 kW centrifugal pump (2/1.5 B-WX, Atlas Co.) and a variable frequency drive. Once the desired mass of particles is added to the flow loop, the feeding tank is isolated from the loop and the flow circulates through a closed loop. The temperature is maintained at 25°C throughout each experiment with a double pipe heat exchanger. Flow measurements are made with a magnetic flow meter (FoxBoro IM T25). As shown in Fig.5-1, the test section is situated more than 80D after the nearest upstream bend on the upward leg of the test loop, allowing sufficient entry length to reach fully developed flow conditions. The transparent test section is made of acrylic pipe. To minimize image distortion created by the curvature of the pipe wall, the test section is encased in an acrylic box filled with water. A more detailed description of the experimental setup is given in Shokri (2015) and Shokri et al. (2015a).

The particulate phase consists of glass beads with nominal average diameter 2 mm, tested at two different volumetric concentrations (ϕ_v) of 0.8 and 1.6%. Table 5-1 summarizes the test conditions of this study along with the particle-related data. The glass beads (Potters

Industries Inc.) have a true density of 2500kg/m³ resulting in $\rho_p / \rho_f = 2.5$. During the test, average (bulk) velocity (U_b) was varied from 0.91 to 5.72 m/s, which corresponds to Reynolds numbers of 52 000 to 320 000. The particle terminal velocity (V_t) and Reynolds number (Re_p) are about 0.27 m/s and 607, respectively. The particle response time (τ_p) is about 28.1 ms which is obtained from the following expression:

$$\tau_p = \frac{(\rho_p - \rho_f)d_p^2}{18\mu_f f_d} \quad (5-2)$$

where f_d is a correction factor of the drag coefficient for deviation from Stokes' flow and is calculated as (Kussin and Sommerfeld, 2002):

$$f_d = 1 + 0.15Re_p^{0.687} \quad (5-3)$$

In fluid-particle systems, the Stokes' number is considered to be a very important parameter. It is defined as the ratio of particle response time to a characteristic fluid time scale. There are often two time scales considered for a turbulent flow: the integral time scale (τ_L) and the Kolmogorov time scale (τ_k) (Kussin and Sommerfeld, 2002):

$$\tau_L = \frac{2k}{9\varepsilon} \quad (5-4)$$

$$\tau_k = \left(\frac{\nu}{\varepsilon}\right)^{1/2} \quad (5-5)$$

where the turbulent kinetic energy k and the dissipation rate ε can be obtained from (Milojevic, 1990):

$$k = 0.5(\langle u^2 \rangle + 2 \langle v^2 \rangle) \quad (5-6)$$

$$\varepsilon = C_{\mu}^{0.75} \frac{k^{1.5}}{l_m} \quad (5-7)$$

In order to obtain k , the streamwise and radial fluctuating velocities (u and v respectively) can be taken from PIV measurements of the unladen flow at the pipe centerline. Dissipation rate and finally τ_L and τ_k are calculated at the pipe centerline using the estimations of mixing length (l_m) and the coefficient C_{μ} . The mixing length can be estimated as $l_m/R=0.14-0.08(r/R)^2-0.06(r/R)^4$ (Schlichting, 1979). The coefficient C_{μ} is considered to be equal to 0.09, as in the standard k - ε model (Milojevic, 1990). The calculations shown in Table 1 indicate that the particles are responsive to the large scale eddies but they are responsive to the small scale turbulence only at $Re \leq 100\ 000$ at $r/R=0$ (Varaksin, 2007; Varaksin et al., 2000). However, calculations for St_L in near-wall region ($r/R=0.96$) show that the particles are almost non-responsive at $Re = 320\ 000$ and they become partially responsive in this region as Re decreases.

Table 5-1. Matrix of the experiments

d_p (mm)	τ_p (ms)	Re_p	V_t (m/s)	St_k ($r/R=0$)	St_L ($r/R=0$)	St_L ($r/R=0.96$)	Re	U_b (m/s)	ϕ_v (vol%)
2	28.1	607	0.27	1.3	0.20	3.5	52 000	0.91	1.6
				4.6	0.52	8	100 000	1.78	0.8
				14.0	1.25	25	320 000	5.72	0.8

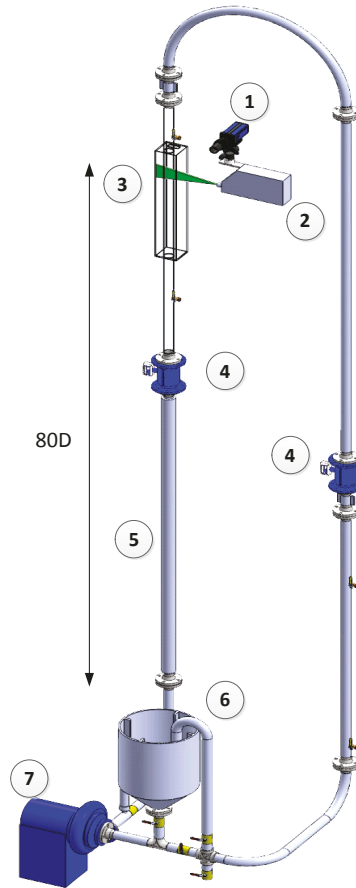


Figure 5-1. A schematic of the experimental setup consisting of (1) camera, (2) laser, (3) acrylic pipe and viewing box, (4) magnetic flow meters, (5) double-pipe heat exchanger, (6) feeding tank, (7) and the centrifugal pump.

A two dimensional PIV/PTV technique is used to simultaneously measure the instantaneous velocities of the liquid and the solid phases. The PIV/PTV system is comprised of a camera and a laser as shown in Fig.5-1. Hollow glass beads (60P18 Potters Industries) that are 18 μm in diameter and have density of 600 kg/m^3 are used as flow tracers. Images are obtained with a CCD camera (Imager Intense, Lavision) that has

1376×1040 pixel resolution. A Nd:YAG laser (Solo III-15, New Wave Research) creates a light sheet with thickness less than 1 mm, which illuminates the middle plane of the pipe. For PIV analysis of the liquid phase, all the 2 mm particles are detected using the “imfindcircle” function of MATLAB (MATLAB Release R2013a) which is based on Hough transform for detecting the circular objects. Those particles are then masked out from images and the cross correlation technique is applied to the images to obtain the instantaneous velocity vector field of the liquid phase. Only in-focus particles are selected for the particulate phase analysis (PTV technique). The center locations of those particles are utilized to obtain the instantaneous particle velocity and particle distribution (concentration profile) using a PTV code in Matlab. Additional details of the PIV/PTV technique can be found in Shokri (2015) and Shokri et al. (2015a).

5.3 Results

To investigate the impact of the Reynolds number on the turbulence statistics of the particulate and carrier phases, vertical pipe flow tests were carried out using mixtures of water and 2 mm glass beads at three Reynolds numbers (52 000, 100 000 and 320 000). The measurements were made with the aforementioned PIV/PTV technique. Mean velocity profiles, liquid/solid turbulent fluctuations along with the concentration profiles are provided in this section. In the results shown here, the radial direction is indicated by r starting such that the center of the pipe is $r = 0$ ($r/R=0$) and the pipe wall is located at $r = 25.3$ mm ($r/R=1$). The symbols (U , V) and (u , v) are the mean velocity and fluctuating velocities in the streamwise and radial directions, respectively. Moreover, the particles are binned into $0.08R$

radial intervals from $r/R= 0$ to 0.96 in all the figures where particle-related statistics are presented in this section.

5.3.1 Mean velocity profiles

The mean velocity profiles and the velocity profiles normalized with the centerline liquid velocity for both the liquid and solid phases are shown in Figs.5-2a and 5-2b. As shown in Fig.5-2a, the presence of 2 mm particles does not significantly affect the liquid mean velocity profiles. This can be attributed to the relatively high Re (high flowrates) and low particle concentrations for the conditions tested here. The results also show that the particles travel more slowly than the liquid phase in the core of the flow. The slip velocity at the pipe centerline can be reasonably approximated by the particle terminal settling velocity and remains almost constant over the range of Re tested here. The particle velocity becomes comparable to or even higher than the liquid velocity in the near-wall region causing the velocity profiles intercept at the “crossing point”. As shown in Fig.5-2a, the crossing point varies when Re decreases. The crossing point at $Re = 320\ 000$ occurs at $r/R=0.85$ and it moves to $r/R=0.96$ at $Re =100\ 000$. No crossing point is observed at $Re = 52\ 000$. In other words, this point shifts towards the wall as the Re decreases. The main reason of particles having comparable to or even higher velocity than the carrier phase in the near-wall region can lie in the boundary condition differences at the wall for the particles and fluid phase. The fluid is subject to the no-slip boundary condition at the wall which leads to the high fluid velocity gradient in this region. The particles do not follow the no-slip condition (Tsuji et al., 1984), and can collide with the wall and return to the main flow (Sommerfeld and Huber, 1999; Sommerfeld, 1992). Consequently, these particles may acquire higher velocity

than the liquid phase in the near-wall region. Velocity profiles of the liquid and solid phases eventually intercept each other at the crossing point. As mentioned earlier, the results however show that the crossing point locations are not constant at different Re .

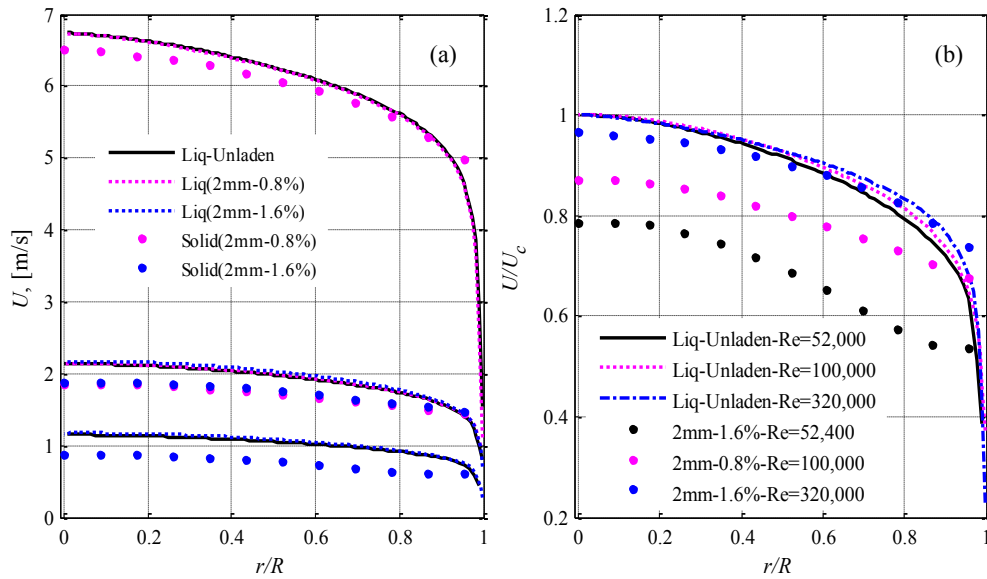


Figure 5-2. (a) Mean velocity profiles of liquid and 2mm glass beads, (b) velocity profiles of unladen liquid and 2mm glass beads normalized by the centerline liquid velocity (U_c) at different Re .

In order to cast a light on the issue of shift in the crossing point, the velocity profiles of unladen liquid and the particles normalized by the corresponding centerline liquid velocity are shown in Fig.5-2b. Although the slip velocity does not change when Re is decreased, Fig.5-2b shows that the ratio of the particle velocity to the liquid velocity decreases considerably. Accordingly, the particles have lower velocity at lower Re with respect to the liquid velocity. This can apparently explain the shift in the crossing point. However, the real reason might stem from the particle/carrier phase turbulence interaction in

the near wall region. As provided in Table 1, St_L in near-wall region ($r/R=0.96$) is reduced from 25 to 3.5 as Re decreases from 320 000 to 52 000. This implies that the particles easily respond to the fluid turbulence in the near-wall region as Re decreases. Highly influenced by the fluid flow in near-wall region at lower Re , the particle velocity, consequently, approaches to that of the carrier phase in this region for lower Re .

5.3.2 Concentration profile

Particle radial concentration distributions are obtained by detecting the number of particles at each radial position (N_p) and scaling that by the total number of particles detected (N_{total}). Concentration profiles obtained this way are shown in Fig.5-3. The results indicate that the 2 mm particles tend to accumulate in the central region of the flow at the highest Re . By decreasing Re to 100 000, a local peak in the particle distribution is formed at $r/R=0.7$. By further decreasing Re , the peak becomes more pronounced and its location moves towards the wall. This trend in concentration profiles is in agreement with other experimental works for vertical particle-laden flows e.g. Akagawa et al. (1989) and Furuta et al. (1977). In an upward pipe flow, Furuta et al. (1977) observed that the 1.87 mm glass beads formed a core-peaking concentration profile at high Re (=150 000), while a near-wall peak appeared in the concentration profile at lower Re (=84 000). By further decrease in Re to 37 000, the near-wall peak became larger and shifted more towards the wall.

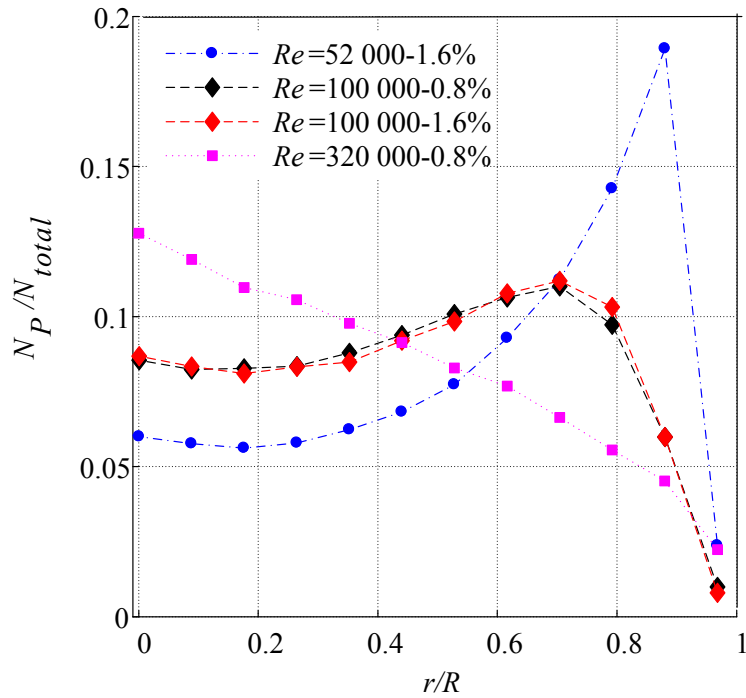


Figure 5-3. Concentration profile of 2 mm particles at different Re .

The radial forces play an important role in distributing the particulate phase over the cross section (Lucas et al., 2007; Sumner et al., 1990). The main radial forces are the turbulence dispersion, particle-particle collisions and a lift force. Particle-particle collisions and turbulence dispersion will spread the particles over the cross section (Burns et al., 2004; Huber and Sommerfeld, 1994). If these forces dominate, relatively flat concentration profiles will be observed. The lift force usually pushes the particles away from the wall, towards the center of the pipe (Auton, 1987; Lee and Durst, 1982). This force stems from the high shear rate of the liquid phase in the near wall region. When a lagging particle is subjected to the high gradient velocity field in the near-wall region, the lift force towards the pipe center is applied to the particle (Lee and Durst, 1982).

The concentration profile measured at $Re = 320\ 000$ suggests that particles are pushed away from the wall towards the core of the flow by the lift force. At lower Reynolds numbers ($Re = 100\ 000$ and $52\ 000$), wall-peaking is observed. The shapes of these concentration profiles are very difficult to explain. The concentration profile is relatively flat in the core region, which indicates that dispersive forces e.g. turbulent dispersion and particle-particle collisions are dominant in this region. Formation of a near-wall concentration peak suggests the emergence of a mechanism that pushes the particles towards the wall as Re decreases. Wall-peaked concentration profiles were also observed in Direct Numerical Simulation (DNS) results for particulate upward flows at low Re (< 5000) (Marchioli et al., 2003; Pang et al., 2011a). Pang et al. (2011) state that the particles are brought to the near-wall region by the sweep motions and then they will be pushed away from the wall by the ejection events of the carrier phase turbulence. Finally, the particles concentrate in an appropriate location near the wall by the net effect of the sweep and ejection events. As discussed earlier, the particles become more responsive to the fluid turbulence in the near-wall region as the Re decreases. Therefore, the formation of the near wall concentration peak could be attributed to the higher interaction between the particles and the fluid turbulence in the near-wall region at lower Re .

5.3.3 Turbulent fluctuations

The axial and radial turbulent fluctuating velocities of the liquid and solid phases are plotted as a function of radial position in Fig.5-4. As shown in Fig.5-4a, when $\varphi_v = 1.6\%$, the 2 mm particles significantly augment the axial liquid turbulence at $Re = 52\ 000$ (about +100% at the pipe centerline). At $Re = 100\ 000$ and $\varphi_v = 1.6\%$, the axial turbulence

augmentation of the carrier phase is reduced, +20% at the pipe centerline (Fig.5-4c). Interestingly, at $Re = 100\ 000$ but at lower particle concentration ($\phi_v=0.8\%$) no significant liquid axial turbulence modulation is observed. The 2 mm particles (with $\phi_v=0.8\%$) do not have any considerable effect on the axial fluid turbulence at the $Re = 320\ 000$ (Fig.5-4e). A good agreement between the results of the present study at low Re ($= 52\ 000$) and Hosokawa and Tomiyama, (2004) can be observed. Hosokawa and Tomiyama, (2004) also showed that 1, 2.5, and 4 mm ceramic particles demonstrated about +100% axial liquid turbulence augmentation at the pipe centerline for $Re = 15\ 000$ which is in agreement with our results at the lowest Re . However, the results for higher Reynolds number show much lower turbulence augmentation in comparison with the results of Hosokawa and Tomiyama, (2004). Results of the present study clearly show that an increase in the Reynolds number leads to a decrease in the axial turbulence augmentation caused by these large particles. As suggested by Shokri et al. (2015a), the liquid turbulence modulation for large particles is directly related to the ratio of the slip velocity between two phases to the bulk velocity (U_s/U_b), where the slip velocity can be estimated as the particle terminal settling velocity (V_t). As Re increases, the aforementioned velocity ratio approaches zero. Consequently, the magnitude of the augmentation should be expected to decrease. The effect of Re , along with the other parameters including Re_p , St_L , d_p/l_e , interspacing ratio (λ/d_p), and density ratios will be further discussed in Section 5-4.

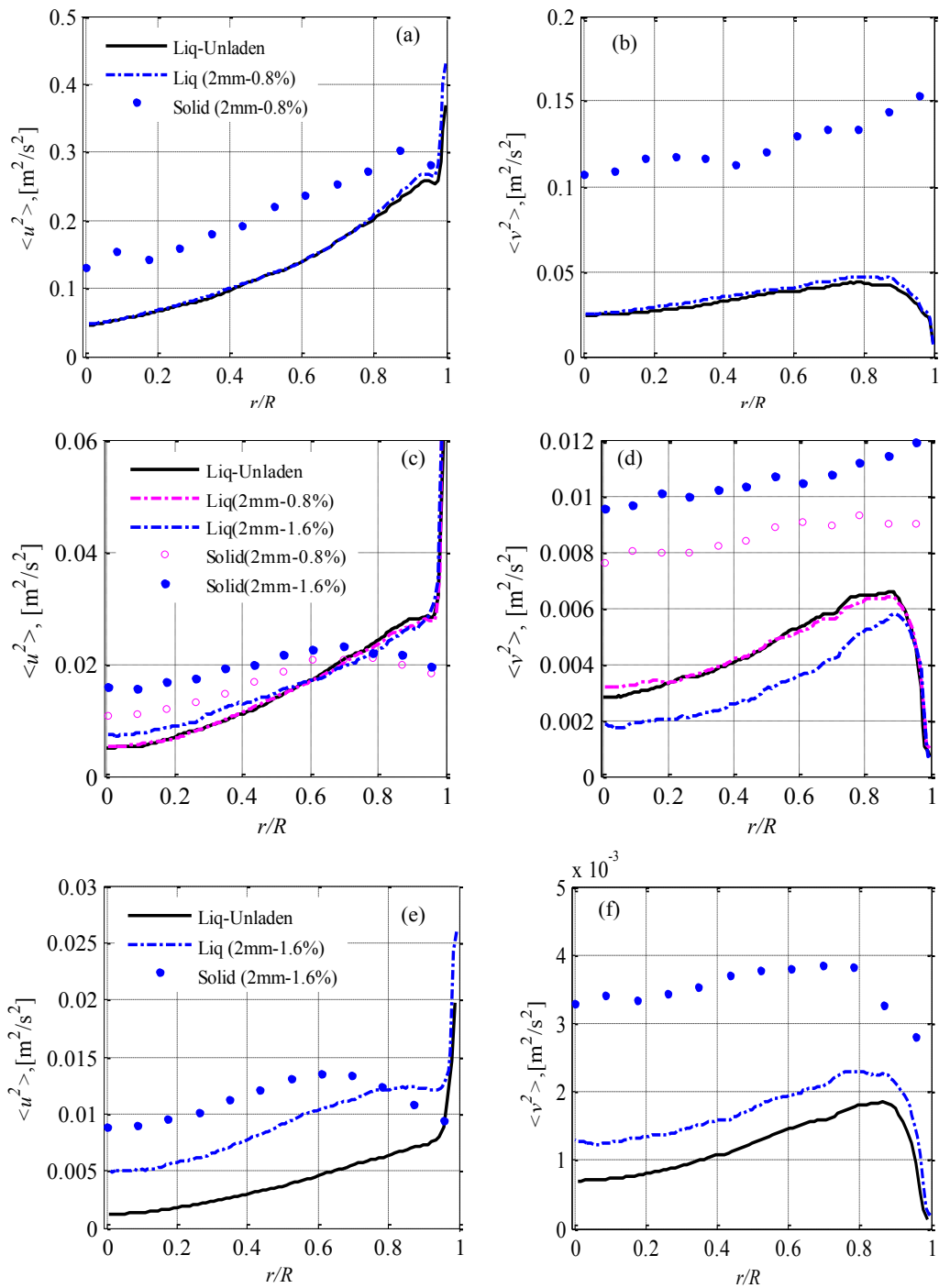


Figure 5-4. Streamwise and radial fluctuations of liquid and solid particles. The legends of the plot on the right side are the same as the left one.

The results obtained here also show that these 2 mm particles produce liquid radial turbulence modulation that is very different from the axial direction. In Fig.5-4b, particles with concentration of 1.6% considerably augment radial liquid turbulence at $Re = 52\ 000$, to a value of approximately +35% at the pipe centerline. However, augmentation of the radial liquid turbulence is much smaller than that of the axial direction at the aforementioned Re . The results show that the particles at $Re = 100\ 000$ and $\phi_v=0.8\%$ do not cause any significant change in the radial liquid fluctuating velocities (Fig.5-4d). By increasing the concentration to 1.6%, the radial liquid turbulence is attenuated about -20% at the pipe centerline, as illustrated in Fig.4d. Moreover, the radial liquid fluctuations do not illustrate any change for $Re = 320\ 000$ upon addition of the 2 mm particles (Fig.5-4f).

The results show that, except for the cases that there is no turbulence modulation in either direction, the radial turbulence modulation is smaller than that of the axial direction. The axial turbulence modulation is about +100 at the centerline for $Re = 52\ 000$ while the radial modulation is $\sim +35$. Also, the axial turbulence modulation reaches a maximum of +20% at the centerline for $Re = 100\ 000$ and $\phi_v=1.6\%$ while the radial turbulence is attenuated ($M_r = -20\%$). Sato et al. (1995) found in their experiments that the magnitude of the radial liquid turbulence modulation was much lower than the axial one. Since the majority of earlier experimental studies of carrier phase turbulence modulation focused only on the streamwise direction, the available criteria for classifying turbulence modulation (Crowe, 2000; Gore and Crowe, 1989; Hetsroni, 1989; Kenning and Crowe, 1997; Kim et

al., 2005), as well as most numerical simulations of these flows (Lightstone and Hodgson, 2004; Mandø et al., 2009; Yan et al., 2006), also consider only streamwise turbulence modulation. Therefore, our understanding of the subject is still limited and more experimental data showing the radial turbulence modulation are needed.

Now focusing on the particle fluctuation, the axial and radial fluctuating velocities of the particulate phase are also provided for all three Re in Fig.5-4. The results show that particle fluctuations are generally much larger than those of the single phase liquid flow. Additionally, the Reynolds number has a direct impact on the particle fluctuating velocities. The radial/axial particle fluctuations are drastically enhanced as Re increases. It should be expected since by increasing the Re , the bulk velocity increases which leads to higher particle fluctuating velocities. Moreover, increase in the concentration from $\phi_v=0.8$ to 1.6 % at $Re= 100\ 000$ causes an enhancement in particle fluctuating velocities in both radial and axial directions (Fig.5-4c and 5-4d). In section 5-4, a study is conducted to empirically quantify the impact of the Re and concentration (ϕ_v) as well as other influential parameters on the particle turbulent fluctuations including Re_p and Stokes' number by employing a broader range of experimental data from the literature

5.3.4 Correlation between streamwise and radial fluctuations

The impact of the particles on the Reynolds shear stress ($-\langle uv \rangle$) profiles of the liquid and solid phases are shown in Fig.5-5. Also the correlation coefficient of u and v (C_{uv}) is plotted for both the liquid and solid phases in Fig.5-5. The C_{uv} can be obtained by the following equation (Kim et al., 1987):

$$C_{uv} = \frac{\langle uv \rangle}{(\langle u^2 \rangle^{0.5})(\langle v^2 \rangle^{0.5})} \quad (5-8)$$

The obtained C_{uv} profiles for unladen liquid flows agree well with the literature (Caraman et al., 2003; Kim et al., 1987; Sabot and Comte-Bellot, 1976).

The results show an interesting trend in terms of the effect of the particles on the shear Reynolds stresses and C_{uv} of the liquid phase at the different Reynolds numbers. The particles enhance liquid $\langle uv \rangle$ while they reduce liquid C_{uv} at $Re = 52\ 000$ (Fig.5-5a and 5-5b). As shown in Fig.5c, these particles do not notably change the liquid $\langle uv \rangle$ and C_{uv} at $Re = 100\ 000$ and $\varphi_v=0.8\%$. However, both $\langle uv \rangle$ and C_{uv} of the liquid phase are reduced, as the particle concentration is increased to 1.6% (Fig.5-5d). Finally, there is no significant change in the liquid $\langle uv \rangle$ or C_{uv} upon addition of the 2 mm particles at $Re = 320\ 000$, as seen in Figs.5e and 5f. As pointed out in the previous section, the 2mm particles have almost no impact on the both axial and radial liquid phase turbulence at $Re = 100\ 000$ and $320\ 000$ with $\varphi_v=0.8\%$. Therefore, no considerable change is expected in the $\langle uv \rangle$ and C_{uv} profiles of the liquid phase at these conditions.

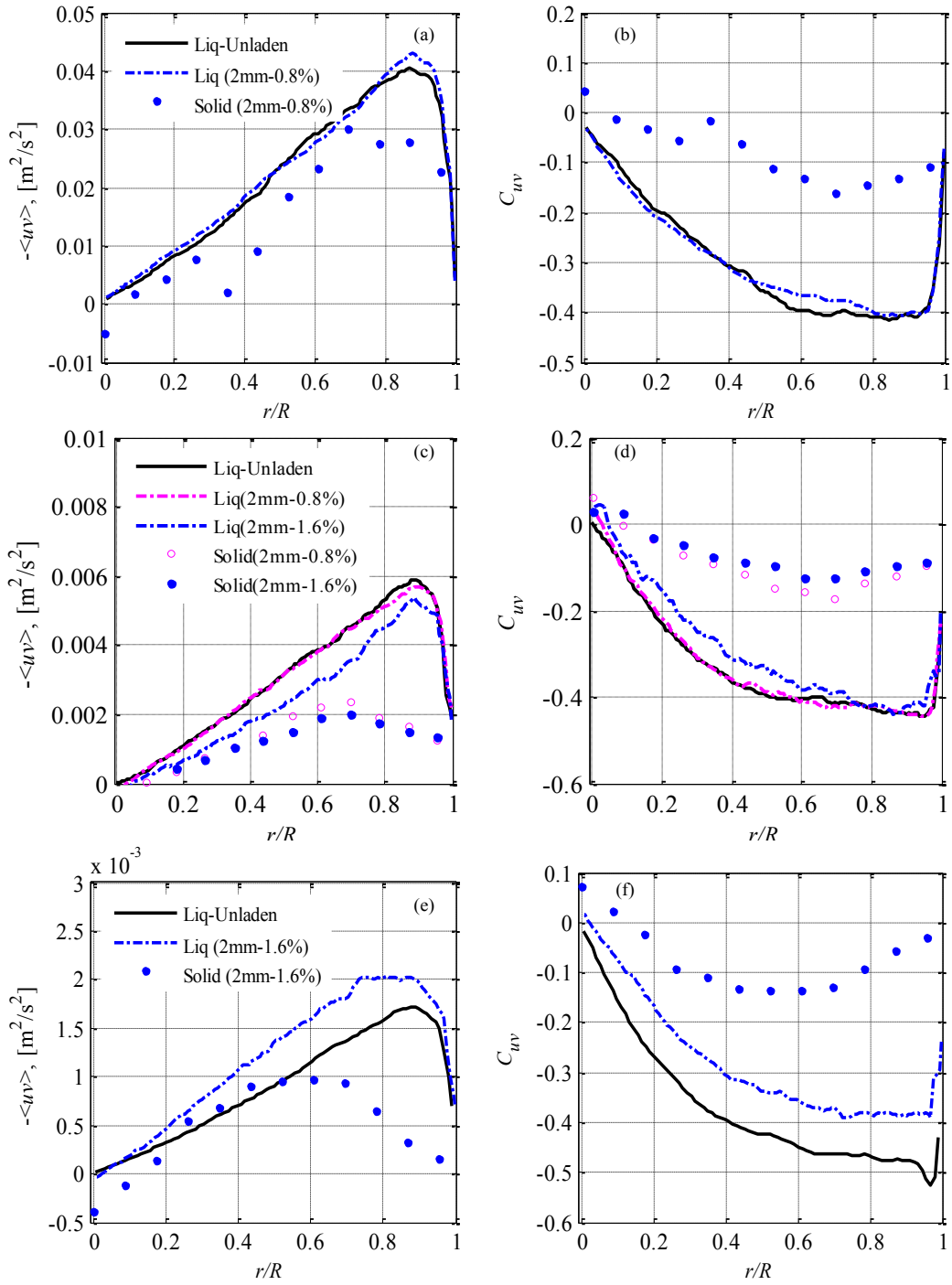


Figure 5-5. $\langle uv \rangle$ correlation and C_{uv} of liquid and solid particles over pipe cross section. The legends of the plot on the right side are the same as the left one

Very interesting results were obtained for the particle-laden flows at $Re = 52\ 000$ and $Re = 100\ 000$ (with $\phi_v=1.6\%$). We consider first the changes in liquid phase C_{uv} at these conditions. The reduction in liquid phase C_{uv} is observed at both conditions, meaning that the particles have influenced the liquid phase turbulence and some portion of liquid phase turbulent structures is produced by the presence of particles. These structures do not follow the sweep and ejection pattern of the liquid phase and thus the correlation C_{uv} is weakened (Caraman et al., 2003; Shokri et al., 2016a). On the other hand, the particle effect on $-\langle uv \rangle$ is different for these two conditions, i.e. it depends on Re . At $Re = 100\ 000$, the particles cause a decrease in $-\langle uv \rangle$ profile of the liquid phase over the pipe cross section whereas they increase the liquid phase Reynolds shear stresses at $Re = 52\ 000$. The increase in Reynolds shear stresses at $Re = 52\ 000$ can be attributed to the fact that both streamwise and radial fluctuation velocities are significantly augmented at this Re . However the decrease in $-\langle uv \rangle$ profile over the cross section at $Re = 100\ 000$ is more difficult to explain since axial turbulence augmentation and radial turbulence attenuation are simultaneously observed at this condition. The reduction of $-\langle uv \rangle$ at $Re = 100,000$ can be attributed to the fact that the axial augmentation cannot compensate for the combined effect of the radial turbulence attenuation and weakened liquid phase correlation (lower C_{uv}).

Also Fig.5-5 also shows that the Reynolds shear stresses $-\langle uv \rangle$ of the particulate phase are generally almost equal to or smaller than those of the liquid phase, but that the particle $-\langle uv \rangle$ drastically increases as the Reynolds number increases. This is expected because the increase in Re is really an increase in the bulk velocity. However, C_{uv} profiles of 2mm particles do not vary much at all over the range of Re values tested here. Moreover, the

solid phase C_{uv} is much smaller than that of the liquid phase although the particles have much higher fluctuating velocities than the liquid phase, implying that the particle turbulence in the streamwise and radial directions is not well-correlated. In other words, these large particles are not solely affected by the carrier phase turbulence. They are more likely to be affected by other non-correlating sources, such as lift forces and particle-particle interactions/collisions (Oliveira et al., 2015; Shokri et al., 2016a).

5.4 Discussion

In this section, the important parameters, contributing the particle turbulent fluctuations as well as the fluid turbulence modulation are discussed and finally new empirical correlations are proposed by quantifying the contribution of each parameter.

5.4.1 Turbulent fluctuations of particles

To the best of the authors' knowledge, there has not been any consolidating study in the literature so far which investigates all the important parameters affecting the particle fluctuations to propose a correlation for particulate phase turbulence. Therefore, the objective of this study is to collectively investigate all the influential parameters on the particle turbulence (such as Re , Re_p , St and ϕ_v) and illustrate the weight of each parameter using empiricism with the available experimental data in the literature. The first step is to employ a more general (non-dimensionalized) term for the turbulent statistics rather than the fluctuating velocities. Non-dimensionalization decreases the number of the parameters involved and also it can help to reduce the dependence on the scale and flow conditions among different data sets (scaling laws) (White, 2009). Turbulence intensity is typically

defined as the ratio of the turbulent fluctuating velocity to the bulk velocity. For instance, the axial turbulence intensity can be defined as $Ti_x = \langle u^2 \rangle^{0.5} / U_b$. It is well known that the fluid axial turbulence intensity at the pipe centerline is solely dependent upon Re and can be estimated using $Ti_x = 0.16Re^{-\frac{1}{8}}$ (Fluent, Release 16.0). The important question is if similar functionality can be proposed for the particles as well.

In order to understand the effect of different parameters on the particle turbulence intensity (particle turbulent fluctuating velocity scaled by the bulk velocity), these quantities at the pipe centerline are examined. The data from the present study are considered alongside other experimental data, which are listed in Table 5-2. Note that the experimental data in this work and the two other previous works from the authors (Shokri et al., 2016a, 2016b) are combined into one data set and it is called “EXP. Data” in Fig.5-6 to Fig.5-8. The employed data sets cover a broad range of Re from 4 200 to 320 000 as well as the particle size range of 0.2 mm to 2 mm, as seen in Table 5-2.

Table 5-2. Experimental data used in Figs.5-6 and 5-7.

Reference	Flow Orientation	d_p (mm)	Re
EXP. Data	Up	0.5, 1, 2	52 000, 100 000, 320000
(Kameyama et al., 2014)	Up/Down	0.625	19 500
(Kiger and Pan, 2002)	Horizontal	0.2	20 000
(Suzuki et al., 2000)	Down	0.4	5 200
Sato et al. (1995)	Down	0.34, 0.5	4 200

As mentioned earlier, the particle fluctuations in particle-laden flows can be function of flow parameters such as Re , Re_p , St , φ_v , and ρ_p / ρ_f (Shokri et al., 2016a). With using analogy of the fluid phase turbulence intensity, the particle turbulence intensity must be

function of Re and the functionality should be an inverse one. The other parameter affecting the particle turbulence is Re_p and, based on the data sets employed here, it can be observed that the particle turbulence intensity is directly proportional to Re_p . The other source of particle fluctuations is the carrier phase turbulence (Borée and Caraman, 2005; Caraman et al., 2003; Varaksin et al., 2000). The parameter which can specify the involvement of the particle with the fluid turbulence is the particle Stokes number. Since Gore and Crowe (1989) suggested that the particles mostly interact with the large (integral) scale turbulence, St_L is considered for this study. Since higher St_L implies lower contribution of the fluid turbulence to the particle turbulence, St_L is expected to be inversely related to the particle turbulence. Moreover, particle concentration (ϕ_v) can affect the particle fluctuations through the particle-particle interactions (Borée and Caraman, 2005; Caraman et al., 2003; Kussin and Sommerfeld, 2002). In order to incorporate the particle-particle interactions, a new parameter “collision Stokes number” (St_c) is proposed which is defined as $St_c = \tau_p / \tau_c$ where τ_c is the time between collisions and can be obtained by (Caraman et al., 2003):

$$\tau_c = \frac{1}{N_d \pi d_p^2 \sqrt{\left[\frac{16}{3\pi} \langle u_p^2 \rangle + 2 \langle v_p^2 \rangle \right]}} \quad (5-9)$$

where u_p and v_p are the particle fluctuating velocities in the axial and radial directions, respectively. The collision Stokes number represents the importance of particle-particle collisions on the particle motion through the fluid. Therefore, $St_c \ll 1$ means that the particle motion is not affected by the collisions while the particle motions are heavily influenced by collisions when $St_c \gg 1$. Shokri et al. (2015b) showed that the increase in the particle

concentration usually (but not always) led to no change or an increase in the particle turbulence. Because $\varphi_v \propto St_c$, consequently, St_c must also be directly related to the particle turbulence intensities. As mentioned earlier, another influential parameter for the particle turbulence is the density ratio (ρ_p / ρ_f). This ratio is ignored in this study mainly due to the close density ratio among the employed data sets. It is therefore possible to represent the particle turbulence intensity as a function of a parameter Ψ , which is defined as:

$$\Psi = 10^6 \times (Re_p^{0.75} \times St_c^{0.25} \times St_L^{-0.5}) / Re^{1.25} \quad (5-10)$$

The sign of each exponent was assigned based on the known or expected functionality, while the actual numeric value was obtained empirically using trial and error. The data available for the particle streamwise and radial turbulence intensity from this study and other studies summarized in Table 2 have been plotted against Ψ in Fig.5-6. As shown in Fig.5-6a, the axial particle turbulence intensity dramatically increases at larger values of Ψ (>100). Conversely, the turbulence intensity at low values of Ψ (<100), becomes almost constant. A similar trend is observed for the radial particle turbulence intensity (Fig.5-6b) except that the extent of change at larger values of Ψ (>100) is less dramatic than was observed for the axial particle turbulence intensity. In addition, the radial particle turbulence intensity data show more scatter and thus poor fit with Ψ than the axial data. The scatter in the radial particle turbulence intensities are most likely attributed to the greater experimental uncertainties associated with radial turbulence measurements (Varaksin et al., 2000). As shown in Fig.5-6, it is possible to relate the particle turbulence intensity to Ψ using empirical correlation:

$$Ti_{xp} = 0.052 \exp(0.0035\Psi) \quad (5-11)$$

$$Ti_{rp} = 0.0416 \exp(0.0025\Psi) \quad (5-12)$$

As shown in Fig.5-6, the proposed correlations fit the available experimental data reasonably well. However, it must be noted that these correlations were developed for dilute solid-liquid flows and should not be expected to provide good predictions outside of the range of values of Re_p , Re , St_L and St_c used to produce the correlations. Moreover, two data points of the present study substantially deviate from the proposed correlation in the radial direction. This can be attributed to the peculiarities related to the corresponding test conditions. These data points are: $(\Psi, Ti_{rp}) = (12, 0.057)$ and $(\Psi, Ti_{rp}) = (20, 0.079)$ as shown in Fig.5-6b. The former corresponds to a test with 0.5 mm particles with $\phi_v=0.05\%$ and $Re=100\ 000$ which falls in the category of two-way coupling flows. This can be viewed as the primary cause for the deviation when one realizes that remainder of the data is in the 4-way coupling region ($\phi_v \geq 0.1\%$). The latter data point corresponds to the 2 mm particles with $\phi_v=1.6\%$ and $Re=52\ 000$ in which the particles have strong interactions with the sweep and ejection motions of the carrier phase turbulence. The deviation here might be attributed to the fact that the proposed correlation fails to correctly incorporate the aforementioned phenomenon in the radial direction.

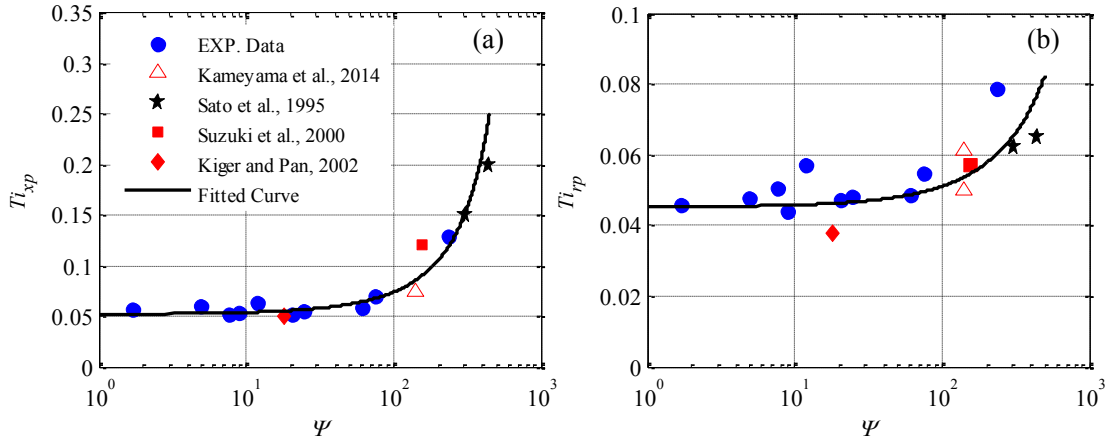


Figure 5-6. $\langle uv \rangle$ correlation Streamwise turbulence intensity and (b) radial turbulence intensity of particles vs Ψ' . The legend applies to both graphs.

During the development of the empirical correlation above, we realized that the largest variations in particle turbulence intensities were caused by Re and Re_p . Therefore, particle turbulent intensities are plotted against only Re and Re_p , i.e. $\Psi' = Re_p^{0.75} \times Re^{-1.25} \times 10^6$ in Fig.5-7. The graphs show that these parameters can present some functionality with the particle turbulent intensities especially in axial direction. It implies that the Re_p and Re are the far more important parameters contributing to the particle turbulence intensities than the other two (St_L and St_c).

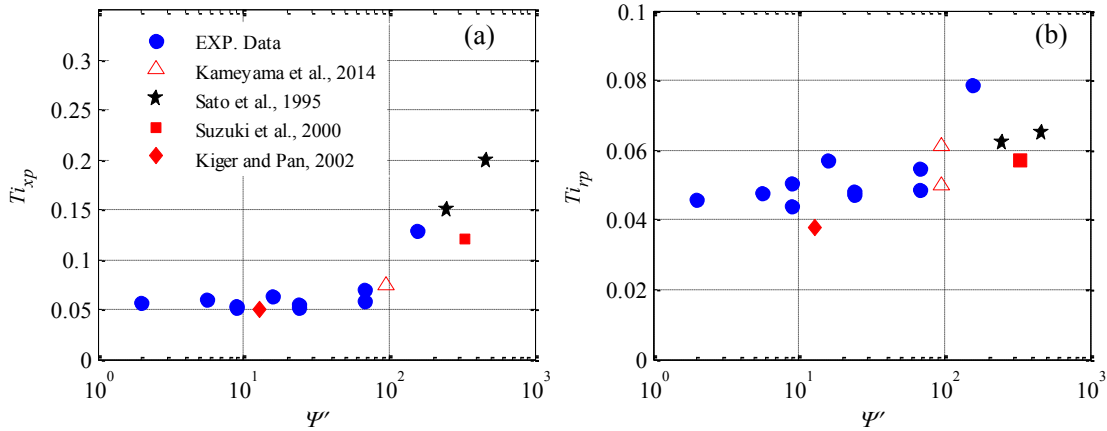


Figure 5-7. Streamwise turbulence intensity (Ti_{xp}) and (b) radial turbulence intensity (Ti_{rp}) of particles vs. Ψ and fitted curves. The legend applies to both plots.

5.4.2 Turbulence modulation of the liquid phase

As mentioned earlier, Gore and Crowe (1989) and Hetsroni (1989) criteria are the two most well-known criteria for classifying the augmentation or attenuation of the fluid turbulence due to presence of particles. Since $d_p/l_e = 0.4$ and $Re_p = 607$, both criteria suggest that the 2mm particles in the experimented conditions must strongly augment the fluid turbulence which is not accurate. This shows that they cannot predict the onset of the augmentation very well. Moreover, they are totally incapable of predicting the magnitude of the change in fluid turbulence. The results show that the magnitude of change greatly varies from no change to 100% augmentation of the axial liquid turbulence depending on Re . Since the particles used in this investigation are large particles which may end up causing the augmentation therefore, the effort is aimed to find the important parameters affecting the turbulence augmentation and quantifying its magnitude. Moreover if the inception of

augmentation is well predicted then the suggested correlation can be regarded as a criterion to classify the augmentation and attenuation/no-modulation phenomena.

The turbulence modulation can be function of particulate flow parameters such as Re , Re_p , d_p/l_e , φ_v , and ρ_p/ρ_f (Gore and Crowe, 1991). As shown in Fig.5-2b, the ratio of the slip velocity to the fluid velocity (U_s/U_f) increases as Re decreases. Moreover, Fig.5-4 illustrates that the axial turbulence augmentation of the carrier phase is reduced as Re decreases. By approximating the slip velocity with the particle terminal velocity (V_t), therefore, the carrier phase turbulence augmentation is found to be a direct function of V_t/U_b as postulated by Shokri et al. (2015a). The parameters V_t and U_b can be represented with their corresponding non-dimensional numbers i.e. Re_p and Re , respectively. Hence, the functionality becomes $M_x \propto Re_p/Re$. In other words, it is expected that the Re_p have a direct impact on the turbulence augmentation which agrees with the interpretation of the turbulence modulation given by Hetsroni (1989). In addition, the functionality suggests that Re has an inverse relationship with the M_x which is aligned with the results of the present experimental study. As suggested by Gore and Crowe (1989), d_p/l_e should have a direct relationship with the turbulence augmentation. Moreover, the literature shows that the increase in the large particle concentration (φ_v) leads to higher carrier phase turbulence augmentation in axial direction (Shokri et al., 2016b). In order to incorporate the particle concentration in a scaled term rather than the exact value, the interspacing ratio (λ/d_p), proposed by Kenning and Crowe (1997) was employed. The interspacing ratio can be calculated by $\{\lambda/d_p = [\pi/(6\varphi_v)]^{1/3} - 1\}$ (Kenning and Crowe, 1997). Since $\varphi_v \propto (\lambda/d_p)^{-1}$, the interspacing ratio is expected to have an inverse relationship with M_x . Elghobashi (1994)

proposed that the particles with larger St_L are most likely to augment the carrier phase turbulence. Therefore, a direct functionality is expected i.e. $M_x \propto St_L$. Finally, the density ratio becomes a very important parameter in this study due to the vast difference between liquid and gas particle-laden flows. The ultimate parameter (χ) can be reached as following:

$$\chi = 10^{11} \times St_l^{0.15} \times \left(\frac{Re_p^{0.75}}{Re^{2.75}} \right) \left(\frac{d_p}{l_e} \right) \left(\frac{\rho_p}{\rho_f} \right)^7 \left(\frac{\rho_f}{\rho_w} \right)^{-5.4} \left(\frac{\lambda}{d_p} \right)^{-3} \quad (5-13)$$

where ρ_w is the water density. Although the numeric values of the exponents were obtained using trial and error, the signs completely agree with the known or expected functionality. The experimental data of the mean axial turbulence modulations (\bar{M}_x) from present study along with other data from previous work for both gas-solid and liquid-solid channel/pipe flows (see Table 5-3) are plotted against the $\log(\chi)$ in Fig.5-8.

Table 5-3. Experimental data used in Fig.5-8

Reference	Carrier phase	Flow Orientation	d_p (mm)	Re
Varaksin et al. (2000)	Gas	Down	0.05	13 000
Tsuji et al. (1984)	Gas	Up	0.2, 0.5, 1, 3	22 000
Lee and Durst (1982)	Gas	Up	0.8	13 000
(Tsuji and Morikawa, 1982)	Gas	Horizontal	3.4	20 000, 40 000
EXP. Data	Liquid	Up	0.5, 1, 2	52 000, 100 000, 320000
(Kameyama et al., 2014)	Liquid	Up/Down	0.625	19 500
(Hosokawa and Tomiyama, 2004)	Liquid	Up	1, 2.5, 4	15 000
Sato et al. (1995)	Liquid	Down	0.34, 0.5	4 200
Zisselmar and Molerus (1979)	Liquid	Horizontal	0.053	100 000

The results show that if $\log(\chi) > 0$ (or $\chi > 1$) then the axial turbulence augmentation occurs and the magnitude of the augmentation is directly related to the $\log(\chi)$. By fitting a linear regression, one can obtain following linear correlation:

$$\bar{M}_x = 19.5 \log(\chi)$$

(5-14)

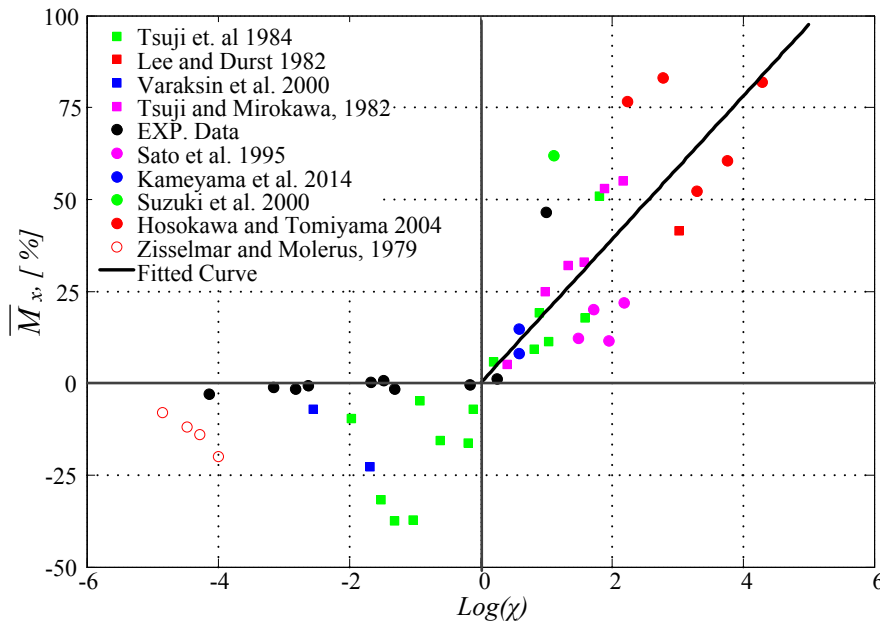


Figure 5-8. Mean streamwise turbulence modulation (\bar{M}_x) vs $\log(\chi)$ and proposed correlation

The above equation can predict well the onset of the turbulence augmentation as well as its magnitude. This is a great advancement from the existing criteria which are unable to provide any estimation for either the onset or the magnitude of turbulence augmentation. Moreover, this correlation can be used as a criterion to classify the carrier phase turbulence augmentation/attenuation.

5.5 Conclusion

In order to study the Re effect on the turbulent motions of particles and carrier phase, a comprehensive experimental investigation has been performed in an upward dilute particulate liquid flow at Reynolds numbers of 52 000, 100 000 and 320 000. Measurements

of mean and fluctuating velocities of water and 2 mm glass beads with concentration of 0.8 and 1.6 vol% are done by using a combined PIV/PTV technique.

Results show that particles lag behind the liquid phase at the centerline. The particle and liquid phase mean velocity profiles intercept at the near wall region. However, the “crossing point” shifted towards the wall as Re decreased. Particles tend to accumulate in the center of the pipe at high Re ($Re=320\ 000$). However, a peak in concentration appears near the wall at $Re =100\ 000$ which grows larger by further lowering the Re to 52 000.

Magnitude of the axial turbulence augmentation of the liquid phase by 2mm particles was decreased by an increase in Re . Also the radial turbulence modulation was different (less) than that of the axial direction except for the cases that no modulation occurs in either direction. Overall, the results showed that the particles are likely to have greater impact on the fluid turbulence statistics ($\langle u^2 \rangle$, $\langle v^2 \rangle$, $\langle uv \rangle$ and C_{uv}) at lower Re . On the other hand, the Reynolds stresses ($\langle u^2 \rangle$, $\langle v^2 \rangle$ and $\langle uv \rangle$) of the particulate phase were drastically enhanced as Re increased, while the Re impact on the particle C_{uv} was insignificant.

Finally two studies were performed to quantify the contribution of influential parameters to the particle turbulence intensities and axial fluid turbulence modulation and propose two novel empirical correlations for the aforementioned parameters. First, a novel correlation is empirically developed for estimating the particle turbulence intensity at the pipe centerline for solid-liquid flows. The particle turbulence intensity was found to be a function of $(Re_p^{0.75} \times St_c^{0.25} \times St_L^{-0.5} \times Re^{-1.25})$. The particle turbulence intensities also illustrated an acceptable functionality with $(Re_p^{0.75} \times Re^{-1.25})$, implying that Re and Re_p has far

more weight in the particle turbulence intensities than the other two parameters. In addition, a new empirical expression (χ) is proposed for the axial turbulence augmentation of the carrier phase using all the influential parameters. It is shown that the axial turbulence augmentation of the carrier phase for both solid-liquid and solid-gas flows is directly related to the $\log(\chi)$. Moreover, the new correlation predicts that the onset of the augmentation occurs when the $\log(\chi) = 0$ (or $\chi=1$). The aforementioned correlation can also be used to classify the axial fluid turbulence augmentation/attenuation.

6 Conclusion and Future Work

6.1 General Conclusion

Turbulent motions of solid particles and the surrounding liquid phase have been investigated in an upward pipe flow using dilute mixtures of water and glass beads. The glass beads had diameters of 0.5, 1 and 2mm and volumetric concentrations ranging from 0.05 to 1.6% were tested. Experiments were performed at three different Re (52 000, 100 000 and 320 000). The measurements were made by employing a combined PIV/PTV technique.

Measurements showed that the relatively large particles tested here lagged behind the liquid phase in the core of the flow. The slip velocity between the particles and the liquid phase at the pipe centerline was almost equal to the terminal velocity of the corresponding particle. Due to the “slip boundary” condition for the particles (contrary to the “no-slip” boundary condition for the liquid phase) at the wall as well as the long response time of those particles to the surrounding liquid phase, the particles typically had a higher velocity than the liquid phase in the near-wall region. Consequently, the liquid phase and particle mean velocity profiles inevitably intercept at a “crossing point”, the location of was independent of particle size but shifted towards the wall as the flow Re decreased. The crossing point for 2 mm particles was located at $r/R=0.85$ for $Re = 320\ 000$, $r/R=0.96$ for $Re = 100\ 000$ and no crossing point was observed for $Re = 52\ 000$. This is most likely

attributable to the lower Stokes' number in the near-wall region at the lower Re value. This implies that the particles become more responsive to the liquid phase in the near-wall region as the Re decreases.

The concentration profiles of 0.5 and 1 mm particles showed an almost flat distribution over most of the cross section of the pipe, with a sharp decline in the near-wall region at high Re . The concentration profiles for 2 mm particles had different shapes: they were linearly increasing from wall towards the center of the pipe. The low concentration of particles near the wall can be attributed primarily to the lift force which pushes the particles away from the wall. The linear profile of 2 mm particles was attributed to the larger lift force due to their larger size. At $Re = 100\ 000$, a local peak appeared in the concentration profiles of the 2 mm particles at $r/R=0.8$. This local peak grew larger and shifted towards the wall at $Re = 52\ 000$. The local peak for these large particles was attributed to the higher interactions of these particles with fluid turbulence at lower Re in the near-wall region. Finally, it can be concluded that the particle concentration profiles are affected significantly by particle size and Re for the conditions tested here.

Turbulence modulation of the liquid phase, caused by the particulate phase, was strongly dependent on both the particle size and the Reynolds number. The 2 mm particles produced significant augmentation of the liquid-phase axial turbulence at low Re (52 000). The magnitude of the augmentation reduced as the Re increased. Generally, the carrier phase turbulence modulation in the radial direction was observed to be less than that observed for the axial direction. The existing criteria for prediction of augmentation/attenuation, such as

those of Hetsroni (1989), Gore and Crowe (1989) and Tanaka and Eaton (2008), were not particularly successful in classifying the type of modulation in either the axial or radial directions. The results showed that the turbulence augmentation was directly related to the ratio of the terminal velocity to the bulk velocity (V_t/U_b). Finally, a new empirical correlation was proposed for the axial-direction, carrier-phase (liquid or solid) turbulence augmentation, and was shown to be directly related to $\log(\chi)$ where

$$\chi = 10^{11} \times St_t^{0.15} \times \left(\frac{Re_p^{0.75}}{Re^{2.75}} \right) \left(\frac{d_p}{l_e} \right) \left(\frac{\rho_p}{\rho_f} \right)^7 \left(\frac{\rho_f}{\rho_w} \right)^{-5.4} \left(\frac{\lambda}{d_p} \right)^{-3}.$$

Also the new correlation predicts that the onset of the augmentation occurs when the $\log(\chi)=0$ (or $\chi=1$).

It was also shown that the particles had higher fluctuating velocities than those of the liquid phase in both the radial and axial directions. In order to investigate the important parameters affecting particulate-phase turbulence, their fluctuating velocities were scaled with the bulk velocity (U_b) so that the particle turbulence intensity could be evaluated. Values of particle turbulence intensity were generally greater for the larger particles than for the smaller ones. Moreover, particle turbulence intensity was significantly increased at the low Reynolds number ($Re=52\ 000$) tested here. The results of the present work were combined with other available experimental data in the literature to show that the particle turbulence intensity is mainly proportional to $Re_p^{0.75}/Re^{1.25}$. Finally, a novel correlation is proposed for estimating the particle turbulence intensity at the pipe centerline for solid-

liquid flows. The particle turbulence intensity of was found to be function of Ψ , where $\Psi=10^6 \times (Re_p^{0.75} \times St_c^{0.25} \times St_L^{-0.5}) / Re^{1.25}$.

The shear Reynolds stresses ($\langle uv \rangle$) of both the liquid and solid phases were enhanced as Re increased simply due to the higher bulk velocity and Re . The results showed that the particle concentration effect on both $\langle uv \rangle$ and the correlating coefficient C_{uv} of the liquid phase was greater at lower Re . In addition, shear Reynolds stresses ($\langle uv \rangle$) of the particles were decreased by increasing the size of particle. The 2 mm particles always had lower shear Reynolds stresses than the liquid phase, which is interesting since their fluctuations in both the axial and radial directions were generally greater than those of the liquid phase. This was attributed to the weaker correlation between u and v (C_{uv}) for the 2 mm particles. The correlation C_{uv} showed that the particle fluctuating velocities are always less correlated than they are for the liquid phase. This was attributed to the fact that the particles can be also affected by non-correlating forces, e.g. particle-particle interactions and lift forces. Moreover, the particle C_{uv} was observed to be significantly affected by the particle size while changes in the flow Re produced an insignificant effect.

6.2 Novel contributions

New experimental data sets are provided

Comprehensive experimental investigations were carried out to provide new experimental data sets. These measurements, especially those obtained at high Re , which were first of their kind reported in the literature, improve the current level of knowledge

about particle-fluid interactions. These experimental data are expected to be extremely beneficial to evaluate/improve existing particle-laden turbulent flow models.

A novel functionality is proposed for the particle turbulence intensity

Based on the key dimensionless parameters, a novel functionality was proposed for predicting the particle turbulence intensity behaviour at the pipe centerline for solid-liquid flows. In the development of this correlation, the data from the present study were evaluated in combination with other results taken from the literature. The new correlation illustrates the weight of each important parameter has in affecting particle turbulence. Both the combination of the existing data and the correlation itself are novel.

A novel correlation for predicting the carrier phase turbulence augmentation

A novel empirical correlation was proposed to estimate the magnitude of the carrier-phase axial turbulence augmentation which is applicable for both gas and liquid flows. This new correlation accurately predicts the onset of turbulence modulation (in the axial direction only). Consequently, it can be also used as a criterion for classifying the carrier phase turbulence modulation in the axial direction. In addition, the new correlation can be beneficial for understanding the phenomena in which turbulence modulation is important, such as oil sands lump ablation rate in oil sands hydrotransport pipelines and pipe wear rate.

6.3 Recommendations for future work

A study such as this is able to cover only some of the research that is necessary because of time constraints as well as unexpected physical and technical

limitations/challenges. Therefore, additional studies must be done to complement the results of the present study. In this section, some recommendations for future work in this field are presented. These recommendations can be placed into three categories:

- I. PIV/PTV measurements
- II. Expanding the matrix of experiments
- III. Correlations and models

Each category is discussed in the following subsections.

6.3.1 PIV/PTV measurements

The main challenge in the present study was the quality of the measurements made near the wall ($r/R > 0.9$). Near-wall measurements in wall-bounded turbulent flows are always of great interest simply due to the fact that important turbulent phenomena, like sweep and ejection motions, occur in this region. In the present study, the low camera resolution and curvature of the pipe wall reduced the resolution of the near-wall measurements. One way to tackle this problem is to use a liquid and pipe whose refractive indices are identical, e.g. water and Teflon pipe (Toonder and Nieuwstadt, 1997). Another method is to employ a separate camera targeting only the near-wall region. The camera must be carefully calibrated to eliminate the image distortion caused by the pipe wall curvature.

The other limitation of this work was higher uncertainties in the PTV measurements at $r/R = 0.96$, especially for the 2 mm particles, simply due to the very low particle concentration in this region.. A simple solution would be to acquire many more images

(maybe about 100 000 images versus 20 000 images taken in the present study). Also, this can help increase the PTV measurement resolution. For example the PTV resolution in the radial direction can be increased from 12 points (2.1 mm wide) to a much higher number. Of course, the large number of images makes the process extremely costly in terms of time needed for image processing.

The present study showed that the effects of Re and particle concentration on both the particle and fluid turbulence in the axial direction differed from those of the radial direction. By implication, azimuthal turbulence measurements in particle-laden flows must disclose new information as well. The available 3D measurements in particle-laden turbulent flows are currently very scarce. Therefore, new 3D PIV/PTV measurements in this field are highly recommended.

6.3.2 Expanding the matrix of experiments

Nearly all experimental studies of particle-laden flows are limited to low particle concentrations ($\varphi_v \leq 2\%$). Based on the effects of particle concentration on the fluid and particle turbulence statistics shown here, experimental investigations at much higher concentrations are recommended. However, standard PIV measurements are not applicable since the system becomes opaque at high concentrations. The solution is to use the refractive index matched mixture of liquid and particles such as Plexiglass and p-Cymene. In this method, the particles become invisible and PIV cameras captures only the flow tracers. For more information about the possible refractive index matched mixtures see, for example,

Hassan and Dominguez-Ontiveros (2008), Haam et al. (2000), Cui and Adrian (1997), and Budwig (1994).

The present study is the only work done on the effects of particle concentration on particulate phase turbulence. Two different particle concentrations for each particle diameter were studied and the results showed that increasing the particle concentration had mixed effects (i.e. both attenuation and augmentation) on the particle turbulence. Due to the limited information available and the complicated effects of particle concentration, they are still not well understood. Therefore, it is highly recommended to conduct experimental investigations over a much broader range of particle concentrations.

6.3.3 Correlations and models

A novel correlation for particle turbulence intensity in solid-liquid flows was obtained using the data from this study and the relevant experimental data available in the literature. This study represents the first attempt at the subject and, without a doubt, is far from perfect. The correlation still needs more development using much more experimental data. Also, the correlation can be further developed to cover gas-solid turbulent flows. Moreover, departing from empiricism and developing some mechanistic models to describe particle turbulence at high Reynolds numbers represents a very interesting subject for future work.

A new empirical correlation was proposed in this project which can predict the onset and magnitude of the carrier phase turbulence augmentation in the axial direction. Clearly, one of the recommendations is to perform such study for carrier phase turbulence

attenuation. It has been clearly demonstrated here that carrier phase turbulence modulation in the radial direction greatly differs from that in the axial direction. Yet, all available criteria for classifying the carrier phase turbulence modulation are restricted to the axial direction. Therefore, any attempt to expand/develop correlations for the radial direction would be extremely valuable.

Finally, the new experimental data sets can be used to evaluate and/or improve existing two-phase flow models. The first step is to simulate the experimental data provided here using existing modified $k-\varepsilon$ methods for particle-laden flows (see, for example, Mando and Yin, 2012; Yan et al., 2006; Lightstone and Hodgson, 2004; Chen and Wood, 1985). The next step can be to use more accurate numerical models such as Large Eddy Simulation (LES) to model the turbulent flows of the present study (see, for example, Vreman et al., 2009; Vreman, 2007).

References

- Adrian, R.J., 2005. Twenty years of particle image velocimetry. *Exp. Fluids* 39, 159–169.
doi:10.1007/s00348-005-0991-7
- Adrian, R.J., Westerweel, J., 2011. *Particle Image Velocimetry*. Cambridge University Press, New York.
- Akagawa, K., Fujii, T., Takenaka, N., Takagi, N., Hayashi, K., 1989. The effects of the density ratio in a vertically rising solid-liquid two-phase flow, in: *International Conference on Mechanics of Two-Phase Flows*. Taipei, Taiwan, pp. 203–208.
- Alajbegovic, A., Assad, A., Bonetto, F., Lahey Jr, R.T., 1994. Phase distribution and turbulence structure for solid/fluid upflow in a pipe. *Int. J. Multiph. Flow* 20, 453–479.
- Alberta Energy, 2015. *Alberta's energy reserves 2014 and supply/demand outlook 2015-2024*. Calgary, AB.
- Aliseda, A., Cartellier, A., Hainaux, F., Lasheras, J.C., 2002. Effect of preferential concentration on the settling velocity of heavy particles in homogeneous isotropic turbulence. *J. Fluid Mech.* 468, 77–105. doi:10.1017/S0022112002001593
- Alvandifar, N., Abkar, M., Mansoori, Z., Avval, M.S., Ahmadi, G., 2011. Turbulence

- modulation for gas – particle flow in vertical tube and horizontal channel using four-way Eulerian–Lagrangian approach. *Int. J. Heat Fluid Flow* 32, 826–833. doi:10.1016/j.ijheatfluidflow.2011.05.008
- ANSYS Inc, 2013. ANSYS Fluent: Theory guide 15317, 724–746.
- Armenio, V., Fiorotto, V., 2001. The importance of the forces acting on particles in turbulent flows. *Phys. Fluids* 13, 2437–2440. doi:10.1063/1.1385390
- Atherton, T.J., Kerbyson, D.J., 1999. Size invariant circle detection. *Image Vis. Comput.* 17, 795–803.
- Auton, T.R., 1987. The lift force on a spherical body in a rotational flow. *J. Fluid Mech.* 183, 199. doi:10.1017/S002211208700260X
- Baek, S.J., Lee, S.J., 1996. A new two-frame particle tracking algorithm using match probability. *Exp. Fluids* 22, 23–32. doi:10.1007/BF01893303
- Bagchi, P., Balachandar, S., 2003. Effect of turbulence on the drag and lift of a particle. *Phys. Fluids* 15, 3496. doi:10.1063/1.1616031
- Balachandar, S., Eaton, J.K., 2010. Turbulent dispersed multiphase flow. *Annu. Rev. Fluid Mech.* 42, 111–133. doi:10.1146/annurev.fluid.010908.165243
- Barnocky, G., Davis, R.H., 1989. The lubrication force between spherical drops, bubbles and rigid particles in a viscous fluid. *Int. J. Multiph. Flow* 15, 627–638. doi:10.1016/0301-9322(89)90057-8

- Bennett, S.J., Best, J.L., 1995. Mean flow and turbulence structure over fixed, two-dimensional dunes: Implications for sediment transport and bedform stability. *Sedimentology* 42, 491–513. doi:10.1111/j.1365-3091.1995.tb00386.x
- Bernards, P.S., Wallace, J.M., 2002. *Turbulent flow: Analysis, measurement, and prediction*. John Wiley & Sons Inc., Hobokon, New Jersey.
- Boemer, A., Qi, H., Renz, U., 1997. Eulerian simulation of bubble formation at a jet in a two-dimensional fluidized bed. *Int. J. Multiph. Flow* 23, 927–944. doi:10.1016/S0301-9322(97)00018-9
- Boivin, M., Simonin, O., Squires, K.D., 2000. On the prediction of gas-solid flows with two-way coupling using large eddy simulation. *Phys. Fluids* 12, 2080–2090. doi:10.1063/1.870453
- Borée, J., Caraman, N., 2005. Dilute bidispersed tube flow: Role of interclass collisions at increased loadings. *Phys. Fluids* 17, 055108–1–9. doi:10.1063/1.1897636
- Bröder, D., Sommerfeld, M., 2002. An advanced LIF-PLV system for analysing the hydrodynamics in a laboratory bubble column at higher void fractions. *Exp. Fluids* 33, 826–837. doi:10.1007/s00348-002-0502-z
- Budwig, R., 1994. Refractive index matching methods for liquid flow investigations. *Exp. Fluids* 17, 350–355. doi:10.1007/BF01874416
- Burns, A., Frank, T., Hamill, I., Shi, J., 2004. The Favre averaged drag model for turbulent

dispersion in Eulerian multi-phase flows, in: 5th International Conference on Multiphase Flow. Yokohama, Japan, pp. 1–17.

Caraman, N., Borée, J., Simonin, O., 2003. Effect of collisions on the dispersed phase fluctuation in a dilute tube flow: Experimental and theoretical analysis. *Phys. Fluids* 15, 3602–3612. doi:10.1063/1.1619136

Chen, C.P., Wood, P.E., 1985. A turbulence closure model for dilute gas-particle flows. *Can. J. Chem. Eng.* 63, 349–360.

Cowen, E.A., Monismith, S.G., 1997. A hybrid digital particle tracking velocimetry technique. *Exp. Fluids* 22, 199–211. doi:10.1007/s003480050038

Crawford, N.M., Cunningham, G., Spence, S.W.T., 2007. An experimental investigation into the pressure drop for turbulent flow in 90° elbow bends. *Proc. Inst. Mech. Eng. Part E J. Process Mech. Eng.* 221, 77–88. doi:10.1243/0954408JPME84

Crowe, C.T., 2000. On models for turbulence modulation in fluid-particle flows. *Int. J. Multiph. Flow* 26, 719–727.

Cui, M.M., Adrian, R.J., 1997. Refractive index matching and marking methods for highly concentrated solid-liquid flows. *Exp. Fluids* 22, 261–264.

Davies, E.R., 2012. *Computer & machine vision: Theory, algorithms, practicalities*, 4th ed. Elsevier.

De Jong, J.F., Dang, T.Y.N., Van Sint Annaland, M., Kuipers, J.A.M., 2012. Comparison of

- a discrete particle model and a two-fluid model to experiments of a fluidized bed with flat membranes. *Powder Technol.* 230, 93–105. doi:10.1016/j.powtec.2012.06.059
- Ding, J., Gidaspow, D., 1990. A bubbling fluidization model using kinetic theory of granular flow. *AIChE J.* 36, 523–538. doi:10.1002/aic.690360404
- Doron, P., Barnea, D., 1993. A three-layer model for solid-liquid flow in horizontal pipes. *Int. J. Multiph. Flow* 19, 1029–1043. doi:10.1016/0301-9322(93)90076-7
- Doron, P., Granica, D., Barnea, D., 1987. Slurry flow in horizontal pipes-experimental and modeling. *Int. J. Multiph. Flow* 13, 535–547. doi:10.1016/0301-9322(87)90020-6
- Doroodchi, E., Evans, G.M., Schwarz, M.P., Lane, G.L., Shah, N., Nguyen, a., 2008. Influence of turbulence intensity on particle drag coefficients. *Chem. Eng. J.* 135, 129–134. doi:10.1016/j.cej.2007.03.026
- Ekambara, K., Sanders, R.S., Nandakumar, K., Masliyah, J.H., 2009. Hydrodynamic simulation of horizontal slurry pipeline flow using ANSYS-CFX. *Ind. Eng. Chem. Res.* 48, 8159–8171. doi:10.1021/ie801505z
- Elghobashi, S., 1994. On predicting particle-laden turbulent flows. *Appl. Sci. Res.* 52, 309–329.
- Elghobashi, S., 1991. Particle-laden turbulent flows: Direct simulation and closure models. *Appl. Sci. Res.* 48, 301–314.
- Eswaran, V., 2002. *Turbulent flows: Fundamentals, experiments and modeling.* CRC Press,

Florida, USA.

Ferry, J., Balachandar, S., 2001. A fast Eulerian method for dispersive two-phase flow. *Int. J. Multiph. Flow* 27, 1199–1226.

Flow Master, 2007. Product-Manual for Davis 7.2.

Fujiwara, a., Danmoto, Y., Hishida, K., Maeda, M., 2004. Bubble deformation and flow structure measured by double shadow images and PIV/LIF. *Exp. Fluids* 36, 157–165.
doi:10.1007/s00348-003-0691-0

Furuta, T., Tsujimoto, S., Toshima, M., Okazaki, M., Toei, R., 1977. Concentration distribution of particles in solid-liquid two-phase flow through vertical pipe. *Mem. Fac. Eng. Kyoto Univ.*

Ghaemi, S., Rahimi, P., Nobes, D.S., 2010. Evaluation of digital image discretization error in droplet shape measurement using simulation. *Part. Part. Syst. Charact.* 26, 243–255.
doi:10.1002/ppsc.200900069

Ghaemi, S., Scarano, F., 2011. Counter-hairpin vortices in the turbulent wake of a sharp trailing edge. *J. Fluid Mech.* 689, 317–356. doi:10.1017/jfm.2011.431

Ghatage, S. V., Sathe, M.J., Doroodchi, E., Joshi, J.B., Evans, G.M., 2013. Effect of turbulence on particle and bubble slip velocity. *Chem. Eng. Sci.* 100, 120–136.
doi:10.1016/j.ces.2013.03.031

Gidaspow, D., 1994. *Multiphase flow and fluidization: Continuum and kinetic theory*

description. Academic Press, San Diego, CA.

Gillies, R.G., Schaan, J., Sumner, R.J., McKibben, M.J., Shook, C.A., 2000. Deposition velocities for newtonian slurries in turbulent flow. *Can. J. Chem. Eng.* 78, 704–708. doi:10.1002/cjce.5450780412

Gillies, R.G., Shook, C.A., 2000. Modelling high concentration slurry flows. *Can. J. Chem. Eng.* 78, 709–716.

Gillies, R.G., Shook, C.A., Xu, J., 2004. Modelling heterogeneous slurry flows at high velocities. *Can. J. Chem. Eng.* 82, 1060–1065.

Gore, A.R., Crowe, C.T., 1991. Modulation of turbulence by a dispersed phase. *J. Fluid Eng.* 113, 304–307.

Gore, A.R., Crowe, C.T., 1989. Effect of particle size on modulating turbulent intensity. *Int. J. Multiph. Flow* 15, 279–285.

Grace, J.R., Taghipour, F., 2004. Verification and validation of CFD models and dynamic similarity for fluidized beds. *Powder Technol.* 139, 99–110. doi:10.1016/j.powtec.2003.10.006

Haam, S.J., Brodkey, R.S., Fort, I., Klaboch, L., Placnik, M., Vanecek, V., 2000. Laser Doppler anemometry measurements in an index of refraction matched column in the presence of dispersed beads Part I. *Int. J. Multiph. Flow* 26, 1401–1418.

Hassan, Y. a., Dominguez-Ontiveros, E.E., 2008. Flow visualization in a pebble bed reactor

- experiment using PIV and refractive index matching techniques. *Nucl. Eng. Des.* 238, 3080–3085. doi:10.1016/j.nucengdes.2008.01.027
- Hetsroni, G., 1989. Particles-turbulence interaction. *Int. J. Multiph. Flow* 15, 735–746. doi:10.1016/0301-9322(89)90037-2
- Hinz, J.O., 1959. *Turbulence*. Mc Grew Hill Book Co., New York, USA.
- Hoomans, B.P.B., Kuipers, J.A.M., Briels, W.J., Van Swaaij, W.P.M., 1996. Discrete particle simulation of bubble and slug formation in a two-dimensional gas-fluidised bed: A hard-sphere approach. *Chem. Eng. Sci.* 51, 99–118. doi:10.1016/0009-2509(95)00271-5
- Hosokawa, S., Tomiyama, A., 2004. Turbulence modification in gas–liquid and solid–liquid dispersed two-phase pipe flows. *Int. J. Heat Fluid Flow* 25, 489–498. doi:10.1016/j.ijheatfluidflow.2004.02.001
- Hrenya, C.M., Bolio, E. j., Chakrabarti, D., Sinclair, J.L., 1995. Comparison of low Reynolds number k – ϵ turbulence models in predicting fully developed pipe flow. *Chem. Eng. Sci.* 50, 1923–1941. doi:10.1016/0009-2509(95)00035-4
- Huber, N., Sommerfeld, M., 1994. Characterization of the cross-sectional particle concentration distribution in pneumatic conveying systems. *Powder Technol.* 79, 191–210. doi:10.1016/0032-5910(94)02823-0
- Huilin, L., Gidaspow, D., 2003. Hydrodynamics of binary fluidization in a riser: CFD

simulation using two granular temperatures. *Chem. Eng. Sci.* 58, 3777–3792.
doi:10.1016/S0009-2509(03)00238-0

Hutchinson, P., Hewitt, G.F., Dukler, A.E., 1971. Deposition of liquid or solid dispersions from turbulent gas streams: a stochastic model. *Chem. Eng. Sci.* 26, 419–439.

Ishii, M., Mishima, K., 1984. Two-fluid model and hydrodynamic constitutive relations. *Nucl. Eng. Des.* 82, 107–126. doi:10.1016/0029-5493(84)90207-3

Jing, L., Zhao-Hui, L., Han-Feng, W., Sheng, C., Ya-Ming, L., Hai-Feng, H., Chu-Guang, Z., 2010. Turbulence modulations in the boundary layer of a horizontal particle-laden channel flow. *Chinese Phys. Lett.* 27, 064701. doi:10.1088/0256-307X/27/6/064701

Kähler, C.J., Scharnowski, S., Cierpka, C., 2012. On the uncertainty of digital PIV and PTV near walls. *Exp. Fluids* 52, 1641–1656. doi:10.1007/s00348-012-1307-3

Kameyama, K., Kanai, H., Kawashima, H., Ishima, T., 2014. Evaluation of particle motion in solid-liquid two-phase pipe flow with downward/upward flow directions, in: 17th International Symposium on Applications of Laser Techniques to Fluid Mechanics. pp. 1–15.

Kenning, V.M., Crowe, C.T., 1997. Brief communication on the effect of particles on carrier phase turbulence in gas-particle flows. *Int. J. Multiph. flow* 23, 403–408.

Kiger, K.T., Pan, C., 2002. Suspension and turbulence modification effects of solid particulates on a horizontal turbulent channel flow. *J. Turbul.* 3, N19.

doi:10.1088/1468-5248/3/1/019

Kim, J., Moin, P., Moser, R., 1987. Turbulence statistics in fully developed channel flow at low Reynolds number. *J. Fluid Mech.* 177, 133–166. doi:10.1017/S0022112087000892

Kim, S., Lee, K.B., Lee, C.G., 2005. Theoretical approach on the turbulence intensity of the carrier fluid in dilute two-phase flows. *Int. Commun. Heat Mass Transf.* 32, 435–444. doi:10.1016/j.icheatmasstransfer.2004.07.003

Kleinstreuer, C., 2003. Two-phase flow, Theory and applications. Taylor & Francis Books, Inc., New York.

Kolev, N.I., 2012. Multiphase Flow Dynamics 4: Turbulence, Gas Adsorption and Release, Diesel Fuel Properties. Springer Berlin Heidelberg, Berlin, Heidelberg. doi:10.1007/978-3-642-20749-5_2

Kosiwczuk, W., Cessou, A., Trinité, M., Lecordier, B., 2005. Simultaneous velocity field measurements in two-phase flows for turbulent mixing of sprays by means of two-phase PIV. *Exp. Fluids* 39, 895–908. doi:10.1007/s00348-005-0027-3

Kulick, J.D., Fessler, J.R., Eaton, J.K., 1994. Particle response and turbulence modification in fully developed channel flow. *J. Fluid Mech.* 277, 109–134. doi:10.1017/S0022112094002703

Kussin, J., Sommerfeld, M., 2002. Experimental studies on particle behaviour and turbulence modification in horizontal channel flow with different wall roughness. *Exp.*

Fluids 33, 143–159. doi:10.1007/s00348-002-0485-9

Lai, J.C.S., Yang, C.Y., 1997. Numerical simulation of turbulence suppression: Comparisons of the performance of four k-e turbulence models. *Int. J. Heat Fluid Flow* 18, 575–584. doi:10.1016/S0142-727X(97)00003-9

Lain, S., Sommerfeld, M., 2003. Turbulence modulation in dispersed two-phase flow laden with solids from a Lagrangian perspective. *Int. J. Heat Fluid Flow* 24, 616–625. doi:10.1016/S0142-727X(03)00055-9

Lee, M., Moser, R.D., 2015. Direct numerical simulation of turbulent channel flow up to $Re_T=5200$. *J. Fluid Mech.* 774, 395–415. doi:10.1017/jfm.2015.268

Lee, S.L., 1987. Particle drag in a dilute turbulent two-phase suspension flow. *Int. J. Multiph. Flow* 13, 247–256.

Lee, S.L., Durst, F., 1982. On the motion of particles in turbulent duct flows. *Int. J. Multiph. Flow* 8, 125–146.

Lightstone, M.F., Hodgson, S.M., 2004. Turbulence modulation in gas-particle flow: A comparison of selected models. *Can. J. Chem. Eng.* 82, 209–219.

Lindken, R., Merzkirch, W., 2002. A novel PIV technique for measurements in multi-phase flows and its application to two-phase bubbly flows. *Exp. Fluids* 33, 814–8. doi:10.1007/s00348-002-0500-1

Liu, D., Bu, C., Chen, X., 2013. Development and test of CFD-DEM model for complex

- geometry: A coupling algorithm for Fluent and DEM. *Comput. Chem. Eng.* 58, 260–268. doi:10.1016/j.compchemeng.2013.07.006
- Lu, S.S., Willmarth, W.W., 1973. Measurements of the structure of the Reynolds stress in a turbulent boundary layer. *J. Fluid Mech.* 60, 481. doi:10.1017/S0022112073000315
- Lucas, D., Krepper, E., Prasser, H.M., 2007. Use of models for lift, wall and turbulent dispersion forces acting on bubbles for poly-disperse flows. *Chem. Eng. Sci.* 62, 4146–4157. doi:10.1016/j.ces.2007.04.035
- Mandø, M., Lightstone, M.F., Rosendahl, L., Yin, C., Sørensen, H., 2009. Turbulence modulation in dilute particle-laden flow. *Int. J. Heat Fluid Flow* 30, 331–338. doi:10.1016/j.ijheatfluidflow.2008.12.005
- Mando, M., Yin, C., 2012. Euler–Lagrange simulation of gas–solid pipe flow with smooth and rough wall boundary conditions. *Powder Technol.* 225, 32–42. doi:10.1016/j.powtec.2012.03.029
- Marchioli, C., Giusti, A., Salvetti, M.V., Soldati, A., 2003. Direct numerical simulation of particle wall transfer and deposition in upward turbulent pipe flow. *Int. J. Multiph. Flow* 29, 1017–1038. doi:10.1016/S0301-9322(03)00036-3
- Marchioli, C., Picciotto, M., Soldati, A., 2007. Influence of gravity and lift on particle velocity statistics and transfer rates in turbulent vertical channel flow. *Int. J. Multiph. Flow* 33, 227–251. doi:10.1016/j.ijmultiphaseflow.2006.09.005

- Masliyah, J.H., 2009. Oil sands extraction and upgrading. Department of Chemicals and Materials Engineering, University of Alberta, Edmonton, AB, Canada.
- MATLAB Release R2013a, The MathWorks Inc. Natick, Massachusetts, USA.
- Maxey, M.R., Riley, J.J., 1983. Equation of motion for a small rigid sphere in a nonuniform flow. *Phys. Fluids* 26, 883. doi:10.1063/1.864230
- Messa, G. V., Malavasi, S., 2014. Numerical prediction of dispersed turbulent liquid–solid flows in vertical pipes. *J. Hydraul. Res.* 52, 684–692. doi:10.1080/00221686.2014.939110
- Milojevic, D., 1990. Lagrangian Stochastic-Deterministic (LSD) predictions of particle dispersion in turbulence. *Part. Part. Syst. Charact.* 7, 181–190.
- Moraga, F.J., Bonetto, F.J., Lahey, R.T., 1999. Lateral forces on spheres in turbulent uniform shear flow. *Int. J. Multiph. Flow* 25, 1321–1372. doi:10.1016/S0301-9322(99)00045-2
- Mostafa, A.A., Mongia, H.C., 1988. On the interaction of particles and turbulent fluid flow. *Int. Commun. Heat Mass Transf.* 31, 2063–2075.
- Muste, M., Fujita, I., Kruger, a., 1998. Experimental comparison of two laser-based velocimeters for flows with alluvial sand. *Exp. Fluids* 24, 273–284. doi:10.1007/s003480050174
- Muste, M., Yu, K., Fujita, I., Ettema, R., 2008. Two-phase flow insights into open-channel

flows with suspended particles of different densities. *Environ. Fluid Mech.* 9, 161–186.
doi:10.1007/s10652-008-9102-7

Nezu, I., Asce, M., Azuma, R., 2004. Turbulence characteristics and interaction between particles and fluid in particle-laden open channel flows. *J. Hydraul. Eng.* 130, 988–1002. doi:10.1061/(ASCE)0733-9429(2004)130

Noguchi, K., Nezu, I., 2009. Particle–turbulence interaction and local particle concentration in sediment-laden open-channel flows. *J. Hydro-environment Res.* 3, 54–68.
doi:10.1016/j.jher.2009.07.001

Oliveira, J.L.G., van der Geld, C.W.M., Kuerten, J.G.M., 2015. Lagrangian velocity and acceleration statistics of fluid and inertial particles measured in pipe flow with 3D particle tracking velocimetry. *Int. J. Multiph. Flow* 73, 97–107.
doi:10.1016/j.ijmultiphaseflow.2015.03.017

Pang, M., Wei, J., Yu, B., 2011a. Numerical investigation of phase distribution and liquid turbulence modulation in dilute particle-laden Flow. *Part. Sci. Technol.* 29, 554–576.
doi:10.1080/02726351.2010.536304

Pang, M., Wei, J., Yu, B., 2011b. Numerical Investigation of Phase Distribution and Liquid Turbulence Modulation in Dilute Particle-Laden Flow. *Part. Sci. Technol.* 29, 554–576.
doi:10.1080/02726351.2010.536304

Pope, S.B., 2006. *Turbulent flows*. Cambridge University Press, New York.

- Quenot, G., Rambert, A., Lusseyran, F., Gougat, P., 2001. Simple and accurate PIV camera calibration using a single target image and camera focal length, in: 4th International Symposium on Particle Image Velocimetry. Gottingen, Germany, pp. 1–10.
- Raffel, M., Willert, C.E., Wereley, S.T., Kompenhans, J., 2007. Particle Image Velocimetry, 2nd ed. Springer, Heidelberg, Germany.
- Sabot, J., Comte-Bellot, G., 1976. Intermittency of coherent structures in the core region of fully developed turbulent pipe flow. *J. Fluid Mech.* 74, 767–796.
- Santiago, J.G., Wereley, S.T., Meinhart, C.D., Beebe, D.J., Adrian, R.J., 1998. A particle image velocimetry system for microfluidics. *Exp. Fluids* 25, 316–319. doi:10.1007/s003480050235
- Sathe, M.J., Thaker, I.H., Strand, T.E., Joshi, J.B., 2010. Advanced PIV/LIF and shadowgraphy system to visualize flow structure in two-phase bubbly flows. *Chem. Eng. Sci.* 65, 2431–2442. doi:10.1016/j.ces.2009.11.014
- Sato, Y., Fukuichi, U., Hishida, K., 2000. Effect of inter-particle spacing on turbulence modulation by Lagrangian PIV. *Int. J. Heat Fluid Flow* 21, 554–561.
- Sato, Y., Hanzawa, A., Hishida, K., Maeda, M., 1995. Interaction between particle wake and turbulence in a water channel flow (PIV measurements and modelling for turbulence modification), in: Serizawa, A., Fukano, T., Bataille, J. (Eds.), *Advances in Multiphase Flow*.

- Sato, Y., Hishida, K., 1996. Transport process of turbulence energy in particle-laden turbulent flow. *Int. J. Heat Fluid Flow* 17, 202–210.
- Schlichting, H., 1979. *Boundary layer theory*, 7th ed. Mc Grew Hill Co., New York, USA.
- Schultz, M.P., Flack, K. a., 2013. Reynolds-number scaling of turbulent channel flow. *Phys. Fluids* 25. doi:10.1063/1.4791606
- Shams, E., Finn, J., Apte, S. V, 2010. A Numerical Scheme for Euler-Lagrange Simulation of Bubbly Flows in Complex Systems. *Int. J. Numer. Methods Fluids* 0001406106, 1–41.
- Shokri, R., 2016. Experimental investigation on the turbulence in the particle-laden liquid flows. University of Alberta.
- Shokri, R., Ghaemi, S., Nobes, D.S., Sanders, R.S., 2016a. High-Reynolds-number experimental investigation of particle-laden turbulent pipe flow using PIV/PTV technique. *Int. J. Multiph. Flow*.
- Shokri, R., Ghaemi, S., Nobes, D.S., Sanders, R.S., 2016b. Experimental investigation of fluid-particle interactions in vertical pipe flow of a liquid-continuous suspension. *Int. J. Heat Fluid Flow*.
- Shook, C.A., Gillies, R.G., Sanders, R.S., 2002. *Pipeline hydrotransport: With applications in the oil sand industry*. SRC Publication, Saskatoon, SK.
- Shook, C.A., McKibben, M., Small, M., 1990. Experimental investigation of some

- hydrodynamic factors affecting slurry pipeline wall erosion. *Can. J. Chem. Eng.* 68, 17–23. doi:10.1002/cjce.5450680102
- Sivakumar, S., Chidambaram, M., Shankar, H.S., 1988. On the effect of particle size on heat transfer in vertical upflow of gas-solids suspension. *Can. J. Chem. Eng.* 66, 1000–1004.
- Smits, A.J., McKeon, B.J., Marusic, I., 2011. High-Reynolds number wall turbulence. *Annu. Rev. Fluid Mech.* 43, 353–375. doi:10.1146/annurev-fluid-122109-160753
- Sommerfeld, M., 1992. Modelling of particle-wall collisions in confined gas-particle flows. *Int. J. Multiph. Flow* 18, 905–926. doi:10.1016/0301-9322(92)90067-Q
- Sommerfeld, M., Huber, N., 1999. Experimental analysis of modelling of particle-wall collisions. *Int. J. Multiph. Flow* 25, 1457–1489. doi:10.1016/S0301-9322(99)00047-6
- Spelay, R.B., Gillies, R.G., Hashemi, S.A., Sanders, R.S., 2015. Effect of pipe inclination on deposition velocity of settling slurries. *Can. J. Chem. Eng.*
- Spelay, R.B., Hashemi, S.A., Gillies, R.G., Gillies, D.P., Hegde, R., Sanders, R.S., 2013. Governing friction loss mechanisms and the importance of off-line characterization tests in the pipeline transport of dense coarse-particle slurries, in: *ASME 2013 Fluids Engineering Summer Meeting (FEDSM2013)*. Incline Village, NV, USA, pp. V01CT20A013–019. doi:10.1115/FEDSM2013-16464
- Stanislas, M., Perret, L., Foucaut, J.-M., 2008. Vortical structures in the turbulent boundary layer: a possible route to a universal representation. *J. Fluid Mech.* 602, 327–382.

doi:10.1017/S0022112008000803

Sumner, R.J., McKibben, M.J., Shook, C.A., 1990. Concentration and Velocity Distribution in Turbulent vertical Slurry Flows. *Ecoulements Solide Liq.* 2, 33–42.

Suzuki, Y., Ikenoya, M., Kasagi, N., 2000. Simultaneous measurement of fluid and dispersed phases in a particle-laden turbulent channel flow with the aid of 3-D PTV. *Exp. Fluids* 29, S185–S193. doi:10.1007/s003480070020

Takeuchi, J., Satake, S., Morley, N.B., Yokomine, T., Kunugi, T., Abdou, M.A., 2005. PIV measurements of turbulence statistics and near-wall structure of fully developed pipe flow at high Reynolds number, in: 6th International Symposium on Particle Image Velocimetry. Pasadena, California, USA, pp. 1–9.

Tanaka, T., Eaton, J., 2008. Classification of turbulence modification by dispersed spheres using a novel dimensionless number. *Phys. Rev. Lett.* 101, 114502–1–4. doi:10.1103/PhysRevLett.101.114502

Taniere, A., Oesterle, B., Monnier, J.C., 1997. On the behaviour of solid particles in a horizontal boundary layer with turbulence and saltation effects. *Exp. Fluids* 23, 463–471. doi:10.1007/s003480050136

Tennekes, H., Lumley, J.L., 1972. *A first course in turbulence*. MIT Press, Cambridge.

Thomas, A.D., 1979. Predicting the deposit velocity for horizontal turbulence pipe flow of slurries. *Int. J. Multiph. Flow* 5, 113–129.

- Toonder, J.M.J. Den, Nieuwstadt, F.T.M., 1997. Reynolds number effects in a turbulent pipe flow for low to moderate Re. *Am. Inst. Phys.* 9, 3398–3409.
- Tsuji, Y., Kawaguchi, T., Tanaka, T., 1993. Discrete particle simulation of two-dimensional fluidized bed. *Powder Technol.* 77, 79–87. doi:10.1016/0032-5910(93)85010-7
- Tsuji, Y., Morikawa, Y., 1982. LDV measurements of an air-solid two-phase flow in a horizontal pipe. *J. Fluid Mech.* 120, 385–409.
- Tsuji, Y., Morikawa, Y., Shiomi, H., 1984. LDV measurements of an air-solid two-phase flow in a vertical pipe. *J. Fluid Mech.* 139, 417–434. doi:10.1017/S0022112084000422
- Tsuji, Y., Tanaka, T., Ishida, T., 1992. Lagrangian numerical simulation of plug flow of cohesionless particles in a horizontal pipe. *Powder Technol.* 71, 239–250. doi:10.1016/0032-5910(92)88030-L
- Tu, J. Y., Fletcher, C.A.J., 1994. An improved model for particulate turbulence modulation in confined two-phase flows. *International Commun. Heat Mass Transf.* 21, 775–783.
- Varaksin, A.Y., 2007. *Turbulent particle-laden gas flow*. Springer Berlin Heidelberg, New York.
- Varaksin, A.Y., Polezhaev, Y. V, Polyakov, A.F., 2000. Effect of particle concentration on fluctuating velocity of the disperse phase for turbulent pipe flow. *Int. J. Heat Fluid Flow* 21, 562–567.
- Versteeg, H.K., Malalasekera, W., 1995. *An introduction to computational fluid dynamics-*

the finite volume method. Pearson Education, Essex.

Vreman, A.W., 2007. Turbulence characteristics of particle-laden pipe flow. *J. Fluid Mech.* 584, 235–279. doi:10.1017/S0022112007006556

Vreman, B., Geurts, B.J., Deen, N.G., Kuipers, J.A.M., Kuerten, J.G.M., 2009. Two- and four-way coupled Euler–Lagrangian large-eddy simulation of turbulent particle-laden channel flow. *Flow, Turbul. Combust.* 82, 47–71. doi:10.1007/s10494-008-9173-z

Westerweel, J., Draad, A.A., Oord, I. Van, 1996. Measurement of fully-developed turbulent pipe flow with digital particle image velocimetry. *Exp. Fluids* 20, 165–177.

Wheeler, A.J., Ganji, A.R., 1996. *Introduction To engineering experimentation*. Prentice Hall Inc., Upper Saddle River, New Jersey.

White, F.M., 2009. *Fluid Mechanics*, 7th ed. Mc Graw Hill Book Co., New York, USA.

Wilson, K.C., Addie, G.R., Sellgren, A., Clift, R., 2006. *Slurry Transport Using Centrifugal Pumps*, 3rd ed. Springer US, New York, USA. doi:10.1007/b101079

Wu, Y., Wang, H., Liu, Z., Li, J., Zhang, L., Zheng, C., 2006. Experimental investigation on turbulence modification in a horizontal channel flow at relatively low mass loading. *Acta Mech. Sin.* 22, 99–108. doi:10.1007/s10409-006-0103-9

Xu, B.H., Yu, a. B., 1997. Numerical simulation of the gas-solid flow in a fluidized bed by combining discrete particle method with computational fluid dynamics. *Chem. Eng. Sci.* 52, 2785–2809. doi:10.1016/S0009-2509(97)00081-X

- Yan, F., Lightstone, M.F., Wood, P.E., 2006. Numerical study on turbulence modulation in gas–particle flows. *Heat Mass Transf.* 43, 243–253. doi:10.1007/s00231-006-0103-0
- Yoon, S., Chung, J.T., Kang, Y.T., 2014. The particle hydrodynamic effect on the mass transfer in a buoyant CO₂-bubble through the experimental and computational studies. *Int. J. Heat Mass Transf.* 73, 399–409. doi:10.1016/j.ijheatmasstransfer.2014.02.025
- Young, D.F., Munson, B.R., Okiishi, T.H., 2004. A brief introduction to fluid mechanics, 3rd ed. John Wiley & Sons Inc., USA.
- Yuan, Z., Michaelides, E.E., 1992. Turbulence modulation in particulate flows-a Theoretical approach. *Int. J. Multiph. Flow* 18, 779–785.
- Yuen, H. k., Princen, J., Illingworth, J., Kittler, J., 1990. Comparative study of Hough transform methods for circle finding. *Image Vis. Comput.* 8, 71–77. doi:10.1016/0262-8856(90)90059-E
- Zhang, W., Noda, R., Horio, M., 2005. Evaluation of lubrication force on colliding particles for DEM simulation of fluidized beds. *Powder Technol.* 158, 92–101. doi:10.1016/j.powtec.2005.04.021
- Zisselmar, R., Molerus, O., 1979. Investigation of solid-liquid pipe flow with regard to turbulence modification. *Chem. Eng. J.* 18, 233–239.

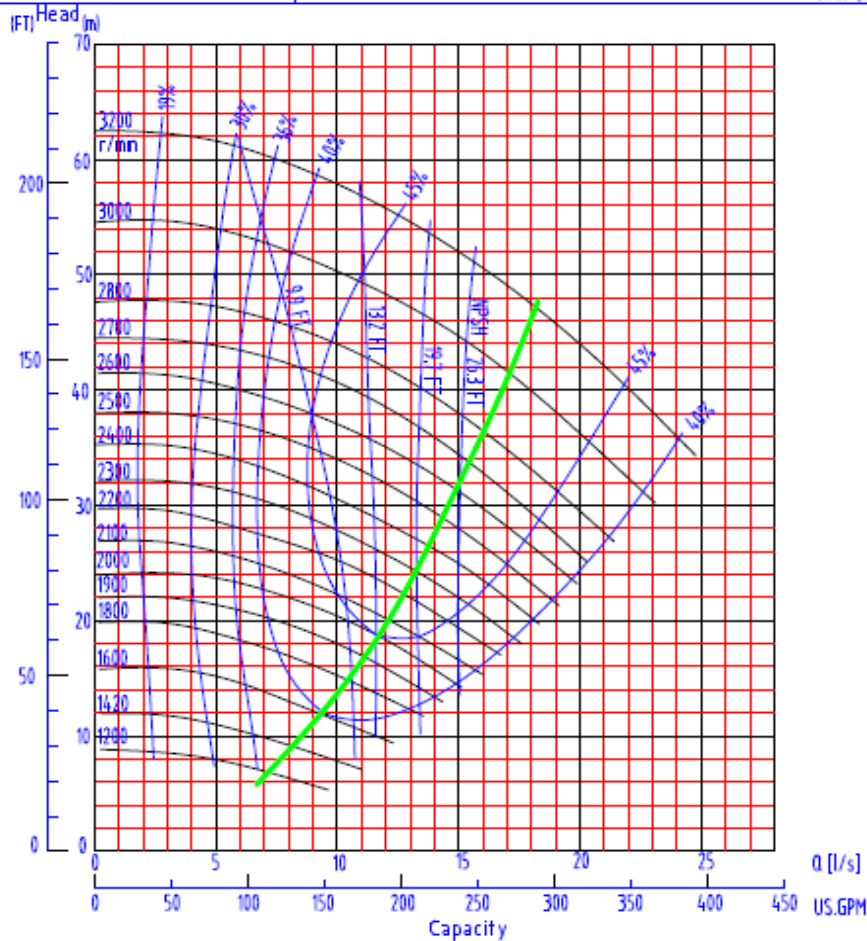
Appendix A. Pump curve

BATTLEMOUNTAIN				VARIABLE SPEED PERFORMANCE CURVE							
Size/Type	2x1.5	WX	Model	2x1.5 WX-B	Max Speed	RPM	NO. Vanes-Type	SVO	Sealing Method	Packed Box	
Brg. Frame	B			Metal Liner.	3200		Max. Dia. (in.)	7.24		Max Solids (in.)	0.75
Max BHP	20			Elast. Line.			Impeller Mtl	Metal		Curve No.	AMC 215801
				Impeller No.	AB15101		Liner Mtl	Metal		Rev. Date.	10-30-2007

Note: This performance curve is based on water only. All other fluids must be corrected for SP.GR, viscosity and other parameters.
 Bearing Frame selection is based on the actual conditions of service. Impeller & Expeller Seal compatibility need to be checked for every application.
 This pump is manufactured by Atlas Manufacturing LTD and all numbers are for reference and do not indicate manufacture by any other than Atlas.

Commercial Data:		Technical Data:	
Customer:	_____	Liquid:	_____
Plant Location:	_____	FLOW:	_____
RFO/PO No:	_____	TDH:	_____
Item No:	_____	Speed:	_____
Equip. No:	_____	Eff. Rated:	_____
		BHP Rated:	_____
		NPSHr:	_____
Certified by:	_____	Eff. Max:	_____
Date:	_____	BHP Max:	_____

© Atlas Ltd.



Appendix B. Comparison of measured single phase turbulence intensities with the literature

In order to understand how well we measure the fluctuations of the liquid phase, the results are going to be compared with the reliable sources at the closest Re possible. In this investigation, the turbulence intensities (defined as fluctuating velocity divided by the bulk velocity) of our experimental data are going to be compared with other data from the literature. Two sets of data were selected including the DNS results from Lee & Moser (2015) and experimental data from Schultz & Flack (2013) which are denoted as “LM” and “SF” in the subsequent plots respectively. For easier referencing, the Re of 52,000, 100,000, and 320,000 are sometimes referred as the low, medium, and high Re , respectively.

First the turbulent intensities of the liquid phase obtained at $Re=52,000$ are compared with the results of Schultz & Flack (2013) and Lee & Moser (2015) for channel flow at $Re=40,000$. Their Reynolds number is about 25% smaller therefore; our results of the turbulence intensities are expected to be slightly smaller. Fig.B-1 shows the streamwise and radial turbulence intensities, Ti_x and Ti_r respectively, of above mentioned data sets. The agreement between our results and the results from “LM” and “SF” for both streamwise and radial turbulence intensities is very good up to $r/R=0.9$. The agreement becomes less strong in the near wall region. The discrepancy between our results and the DNS results of Lee & Moser (2015) for the streamwise turbulence is still less than 10% and while it is around 10-

15% for lateral turbulence intensity in the near wall region ($r/R > 0.9$). It is worth reminding that the a few percentage of difference is expectable due to the difference in Re .

Fig.B-2 demonstrates the Ti_x and Ti_r results from our experimental data at $Re=100,000$ and Schultz & Flack (2013) at $Re=84,000$ and Lee & Moser (2015) at $Re=80,000$. Almost the same conclusion as above can be drawn for this Re as well. The results s showed very good agreement up to $r/R=0.9$. The discrepancy for streamwise turbulence still stays below 10% in the near wall region ($r/R > 0.9$). However, Ti_r demonstrates poorer agreement in the region $r/R > 0.9$ and the difference is about 12% at $r/R=0.9$ and it increasingly deteriorates afterwards.

The turbulent intensities of the liquid phase at $Re=320,000$ are shown in fig.3 along with the results of Schultz & Flack (2013) at $Re=286,000$ and Lee & Moser (2015) at $Re=250,000$. Again, the Reynolds number is about 15-20% smaller which means that a few percent differences are expectable. As shown in fig.B-3, the results show a good agreement with the literature in the core of the flow. However the discrepancy becomes larger in the near wall area. The accuracy of the results for the axial turbulence intensity starts to deteriorate at $r/R > 0.9$. Although the results from literature show a little of flatness near the wall, the experimental results show much higher degree of flatness which is most probably stemming from the error in capturing the fluctuations in this region. All in all, the error for the streamwise fluctuations is always below 10% in the near wall region ($r/R > 0.9$). The plot shows the error for radial fluctuations is higher than the streamwise ones. The error is more than 15% at the region $r/R > 0.8$.

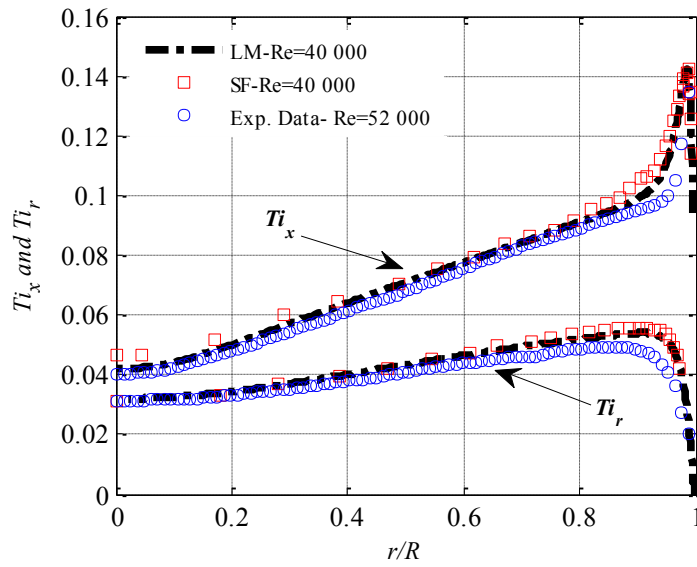


Fig.B-1. Comparison of the experimental data on the turbulence intensity with literature at Low Re

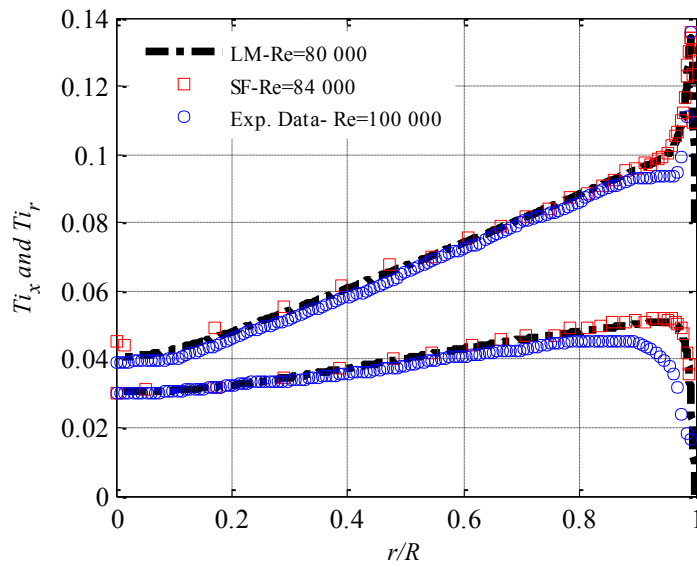


Fig.B-2. Comparison of the experimental data on the turbulence intensity with literature at Medium Re

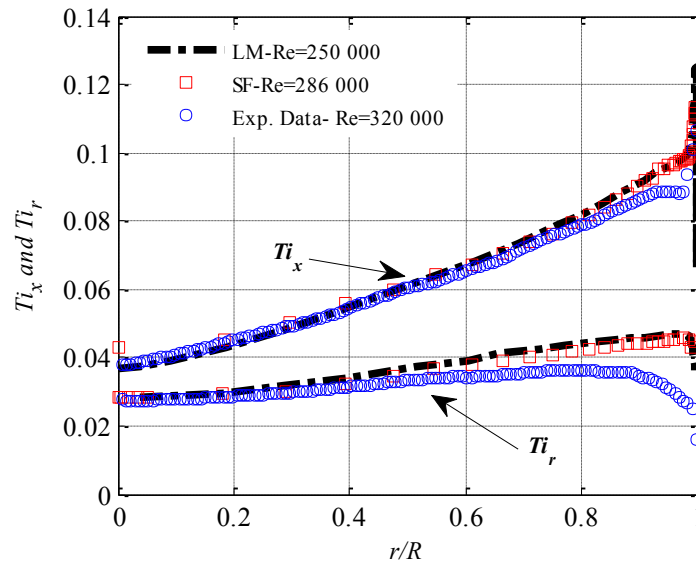


Fig.B-3. Comparison of the experimental data on the turbulence intensity with literature at high Re

One can conclude that the discrepancy is larger in the near wall than the core and it is worse for the radial fluctuations in this region. Also the comparisons show that the discrepancy for radial fluctuations enhances by increasing the Re . The main reasons for the lower accuracy of the data in the near wall region and especially for Ti_r are believed to be the “high distortion in the image” and “glare and reflection” in the near wall region. Also the other reason can be the “low resolution of the PIV measurements” specifically at higher Reynolds numbers. The last one can be attributed to the window size which is not sufficiently small. The window size is $32 \times 32 \text{ pixel}^2$ in these PIV calculations which is approximately equal to $0.77 \times 0.77 \text{ mm}^2$. This size of the window is too large for resolving turbulence in all scales in near wall region especially at $Re=320,000$. Therefore, some of the turbulence will be filtered and the final results become dampened in near wall region (Ghaemi and Scarano, 2011).

When the streamwise fluctuations are plotted as $\langle u^2 \rangle^+$ versus y^+ , the emergence of a plateau in the near wall region can be observed for very high Reynolds numbers (Schultz and Flack, 2013; Smits et al., 2011). The formation of the plateau can be attributed to the influence of the outer layer on the motions of the inner layer near the wall. If the streamwise turbulence is decomposed based on two length scales; small and large scales, (Smits et al., 2011) showed that the small scales contribution which is higher in the inner-layer don't change with increasing the Re while the large scale contribution of the streamwise turbulence which peaks in the log-region increases with increasing Re (figB-4b). The total signal of streamwise turbulence can be obtained by the superimposing these two parts (Fig.B-4a)) and therefore, the plateau is observed at high Re .

For calculating the $\langle u^2 \rangle^+$ and y^+ , the best and most reliable way is to obtain it using the experimental data where the laminar sub-layer is fully resolved. However, a good approximation can be achieved by using below procedure and equations. The $\langle u^2 \rangle^+$ is defined as below:

$$\langle u^2 \rangle^+ = \frac{\langle u^2 \rangle}{U_\tau^2} \quad (\text{B-1})$$

The U_τ is the frictional velocity and can be obtained by following equation.

$$U_\tau = \sqrt{\frac{\tau_w}{\rho_f}} \quad (\text{B-2})$$

The wall shear stress, τ_w , is defined as below:

$$\tau_w = f_f \frac{\rho_f U_b^2}{2} \quad (\text{B-3})$$

In the equation above, U_b is the bulk velocity and f_f is the Fanning friction factor which can be calculated from Colbroke-white equation as below:

$$\frac{1}{\sqrt{f_f}} = -4.0 \text{Log} \left(\frac{\varepsilon/D}{3.7} + \frac{1.256}{Re\sqrt{f_f}} \right) \quad (\text{B-4})$$

The ε is hydrodynamic roughness. Also y^+ is defined as $y^+ = \frac{U_{\tau} y}{\nu_f}$ where $y=R-r$ and ν_f is dynamic viscosity of the fluid.

Figures.B-5 through B-7 show the variation of $\langle u^2 \rangle^+$ of the experimental data versus y^+ along with the data from Lee & Moser (2015) and Schultz & Flack (2013) at different Reynolds numbers. As illustrated in Fig.B-5, only a deflection point can be seen around $y^+=100$ in all the experimental data at low Re . However, the plateau is yet to be formed at this Re . At the medium Re , a slanted plateau can be detected between two deflection points (Fig.B-6). The lower and higher bound of these two deflection points are at around $y^+=90$ and $y^+=250$ respectively. Although the measurement error is high in this region, the experimental data can capture the lower and higher bounds well. The plot for high Re (Fig.B-7) shows that a larger and flatter plateau is formed located between deflection points of $y^+=70$ and $y^+=500$. The experimental data also shows larger plateau in terms of y^+ and the higher bound is predicted well. However, as discussed earlier, the error is much higher at this Reynolds number in this region which causes poor agreement with the literature.

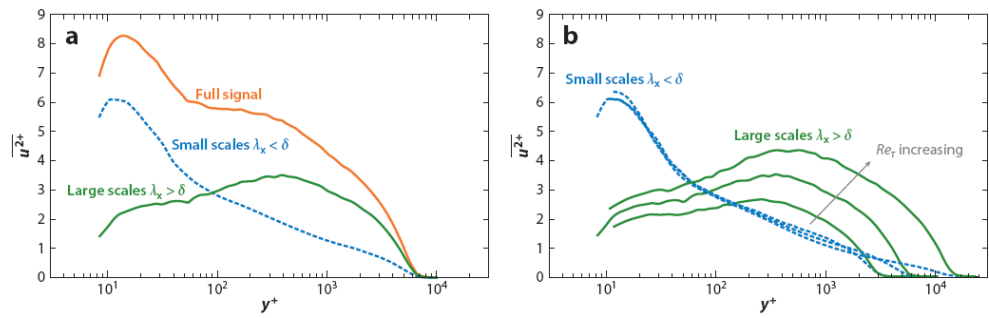


Fig.B-4. Decomposition of the streamwise turbulence (Smits et al., 2011)

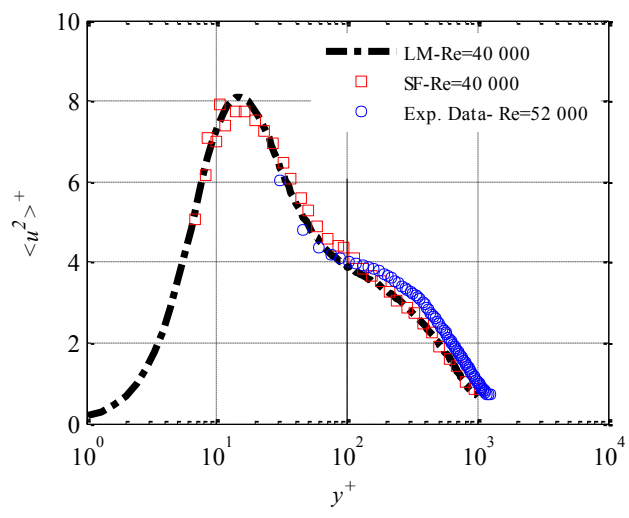


Fig.B-5. $\langle u^2 \rangle_+$ vs y^+ at low Re

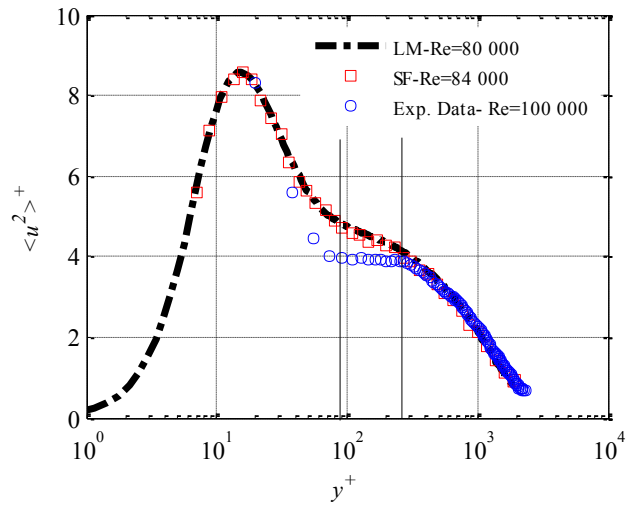


Fig.B-6. $\langle u^2 \rangle^+$ vs y^+ at medium Re

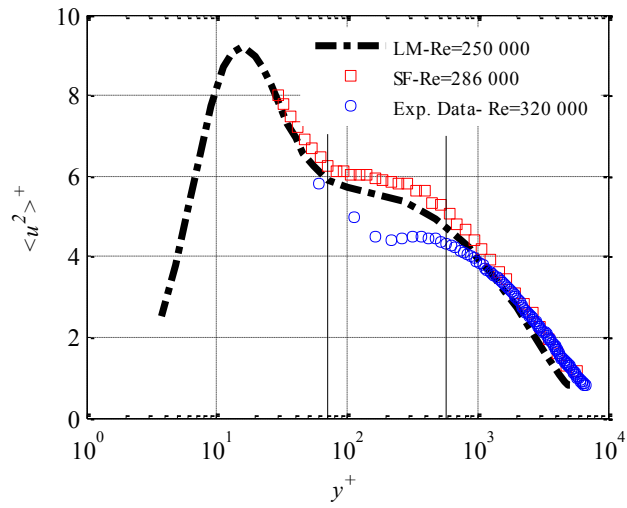


Fig.B-7. $\langle u^2 \rangle^+$ vs y^+ at high Re

References:

- Ghaemi, S. & Scarano, F., 2011. Counter-hairpin vortices in the turbulent wake of a sharp trailing edge. *Journal of Fluid Mechanics*, 689, pp.317–356.
- Lee, M. & Moser, R.D., 2015. Direct Numerical Simulation of Turbulent Channel Flow up to $Re\tau=5200$. *Journal of Fluid Mechanics*, 774, pp.395–415.
- Schultz, M.P. & Flack, K. a., 2013. Reynolds-number scaling of turbulent channel flow. *Physics of Fluids*, 25.
- Smits, A.J., McKeon, B.J. & Marusic, I., 2011. High–Reynolds Number Wall Turbulence. *Annual Review of Fluid Mechanics*, 43(1), pp.353–375.

Appendix C. Symmetry of the velocity profiles

The profiles of the mean axial velocity, axial and radial turbulence intensities, and $\langle uv \rangle$ profiles for the full cross section of the pipe are depicted in Fig.C-1 to Fig.C-3 at all three Reynolds number. Also a graph of power-law velocity profile for $\langle U_x \rangle / U_c$ is also provided at each Re for visual assistance. Although the graphs show a good symmetry, by a closer look, one can realize that the full symmetry has not been achieved and the profiles are slightly shifted towards right. The main reason can be remaining large vortices from the pump or the secondary flows caused by the large arc after the test section. The best way to find the center location for velocity profiles is where $\langle uv \rangle$ becomes zero. As shown in Figs.1(c), 2(c) and 3(c), the center location is located about (1.3-1.7) mm to the right of the pipe centerline or in other words, they locate at $r/R=+0.05$ to $r/R=+0.065$. The average error between left and right half of the profiles for $\langle U_x \rangle$, $\langle u \rangle$, $\langle v \rangle$, and $\langle uv \rangle$ are in the ranges of (1%-2.2%), (1.5%-5.2%), (0.2%-2.1%), and (0.5%-8%), respectively.

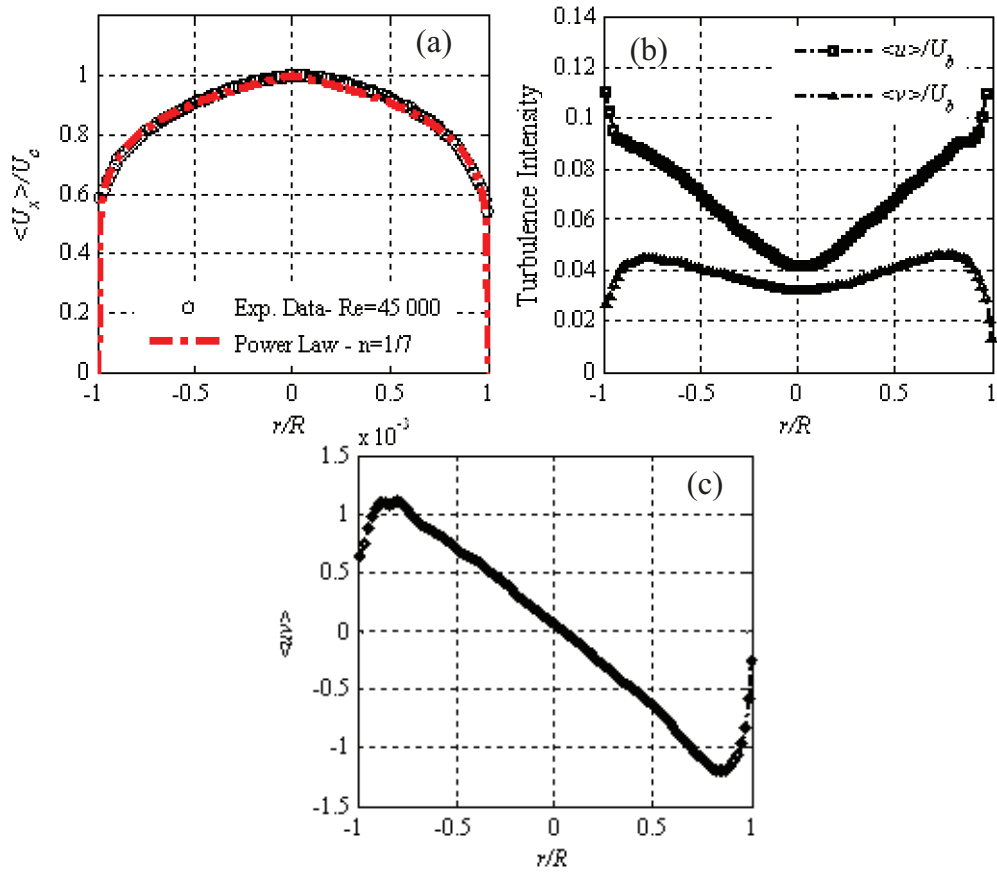


Fig.C-1. (a) velocity profile, (b) Turbulence intensity profiles, (c) $\langle uv \rangle$ profile

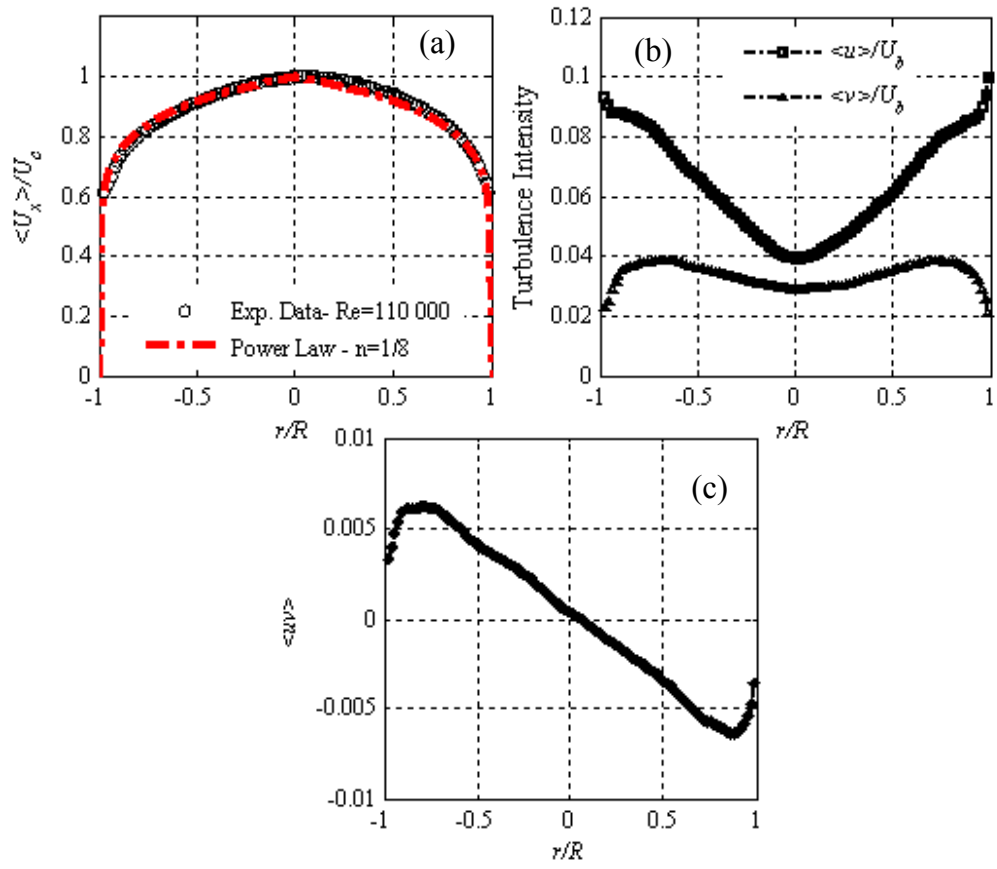


Fig.C-2. (a) velocity profile, (b) Turbulence intensity profiles, (c) $\langle uv \rangle$ profile

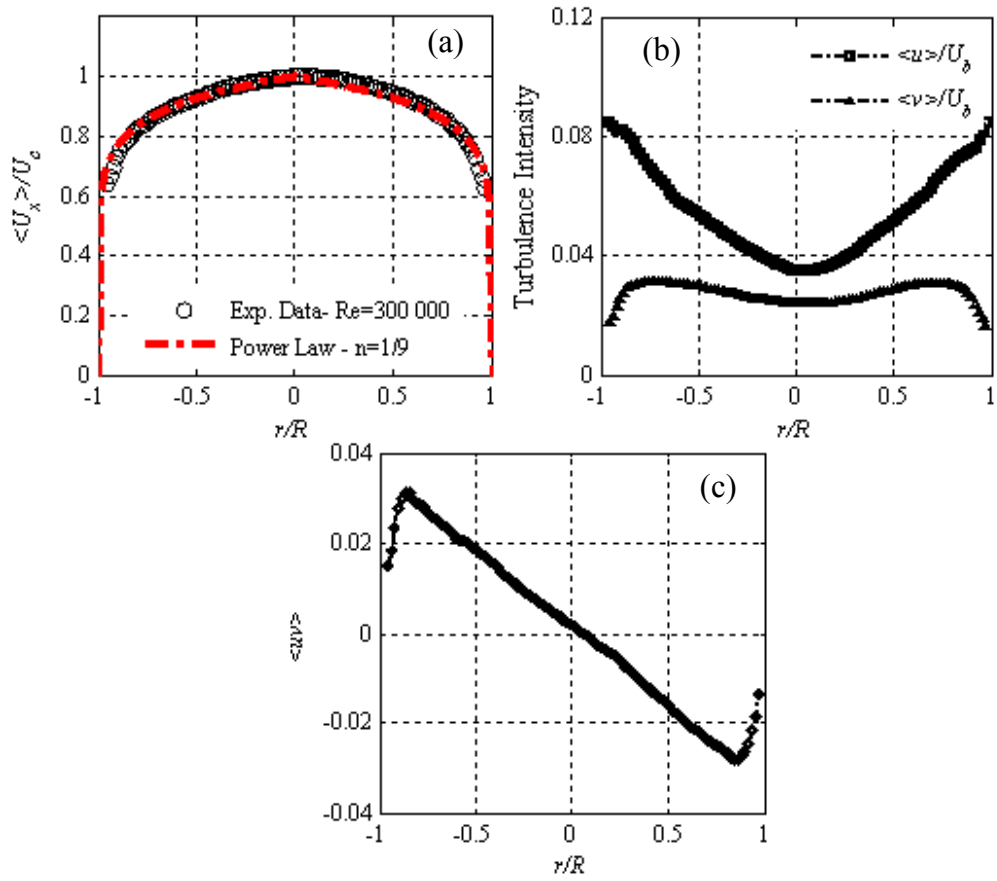


Fig.C-3. (a) velocity profile, (b) Turbulence intensity profiles, (c) $\langle uv \rangle$ profile

Appendix D. Extra Plot

In the present study, the concentration profiles and particle-particle interaction index for the 0.5, 1, and 2 mm glass beads at $Re= 100\ 000$ were obtained, as shown in Fig.D-1.

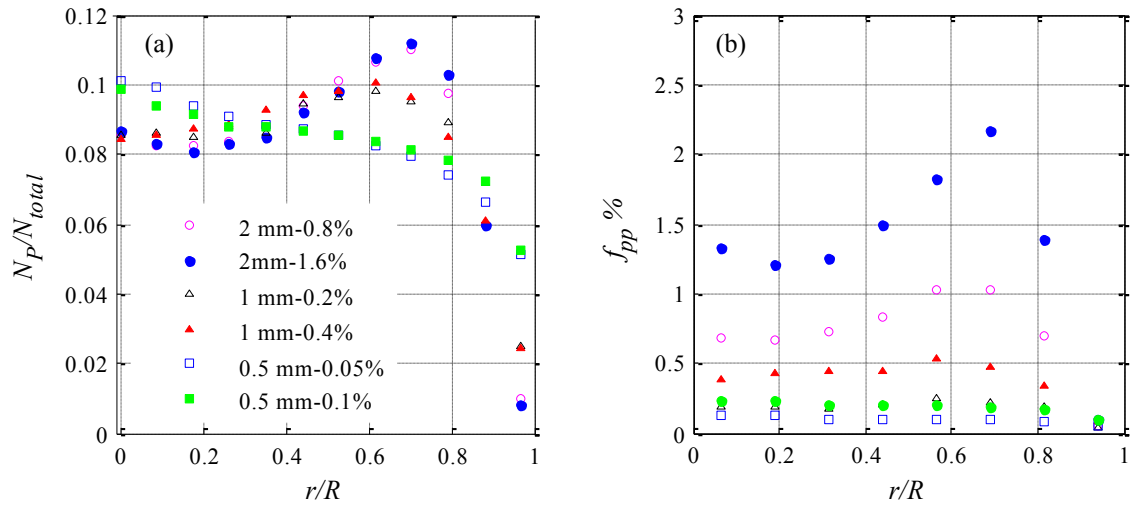


Fig.D-1. (a) Concentration profile and (b) particle-particle interaction index profiles for 0.5, 1 and 2 mm particle at $Re = 100\ 000$

Appendix E. Uncertainty Plots

The uncertainty levels are reported here. First Table.1 and Table.2 provide the uncertainty of the mean and fluctuating velocities of particles and carrier phase respectively. The uncertainties are reported for 3 locations: $r/R=0$, $r/R=0.5$ and $r/R=0.96$. Finally the convergence of those parameters is plotted against the sample number.

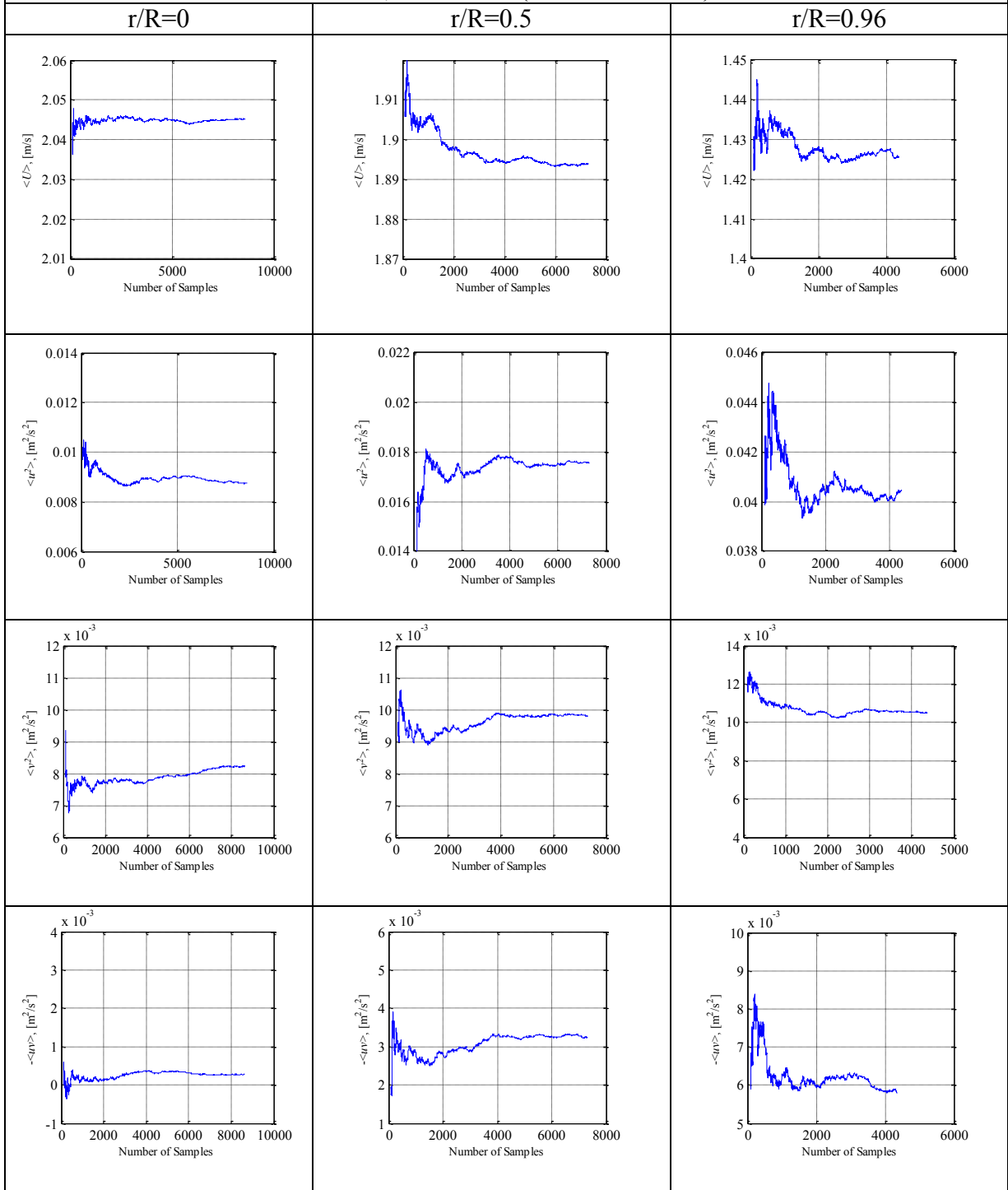
Table E-1. Random uncertainty of the particles

Re	d_p (mm)	ϕ_v %	Standard deviation(<U>)			Standard deviation (<u ² >)		
			r/R=0	r/R=0.5	r/R=0.96	r/R=0	r/R=0.5	r/R=0.96
52 000	2	1.6	4.3×10^{-3}	3.4×10^{-3}	2.8×10^{-3}	6.2×10^{-4}	2.7×10^{-4}	2.0×10^{-4}
100 000	0.5	0.05	4.2×10^{-4}	3.2×10^{-3}	2.9×10^{-3}	1.3×10^{-4}	2.4×10^{-4}	6.6×10^{-4}
100 000	0.5	0.1	6.4×10^{-4}	2.6×10^{-3}	1.1×10^{-3}	1.7×10^{-4}	1.9×10^{-4}	3.8×10^{-4}
100 000	1	0.2	$1.5e^{-3}$	1.4×10^{-3}	5.7×10^{-3}	1.7×10^{-4}	5.3×10^{-4}	1.5×10^{-4}
100 000	1	0.4	1.1×10^{-3}	5.4×10^{-4}	2.6×10^{-3}	2.0×10^{-4}	1.2×10^{-4}	8.2×10^{-4}
100 000	2	0.8	1.2×10^{-3}	8.2×10^{-4}	2.6×10^{-3}	1.0×10^{-4}	1.8×10^{-4}	7.3×10^{-4}
100 000	2	1.6	1.9×10^{-3}	6.6×10^{-4}	4.6×10^{-3}	9.4×10^{-5}	1.7×10^{-4}	1.6×10^{-3}
320 000	0.5	0.1	1.9×10^{-3}	2.3×10^{-3}	5.6×10^{-3}	2.7×10^{-3}	3.3×10^{-3}	4.5×10^{-3}
320 000	1	0.4	2.5×10^{-3}	5.4×10^{-3}	3.5×10^{-3}	2.1×10^{-3}	2.4×10^{-3}	1.1×10^{-3}
320 000	2	0.8	4.5×10^{-3}	7.9×10^{-3}	9.5×10^{-3}	1.7×10^{-3}	4.1×10^{-3}	1×10^{-3}
Re	d_p (mm)	ϕ_v %	Standard deviation (<v ² >)			Standard deviation (<uv>)		
Re	d_p (mm)	ϕ_v %	r/R=0	r/R=0.5	r/R=0.96	r/R=0	r/R=0.5	r/R=0.96
52 000	2	1.6	6.9×10^{-5}	1.0×10^{-4}	6.5×10^{-5}	4.9×10^{-5}	5×10^{-5}	7.5×10^{-5}
100 000	0.5	0.05	1.9×10^{-4}	2.6×10^{-4}	1.9×10^{-4}	7.5×10^{-5}	2.4×10^{-4}	2.5×10^{-4}
100 000	0.5	0.1	5.2×10^{-5}	8.3×10^{-5}	7.1×10^{-5}	5.3×10^{-5}	5.9×10^{-5}	2.3×10^{-4}
100 000	1	0.2	1.8×10^{-4}	1.7×10^{-4}	4.7×10^{-4}	9.2×10^{-5}	7.8×10^{-5}	3×10^{-4}
100 000	1	0.4	1.5×10^{-4}	1.4×10^{-5}	2.2×10^{-4}	3.7×10^{-5}	1.2×10^{-4}	3.4×10^{-4}
100 000	2	0.8	1.8×10^{-4}	2.4×10^{-4}	4.6×10^{-4}	8.7×10^{-5}	7×10^{-5}	3.2×10^{-4}
100 000	2	1.6	8.1×10^{-5}	1.5×10^{-4}	5.5×10^{-4}	4.9×10^{-5}	5×10^{-5}	7.5×10^{-5}
320 000	0.5	0.1	1.0×10^{-3}	1.0×10^{-3}	2.1×10^{-3}	8.8×10^{-4}	9.6×10^{-4}	3.3×10^{-3}
320 000	1	0.4	1.8×10^{-3}	9.1×10^{-4}	2.4×10^{-3}	8.8×10^{-4}	7.6×10^{-4}	3.6×10^{-3}
320 000	2	0.8	1.7×10^{-3}	3.2×10^{-3}	5.9×10^{-3}	2.8×10^{-3}	2×10^{-3}	8.4×10^{-3}

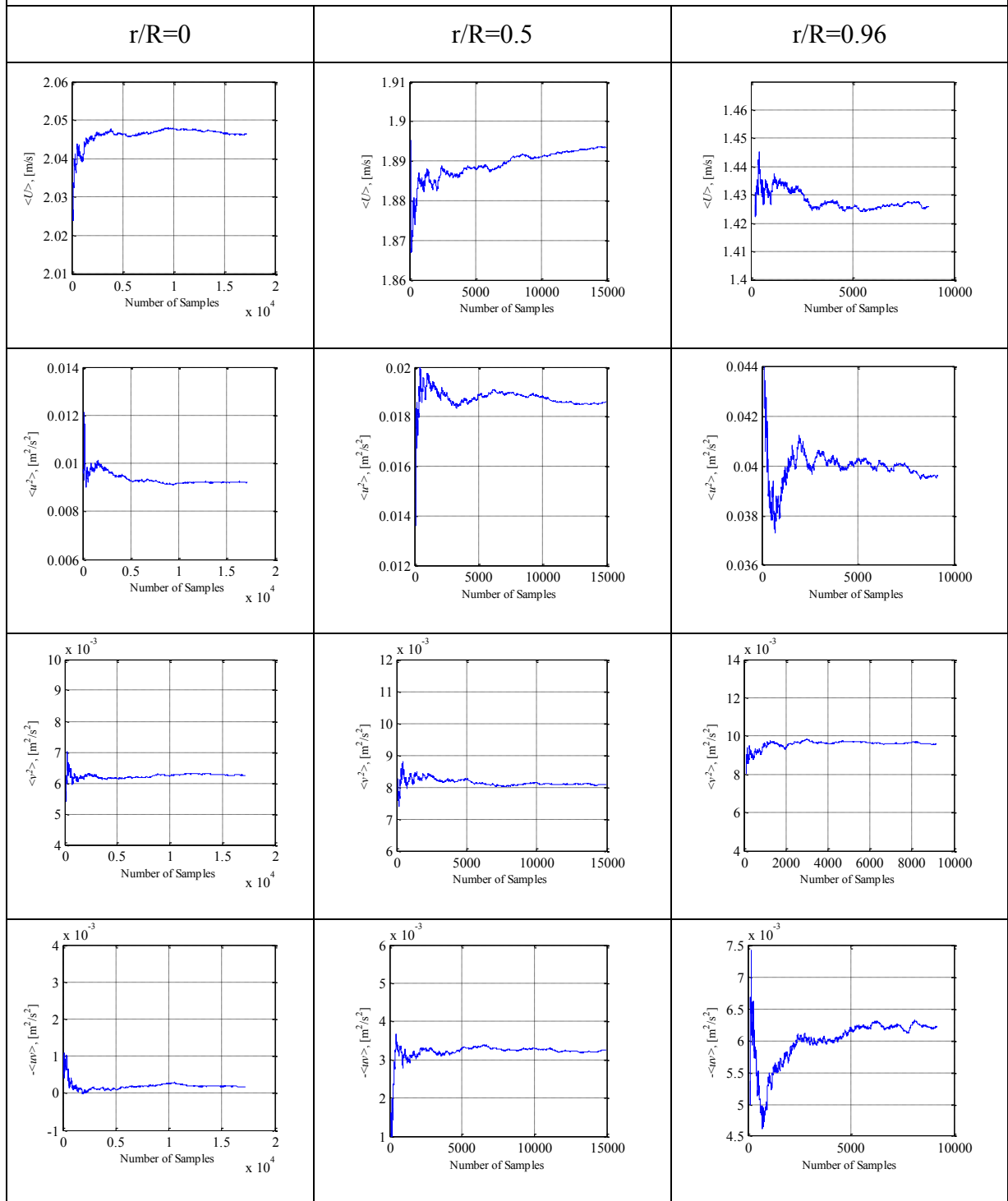
Table E-2. Random uncertainty of the liquid phase

						Standard deviation ($\langle U \rangle$)		Standard deviation ($\langle u^2 \rangle$)	
Re	d_p (mm)	ϕ_v %	r/R=0	r/R=0.5	r/R=0.96	r/R=0	r/R=0.5	r/R=0.96	
52 000	Unladen	Unladen	3.8×10^{-4}	1.3×10^{-3}	2.3×10^{-3}	1.3×10^{-5}	5.0×10^{-5}	1.1×10^{-4}	
52 000	2	1.6	2.2×10^{-3}	2.2×10^{-3}	3.1×10^{-3}	5.9×10^{-5}	1.9×10^{-4}	2.0×10^{-4}	
100 000	Unladen	Unladen	1.2×10^{-3}	2.4×10^{-3}	2.1×10^{-3}	1.1×10^{-4}	1.5×10^{-4}	3.5×10^{-4}	
100 000	0.5	0.05	1.5×10^{-3}	2.6×10^{-3}	3.8×10^{-3}	1.2×10^{-4}	3.2×10^{-4}	6.3×10^{-4}	
100 000	0.5	0.1	9.8×10^{-4}	1.3×10^{-3}	2.2×10^{-3}	2.5×10^{-4}	3.7×10^{-4}	6.7×10^{-4}	
100 000	1	0.2	2.4×10^{-3}	9.5×10^{-4}	3.6×10^{-3}	1.2×10^{-4}	3.4×10^{-4}	2.5×10^{-4}	
100 000	1	0.4	2.2×10^{-3}	2×10^{-3}	1.2×10^{-3}	2.1×10^{-4}	3.5×10^{-4}	2.7×10^{-4}	
100 000	2	0.8	4.1×10^{-4}	6.9×10^{-4}	2.1×10^{-3}	2.6×10^{-4}	1.8×10^{-4}	3.1×10^{-4}	
100 000	2	1.6	2.7×10^{-3}	5.8×10^{-3}	2.1×10^{-3}	2.1×10^{-4}	9.6×10^{-4}	6.2×10^{-4}	
300 000	Unladen	Unladen	2.1×10^{-3}	4×10^{-3}	3.9×10^{-3}	6.8×10^{-4}	1×10^{-3}	1.6×10^{-3}	
320 000	0.5	0.1	2.1×10^{-3}	4×10^{-3}	3.9×10^{-3}	6.8×10^{-4}	1×10^{-3}	1.6×10^{-3}	
320 000	1	0.4	2.7×10^{-3}	3.1×10^{-3}	2.2×10^{-3}	9.2×10^{-4}	1.0×10^{-3}	2.3×10^{-3}	
320 000	2	0.8	1.9×10^{-3}	2.9×10^{-3}	3.9×10^{-3}	1.6×10^{-3}	2.3×10^{-3}	2.8×10^{-3}	
						Standard deviation ($\langle v^2 \rangle$)		Standard deviation ($\langle uv \rangle$)	
Re	d_p (mm)	ϕ_v %	r/R=0	r/R=0.5	r/R=0.96	r/R=0	r/R=0.5	r/R=0.96	
52 000	Unladen	Unladen	1.1×10^{-5}	3.7×10^{-5}	1.6×10^{-5}	1.4×10^{-5}	4.3×10^{-5}	2.6×10^{-5}	
52 000	2	1.6	3.6×10^{-5}	4.7×10^{-5}	3.7×10^{-5}	3.9×10^{-5}	4.7×10^{-5}	6.6×10^{-5}	
100 000	Unladen	Unladen	1.1×10^{-4}	1.1×10^{-4}	9.6×10^{-5}	5.2×10^{-5}	5.9×10^{-5}	9.2×10^{-5}	
100 000	0.5	0.05	9.8×10^{-5}	1.3×10^{-4}	2.1×10^{-4}	5.2×10^{-5}	1.0×10^{-4}	1.9×10^{-4}	
100 000	0.5	0.1	1.2×10^{-4}	2.4×10^{-4}	3.9×10^{-4}	2.5×10^{-4}	3.7×10^{-4}	6.8×10^{-4}	
100 000	1	0.2	1.1×10^{-4}	1.1×10^{-4}	1.2×10^{-4}	1.7×10^{-4}	1.2×10^{-4}	1.4×10^{-4}	
100 000	1	0.4	1.0×10^{-4}	1.5×10^{-4}	5.5×10^{-5}	9.2×10^{-4}	2.0×10^{-4}	2.1×10^{-4}	
100 000	2	0.8	1.7×10^{-4}	1.8×10^{-4}	8.4×10^{-5}	8.1×10^{-5}	1.4×10^{-4}	7.2×10^{-5}	
100 000	2	1.6	1.8×10^{-4}	9.4×10^{-5}	7.7×10^{-5}	7.1×10^{-5}	2.4×10^{-4}	1.3×10^{-4}	
100 000	Unladen	Unladen	1.3×10^{-4}	4.8×10^{-4}	2.6×10^{-4}	4.6×10^{-4}	5.1×10^{-4}	5.9×10^{-4}	
320 000	0.5	0.1	1.8×10^{-4}	2.3×10^{-4}	1.2×10^{-4}	2.0×10^{-4}	4.2×10^{-4}	3.3×10^{-4}	
320 000	1	0.4	1.5×10^{-4}	5.8×10^{-4}	3.1×10^{-4}	2.5×10^{-4}	8.3×10^{-4}	3.1×10^{-4}	
320 000	2	0.8	4.8×10^{-4}	5.3×10^{-4}	1.6×10^{-4}	5.3×10^{-4}	6.3×10^{-4}	5×10^{-4}	

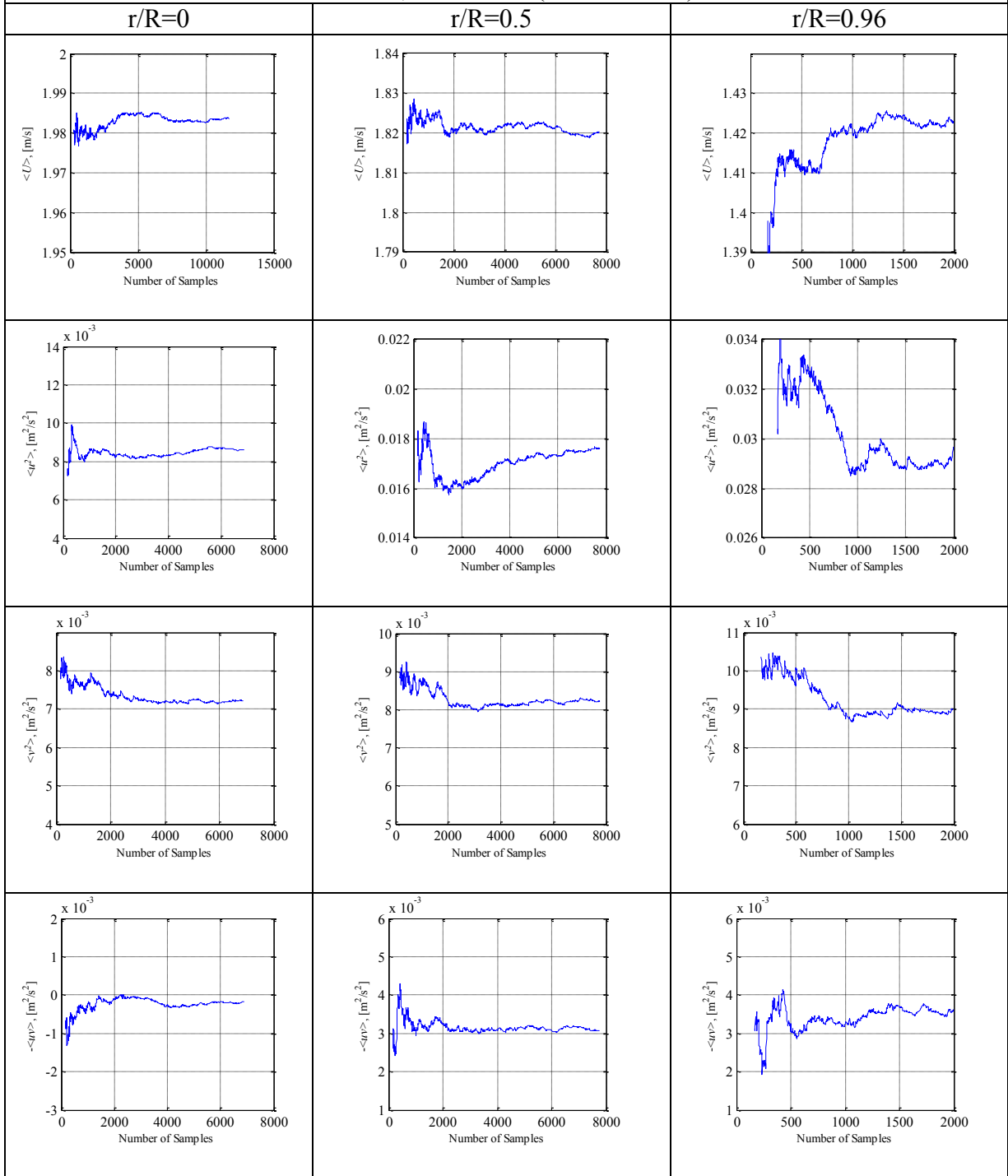
Re=100,000 – Solid (0.5mm – 0.05 %)



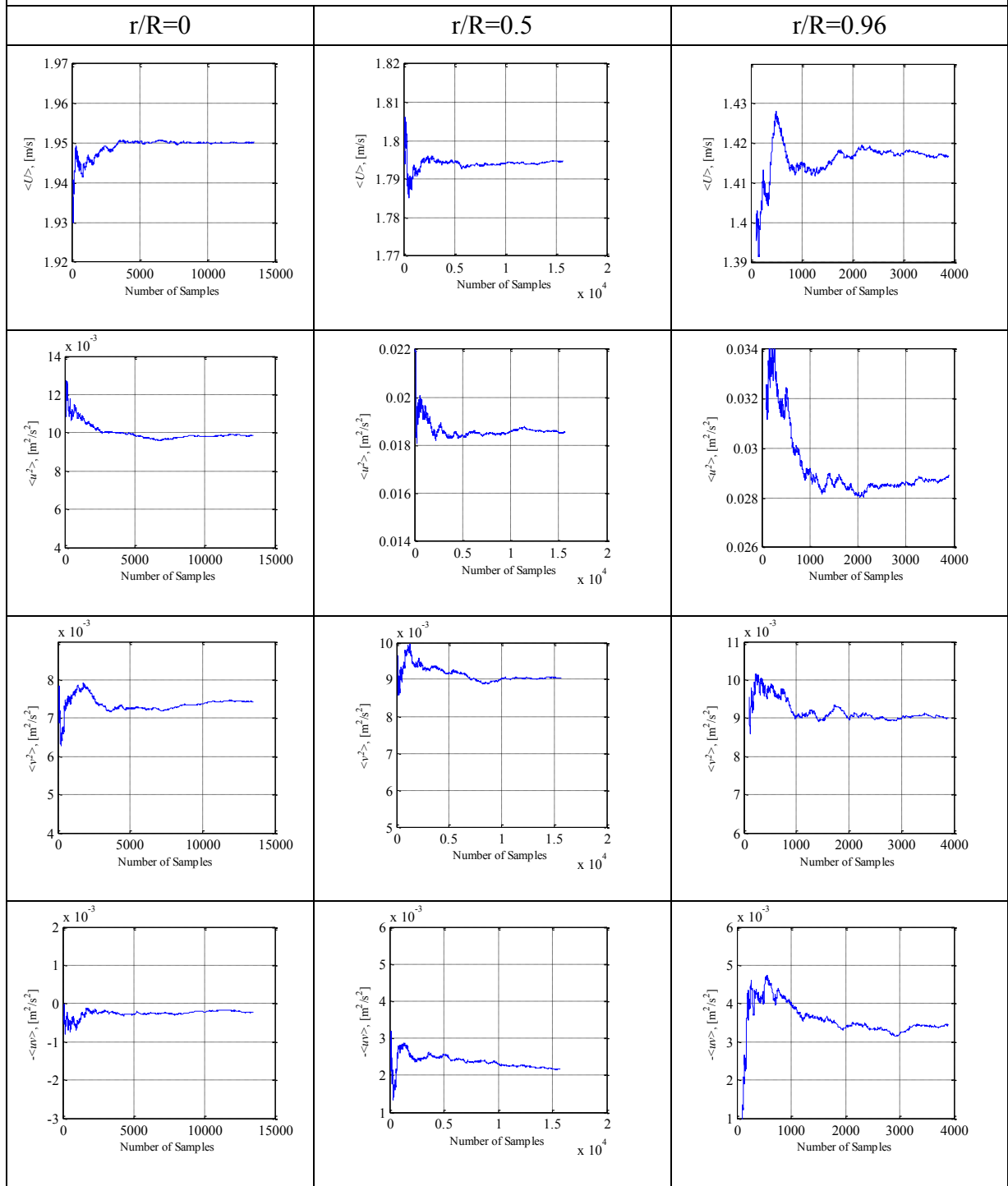
Re=100,000 – Solid (0.5mm – 0.1 %)



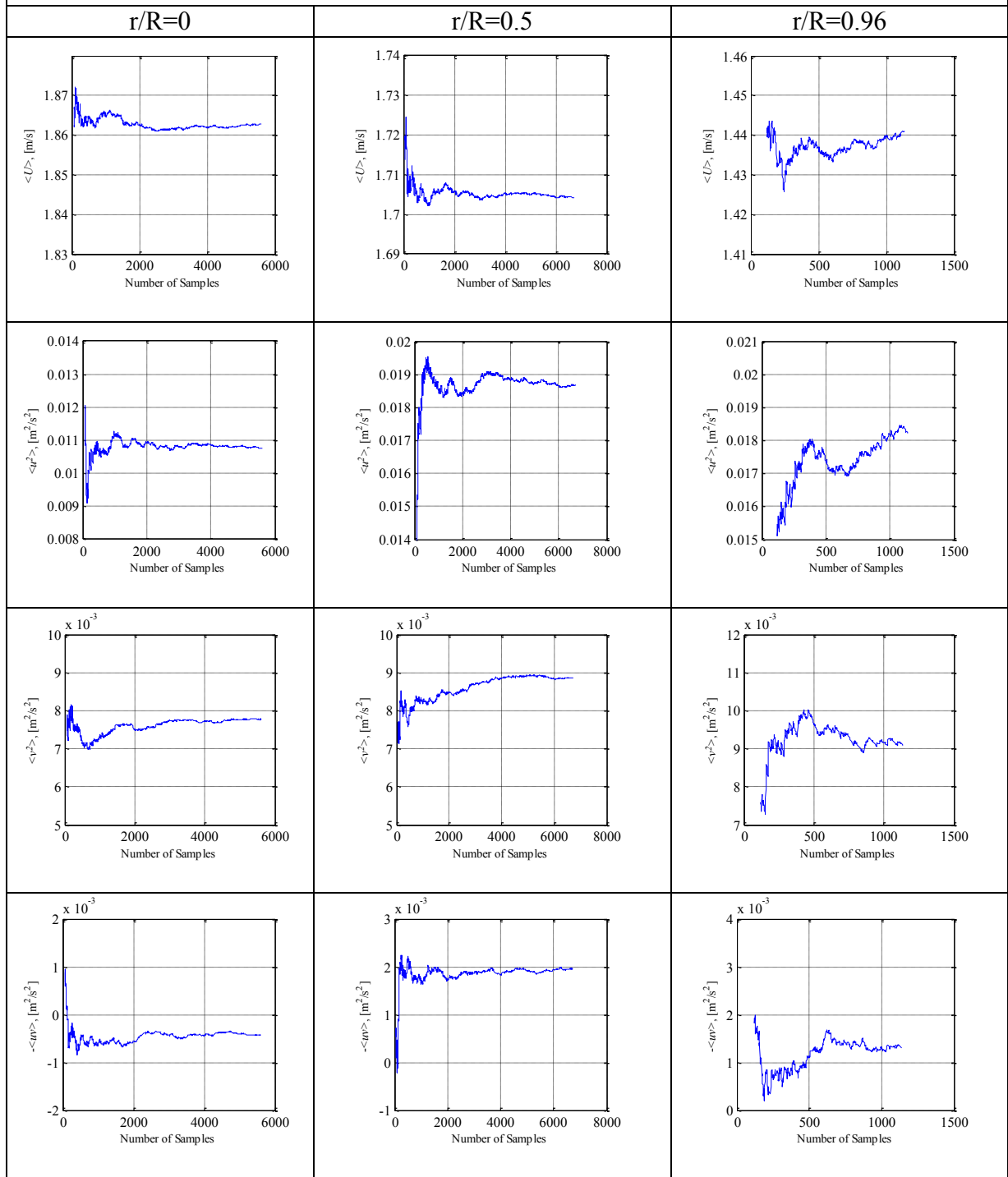
Re=100,000 – Solid (1mm – 0.2 %)



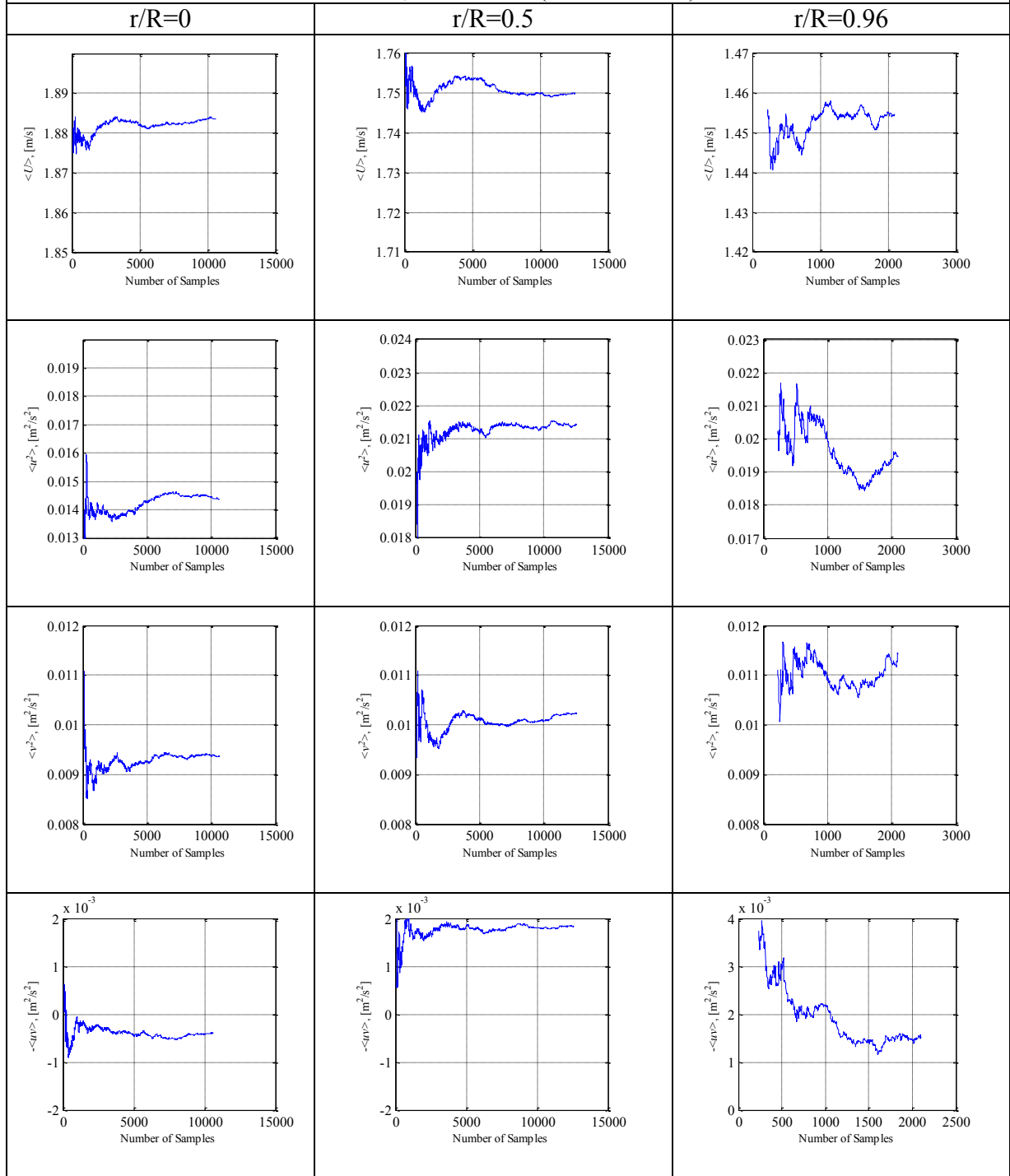
Re=100,000 – Solid (1mm – 0.4 %)



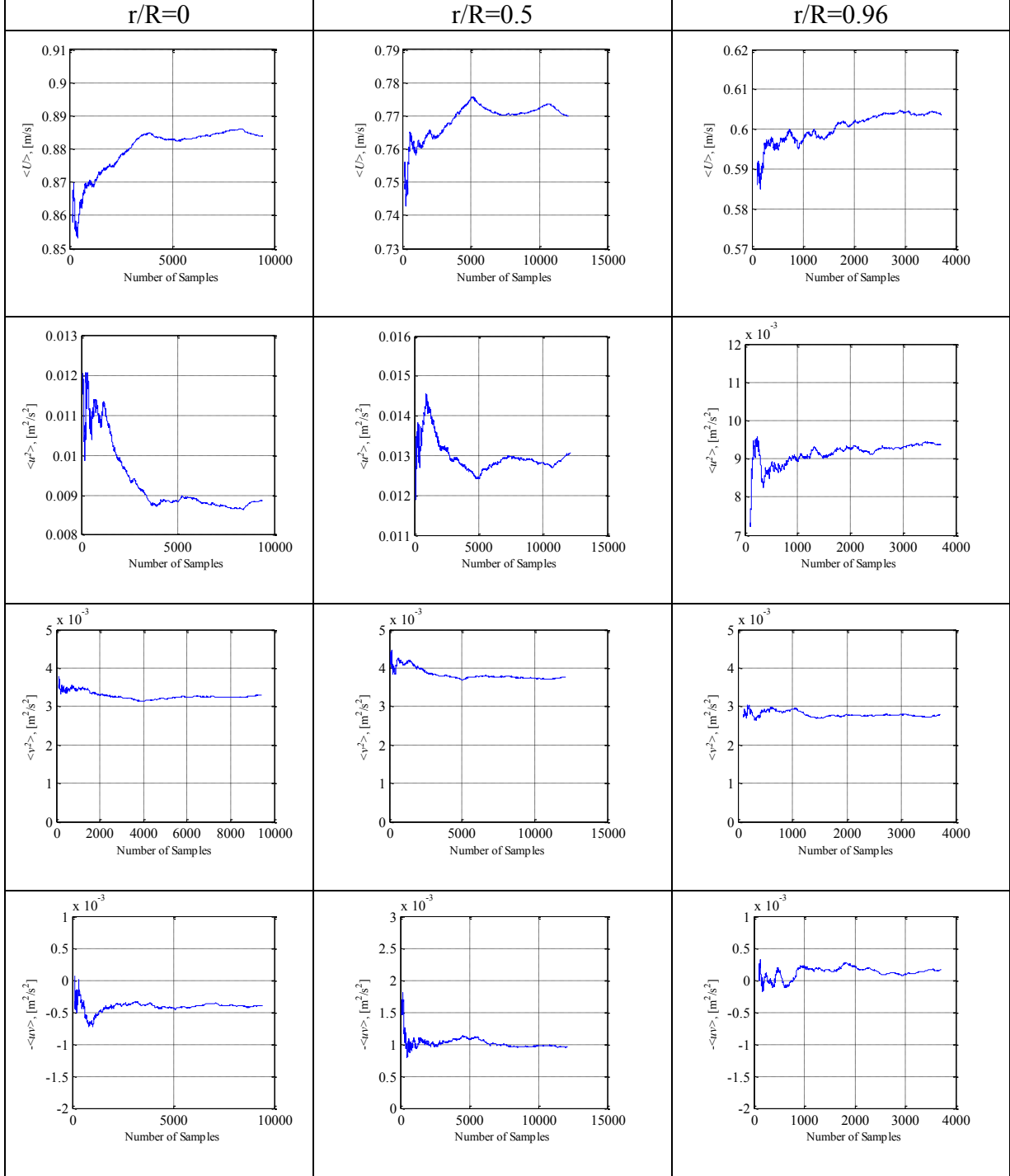
Re=100,000 – Solid (2mm – 0.8 %)



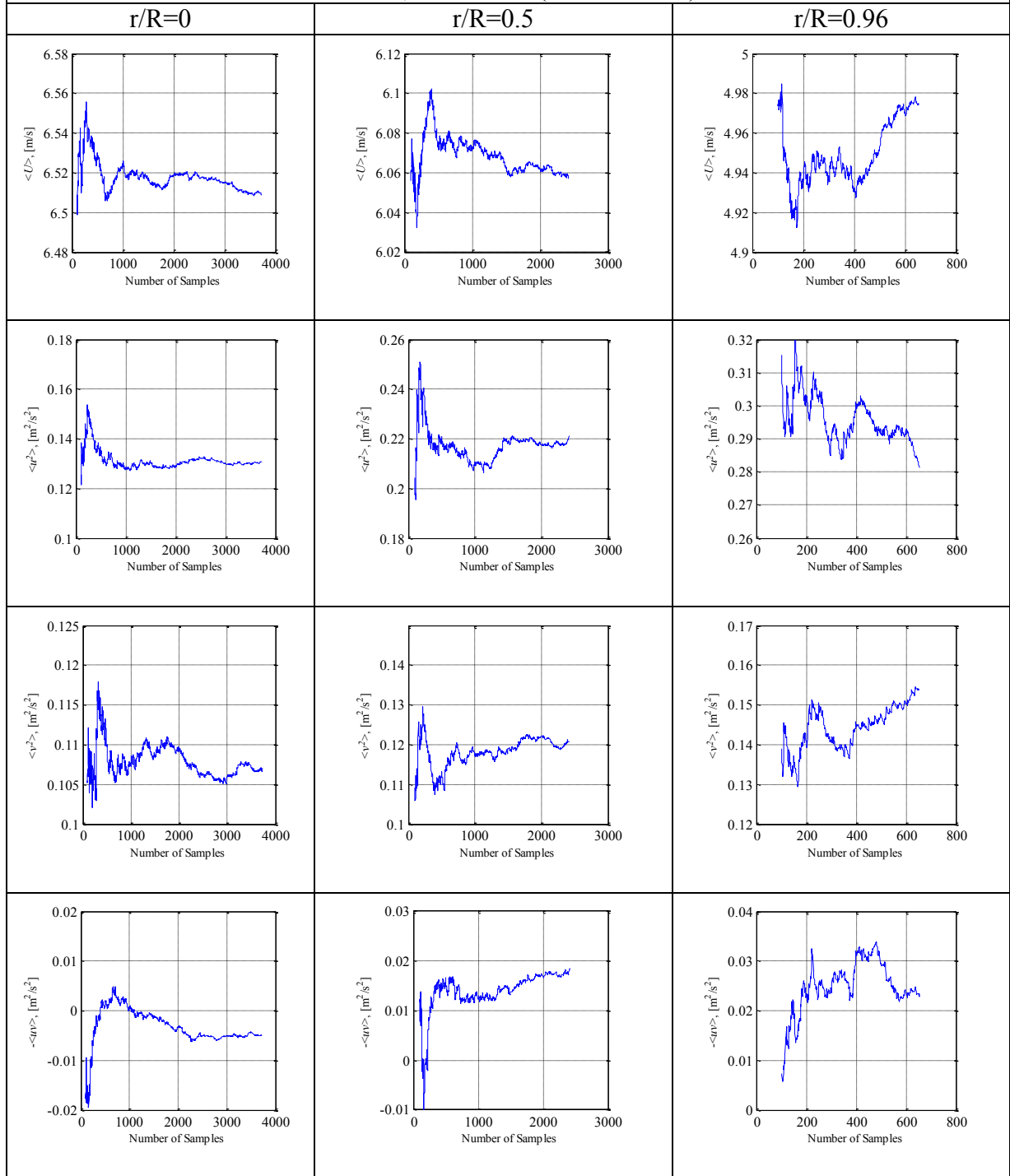
Re=100,000 – Solid (2mm – 1.6 %)



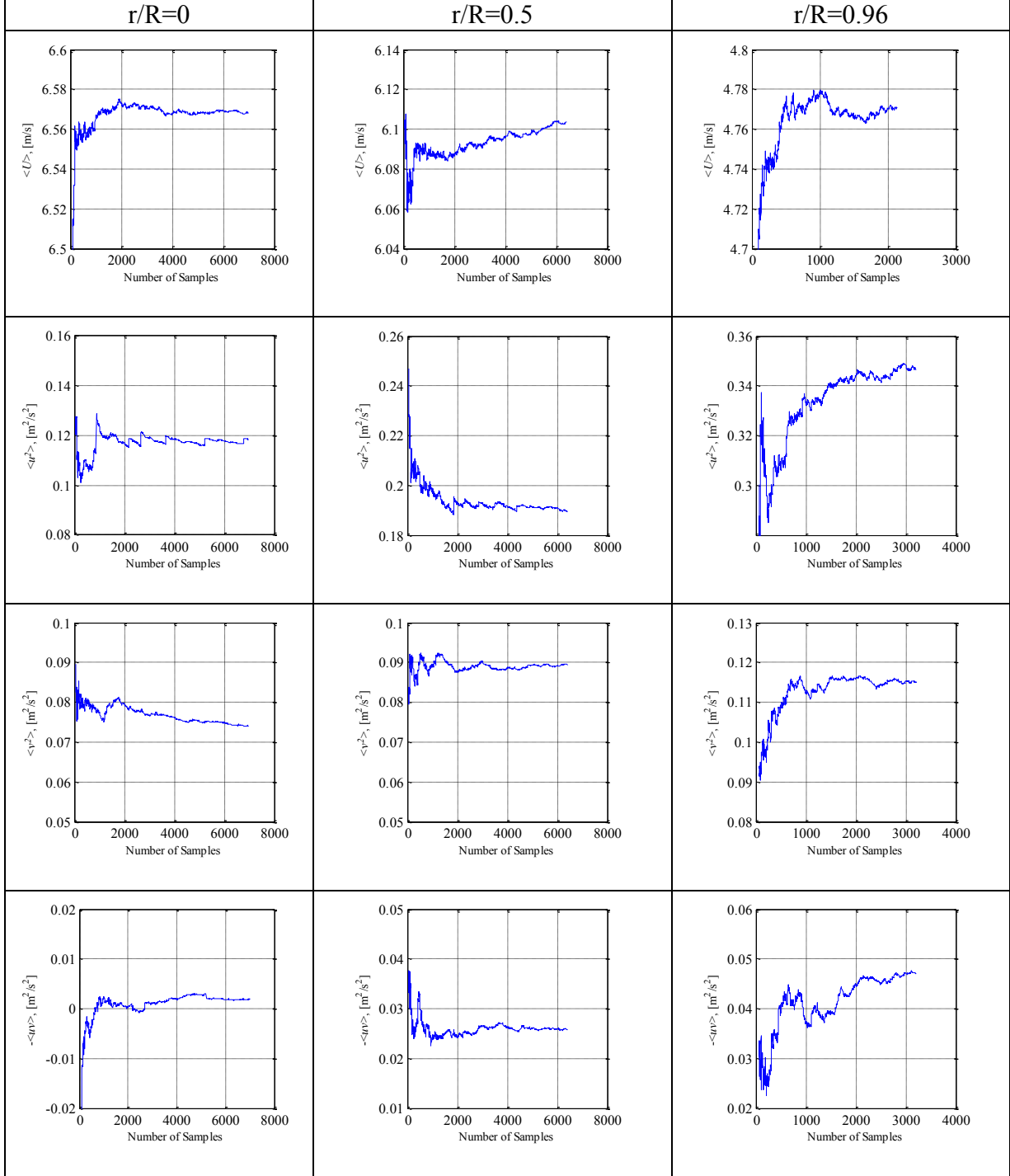
Re=52,000 – Solid (2mm – 1.6 %)



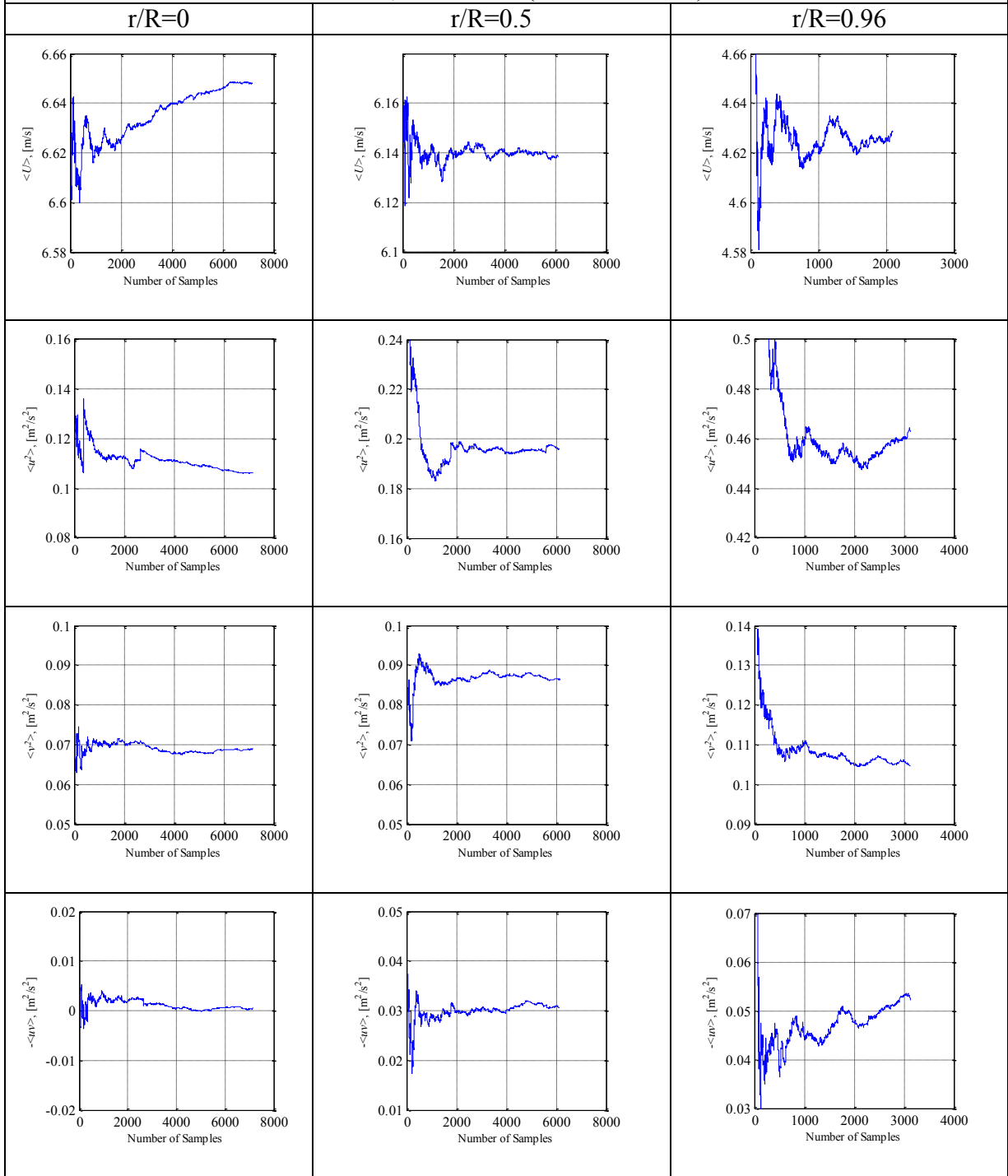
Re=320,000 – Solid (2mm – 0.8 %)



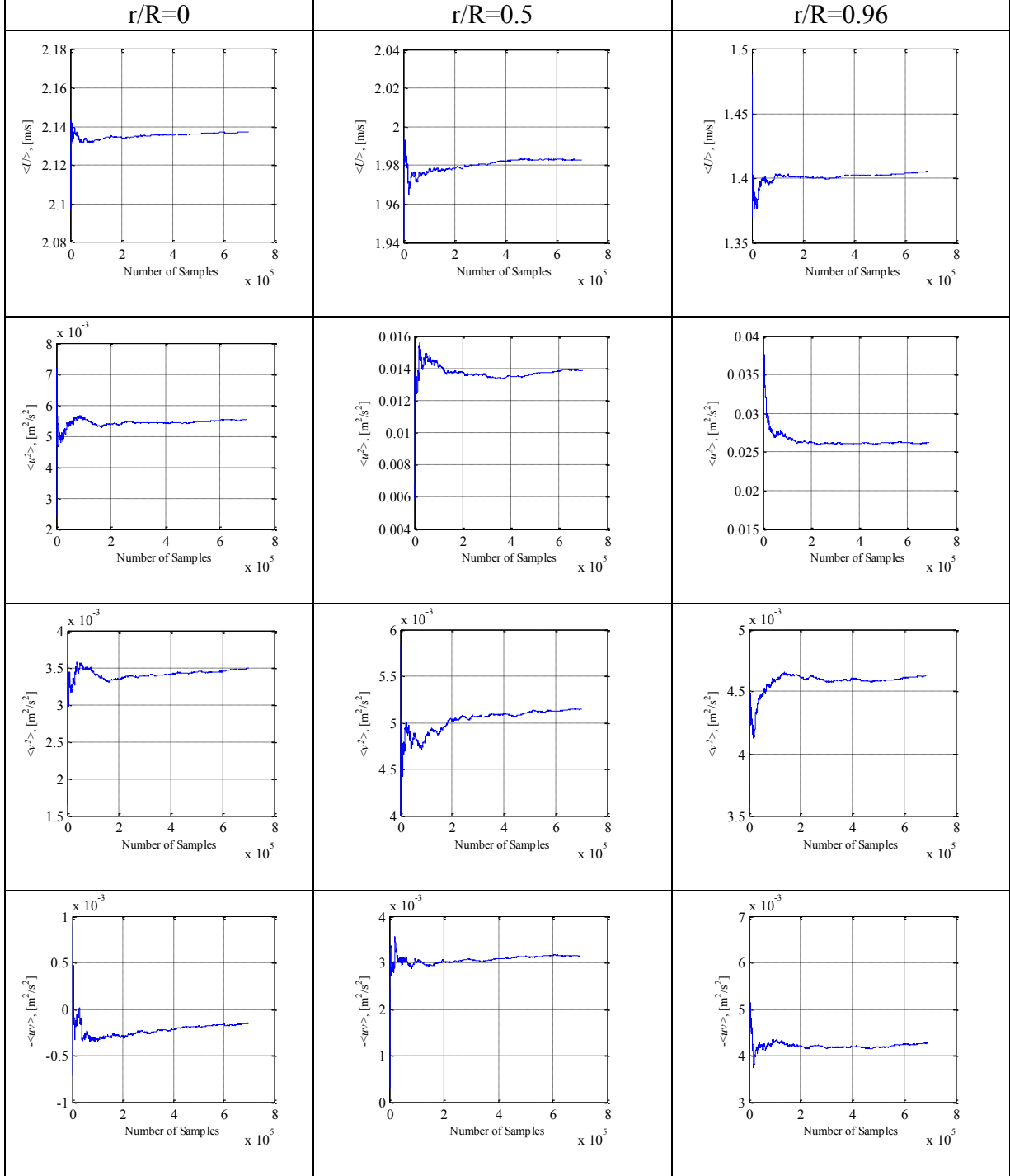
Re=320,000 – Solid (1mm – 0.4 %)



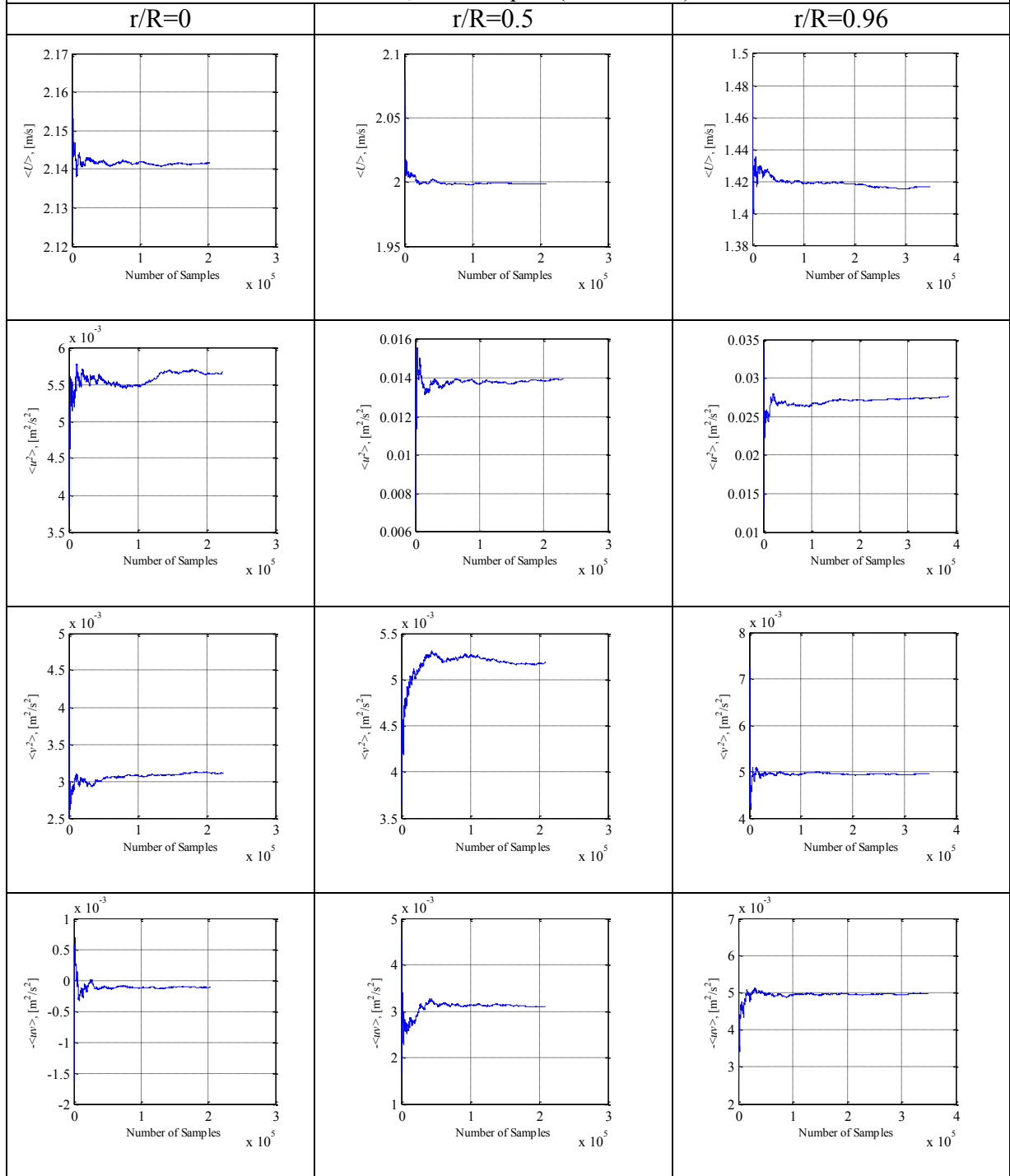
Re=320,000 – Solid (0.5mm – 0.1 %)



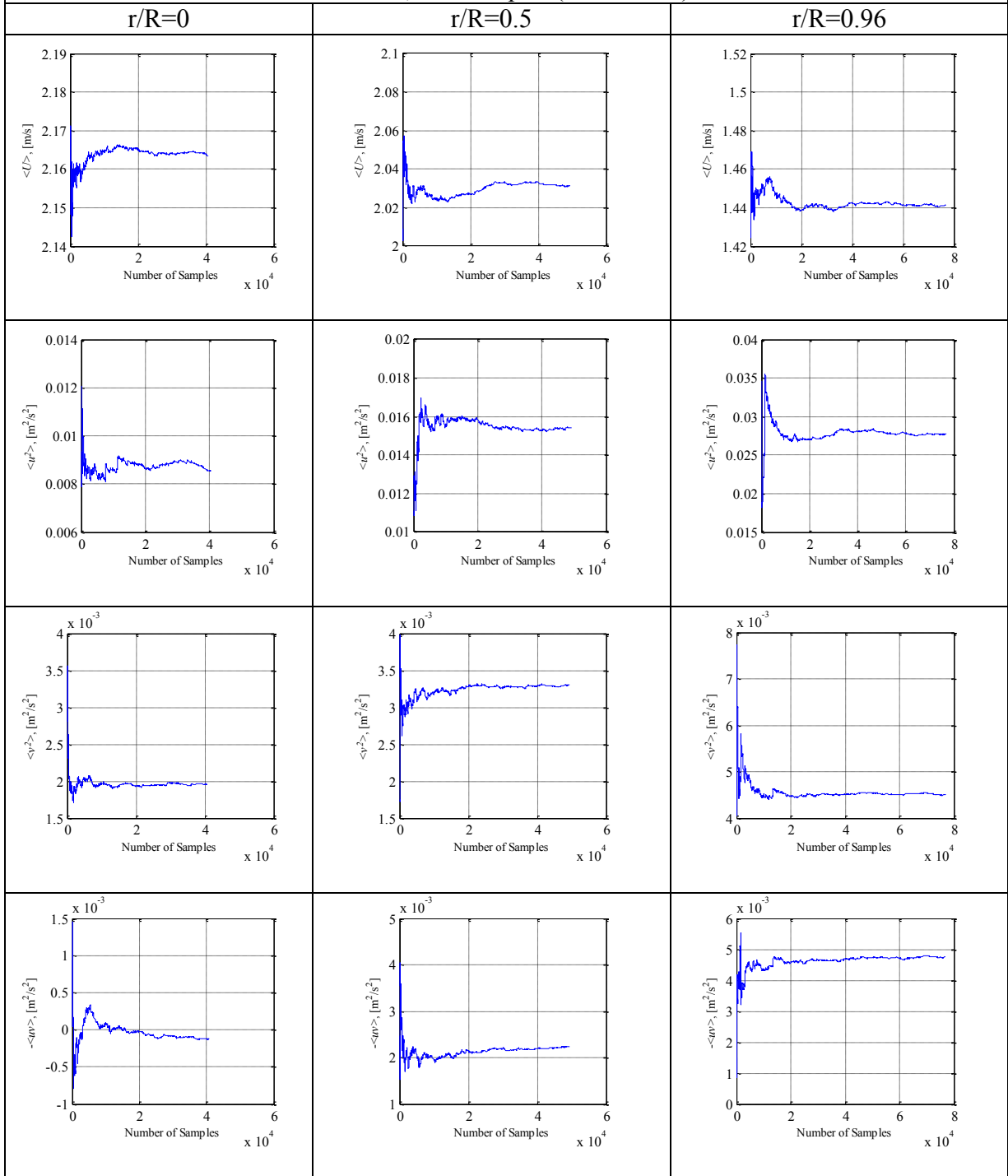
Re=100,000 – Liquid (Unladen)



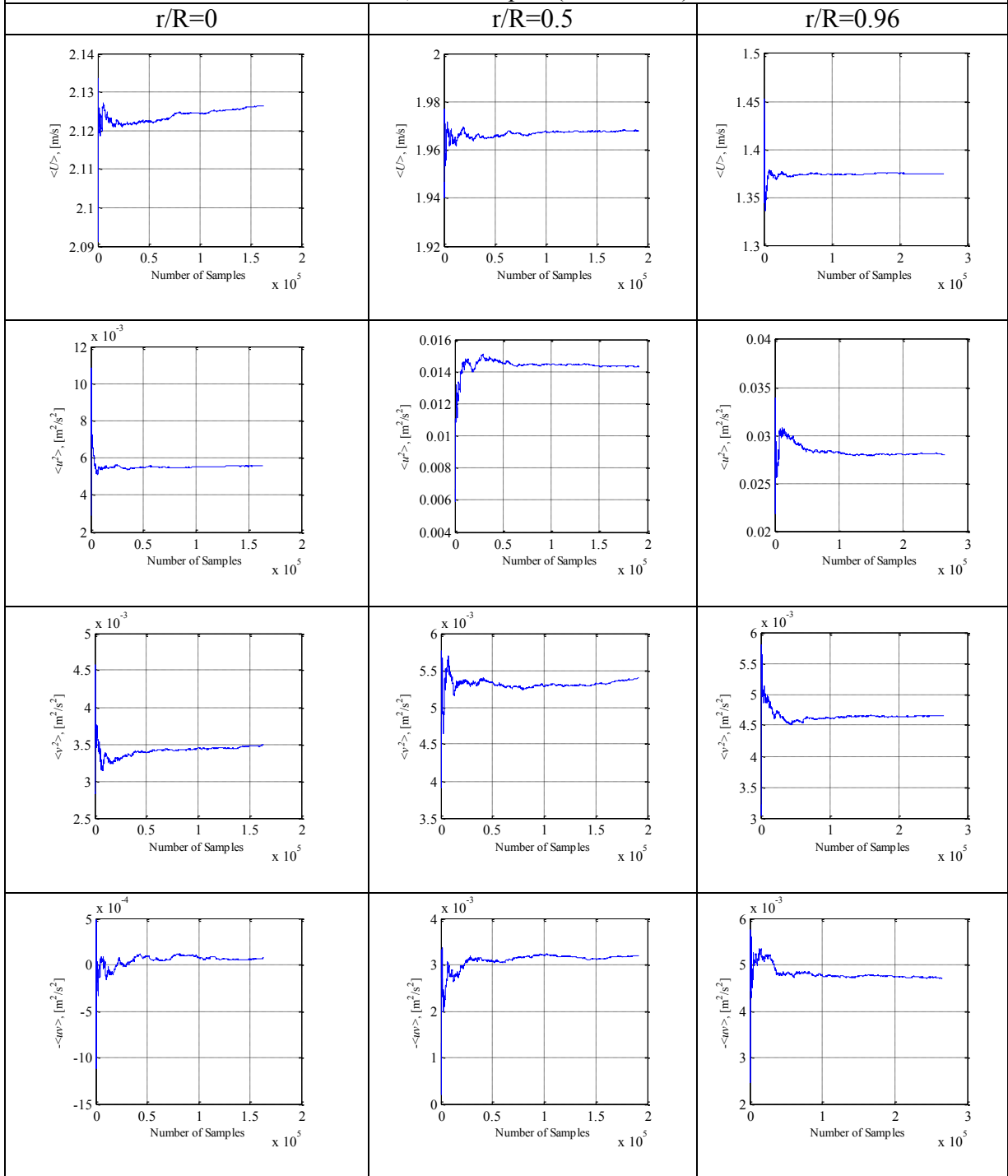
Re=100,000 – Liquid (2mm-0.8%)



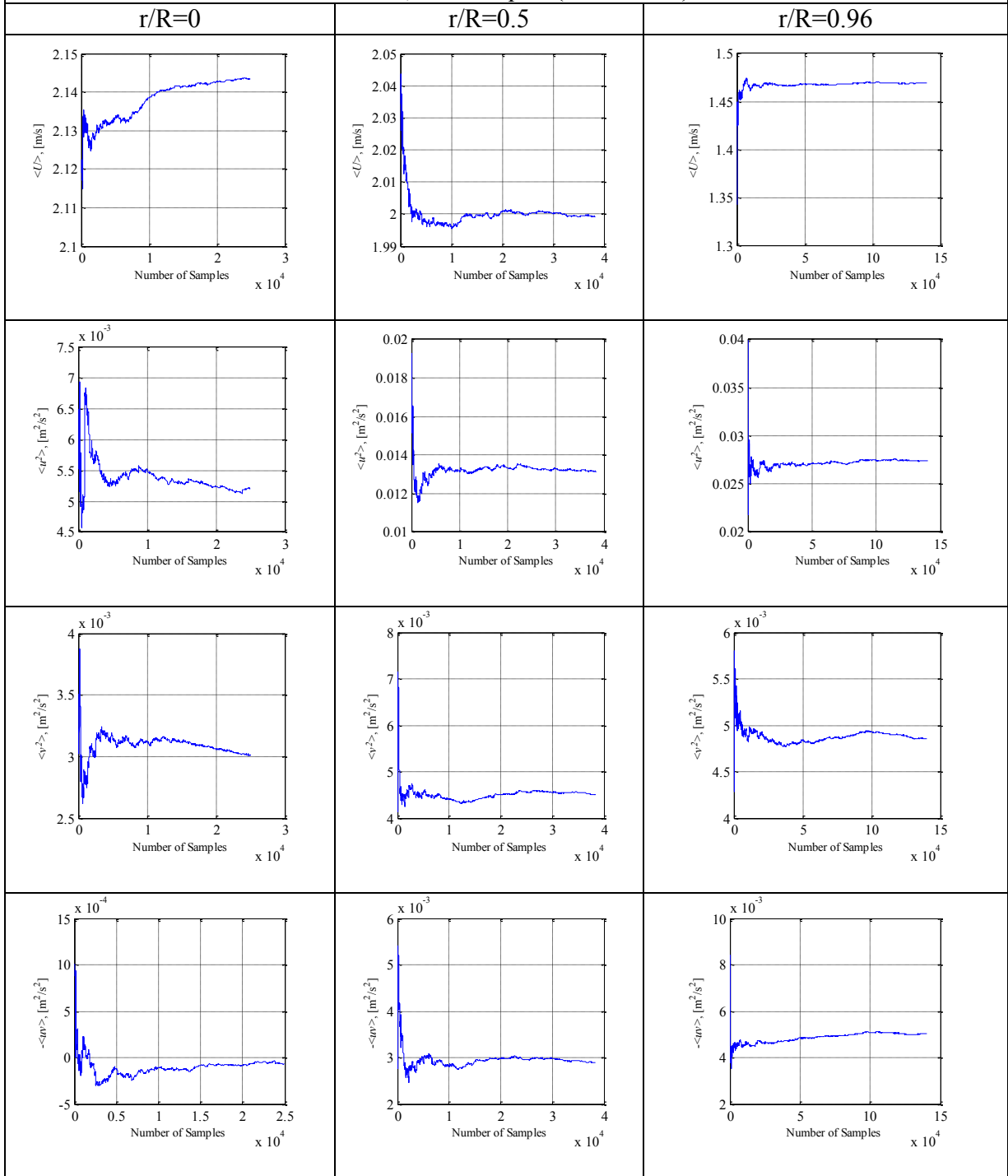
Re=100,000 – Liquid (2mm-1.6%)



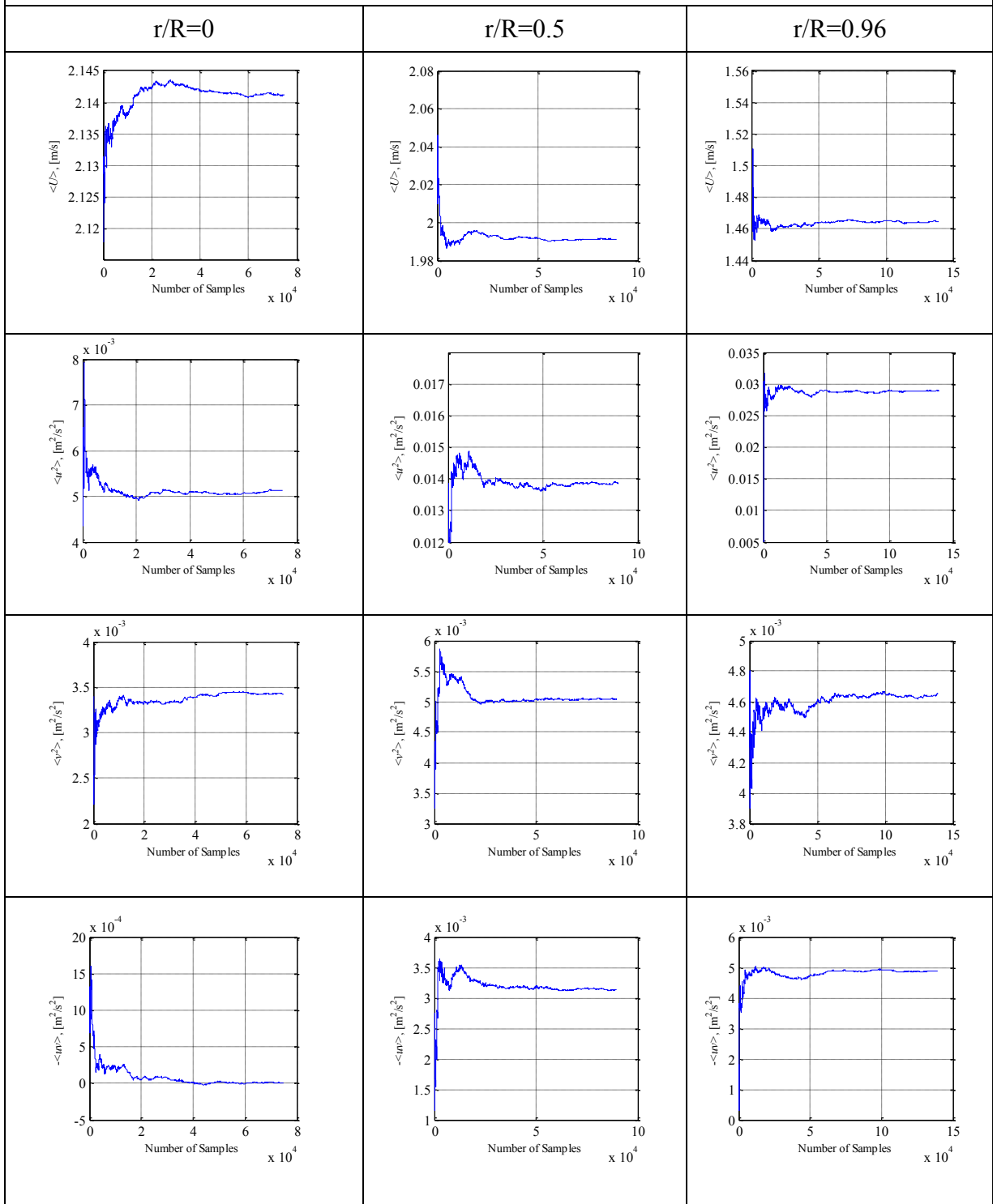
Re=100,000 – Liquid (1mm-0.2%)



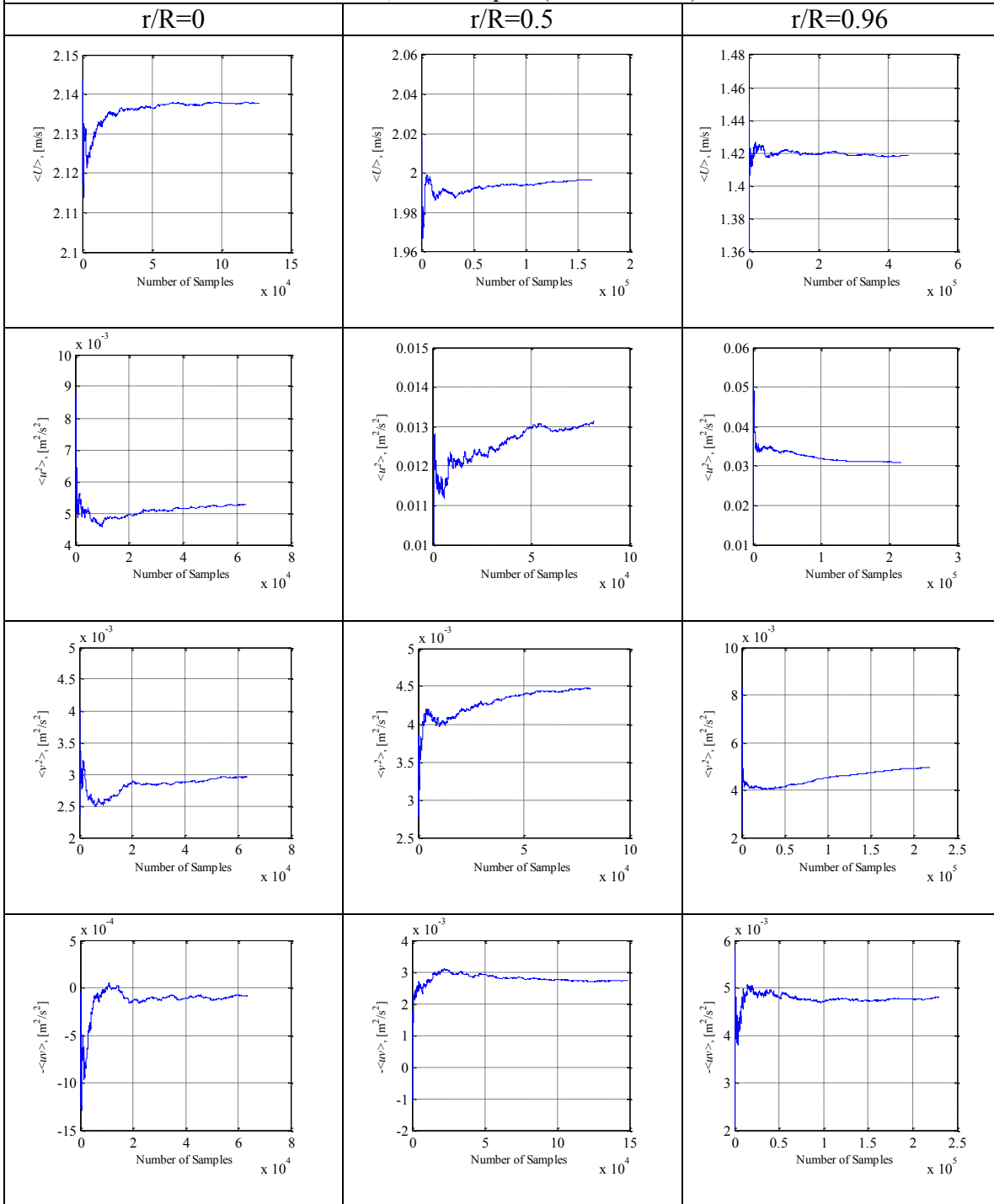
Re=100,000 – Liquid (1mm-0.4%)



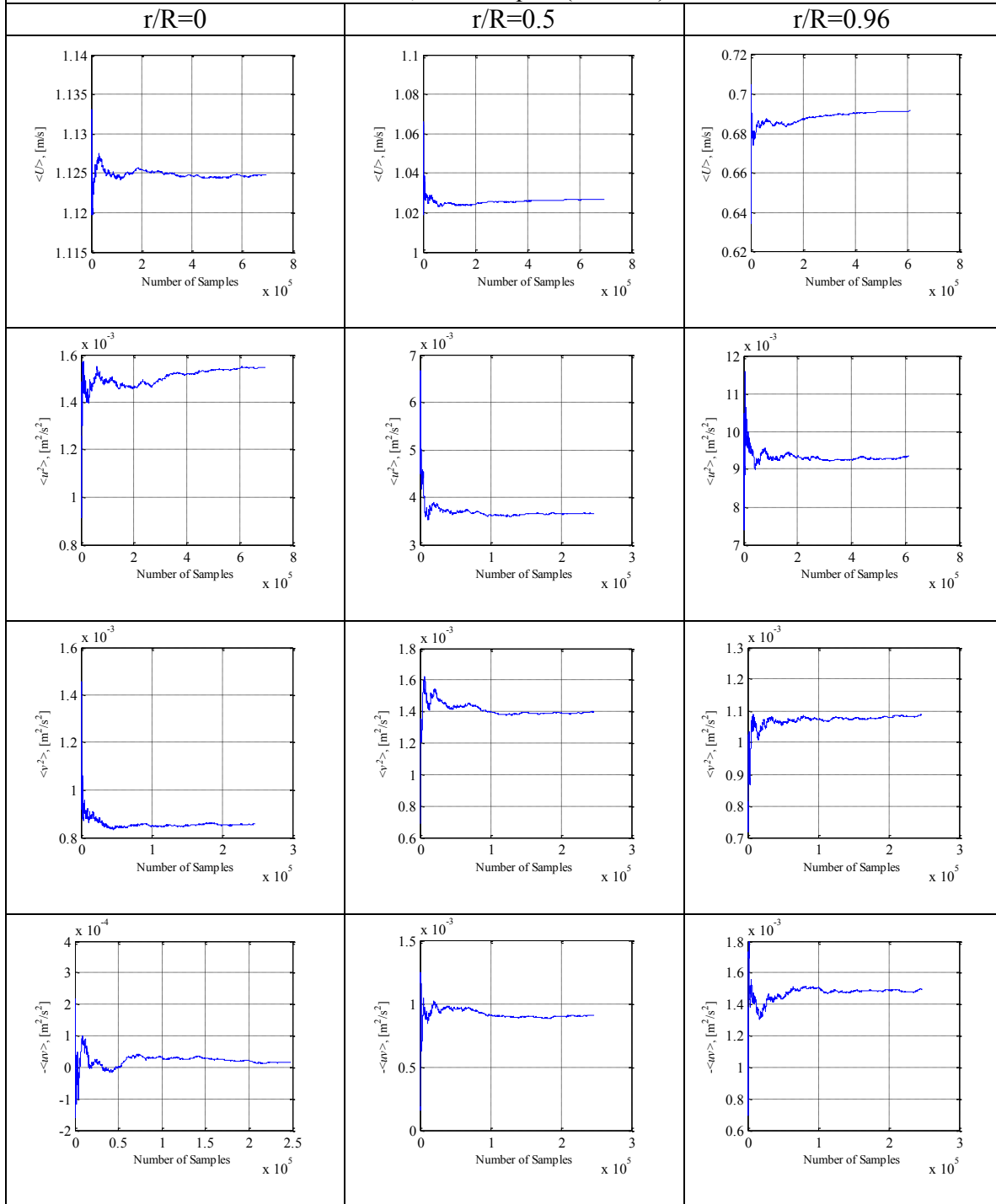
Re=100,000 – Liquid (0.5mm-0.05%)



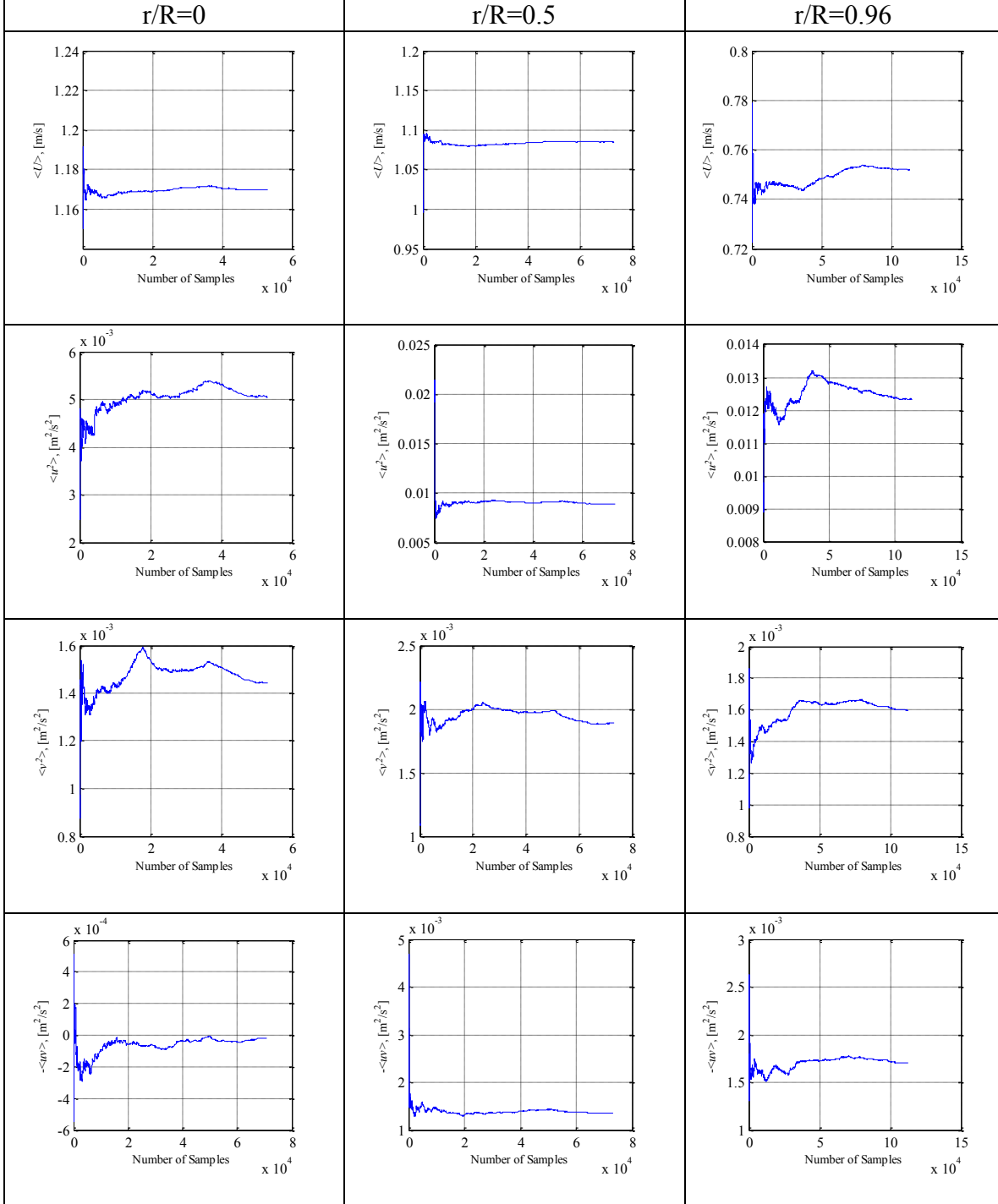
Re=100,000 – Liquid (0.5mm-0.1%)



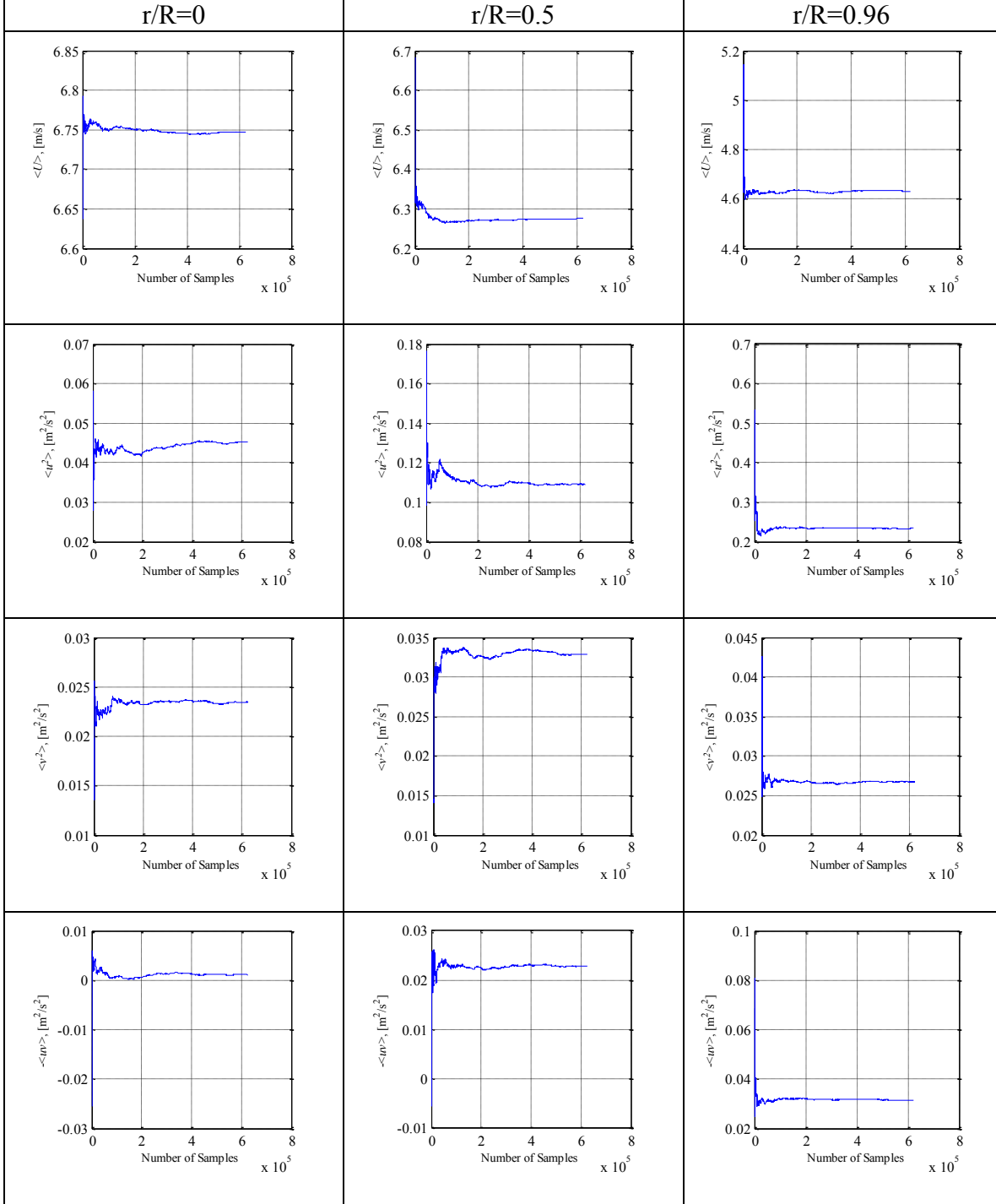
Re=52,000 – Liquid (unladen)

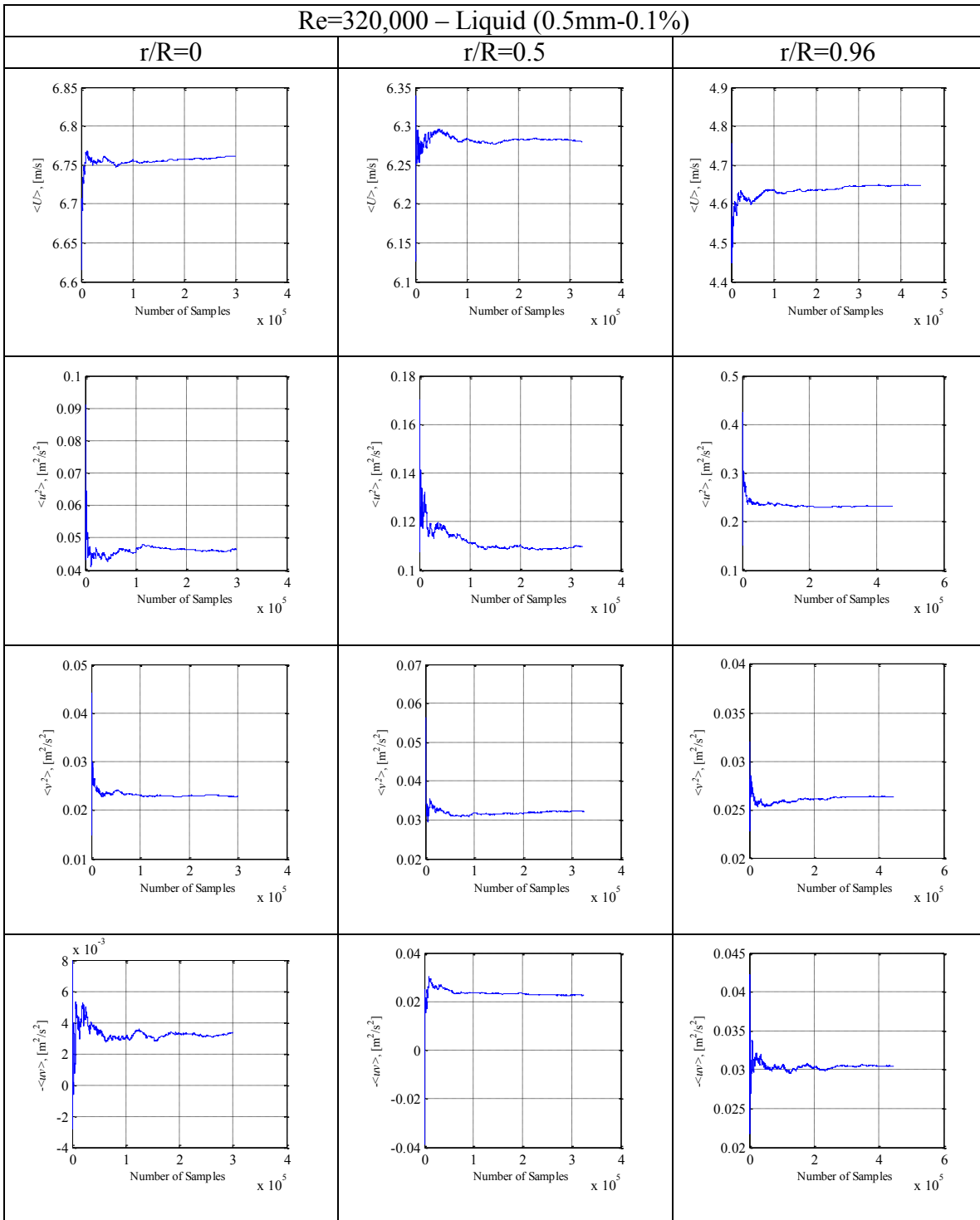


Re=52,000 – Liquid (2mm-1.6%)

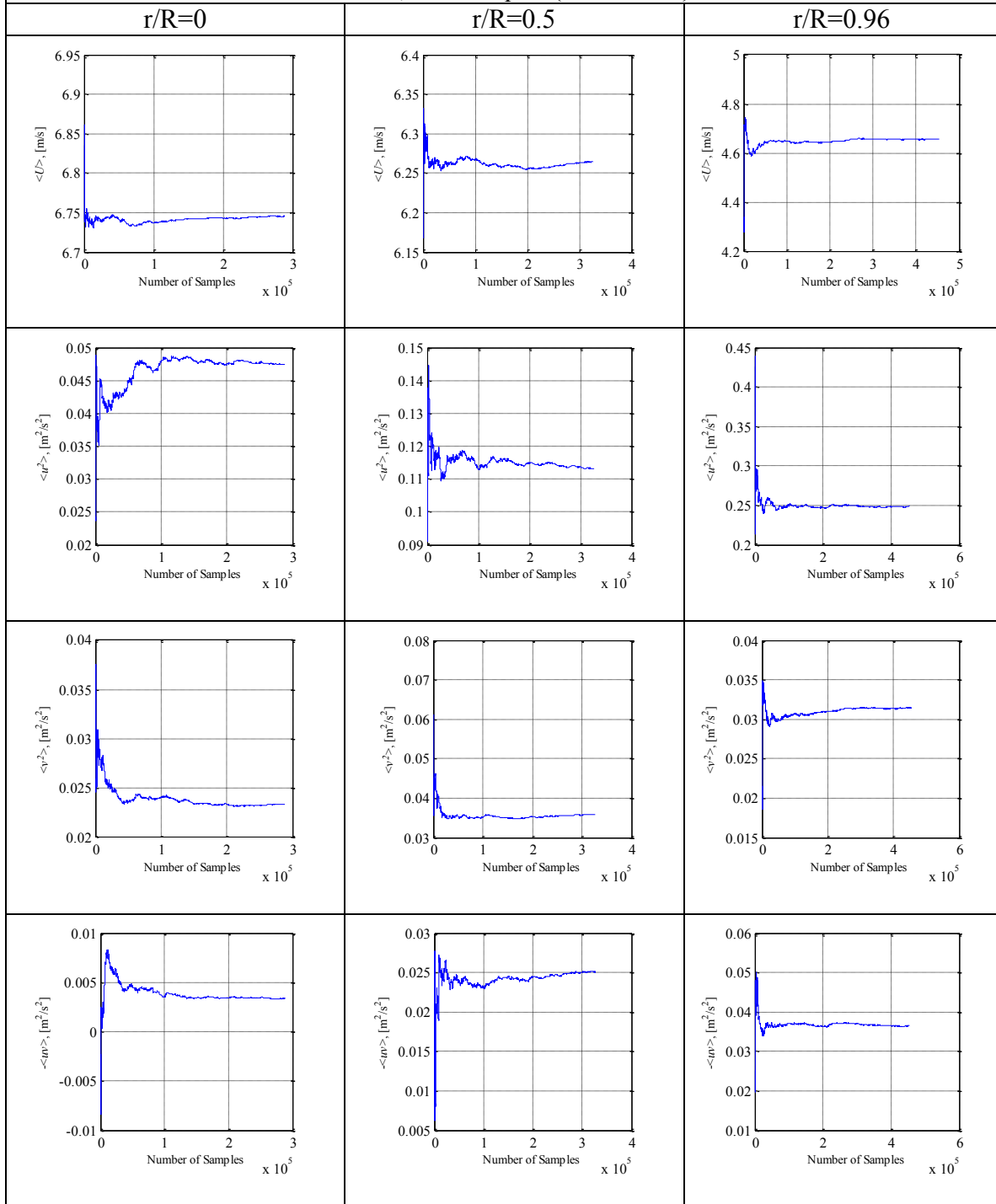


Re=320,000 – Liquid (Unladen)

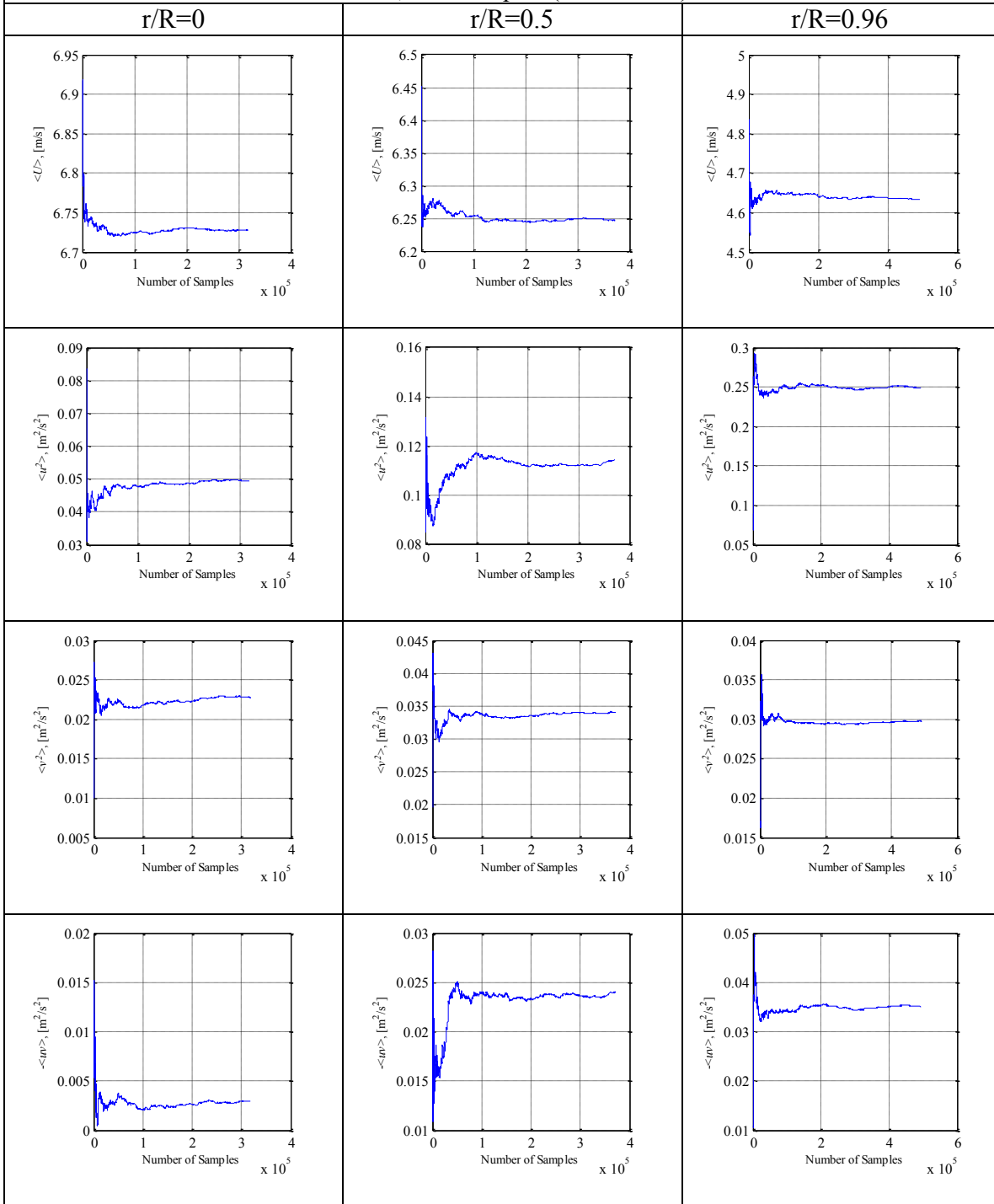




Re=320,000 – Liquid (1mm-0.4%)



Re=320,000 – Liquid (2mm-0.8%)



Appendix F. PIV/PTV Matlab Code

In this appendix, the Matlab codes used for particle detection and tracking are provided.

Particle detection and masking for PIV: all the in-focus and out-of-focus glass beads are first detected. Then they are marked with slightly higher intensity in the images. Finally the marked images are stored in new TIFF files. The modified images will be imported into the Davis 8.1 for PIV processing.

```
clear all;
close all;
clc;
filelist2=dir('the directory to the folder\*.im7');
count_img=length(filelist2);
save filelist2.mat;
for count=1:2:count_img-1
    vecname1= 'the directory to the folder \';
    vecname2=strcat(vecname1,filelist2(count).name);
    v=loadvec(vecname2);
    str1=sprintf('total No. of Images to be processed =%d',count_img);
```

```

disp(str1);

count

img1=v.w;

img1=imrotate(img1,90);

newRange =1;

imgMin = 0;

imgMax = double(max(img1(:)));

%rescaling the image to 0 to 1

img1 = (img1 - imgMin) / (imgMax - imgMin) * newRange;

img1=imadjust(img1,[0.01 0.3],[1]);

edgethresh=0.03;

rmax=50;

rmin=35;

method='phasecode';

disp(' finding circles starts...img_1');

[c, r] = imfindcircles(img1,[rmin rmax],
'Sensitivity',0.95,'Edgethreshold',edgethresh,'method',method);

disp('End of finding circles...img_1');

%Omitting the particles close to the image borders

k=1;

c_pix_1=0;

r_pix_1=0;

for i=1:size(r,1)

    c_x=(c(i,2));

    c_y=c(i,1);

```

```

    r_i=r(i);
    if c_x+r_i<size(img1,1)-3 && c_y+r_i<size(img1,2)-5 && c_x-r_i>20 && c_y-
r_i>3
        c_pix_1(k,2)=c_x;
        c_pix_1(k,1)=c_y;
        r_pix_1(k)=r_i;
        k=k+1;
    end
end
clear c;
clear r;
vecname1= 'the directory to the folder \';
vecname2=strcat(vecname1,filelist2(count+1).name);
v=loadvec(vecname2);
img2=v.w;
img2=imrotate(img1,90);
newRange =1;
imgMin = 0;
imgMax = double(max(img2(:)));
%// rescaling the image to 0 to 1
Img2 = (img2 - imgMin) / (imgMax - imgMin) * newRange;
Img2=imadjust(img2,[0.01 0.3],[]);
edgethresh=0.03;
rmax=50;
rmin=35;

```

```

method='phasecode';

disp(' finding circles starts...img_1');

[c, r] = imfindcircles(img2,[rmin rmax],
'Sensitivity',0.95,'Edgethreshold',edgethresh,'method',method);

disp('End of finding circles...img_2');

%omitting the particles close to the borders of the image

k=1;

c_pix_2=0;

r_pix_2=0;

for i=1:size(r,1)

    c_x=(c(i,2));

    c_y=c(i,1);

    r_i=r(i);

    if c_x+r_i<size(img2,1)-3 && c_y+r_i<size(img2,2)-5 && c_x-r_i>5 && c_y-
r_i>3

        c_pix_2(k,2)=c_x;

        c_pix_2(k,1)=c_y;

        r_pix_2(k)=r_i;

        k=k+1;

    end

end

c_pix_2=c_pix_1;

r_pix_2=r_pix_1;

save('locus','c_pix_1','r_pix_1','c_pix_2','r_pix_2');

N_P(floor(count/2)+1)=length(r_pix_1);

save('N_P','N_P','count');

```

```

clear all;

%%%%%%%%%%Marking the IMAGE_1

load locus.mat;

load N_P.mat;

load filelist2.mat;

vecname1=' the directory to the folder \';

vecname2=strcat(vecname1,filelist2(count).name);

v=loadvec(vecname2);

img1=v.w;

img1=imrotate(img1,90);

newRange =1;

imgMin = 0;

imgMax = double(max(img1(:)));

img1 = (img1 - imgMin) / (imgMax - imgMin) * newRange; %// Scaling the image
intensity

size_img=size(img1);

img1=0.999*img1;

if ~isempty(r_pix_1) || ~isempty(r_pix_2)

    for i=1:size(r_pix_1,2);

        c_x=round(c_pix_1(i,2));

        c_y=round(c_pix_1(i,1));

        r_i=round(r_pix_1(i));

        img1(c_x-r_i:c_x+r_i,c_y)=1;

        img1(c_x,c_y-r_i:c_y+r_i)=1;

        for j=1:r_i

```

```

for k=1:r_i
    if sqrt(j^2+k^2)<=r_i
        img1(c_x+j,c_y+k)=1;
        img1(c_x-j,c_y+k)=1;
        img1(c_x+j,c_y-k)=1;
        img1(c_x-j,c_y-k)=1;
    end
end
end
end
end

```

```

for i=1:size(r_pix_2,2);
    c_x=round(c_pix_2(i,2));
    c_y=round(c_pix_2(i,1));
    r_i=round(r_pix_1(i))+1;
    img1(c_x-r_i:c_x+r_i,c_y)=1;
    img1(c_x,c_y-r_i:c_y+r_i)=1;
    for j=1:r_i
        for k=1:r_i
            if sqrt(j^2+k^2)<=r_i
                img1(c_x+j,c_y+k)=1;
                img1(c_x-j,c_y+k)=1;
                img1(c_x+j,c_y-k)=1;
                img1(c_x-j,c_y-k)=1;
            end
        end
    end
end

```

```

        end

    end

end

end

img1=im2uint16(img1);

img1=img1./16;

disp('saving img_1.....');

%%%%%%***** Saving Marked IMAGE_1
*****

fname2='The directory to the folder where you want to save the files\';

if count<10

    fname1=sprintf('img_final00000%d.tiff',count);

    fname3=strcat(fname2,fname1);

    imwrite(img1,fname3,'compression','none');

else if count>=10 && count<100

    fname1=sprintf('img_final0000%d.tiff',count);

    fname3=strcat(fname2,fname1);

    imwrite(img1,fname3,'compression','none');

else if count>=100 && count<1000

    fname1=sprintf('img_final000%d.tiff',count);

    fname3=strcat(fname2,fname1);

    imwrite(img1,fname3,'compression','none');

else if count>=1000 && count<10000

```

```

        fname1=sprintf('img_final00%d.tiff',count);

        fname3=strcat(fname2,fname1);

        imwrite(img1,fname3,'compression','none');

    else

        fname1=sprintf('img_final%0d.tiff',count);

        fname3=strcat(fname2,fname1);

        imwrite(img1,fname3,'compression','none');

    end

end

end

end

clear all;

%   %%%*****marking particles in IMAGE_2

load N_P.mat;

load filelist2.mat;

load locus;

vecname1 = '\the directory to the folder\';

vecname2=strcat(vecname1,filelist2(count+1).name);

v=loadvec(vecname2);

img1=v.w;

img1=imrotate(img1,90);

newRange =1;

imgMin = double(min(img1(:)));

imgMax = double(max(img1(:)));

```

```

img1 = (img1 - imgMin) / (imgMax - imgMin) * newRange;

img1=0.999*img1;

if ~isempty(r_pix_1) || ~isempty(r_pix_2)

    for i=1:size(r_pix_1,2);

        c_x=round(c_pix_1(i,2));

        c_y=round(c_pix_1(i,1));

        r_i=round(r_pix_1(i))+1;

        img1(c_x-r_i:c_x+r_i,c_y)=1;

        img1(c_x,c_y-r_i:c_y+r_i)=1;

        for j=1:r_i

            for k=1:r_i

                if sqrt(j^2+k^2)<=r_i

                    img1(c_x+j,c_y+k)=1;

                    img1(c_x-j,c_y+k)=1;

                    img1(c_x+j,c_y-k)=1;

                    img1(c_x-j,c_y-k)=1;

                end

            end

        end

    end

end

for i=1:size(r_pix_2,2);

    c_x=round(c_pix_2(i,2));

    c_y=round(c_pix_2(i,1));

    r_i=round(r_pix_2(i));

```

```
img1(c_x-r_i:c_x+r_i,c_y)=1;
img1(c_x,c_y-r_i:c_y+r_i)=1;
for j=1:r_i
    for k=1:r_i
        if sqrt(j^2+k^2)<=r_i
            img1(c_x+j,c_y+k)=1;
            img1(c_x-j,c_y+k)=1;
            img1(c_x+j,c_y-k)=1;
            img1(c_x-j,c_y-k)=1;
        end
    end
end
end
end
end
end
img1=im2uint16(img1);
img1=img1./16;

disp('saving img_2.....');

%%%%%%***** Saving Marked IMAGE_2
*****

fname2='The directory to the folder where you want to save the files\';

if count+1<10
    fname1=sprintf('img_final00000%d.tiff',count+1);
    fname3=strcat(fname2,fname1);
```

```

imwrite(img1,fname3,'compression','none');

else if count+1>=10 && count+1<100

    fname1=sprintf('img_final0000%d.tiff',count+1);

    fname3=strcat(fname2,fname1);

    imwrite(img1,fname3,'compression','none');

else if count+1>=100 && count+1<1000

    fname1=sprintf('img_final000%d.tiff',count+1);

    fname3=strcat(fname2,fname1);

    imwrite(img1,fname3,'compression','none');

else if count+1>=1000 && count+1<10000

    fname1=sprintf('img_final00%d.tiff',count+1);

    fname3=strcat(fname2,fname1);

    imwrite(img1,fname3,'compression','none');

else

    fname1=sprintf('img_final%0d.tiff',count+1);

    fname3=strcat(fname2,fname1);

    imwrite(img1,fname3,'compression','none');

end

end

end

end

clear all;

clc;

delete locus.mat

load N_P.mat;

```

```
load filelist2.mat;

end

clear all;
```

Particle Tracking Code: First the in-focus particles are detected. Then the particles are paired in two frames to obtain the displacements. Finally the velocity vector is obtained by having δt (the time difference between the frames).

```
%%%%%*****In-Focus Particle Detection *****

clear all;

close all;

clc;

filelist2=dir('E:\The directory\*.im7');
count_img=length(filelist2);
save filelist2.mat;
for count=1:count_img-1

    vecname1='E:\The directory\';
    vecname2=strcat(vecname1,filelist2(count).name);
    v=loadvec(vecname2);

    str1=sprintf(' No. of Images to be processed =%d',count_img);
    disp(str1);

    count
```

```

img1=v.w;

img1=imrotate(img1,90);

newRange =1;

imgMin = 0;

imgMax = double(max(img1(:)));

%rescaling the image to 0 to 1

img1 = (img1 - imgMin) / (imgMax - imgMin) * newRange;

img1=imadjust(img1,[0.01 0.3],[[]]);

edgethresh=0.3;

rmax=50;

rmin=35;

method='phasecode';

disp(' finding circles starts...img_1');

[c, r] = imfindcircles(img1,[rmin rmax],
'Sensitivity',0.95,'Edgethreshold',edgethresh,'method',method);

disp('End of finding circles...img_1');

c1=c;

r1=r;

save('locus_temp.mat','c1','r1');

save('count1','count');

clear all;

load count1.mat;

load filelist2.mat;

vecname1='E:\The directory\';

```

```

vecname2=strcat(vecname1,filelist2(count+1).name);

v=loadvec(vecname2);

clear filelist2;

img1=v.w;

img1=imrotate(img1,90);

newRange =1;

imgMin = 0;

imgMax = double(max(img1(:)));

%rescaling the image to 0 to 1

img1 = (img1 - imgMin) / (imgMax - imgMin) * newRange;

img1=imadjust(img1,[0.01 0.3],[1]);

edgethresh=0.3;

rmax=50;

rmin=35;

method='phasecode';

disp(' finding circles starts...img_2');

[c, r] = imfindcircles(img1,[rmin rmax],
'Sensitivity',0.95,'Edgethreshold',edgethresh,'method',method);

disp('End of finding circles...img_2');

c2=c;

r2=r;

load locus_temp;

save('locus_temp','c1','r1','c2','r2');

clear all;

load count1.mat;

```

```

disp('saving .....');

count1=(count+1)/2;

disp('saving the Data.....');

%%%%%%%%*****Saving the detected particles' Data*****

    if count1<10

        movefile('locus_temp.mat',sprintf('locus_0000%d.mat',count1));

    else if count1>=10 && count1<100

        movefile('locus_temp.mat',sprintf('locus_0000%d.mat',count1));

    else if count1>=100 && count1<1000

        movefile('locus_temp.mat',sprintf('locus_000%d.mat',count1));

    else if count1>=1000 && count1<10000

        movefile('locus_temp.mat',sprintf('locus_00%d.mat',count1));

    else

        movefile('locus_temp.mat',sprintf('locus_0%d.mat',count1));

    end

end

end

end

movefile('locus_*.mat','I:\the directory of destination');

load filelist2.mat;

```

```

clc;

end

clear all;

%%%%%%*****particle pairing*****

clear all;

close all;

clc

pwd='E:\the directory';

file_loc=strcat(pwd,'\loc*.mat');

filelist1=dir(file_loc);

count_img=length(filelist1);

s=struct('vp',[,]);

save filelist1.mat;

disp('calculating particle velocity.....>>>>');

fprintf('\n Total No. of files to be processec = %d',count_img);

fprintf('\n');

for count=1:count_img

file_name=strcat(pwd,'/',filelist1(count).name);

load(file_name);

cp1=0;

%%%%%%%%%%%%%% Particle pairing section

if ~isempty(c1)&& ~isempty(c2)

for j=1:length(c1(:,1))

```

```

for k=1:length(c2(:,1))

    if abs(c1(j,1)-c2(k,1))<4 && (c1(j,2)-c2(k,2))<20 && (c1(j,2)-c2(k,2))>3

        cp1(end+1,1:2)=c1(j,1:2);

        cp1(end,3:4)=c2(k,1:2);

        cp1(end,5)=r1(j,1);

        cp1(end,6)=r2(k,1);

    end

end

end

cp1(1,:)=[];

if length(cp1)>0

%%%%%% particle velocity calc. loading to the stuct of s(i).vp (struct)*****

%%%%%% vp has 12 columns: 1st column: Pixel location of center(r-direction) in
frame#1.... 2nd Col: Pixel location of center (x-Direction) in frame#1.... 3rdCol: Pixel
location of center (r-direction) in frame#2...4th col: Pixel direction (x-Direction) in
frame#2.....5th col: radius of particle in pixel in frame#1... 6th Col.: radius of particle
in pixel in frame#2... 7th col: Delta_pix in r-direction....8th Col: Delta_pix in x-direction....
9th col: Velocity in r-direction.... 10th Col: Velocity in x-direction..... 11th Col: r
in mm...12th Col: x in mm

calib=0.0240e-3;%%%%%% m/pix

dt=200e-6;%%%%%% dt between images

cp1(:,7)=cp1(:,1)-cp1(:,3);%%%%%% Delta pix in r direction

cp1(:,8)=cp1(:,2)-cp1(:,4);%%%%%% Delta pix in x-direction

cp1(:,9)=-1*cp1(:,7)*calib/dt;%%%%%% vx (m/s)

cp1(:,10)=cp1(:,8)*calib/dt;%%%%%% vy (m/s)

```

```

cp1(:,11)=-calib*(cp1(:,1)-130)+25.3;%%%%%%%% r- direction
cp1(:,12)=cp1(:,2)*2*calib*1e3;%%%%%%%% x-direction
%%%%%%%%
s(end+1).vp=cp1;
end
clear ('r2','r1','c2','c1','cp1');
end
if count>1
for j=0:log10(count-1)
fprintf('\b'); % delete previous counter display
end
end
fprintf('%d',count);
end
fprintf('\n');
s(1)=[];
save ('struc_vp.mat','s');
clear all;

%%%%%%%%Applying the Delta-r Filter%%%%%%%%
dr_max=0.5;
load struc_vp;
for i=1:length(s)
    del_i=[];
    del_i=find(abs(s(1,i).vp(:,5)-s(1,i).vp(:,6))>dr_max);

```

```

        if ~isempty(del_i) && ~isempty(s(1,i).vp)

            s(1,i).vp(del_i,:)=[];

        end

    end

end

save struc_vp_filter_delta_r.mat

%%%%%%Computing the particle's turbulence statistics%%%%%%%%

clear all;

clc;

load struc_vp_filter_delta_r;

R=25.3;

N_point=13;

X0=-2.81;

Xend=25.3;

dx=(Xend-X0)/N_point;

x=linspace(X0,Xend,N_point+1);

x(end)=[];

x=x+0.5*dx;

%%%%%%%%

s_f=struct('vp_y_final',[],'vp_x_final',[],'delta_pix_y',[],'delta_pix_x',[]);

N_P(1:length(x))=0;

for i=1:length(x)-1

    s_f(end+1).vp_y_final=[];

    s_f(end).vp_x_final=[];

    s_f(end).delta_pix_y=[];

    s_f(end).delta_pix_x=[];

end

```

```

end

for k=1:length(x)
    for i=1:length(s);
        for j=1:length(s(i).vp(:,1))
            if s(i).vp(j,11)>=x(k)-dx/2 && s(i).vp(j,11)<x(k)+dx/2
                N_P(k)=N_P(k)+1;
                s_f(k).vp_x_final(end+1)=s(i).vp(j,9);
                s_f(k).vp_y_final(end+1)=s(i).vp(j,10);
                s_f(k).delta_pix_x(end+1)=s(i).vp(j,7);
                s_f(k).delta_pix_y(end+1)=s(i).vp(j,8);
            end
        end
    end
end

clc;

disp('calculating the velocity at the grid points.....>>>>');

fprintf('\n counter = %d out of %d',k,length(x));

end

save ('struc_vp_final.mat','s_f','x','N_P');

clear all;

%%%%%%%%%%%%%%

load struc_vp_final.mat;

vp_y_mean=zeros(size(x));

vp_x_mean=zeros(size(x));

for i=1:length(x)

```

```

vp_y_mean(i)=mean(s_f(i).vp_y_final);
vp_x_mean(i)=mean(s_f(i).vp_x_final);
end
for i=1:length(x)
s_f(i).vp_u=(s_f(i).vp_y_final-vp_y_mean(i));
s_f(i).vp_v=(s_f(i).vp_x_final-vp_x_mean(i));
end
for i=1:length(x)
vp_u2_mean(i)=mean(s_f(i).vp_u.^2);
vp_v2_mean(i)=mean(s_f(i).vp_v.^2);
vp_uv_mean(i)=mean(s_f(i).vp_u.*s_f(i).vp_v);
end
N_total=sum(N_P);
save ('struc_vp_final.mat','s_f','x','N_P');
clear s_f;
%%%%%%%%%%%%%%
save vp_mean_fluc.mat;
fprintf('\n');
clear all;

```

Particle Size Distributions:

```

clear all;

close all;

clc;

load struc_vp_filter_delta_r;

drp=[];

disp('calculating the d_dp.....>>>>');

r1=[];

r2=[];

for i=1:length(s);

    for j=1:length(s(i).vp(:,1))

        r1(end+1)=s(i).vp(j,5);

        r2(end+1)=s(i).vp(j,6);

        drp(end+1)=s(i).vp(j,6)-s(i).vp(j,5);

    end

end

calib=0.024;%%%%%%%% mm/pix

r=(r1+r2)./2;

r_mm=r.*calib;

dp_mm=r_mm.*2;

min_dp=min(dp_mm);

max_dp=max(dp_mm);

mean_dp=mean(dp_mm);

N_total=length(dp_mm);

s_dp=struct('dp',[[]]);

```

```
n_interval=30;
d_dp=linspace(min_dp,max_dp,n_interval+1);
for i=1:length(d_dp)-1
    s_dp(end+1).dp=find(dp_mm>=d_dp(i) & dp_mm<d_dp(i+1));
end
s_dp(1)=[];
N_percent=0;
for i=1:length(s_dp)
    N_percent(end+1)=length(s_dp(i).dp)/N_total*100;
end
save('PSD.mat');
clear all;
```

PIV Code: The results of PIV from Davis 8.2 are imported to Matlab using PIVMAT 3.1. After importing the data, the velocity vector fields are trimmed and then

stored in a new file. Finally the averaging is applied to the velocity vector fields to obtain the mean and fluctuating velocity profiles.

```
%%% Preparing and Trimming the velocity vector field

close all;

clear all;

clc;

disp('>>>>>>>>>');

disp('Please wait.....');

disp('>>>>>>IMPORTING VC7 FILES TO MATLAB>>>>>>');

filelist=dir('*vc7');

count_img=length(filelist);

N_img=count_img;

save filelist.mat;

fprintf('\n Total No. of VC7 files to be loaded = %d',N_img);

fprintf('\n');

for count=1:N_img

v1(1,count)=loadvec(filelist(count).name);

if count==1

    x=v1(1,1).x;

    y=v1(1,1).y;

    x_shift=9.8;

    y_shift=abs(y(1));

    x=x+x_shift;
```

```
y=y+y_shift;

x_lim1=25.3;

x_lim2=0;

y_lim1=4;

y_lim2=20;

cut_x_1=find(x<x_lim1);

cut_x_2=find(x>x_lim2);

cut_y_1=find(y<y_lim1);

cut_y_2=find(y>y_lim2);

x(cut_x_2(1):cut_x_2(end))=[];

x(cut_x_1(1):cut_x_1(end))=[];

y(cut_y_2(1):cut_y_2(end))=[];

y(cut_y_1(1):cut_y_1(end))=[];

count_x_n=length(x);

count_y_n=length(y);

end

v(1,count).vx=v1(1,count).vx;

v(1,count).vy=v1(1,count).vy;

clear v1;

%%*** Trimming the cells

v(1,count).vx(cut_x_2(1):cut_x_2(end),:)=[];

v(1,count).vy(cut_x_2(1):cut_x_2(end),:)=[];

v(1,count).vx(cut_x_1(1):cut_x_1(end),:)=[];

v(1,count).vy(cut_x_1(1):cut_x_1(end),:)=[];

v(1,count).vx(:,cut_y_2(1):cut_y_2(end))=[];
```



```

vy_lim_min=0.001;
vx_lim=0.75*U_b;

%%%%%%***** Averaging for mean velocity profile

display('Averaging for mean velocity profile');

vx_ave=zeros(count_x_n,count_y_n);
vy_ave=zeros(count_x_n,count_y_n);
count_n_z=zeros(count_x_n,count_y_n);
fprintf('\n Total No. of rows to be processed = %d',count_x_n);
fprintf('\n');
for i=1:count_x_n
    if i>1
        for bk=0:log10(i-1)
            fprintf('\b'); % delete previous counter display
        end
    end
    fprintf('%d',i);

    for j=1:count_y_n
        count_non_zero=0;
        for k=1:N_img
            if v(k).vy(i,j) && v(k).vy(i,j)<vy_lim_max && v(k).vy(i,j)>vy_lim_min &&
abs(v(k).vx(i,j))<vx_lim

```

```

vx_ave(i,j)=vx_ave(i,j)+v(k).vx(i,j);

vy_ave(i,j)=vy_ave(i,j)+v(k).vy(i,j);

count_non_zero=count_non_zero+1;

end

end

count_n_z(i,j)=count_non_zero;

if ~count_non_zero

vx_ave(i,j)=0;

vy_ave(i,j)=0;

else

vx_ave(i,j)=vx_ave(i,j)/count_non_zero;

vy_ave(i,j)=vy_ave(i,j)/count_non_zero;

end

end

end

fprintf('\n');

vx_ave_mean=zeros(1,count_x_n);

vy_ave_mean=zeros(1,count_x_n);

for i=1:count_x_n

vx_ave_mean(1,i)=sum(vx_ave(i,:))/sum(vx_ave(i,:)~=0);

vy_ave_mean(1,i)=sum(vy_ave(i,:))/sum(vy_ave(i,:)~=0);

end

%%%%%%***** Producing average profiles--- Exp vs Theo for U/U_center profiles

x_1=1-abs(x/R);

```

```

U_c=max(vy_ave_mean);
U_theo=U_c*(x_1.^(1/n_power));
x_a_1=(-1:0.01:0);
vy_theo_1=(1-abs(x_a_1)).^(1/n_power);

%%%%%%***** Averaging for fluctuating velocity profiles

display('Averaging for fluctuating velocity');
u2=zeros(count_x_n,count_y_n);
v2=zeros(count_x_n,count_y_n);
uv=zeros(count_x_n,count_y_n);
count_n_z_1=zeros(count_x_n,count_y_n);
fprintf('\n Total No. of rows to be processed = %d',count_x_n);
fprintf('\n');
for i=1:count_x_n
    if i>1
        for bk=0:log10(i-1)
            fprintf('\b'); % delete previous counter display
        end
    end
    fprintf('%d',i);
    for j=1:count_y_n
        count_non_zero=0;
        for k=1:N_img
            if v(k).vy(i,j) && v(k).vy(i,j)<vy_lim_max && v(k).vy(i,j)>vy_lim_min &&
abs(v(k).vx(i,j))<vx_lim

```

```

    u2(i,j)=u2(i,j)+((v(k).vy(i,j)-vy_ave(i,j))^2);

    v2(i,j)=v2(i,j)+((v(k).vx(i,j)-vx_ave(i,j))^2);

    uv(i,j)=uv(i,j)+(v(k).vx(i,j)-vx_ave(i,j))*(v(k).vy(i,j)-vy_ave(i,j));

    count_non_zero=count_non_zero+1;

    end

end

count_n_z_1(i,j)=count_non_zero;

if ~count_non_zero

    v2(i,j)=0;

    u2(i,j)=0;

    uv(i,j)=0;

else

    u2(i,j)=(u2(i,j)/count_non_zero);

    v2(i,j)=(v2(i,j)/count_non_zero);

    uv(i,j)=(uv(i,j)/count_non_zero);

end

end

end

TI_vy=sqrt(u2)/U_b;

TI_vx=sqrt(v2)/U_b;

v2_mean=zeros(1,count_x_n);

u2_mean=zeros(1,count_x_n);

uv_mean=zeros(1,count_x_n);

for i=1:count_x_n

```

```

v2_mean(1,i)=sum(v2(i,:))/sum(v2(i,:)~=0);
u2_mean(1,i)=sum(u2(i,:))/sum(u2(i,:)~=0);
uv_mean(1,i)=sum(uv(i,:))/sum(uv(i,:)~=0);
end

%%%%%%***** Averaging for Turbulence intensity profiles

TI_vy_mean=zeros(1,count_x_n);
TI_vx_mean=zeros(1,count_x_n);
TI_vy_mean(1,1:count_x_n)=sqrt(u2_mean(1,1:count_x_n))/U_b;
TI_vx_mean(1,1:count_x_n)=sqrt(v2_mean(1,1:count_x_n))/U_b;

%%%%%%***** calculating the U_plus and Y_plus

y_plus=(R-abs(x))*U_w/Nu/1000;
U_plus=vy_ave_mean/U_w;
kapa=0.41;
C_plus=5.50;
U_plus_theo=1/kapa*log(y_plus(1:end))+C_plus;

%%%%%%***** saving the variables

clear v;
fprintf('\n');
display('Saving....');

```

